Coincident Detection of Cherenkov Photons for Medical Applications

DISSERTATION
zur Erlangung des Grades eines Doktors
der Naturwissenschaften

vorgelegt von
M.Sc. Reimund Bayerlein

eingereicht bei der Naturwissenschaftlich-Technischen Fakultät
der Universität Siegen
Siegen 2020

Betreuer und erster Gutachter
Prof. Dr. Ivor Fleck
Universität Siegen

Zweiter Gutachter
Priv.-Doz. Dr. Thilo Michel
Universität Erlangen-Nürnberg

Tag der mündlichen Prüfung
25. Juni 2020

Contents

Abstract 1

Zusammenfassung 3

1 Introduction 5
1.1 The Research Topic . . . 5
1.2 Contents and Structure . . . 7

I Thematic Classification 11

2 Particle and Photon Interactions in Matter 13
2.1 Particle Interactions in Matter . . . 13
2.1.1 Energy Loss of Charged Particles in Matter . . . 14
2.1.1.1 Charged Heavy Particles . . . 14
2.1.1.2 Fast Electrons . . . 16
2.1.2 Particle Range and Bragg Peak . . . 18
2.1.3 Multiple Scattering . . . 20
2.1.4 The Cherenkov Effect . . . 22
2.2 Photon Interactions in Matter . . . 28
2.2.1 General Remarks on Photon Interactions . . . 29
2.2.1.1 Attenuation of Photon Beams . . . 29
2.2.1.2 Interaction Probability . . . 30
2.2.2 Photoelectric Effect . . . 33
2.2.3 Compton Effect . . . 36
2.2.3.1 Process Description . . . 36
2.2.3.2 Energy Transfer in Compton Scattering . . . 36
2.2.3.3 Angular Distributions of Compton Scattered Photons and Electrons . . . 38
2.2.4 Pair Production . . . 41

3 Photon Detection in Medical Applications 45
3.1 Introduction . . . 45
3.2 Gamma Ray Detection in Particle Therapy . . . 48
3.2.1 Particle Therapy Treatment . . . 49
3.2.1.1 Introduction and Overview . . . 49
3.2.1.2 Physics of Proton Therapy . . . 51

3.2.1.3 Range Uncertainty in Proton Therapy . . . 53
3.2.2 In vivo Proton Range Verification . . . 54
3.2.3 Prompt-Gamma Detection . . . 57
3.3 The Compton Camera . . . 60
3.3.1 General Concept . . . 60
3.3.2 Resolution and Limitations . . . 61
3.3.3 Potential Improvement Through Electron Tracking . . . 62
3.3.4 Current Research Status . . . 62

4 Single Photon Detectors 65
4.1 Semiconductor Detectors . . . 65
4.1.1 Introduction . . . 65
4.1.2 Thermal Excitation and the Origin of Dark Count . . . 66
4.1.3 The pn-junction . . . 67
4.2 Photodiodes . . . 69
4.2.1 PN and PIN Diodes . . . 69
4.2.2 Avalanche Photodiodes . . . 70
4.3 The Silicon Photomultiplier (SiPM) . . . 72
4.3.1 Physical Principle . . . 72
4.3.2 Properties and Characteristics . . . 74

II Concept and Proof of Principle 79

5 Detection of Electrons Using Cherenkov Light 81
5.1 Detection Principle . . . 82
5.2 Requirements . . . 84
5.3 Challenges . . . 85
5.4 Towards a Proof of Principle . . . 87

6 Set-Up and Detector Components 89
6.1 Overview . . . 89
6.2 Signal Read-Out Using an SiPM Timing Chip (STiC) . . . 91
6.2.1 Technical Layout and Design . . . 93
6.2.2 Signal processing . . . 93
6.3 Charge Sensitive Read-Out Using a 4 GHz Oscilloscope . . . 96
6.4 Silicon Photomultiplier Array . . . 97
6.4.1 Device Description . . . 97
6.4.2 Key Characteristics . . . 98
6.4.3 Temperature Dependencies . . . 101
6.5 Radiator Materials . . . 106
6.5.1 Sample Preparation . . . 106
6.5.2 Transmission Measurements . . . 107
6.5.3 Discussion of Different Material Thicknesses and Types . . . 110
6.5.4 Absorption Coefficient . . . 112

7 Theoretical Expectations **115**
7.1 Estimation of the Number of Generated Cherenkov Photons . . . 115
7.2 Estimation of the Number of Detected Photons . . . 118
7.3 Applications . . . 123
7.3.1 Number of Detected Photons Versus Electron Energy . . . 123
7.3.2 Threshold on the Minimum Number of Detected Photons . . . 123
7.3.3 Photon Spectrum . . . 124
7.4 Discussion . . . 126

8 First Measurements to Prove the Principle **127**
8.1 Coincident Detection of Cherenkov Photons . . . 127
8.1.1 Method Description . . . 128
8.1.1.1 Measurement Procedure . . . 128
8.1.1.2 Coincidence Search Algorithm . . . 128
8.1.1.3 Correction of Inherent Time Differences . . . 130
8.1.2 Measurements . . . 131
8.1.2.1 Coincidence Time Resolution . . . 131
8.1.2.2 Distribution of Coincident Photon Hits . . . 132
8.1.2.3 Light Yield Quantification Using Time over Threshold . . . 133
8.2 Photon Counting Using Charge Integration . . . 135
8.2.1 Calibration . . . 135
8.2.2 Measurement Procedure . . . 138
8.3 Results . . . 139
8.3.1 Measured Light Intensity and Number of Detected Photons . . . 139
8.3.2 Quantification of the Occupancy of the Detector Array . . . 141
8.3.3 Reconstruction of the Electron Source Location from Accumulated Events . . . 142
8.4 Conclusion on the Proof of Principle . . . 142

9 Improved Set-Up Using TOFPET2-ASIC **145**
9.1 Design of the Set-Up . . . 146
9.1.1 Overview . . . 146
9.1.2 Radiator Materials . . . 147
9.1.3 Cooling System . . . 147
9.1.4 Assembling . . . 148
9.2 Signal Read-Out Using the PETsys TOFPET2-ASIC . . . 149
9.2.1 Technical Layout and Design . . . 149
9.2.2 The TOFPET2 ASIC . . . 151
9.2.3 Configuration, Calibration and Data Processing . . . 151
9.3 Commissioning . . . 152
9.3.1 Threshold Setting . . . 152
9.3.2 Characteristics of the Acquisition System at Low Temperatures . . . 153

10 Coincident Detection of Cherenkov Photons on 64 Channels **157**
10.1 Measurement and Analysis Procedure . . . 157
10.2 Distribution of Coincident Cherenkov Photons . . . 159

10.2.1 Sensitivity to Sample Thickness and Source Location . . . 159
10.2.2 Quantifying the Occupancy of the Array . . . 162
10.2.3 Energy Dependence of the Measured Pattern . . . 164
10.2.4 Reconstruction of the Electron Source Location from Accumulated Events . . . 165
10.3 Timing Corrections . . . 166
10.3.1 Problem Description . . . 166
10.3.2 Time Difference Compensation Using Time over Threshold . . . 168
10.3.3 Implementation in the Analysis of Coincidence Measurements . . . 170
10.3.4 Coincidence Time Resolution . . . 170
10.4 Contribution of Random Coincidences . . . 173
10.4.1 Expectation . . . 173
10.4.2 Measured Number of Random Coincidences . . . 175

11 Counting Coincident Cherenkov Photons 177
11.1 Relation between Time over Threshold and Number of Detected Photons . . 178
11.2 Calibration Procedure . . . 179
11.2.1 Data Taking . . . 179
11.2.2 Analysis Procedure . . . 180
11.3 Application to Measurements . . . 181
11.3.1 Number of Detected Photons per Channel . . . 182
11.3.2 Average Number of Detected Photons Per Event . . . 184
11.3.3 Results with Various PMMA Thicknesses . . . 186
11.3.4 Discussion . . . 188
11.4 Applicability to Electron Energy Measurements . . . 191

III Applicability to Photon Detection 197

12 Detection of 511 keV Photons 199
12.1 Dual-Face Coincidence Set-Up . . . 200
12.1.1 Details on the Instrumentation . . . 200
12.1.2 Scintillation Materials and Photon Detectors . . . 203
12.2 Data Processing and Analysis Method . . . 205
12.2.1 Preselected Events . . . 205
12.2.2 List Mode Data . . . 206
12.3 Detector Configuration and Parameter Setting . . . 207
12.3.1 Measurement Settings . . . 208
12.3.2 Analysis Parameters . . . 210
12.3.3 Correction of Inherent Time Differences . . . 213
12.4 Characteristics of the Coincidence Measurement . . . 214
12.4.1 Quality of the Measurement Signal . . . 214
12.4.2 Energy cut on 511 keV . . . 217
12.4.3 Measured coincidence rate . . . 218
12.4.4 Coincidence time resolution (CTR) . . . 219
12.5 Efficiency Estimation for the Detection of 511 keV Photons . . . 220

12.5.1 Derivation of the Efficiency . . . 220
12.5.2 Method Description . . . 221
12.5.3 Background Estimation . . . 223
12.5.4 Efficiency Estimation for NaI and $LaBr_3$(Ce) . . . 227
12.5.5 Investigation of Systematic Uncertainties . . . 227
12.5.6 Final Result and Discussion . . . 230
12.6 Comparison to Simulation Results . . . 231
12.6.1 Implementation . . . 231
12.6.2 Results and Discussion of Systematic Uncertainties . . . 232
12.6.3 Efficiency at Higher Photon Energies . . . 233
12.7 Further Measurements with the Cherenkov Detector . . . 234
12.7.1 Detected Pattern of Coincident Hits . . . 234
12.7.2 Counting Cherenkov Photons from Compton- and Photoelectrons . . . 236
12.7.3 Variable Gamma Source Positions . . . 240
12.8 Summary of the Detection of 511 keV Photons . . . 242

13 Summary and Outlook **245**
13.1 Summary of the Contents . . . 245
13.2 Prospect and Future Potential . . . 247
13.3 Conclusion . . . 249

A Addendum **251**
A.1 Tables and Values . . . 251
A.2 Calculation of Statistical Uncertainties . . . 252
A.2.1 Mean Number of Detected Photons . . . 252
A.2.1.1 Central Limit Theorem (CLT) . . . 252
A.2.1.2 Averaging Weighted Errors . . . 253
A.2.1.3 Conclusions . . . 255
A.2.2 Efficiency estimation: . . . 255
A.3 Number of Detected Photons per Sample Thickness . . . 257
A.4 Log File in Dual-Face Detector Analysis . . . 257

B List of Abbreviations **259**

C List of Figures **261**

D List of Tables **267**

References **267**

Acknowledgements **279**

Gewidmet meiner lieben Mama,
die mich Zeit meines Lebens unterstützt hat.

Abstract

The detection of higher energetic gamma rays ($\geq 1\,\mathrm{MeV}$) is of increasing importance in medical imaging and nuclear medicine. Especially proton therapy treatment could benefit from the ability to measure prompt gammas emitted subsequent to the irradiation of the patient with high-energetic sub-atomic particles like protons. Such an imaging modality would help monitor the treatment process and ensure correct particle range and optimal dose delivery to the tumor while sparing surrounding healthy tissue.

One potential gamma detector for medical applications is the Compton camera – a two-layer detection system, where an incoming gamma scatters in a first detection layer and is absorbed in a second layer. In the first layer, a Compton electron is created, which carries a large part of the momentum information about the incoming gamma. A coincidence measurement of energy and position of both the electron and the absorbed gamma enables to reconstruct the gamma source location to lie on the surface of a cone. Knowledge of the electron momentum direction enables to confine the origin to an arc. The real reconstructed source position is obtained by the measurement and superposition of many of these cones or arcs, respectively.

In this work, a novel detection concept for the Compton scattered electron is presented and investigated, which is based on the coincident measurement of Cherenkov photons created by that electron in an optically transparent radiator material. The photons are emitted along the surface of a cone with a characteristic opening angle that mainly depends on the refractive index of the material and the velocity of the electron. The intersection of this Cherenkov cone with a photon sensitive detector area forms a ring or an ellipse, which can be used to reconstruct the cone and the momentum direction of the electron. The number of emitted photons yields information on the electron energy, while the size of the ellipse contains information on the scattering vertex position.

A first proof of this concept is provided in this thesis. In a first test set-up, a successful coincident measurement of Cherenkov photons on an array of Silicon-Photomultipliers (SiPMs) was performed. The photons were created by electrons from a ^{90}Sr source inside radiator materials of different types and thicknesses. A coincidence time resolution of 242 ps could be achieved using signal read-out based on an application specific integrated circuit (ASIC). The number of detected photons could be counted with a charge integrating measurement and analysis method using an oscilloscope. The width of the distribution of the measured patterns was quantified and was in good agreement with predictions. All results were compared with calculations, which were performed under consideration of electron energy and range, detection efficiency of the SiPM, detector geometry and absorption properties of the radiator. A sensitivity of the measured pattern to the thickness of the sample and to the position of the electron source was observed from accumulated coincident events. These patterns also allowed for a reconstruction of the electron source position with an accuracy better than 1 mm. In the scope of the development of the set-up and measurement method, all detector

components were investigated to find the optimal parameter settings and the most suited radiator materials.
With an improved set-up with a different ASIC and cooled detectors a coincident light detection on single photon level was possible. An extensive correction algorithm allowed for a compensation of time walk effects and inherent time differences between individual ASIC channels. The ability to count the number of detected Cherenkov photons per event and per Silicon Photomultiplier (SiPM) channel was implemented using the Time over Threshold (TOT) information of the SiPM signals. The average number of detected photons per event was measured for various sample thicknesses and the results were compared to calculations and simulations performed with GEANT4.

After these first successful coincidence measurements, the detection principle was applied to the detection of Compton scattered electrons and photo electrons created by 511 keV photons from a ^{22}Na source in UV transparent Polymethyl Metacrylate (PMMA). A detection efficiency on the order of 10^{-3} was found. Simulations indicate a strong increase in the efficiency to about 3 % for higher gamma energies. The number of detected Cherenkov photons from Compton electrons was counted and compared with simulation results. The measured coincidence pattern from accumulated events showed response to a shift of the gamma source position.

The ability to detect Cherenkov photons from Compton electrons in coincidence could be successfully demonstrated. In future works, the patterns of individual events need to be used to reconstruct the Cherenkov cone and the electron momentum direction. The achievements in this thesis constitute a vital step towards an application of this electron detection principle for medical purposes and could help realize prompt gamma detection in particle therapy treatment using a Compton camera.

Zusammenfassung

Die Detektion höherenergetischer Gammastrahlung ($\geq 1\,\mathrm{MeV}$) ist von wachsender Bedeutung für die medizinische Bildgebung und die Nuklearmedizin. Besonders die Partikeltherapie könnte von der Möglichkeit profitieren, prompte Gammastrahlen zu messen, welche in Folge der Bestrahlung des Patienten mit hochenergetischen, subatomaren Teilchen wie Protonen emittiert werden. Solch ein Bildgebungsverfahren würde die Überwachung des Behandlungsprozesses unterstützen und dabei helfen, die korrekte Teilchenreichweite und die optimale Dosisverabreichung im Tumor sicherzustellen und dabei umliegendes Gewebe zu schonen.

Ein Kandidat für einen Gammadetektor in medizinischen Anwendungen ist die Compton Camera – ein zweilagiges Detektorsystem, bei welchem ein einfallendes Gamma in einer ersten Detektorschicht streut und in einer zweiten absorbiert wird. In der ersten Schicht wird ein Compton-Elektron erzeugt, welches einen großen Teil der Impulsinformation des einfallenden Gammas trägt. Eine koinzidente Messung von Energie und Position des Elektrons als auch des gestreuten Gammas ermöglicht es, die Ursprungsrichtung des Gammas auf die Oberfläche eines Kegels einzuschränken. Kenntnis des Elektronenimpulses ermöglicht eine Einschränkung des Usprungs auf einen Kreisbogen. Die tatsächliche rekonstruierte Quellposition wird durch Messung und Überlagerung vieler dieser Kegel beziehungsweise Kreisbögen gewonnen.

In dieser Arbeit wird ein neues Messkonzept für Compton-gestreute Elektronen präsentiert und untersucht, welches auf der koinzidenten Messung von Cherenkovphotonen basiert, die durch das Elektron in einem optisch transparenten Radiatormaterial abgestrahlt werden. Die Photonen werden entlang der Oberfläche eines Kegels mit charakteristischem Öffnungswinkel emittiert, welcher hauptsächlich vom Brechungsindex des Materials und der Geschwindigkeit des Elektrons abhängt. Der Schnitt des Cherenkovkegels mit einer lichtsensitiven Detektorebene erzeugt einen Ring oder eine Ellipse, welche dazu verwendet werden kann, den Kegel und die Impulsinformation des Elektrons zu rekonstruieren. Die Anzahl der emittierten Photonen gibt Aufschluss über die Energie des Elektrons, während die Größe der Ellipse Informationen über die Position des Compton-Streuvertex enthält.

Ein erster Machbarkeitsnachweis wird in dieser Dissertation vorgestellt. Eine erfolgreiche Koinzidenzmessung von Cherenkovphotonen auf einem Array von Silizium-Photomultipliern (SiPMs) wurde mit einem ersten Testaufbau durchgeführt. Die Photonen wurden von Elektronen aus einer ^{90}Sr-Quelle in Radiatormaterialien unterschiedlicher Typen und Stärken erzeugt. Unter Verwendung einer Ausleseelektronik basierend auf einem Application Specific Integrated Circuit (ASIC) konnte eine Koinzidenzzeitauflösung von 242 ps erreicht werden. Die Anzahl der detektierten Photonen konnte mit einem Oszilloskop mittels Ladungsintegration gezählt werden. Die Breite der Verteilung der aufgenommenen Pattern (Hitmuster koinzidenter Photonen) wurde quantifiziert und war in guter Übereinstimmung mit Vorhersagen. Alle Ergebnisse wurden mit Berechnungen verglichen, welche unter Berücksichtigung von Elektronenenergie und -reichweite, Detektionseffizienz des SiPM, Detektorgeometrie

und Absorptionseigenschaften des Radiators angestellt worden waren. Es wurde eine Sensitivität der gemessenen Pattern von akkumulierten Ereignissen hinsichtlich Radiatorstärke und Quellposition beobachtet. Diese Pattern ermöglichten es des Weiteren, die Position der Elektronenquelle mit einer Genauigkeit von unter 1 mm zu rekonstruieren. Im Rahmen der Entwicklung des Messaufbaus und der Messmethode wurden alle Detektorkomponenten untersucht, um die optimalen Einstellungen und die am besten geeigneten Radiatormaterialien zu finden.
Mit einem verbesserten Aufbau unter Verwendung eines anderen ASICs und gekühlten Detektoren war eine koinzidente Lichtdetektion auf Einzelphotonenniveau möglich. Ein aufwändiger Korrekturalgorithmus ermöglichte die Kompensation von Time-Walk-Effekten und inherenten Zeitunterschieden zwischen einzelnen Kanälen des ASICs. Die Möglichkeit, die Anzahl detektierter Cherenkovphotonen zu zählen, wurde unter Verwendung der Time-over-Threshold-Information der SiPM-Signale umgesetzt. Die mittlere Anzahl detektierter Photonen pro Ereignis wurde für unterschiedliche Materialstärken gemessen und mit Berechnungen und GEANT4-Simulationen verglichen.

Nach diesen ersten erfolgreichen Koinzidenzmessungen wurde das Detektionsprinzip für den Nachweis von Compton- und Photoelektronen verwendet, welche in UV-transparentem Polymethylmethacrylat (PMMA) von Photonen mit einer Energie von 511 keV aus einer ^{22}Na Quelle erzeugt wurden. Es wurde eine Detektionseffizienz in der Größenordnung von 10^{-3} ermittelt. Simulationen deuten auf einen starken Anstieg der Effizienz auf etwa 3 % für höherenergetische Gammas hin. Die Anzahl der detektierten Cherenkovphotonen von Comptonelektronen wurde gezählt und mit Simulationsergebnissen verglichen. Die gemessenen Koinzidenzmuster von akkumulierten Ereignissen sprachen auf eine Änderung der Position der Gammaquelle an.

Die Möglichkeit, Cherenkovphotonen vom Comptonelektronen in Koinzidenz zu detektieren, konnte erfolgreich nachgewiesen werden. In zukünftigen Arbeiten müssen die Pattern einzelner Ereignisse verwendet werden, um den Cherenkovkegel und den Elektronenimpuls zu rekonstruieren. Die Erfolge in dieser Dissertation stellen einen wesentlichen Schritt in Richtung einer Anwendung für medizinische Zwecke dar und könnten dazu beitragen, Prompt-Gamma-Detektion in der Partikeltherapie mittels Compton Cameras zu realisieren.

1. Introduction

Contents

1.1 The Research Topic 5
1.2 Contents and Structure 7

1.1. The Research Topic

Seventy-four years after Robert Wilson suggested the use of accelerated particles to treat cancerous tissue [Wil46], particle therapy has become a wide spread treatment method for tumors in countless facilities all over the world [Gro19]. Constantly ongoing developments and improvements regarding treatment quality, treatment method and monitoring devices make it a vivid and fast evolving research field in medical physics.

The term *cancer* describes the uncontrolled growth of abnormal cells that can occur anywhere in the body. It can manifest in over 200 different types, which can have multiple causes like exposure to chemical or toxic components, ionizing radiation or even human genetics. Type and stage of the disease determine the treatment protocol, which in most cases involves one or several of the following therapeutic methods: surgery, chemotherapy or radiation therapy with photons or ionizing particles. [Dav19]

Extensive research on this topic will always be desired, as cancer is still among the leading causes of death worldwide. According to the *International Agency for Research on Cancer* 4.2 million new cancer cases occurred only in Europe in 2018, causing 1.9 million deaths [Glo19]. Worldwide an estimated 9.6 million patients did not survive the disease in the year of 2018. The highest mortality was observed for cancer in lung and bowel (colorectal cancer), which both make up for more than a fourth of the deaths by cancer. Considering that the number of new cancer cases per year is expected to rise to 23.6 million by 2030 [Nat18], cancer – and especially its treatment – is a pressing issue.

Particle therapy constitutes one promising treatment modality. High energetic, subatomic particles are used to damage cancer cells and potentially stop them from growing and dividing. This can eventually kill the cancer cells that have been treated with radiation [SJ16]. It shows an advantageous dose distribution – compared to therapy with photons – with a potentially high conformity between dose delivery and tumor volume while sparing most of the healthy tissue [Bon93]. The finite particle range and the steerable, straight particle beam, furthermore, piqued the interest of the medical community. This treatment method has experienced a large growth of patient numbers especially throughout the last decade. As

reported by the *Particle Therapy Co-Operative Group*, the number of patients that received particle therapy treatment increased by about a factor of three in the years between 2007 and 2018. In 2018 more than 200000 cancer patients have been treated, most of them with proton beams [Gro19]. Carbon ion beam treatment has become an alternative particle therapy type, which has also shown increasing patient numbers throughout the last years. A graphical representation of the development of patient numbers over the last decade is shown in figure 1.1, which impressively demonstrates the growing faith in particle beam therapy as vital part of the various cancer treatment options.

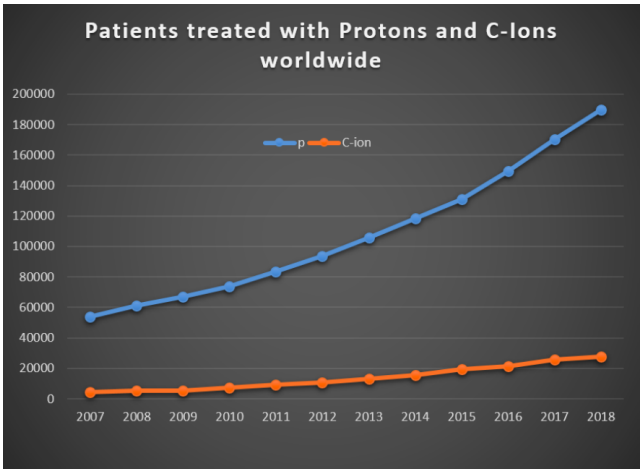

Figure 1.1.: Statistics of patients treated in particle therapy facilities worldwide. [Gro19]

In order to ensure treatment quality and to verify correct dose delivery to the tumor, imaging methods are desired that allow for monitoring and controlling the particle beam during the treatment. One key aspect of beam monitoring is to verify the range of the particles inside the body to ensure optimal dose delivery to the tumor and to spare proximal and distal structures (this is explained in more detail in chapter 3.2). A potential imaging modality for that purpose is the detection of low MeV prompt gammas that are emitted along the beam path subsequent to the irradiation with particles.

Gamma detection concepts already exist for lower energies ($\leq 511\,\mathrm{keV}$) and were successfully tested and implemented in clinical practice like Single Photon Emission Computed Tomography (SPECT). Here, photons are emitted after injection of radioactive tracers into the body. The detection principle requires collimators to obtain momentum information on the photons and to be able to reconstruct the source location. In general, the sensitivity for the detection of emitted photons increases for larger collimator holes, but that impairs the resolution and vice versa. Especially at higher photon energies, resolution and sensitivity become increasingly challenging to maintain. Thus, collimating gamma detection systems like SPECT are impractical at higher energies such that they cannot be considered for prompt gamma detection. [VA+15]
Novel concepts are required for that purpose.

The development and improvement of various detection techniques for higher energetic gammas like the Slit Camera, Prompt Gamma Timing or Single Plane Compton Imaging shows the great interest among the medical physics community. More details on the detection of prompt gammas are provided in section 3.2.3.

The Compton camera constitutes another possible gamma imaging technique. The gamma rays to be detected undergo Compton scattering in a first detector layer and are absorbed in a second layer. Coincident measurement of the position and the energy of the scattered gamma together with the scattering vertex allows to confine the gamma source position to the surface of a cone. The concept requires a position-sensitive measurement of the Compton scattered electron. Measurement of the electron momentum direction can improve the reconstruction of the gamma source location and an energy measurement enables the reconstruction of gammas with unknown initial energy. All details on the Compton camera will be provided in section 3.3.

This thesis investigates a detection modality for Compton electrons using Cherenkov light created by that electron in an optically transparent radiator material. The principle has been proposed in 2012 by T. Peterson, A. Brill and A. Walenta [PBW12]. Cherenkov photons are emitted along the surface of a cone with a characteristic opening angle mostly depending on the refractive index of the material, in which the photons are created. Coincident detection of these photons allows for a reconstruction of the Cherenkov cone and, thus, also the momentum direction of the electron and the scattering vertex position. Counting the number of detected photons yields information on the energy of the Compton electron. Due to the instantaneous nature of Cherenkov light, it is well suited for the use in a coincidence measurement in a gamma detector like the Compton camera.

For the first time since the concept has been proposed, the feasibility of this electron detection principle has been investigated through measurements at the university of Siegen. It unites fundamental physical principles like the Compton and Cherenkov effect in one novel detection system with the purpose of advancing a medical imaging technique. A successful electron measurement with this principle could be a major step towards a working Compton camera prototype for a gamma detector in medical applications.

1.2. Contents and Structure

This thesis is divided into three parts: a thematic classification, a proof of the concept and finally an investigation of the applicability of this electron detection modality to the measurement of gamma rays.

The first part will give an introduction to particle and photon interaction processes that play an important role in this work. In particular, range, energy loss and multiple scattering of electrons play an important role. Special attention will be given to a thorough introduction to the Cherenkov effect, which constitutes the essential physical process in this detection concept. Photon interactions – foremost via Compton scattering – will be covered comprehensively.

The medical context is described afterwards in chapter 3, beginning with the importance of photon detectors in medical applications culminating in the detection of gamma radiation emitted during and after particle therapy treatment. This leads to the Compton camera, which is explained in the last section of chapter 3.

The detection of single photons is of utmost importance for the success of this thesis and the herein investigated concept. Therefore, the semi-conductor based detection devices like the Silicon Photomultiplier (SiPM) used in this thesis are explained in chapter 4.

The second part of this thesis explains the detection concept for electrons using Cherenkov light (chapter 5) and presents the first test set-up capable of demonstrating the principle. The detector components are explained and characterized in chapter 6 and a calculation algorithms for the computation of theoretical expectations is introduced in chapter 7. The measurement and analysis procedures for an application specific integrated circuit (ASIC) based read-out system for coincident photon detection and for an oscilloscope based charge integrating read-out system are discussed in chapter 8. In this chapter the first results for various detector properties are presented – like type and thickness of the radiator material – and are compared to theoretical expectations.

An improved, cooled set-up with a different ASIC and the capability for coincident light detection on single photon level on 64 detector channels is subject of chapter 9. The key characteristics of this set-up will be explained and details on the assembling and commissioning process will be given.

The sensitivity to the source location and a quantification of the width of the measured distribution are discussed in chapter 10. In this chapter an algorithm is presented that was developed to measure and compensate for time walk effects and inherent time differences between channels based on Time over Threshold (TOT) values of the measured signals. The coincidence time resolution is subsequently calculated.

The ability for photon counting using the TOT of SiPM signals is demonstrated in chapter 11. The number of detected Cherenkov photons are counted per channel and event and compared to theoretical expectations and simulations performed in Geant4. The ability to reconstruct information on the electron energy from measuring the number of detected Cherenkov photons is investigated in the last section of chapter 11.

The third part of this work contains the application of this electron detection method to gamma ray measurements. The efficiency for the detection of 511 keV photons from a ^{22}Na source was calculated. The results will be shown in chapter 12 and thoroughly discussed and compared to simulations as well as calculations. The properties of the measurement signal, the number and distribution of detected Cherenkov photons and a simulation based outlook are provided in the same chapter. This third part of the thesis examines the feasibility of the concept for photon detection and allows for first conclusions on the applicability of Cherenkov based electron detection for medical applications like the Compton camera.

The final conclusion will be provided in chapter 13. All findings from measurement, simulation and calculation as well as any remaining open questions will be taken into consideration.

To promote comprehension, this thesis contains a list of abbreviations in the appendix chapter B. One more remark shall be given regarding the citation format: references are often provided at the end of a paragraph and refer to the whole content of that paragraph. This applies especially to Part I. Thematic Classification. Specific values, figures or findings that can be associated with a certain publication or project, are cited directly where they appear in the text.

Part I.

Thematic Classification

2. Particle and Photon Interactions in Matter

Contents

2.1 Particle Interactions in Matter **13**
2.1.1 Energy Loss of Charged Particles in Matter 14
2.1.1.1 Charged Heavy Particles 14
2.1.1.2 Fast Electrons 16
2.1.2 Particle Range and Bragg Peak 18
2.1.3 Multiple Scattering 20
2.1.4 The Cherenkov Effect 22
2.2 Photon Interactions in Matter **28**
2.2.1 General Remarks on Photon Interactions 29
2.2.1.1 Attenuation of Photon Beams 29
2.2.1.2 Interaction Probability 30
2.2.2 Photoelectric Effect 33
2.2.3 Compton Effect 36
2.2.3.1 Process Description 36
2.2.3.2 Energy Transfer in Compton Scattering 36
2.2.3.3 Angular Distributions of Compton Scattered Photons and Electrons 38
2.2.4 Pair Production 41

2.1. Particle Interactions in Matter

The main interaction of charged particles with matter is through ionization and excitation of the medium's atoms. An excited atom will de-excite under emission of electromagnetic radiation, while ionization will remove an electron from the atom, which in some cases can be high energetic. For relativistic particles with a speed close to c (speed of light in vacuum), Bremsstrahlung needs to be taken into consideration as a third channel of energy loss.
This introduction to particle interactions in matter will at first take charged heavy particles into consideration with a mass significantly greater than that of the electrons in the atomic shells. In distinction electrons (and also positrons) as incident particles are treated separately, since in their case incident mass and target mass (electrons in atomic shells) are equal.

2.1.1. Energy Loss of Charged Particles in Matter

2.1.1.1. Charged Heavy Particles

A large fraction of interactions of particles with the medium happens with the electrons of an atom, while nuclear interactions play a minor role [Ber+99]. Therefore, the term *heavy* in this case refers to incident particles with masses much larger than that of electrons ($m \gg m_e$). Examples are protons, alpha particles (Helium-ions) or cosmic muons. Several quantities describe the interaction of charged particles in the medium like the scattering behavior, the range and the energy loss per traveled distance s when traversing a medium of density ρ. The latter one is also called *linear stopping power* and is described by the Bethe-Bloch formula [GS08]:

$$-\frac{\mathrm{d}E}{\mathrm{d}s} = \rho \cdot 4\pi N_A r_e^2 m_e c^2 z^2 \frac{Z}{A}\frac{1}{\beta^2}\left(\ln\frac{2m_e c^2\gamma^2\beta^2}{I} - \beta^2 - \frac{\delta}{2}\right) \tag{2.1}$$

The following constants and parameters have been used:

- z: charge of the particle in units of the elementary charge $1.6 \cdot 10^{-19}\,\mathrm{C}$ [Tie+19]
- Z, A: atomic number and atomic weight of the absorber or target material
- m_e: electron mass $9.109 \cdot 10^{-31}\,\mathrm{kg}$ in SI-units or $511\,{}^{\mathrm{keV}}/_{\mathrm{c}^2}$ given as mass energy equivalent [Tie+19]
- r_e: classical electron radius, which can be expressed as $r_e = \frac{1}{4\pi\varepsilon_0} \cdot \frac{e^2}{m_e c^2}$, where ε_0 is the permittivity of free space [GS08]
- c: vacuum speed of light $(2.998 \cdot 10^8\,{}^{\mathrm{m}}/_{\mathrm{s}})$
- β: speed of the particle given as fraction of the speed of light: $\beta = v/c$
- γ: relativistic gamma factor $\gamma = 1/\sqrt{1-\beta^2}$
- N_A: Avogadro number, which is defined by the International System of Units as the number of atoms per 12 gram ^{12}C (Carbon-12): $N_A = 6.022 \cdot 10^{23}\,{}^{1}/_{\mathrm{mol}}$ [NT19]
- I: mean excitation energy of the absorber material, which can be approximated by $I \approx 16\,Z^{0.9}\,\mathrm{eV}$ (for $Z > 1$)
- δ: parameter that describes how much the extended transverse electric field of incident relativistic particles is screened by the charge density of the atomic electrons. This causes a reduction in energy loss, which is referred to as *density effect* and as the name suggests, is important in dense absorber materials and can be neglected in gases and for lower energetic particles.

The term $2m_e c^2\gamma^2\beta^2$ is identical to the maximum transferable energy $E_{\mathrm{kin}}^{\mathrm{max}}$ from the particle to an electron of the absorber material.
Often, a density independent expression for the energy loss of a particle traversing a medium is desired [MS69]. It is called *mass stopping power* and is roughly independent of the physical

state or the density of the stopping material. The energy loss is then calculated with respect to the area density $x = \rho \cdot s$ with the length units $^{\mathrm{g}}/_{\mathrm{cm}^2}$:

$$-\frac{\mathrm{d}E}{\rho \cdot \mathrm{d}s} = -\frac{\mathrm{d}E}{\mathrm{d}x} \tag{2.2}$$

It has the units $^{\mathrm{MeV \cdot cm}^2}/_{\mathrm{g}}$. Usually, the energy loss of a particle in a specific material is given as mass stopping power (for example in the NIST data base). Thus, to obtain the energy loss per distance (linear stopping power) in units of $^{\mathrm{MeV}}/_{\mathrm{cm}}$ one needs to multiply the *mass* stopping power with the density of the material. As an example, the energy loss of protons in water and ice could be described with the same mass stopping power, but would have different linear stopping power due to the density difference.
The Bethe-Bloch equation (2.1) describes the energy loss via excitation and ionization and is valid for energies with $\beta \gg \alpha \cdot z$, with $\alpha = \frac{e^2}{4\pi\varepsilon_0\hbar c} = \frac{1}{137}$ being the fine structure constant. It cannot be used for small energies similar to that of atomic electrons. The stopping power scales linearly with β in above energy range. Within the valid energy range, however, the stopping power scales with $1/\beta$ until $\beta\gamma > 4$. At this velocity, equation 2.1 reaches a minimum, which is in the range of 10^3 MeV, and therefore also a minimum in the ionization for protons. A particle in that range is also called *minimum ionizing particle* or short *MIP*. Above that range, the energy loss per distance increases again with the logarithmic term in the brackets becoming dominant. For very high energies, the density effect causes the stopping power to saturate.
Figure 2.1 shows the energy loss curve for protons in Polymethyl Metacrylate (PMMA), aluminum and lead. PMMA plays a very important role in this thesis since it serves as radiator material for the creation of Cherenkov photons from higher energetic electrons with a potential application in a Compton camera (see 5.4). Data were taken from the stopping power and range tables for protons provided by the National Institute of Standards and Technology (NIST) [Ber+99]. One can see the linear slope for small energies before the Bethe-Bloch equation can be used at energy values of about 0.1 MeV. After the decrease proportional to $1/\beta$ the minimum ionizing region is reached at about 1000 MeV, before increasing again.

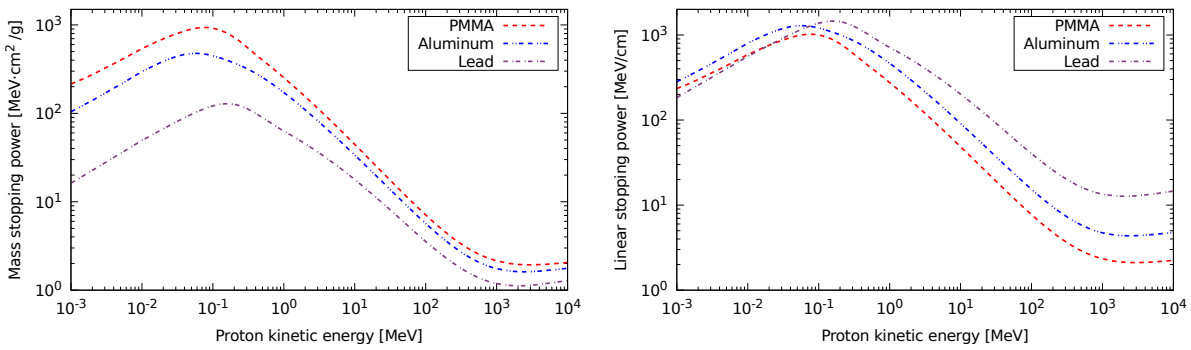

Figure 2.1.: Stopping power (i.e. energy loss per distance) for protons in PMMA, aluminum and lead according to equation 2.1. Left: Density independent mass stopping power. Right: Linear stopping power. Data taken from [Ber+99].

2.1.1.2. Fast Electrons

Fast electrons originate in beta decay processes where a neutron in the nucleus decays into a proton, an electron and an electron-anti-neutrino. Often, this process is accompanied by the emission of gamma radiation when the daughter nucleus was in an excited state. For an investigation of the energy loss per distance in a medium, the electron (and also the positron) plays an exceptional role as incident particle, as it has the same mass as the electrons from the atomic shell it interacts with [GS08]. The energy loss is lower for electrons than for heavier particles like protons [Kno10]. Furthermore, after the collision with an atomic electron, a distinction between initial primary and secondary electron is impossible. To consider this effect in the energy loss equation, one has to take into account all transferable energies between 0 and $\frac{1}{2}(E - m_e c^2)$. This can be used to replace the term for the maximum transfered energy in equation 2.1 using the approximation for relativistic particles $\frac{1}{2}(E - m_e c^2) \approx \frac{E}{2} = \frac{1}{2}\gamma m_e c^2$. The energy-loss equation now reads

$$-\frac{\mathrm{d}E}{\mathrm{d}x} = 4\pi N_A r_e^2 m_e c^2 z^2 \frac{Z}{A}\frac{1}{\beta^2}\left(\ln\frac{\gamma m_e c^2}{2I} - \beta^2 - \frac{\delta^*}{2}\right). \tag{2.3}$$

δ^* takes a slightly different value for electrons than δ did for heavier particles. Modifications to the above expression can be made that consider specific differences between incident heavy particles and electrons. Doing so, one could obtain a more exact formula for the electron energy loss due to ionization and excitation agreeing with the Bethe-Bloch equation within 10-20 %:

$$\begin{aligned} -\frac{\mathrm{d}E}{\mathrm{d}x} = 4\pi N_A r_e^2 m_e c^2 z^2 \frac{Z}{A}\frac{1}{\beta^2}\Bigg(&\ln\frac{\gamma m_e c^2 \beta\sqrt{\gamma-1}}{\sqrt{2}I} + \\ &+ \frac{1}{2}(1-\beta^2) - \frac{2\gamma-1}{2\gamma^2}\ln 2 + \frac{1}{16}\left(\frac{\gamma-1}{\gamma}\right)^2\Bigg) \end{aligned} \tag{2.4}$$

Positrons are treated similarly as they have same mass but opposite charge. There is, however, an additional consideration, which is that positrons are antiparticles annihilating with an electron from the medium when coming to rest.

Figure 2.2 shows the stopping power for electrons again in PMMA, aluminum and lead. Again data were taken from NIST database [Ber+99]. The difference compared to heavy particles gets very distinct especially in the high energy range, where radiation losses (Bremsstrahlung) are the dominant contribution. For heavier particles, Bremsstrahlung is not significant until the GeV range, which is only partly displayed in figure 2.1. The two contributions of energy loss are shown on the example of lead in figure 2.3. In case of Bremsstrahlung, energy loss happens through interaction with the Coulomb field of the nuclei of the medium. The particle decelerates and a fraction of the energy is radiated as photons. While the collision contribution on its own takes a similar shape as described by the Bethe-Bloch equation for heavy particles, the radiation contribution causes a strong increase of the stopping power at energies above 1 MeV.

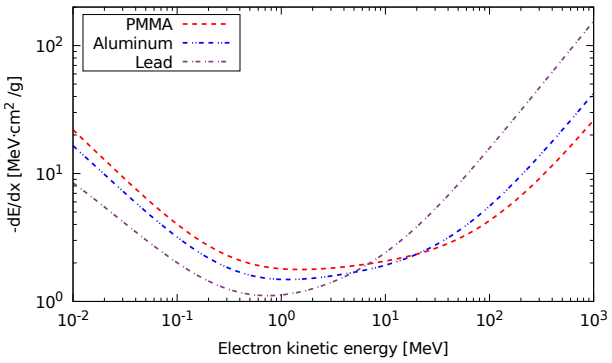

Figure 2.2.: Mass stopping power for electrons in PMMA, aluminum and lead. Data taken from [Ber+99].

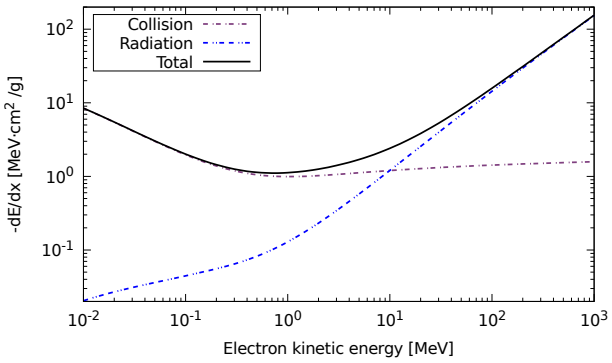

Figure 2.3.: Mass stopping power for electrons in lead. The energy loss via collision and radiation is shown together with the total value. Data taken from [Ber+99].

The energy loss via Bremsstrahlung in case of high energetic electrons can be expressed by [GS08]:

$$-\frac{\mathrm{d}E}{\mathrm{d}x} \approx 4\pi N_A \cdot \frac{Z^2}{A} r_e \cdot E \ln \frac{183}{Z^{1/3}} = \frac{E}{X_0}, \tag{2.5}$$

where X_0 is called the *radiation length*. It is a property of the medium and is defined by the above equation. The interaction of the particle with the Coulomb field of the nuclei explains the proportionality $X_0^{-1} \propto Z^2$. Even though in literature tabulated radiation lengths are meant for electrons, one can define it for other incident particles as well. X_0 would in case of heavier particles be proportional to the mass of the particle squared and is therefore much larger than for electrons. Integration of equation 2.5 leads to a function describing the exponential attenuation of the *energy* of the particle through radiation loss:

$$E = E_0 \exp\left(-\frac{x}{X_0}\right) \tag{2.6}$$

This has similarities to the attenuation of the *intensity* of photons traversing matter as will be shown in section 2.2.1.1. The energy, at which radiation losses (through Bremsstrahlung) and collision losses (though ionization and excitation of the medium) are equal is called *critical energy* E_c and for fixed particle type is a material constant.
In aluminum, the radiation length is $24\,\mathrm{g/cm^2}$ with a critical energy of 40 MeV. In PMMA the radiation length is expectedly larger with a value of $42\,\mathrm{g/cm^2}$, which was calculated using the radiation lengths of each of the components of PMMA (carbon, hydrogen and oxygen) from [GS08] and determining the effective radiation length as follows:

$$X_0 = \frac{1}{\sum_i^N f_i / X_0^i} \tag{2.7}$$

f_i are the mass fractions of the components with their individual radiation length X_0^i. At 1 MeV, the energy loss via Bremsstrahlung for electrons in PMMA according to equation 2.5 is $0.028\,\mathrm{MeV/cm}$. This result incorporates the PMMA density of $1.09\,\mathrm{g/cm^3}$.

2.1.2. Particle Range and Bragg Peak

The distance a particle of a certain energy can travel in a medium is called its *range*. It can be calculated by integrating the inverse mass stopping power over the particle energy range [GS08]:

$$R(E_0) = \int_{E_0}^{m_0 c^2} \frac{\mathrm{d}E}{(\mathrm{d}E/\mathrm{d}x)} \tag{2.8}$$

The range is therefore a function of the start energy of the particle E_0. Since only the kinetic energy can be transfered to the medium, the upper integration boundary is the particle's rest mass $m_0 c^2$. A simple expression for the range is hard to compute, since different energy loss mechanisms exist, like multiple Coulomb scattering or larger energy transfers to atoms of the medium. No analytical form of equation 2.8 exists, so approximations are used in practice and in literature often values from measurements are tabulated.
Due to the integration over the *mass* stopping power, the units of the range are given in $\mathrm{g/cm^2}$. As an alternative name for the range the term *Continuous slowing down approximation range* or short CSDA range is often used [Ber+99].
Figure 2.4 visualizes the effect different materials have on the range of a charged particle: Here, the range of the proton was plotted depending on its energy, meaning that the range value on the ordinate is the total distance a proton of a given energy can travel. Protons in PMMA, aluminum and lead show different ranges. The linear stopping power was used in that representation to make the effect of the density on the range of a particle visible: A proton of the same energy traveles farther in PMMA as it would in lead. Also, the range increases over-proportionally. While a proton of 20 MeV travels only 0.44 cm, protons of twice the energy have a three times larger range (1.53 cm).
The large number of statically distributed collisions and scattering processes cause the actual range of each individual particle to differ from the mean value [MS69]. This effect is referred to as *range straggling* [Kno10] and plays an important role in particle beam therapy, where proton or ion beams are used to deposit energy in a patient's tumor for treatment purposes. The range uncertainty in particle therapy is discussed in chapter 3.2.1 together with appropriate range verification methods. The variation in range is often expressed as fraction of the total mean range $\overline{R}$ of the particle:

$$\Delta R_{\mathrm{rel}} = \frac{R - \overline{R}}{\overline{R}}$$

The reason why particle beams are attractive for this medical purpose lies in the nature of the energy deposition inside a medium: The deposited energy $\mathrm{d}E$ per traveled distance $\mathrm{d}x$ is relatively low and only peaks towards the end of the range. An adjustment of the beam energy to the dimensions of the tumor and the physiology of the patient allows to deposit the maximum energy inside the tumor with a small amount in healthy tissue. Figure 2.5 shows the linear stopping power for a proton of energy 10 MeV in PMMA. The peak at the end of the range is called *Bragg peak* and constitutes the maximum of the stopping power. Actual beam energies in proton therapy are usually one order of magnitude higher. A 100 MeV(200 MeV) proton in PMMA has a calculated range of about 7.3 cm(24.5 cm).

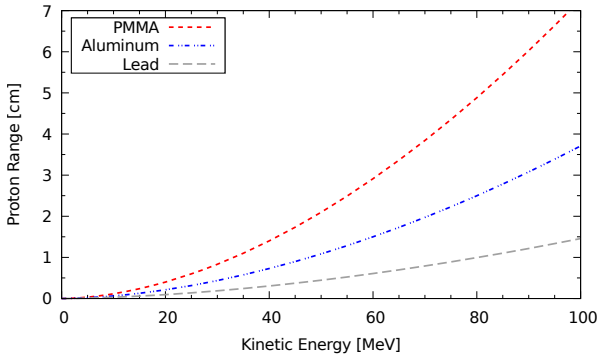

Figure 2.4.: Range of protons depending on their initial energy for different materials. Range data were taken from the NIST data base [Ber+99]

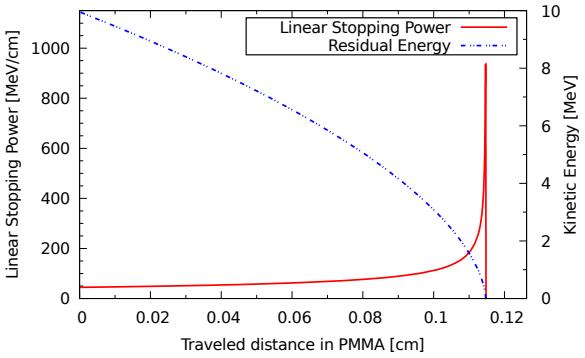

Figure 2.5.: Deposited energy per traveled distance and residual kinetic energy for a 10 MeV proton in PMMA. Data taken from NIST [Ber+99]

For various reasons, electrons – again – take a special role in terms of particle range. Mostly due to the fact that electrons as incident particle have the same mass as their atomic counterparts in the medium, the effect of inelastic and multiple elastic scattering on the range is stronger than for heavier particles (for multiple scattering see section 2.1.3). The path of electrons – especially towards lower energies – can have the nature of a random walk, giving rise to enormous range variations of electrons with the same energy in the same material [MS69]. Electron-nuclear interactions can abruptly change the momentum direction of the electron. Also, Bremsstrahlung of electrons in the absorber medium plays an important role. Finally, *backscattering* complicates the range definition for electrons even more: When entering a medium, the electron can undergo severe deflections so that it re-emerges from the surface of the medium. The range – defined as the distance from start point to the location of thermalization – would then be a negative value. This can have an influence on the signal of particle detectors used for the measurement of externally incident electrons. As an example, 8-10 % of electrons of 1 MeV are backscattered when entering aluminum [Kno10]. In copper this value increases to about 26 %, in gold to almost 50 % while in carbon it is less than 4 %. For sodium-iodine – a common scintillator material – the percentage of backscattered electrons is 37.5 %, and in plastic scintillators about 3.2 %.

In conclusion, a reliable definition of the range for electrons is challenging. The *practical range* can be defined by investigating the intensity of electron beams sent through absorbers of different thicknesses [GS08]. However, already at small thicknesses particle loss occurs even at higher electron energies due to scattering, effectively removing electrons from the beam. On the other hand even at relatively large thicknesses, there can be electrons remaining in the beam that had the least change of their initial direction. The ESTAR (electron stopping power and range) data base provided by NIST calculates the range based on discrete stopping power values obtained via the Bethe-Bloch equation including density-effect corrections. Uncertainties on the range, therefore, originate in uncertainties on the stopping power, which can reach levels of up to 10 % in the energy range between 10 and 100 keV [Ber+99].

The concept of range is less definite for electrons than it is for protons or heavier charged particles, since the total track length can be significantly larger than the distance of penetration.

In this work the range values tabulated by the ESTAR data base were used to estimate the Cherenkov light yield in an optically transparent material taking the energy loss and the traveled distance into consideration. The data base provides the advantage of choosing number and step size of the energy values, for which the range is computed. This made the use of the table quite flexible and the calculations of the Cherenkov light yield more accurate. Figure 2.6 shows the range of electrons in different materials depending on their energy. The data points were computed using ESTAR. Even though the range is subject to aforementioned fluctuations, the tendency of larger traveled distances in less dense materials can be observed.

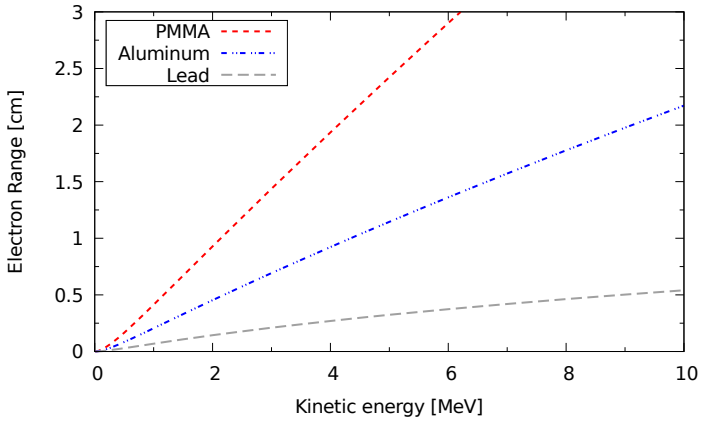

Figure 2.6.: Electron ranges depending on their energy in different materials. Data were taken from the NIST data base [Ber+99].

2.1.3. Multiple Scattering

Multiple scattering is an important issue to be taken into consideration, as will be demonstrated in the description of the detection principle for Compton scattered electrons using Cherenkov photons in chapter 5. A particle traversing matter interacts with the surrounding atoms via Coulomb interactions. Additionally to ionization losses caused by collisions with atomic electrons, deflections in the Coulomb field of nuclei and atomic electrons occur. These interactions cause the particle to be scattered frequently at very small angles with respect to the initial momentum direction. Multiple Coulomb scattering is described by *Molière's theory* and a normal distribution of the scattering angles around an expectation value of $\theta = 0°$ is predicted. Collisions with the nucleus can cause larger scattering angles. The root mean square of the scattering-angle distribution of a particle passing through a scattering layer of thickness d at a velocity close to c can be expressed as follows [GS08]:

$$\theta_{\text{plane}}^{\text{rms}} = \sqrt{\langle\theta^2\rangle} = \frac{13.6\,\text{MeV}}{\beta c p} z \sqrt{\frac{d}{X_0}} \cdot \left(1 + 0.038\,\ln\left(\frac{d}{X_0}\right)\right) \tag{2.9}$$

p is the particle momentum and z its charge, while X_0 denotes the radiation length as defined in expression 2.5. Angle θ in expression 2.9 is the projection onto a plane perpendicular to the initial momentum direction (z-direction, without loss of generality), which is explained in

figure 2.7. Results are most accurate for small thicknesses: $d \ll X_0$ [Eid+04]. Deflections into x- and y-direction are equally distributed and independent from another. The non-projected, spherical distribution is obtained by multiplication with $\sqrt{2}$:

$$\theta_{\text{space}}^{\text{rms}} = \sqrt{2} \cdot \theta_{\text{plane}}^{\text{rms}} \tag{2.10}$$

Equation 2.9 only holds for small $\sqrt{\langle\theta^2\rangle}$ and in the absence of large-angle scatterers [Tan+18]. Due to the complexity of the scattering, equation 2.9 is already an approximation. For electrons – and in general particles with $z = 1$ – it can be further approximated:

$$\theta_{\text{plane}}^{\text{rms}} \approx \frac{13.6\,\text{MeV}}{\beta cp} \cdot \sqrt{\frac{d}{X_0}} \tag{2.11}$$

The root mean square of the angle is a measure for the average deflection of a particle due to scattering of any kind. It can easily be seen that the influence of multiple scattering increases for higher atomic number of the medium due to the dependency on $\sqrt{1/X_0} \propto Z$. Besides, $\sqrt{\langle\theta^2\rangle}$ increases for lighter and also lower-energetic particles as indicated by the factor βcp in the denominator. From that circumstance, one can conclude that the trajectory of a fast, heavy particle in a light, low-Z medium suffers the smallest influence due to multiple scattering. In case of electrons in PMMA one can conclude that the atomic number is beneficial for a limitation of scattering influences, but the electron itself is a light particle and, thus, is subject to increased deflections.

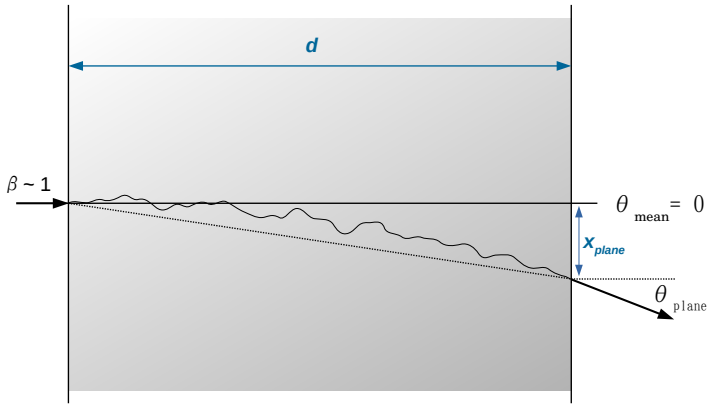

Figure 2.7.: Visualization of the scattering angle for the root mean square of the projected scattering-angle distribution of a particle passing through a scattering layer of thickness d. Adapted from [Tan+18].

Figure 2.8 shows the root mean square of the scattering angle of electrons in PMMA. Electron velocities β from 0.80 till 0.99 have been used. The scattering influence on the deflection of the electron increases with traveled distance and decreases for higher velocities.

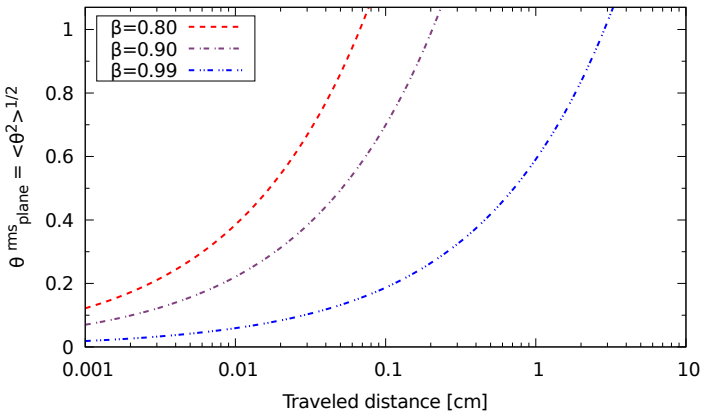

Figure 2.8.: Root mean square of the scattering angle of electrons in PMMA in dependence on the traveled distance. The faster the electron, the smaller the scattering effect and vice versa.

Since the exact calculation is either extensive and complicated or even impossible, simulations for example with the toolkit Geant4 can be employed to estimate the influence of scattering on the outcome on measurements. Geant4 is a software toolkit designed to simulate particle interactions in matter, as indicated by its name, which is an acronym for *GEometry ANd Tracking* [Ago+03].

2.1.4. The Cherenkov Effect

The Cherenkov effect describes the emission of electro-magnetic radiation by charged particles traveling faster than the speed of light c_n in that medium. Its acoustic counterpart is the sonic boost when an object moves at super-sonic velocities ($\approx 330\,\mathrm{m/s}$ in air on sea level). It was first discovered by P.A. Cherenkov in a report about "*visible radiation emitted by pure liquids under the action of fast electrons*" [Č37] in 1934. S.I. Wawilow first interpreted the effect as originating in the retardation of Compton electrons liberated in liquids, until I.M. Frank and I.E. Tamm were able to provide a comprehensive theory. For their achievements, Cherenkov, Tamm and Frank were awarded the Nobel Prize of Physics in 1957 in equal shares [Nob20b].

When a charged particle travels through a dielectric medium polarization of the medium takes place. In the direct vicinity of the charged particle, the atoms – which can usually be assumed to be spherical – are deformed and dipoles are created. If the particle travels at a speed slower than the speed of light in the medium ($v < c/n$), the polarization is spherically symmetric along the axis the particle travels, such that far from the particle the effective dipole field is zero (see figure 2.9, left). The speed of light in a medium can be expressed as $c_n = \frac{c}{n}$, with n being the refractive index of the medium. At velocities larger than that of light in the medium $v > c_n$ the polarization is only symmetric azimuthally around the path but not in direction along the axis. This is due to the fact that the electro-magnetic interaction forming dipoles takes place at the speed of light in that medium, which implies that no dipoles can form in front of the particle. Thus, a dipole field even at large distances

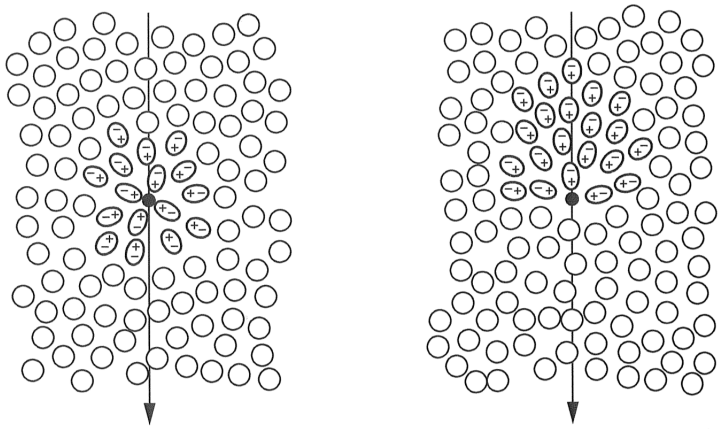

Figure 2.9.: Polarization of a medium by a charged particle. Left: For a speed smaller than the speed of light in the medium c_n, the polarization is symmetric around the particle and no effective dipole far from the particle exists. Right: For velocities faster than c_n the polarization is asymmetric and initiates the emission of electro-magnetic radiation. [KW16].

from the particle exists, which initiates the emission of short electro-magnetic pulses (see figure 2.9, right). The frequency of these pulses form the frequency spectrum of the emitted Cherenkov radiation. [MS69]
For a phenomenological description of the effect, one might use Huygen's principle of the interference of electro-magnetic wavelets (small waves): As long as the particle's speed is smaller than c_n, there is destructive interference of wavelets from adjacent steps of the trajectory. Therefore, remote contributions to the field intensity are canceled out. For $v > c_n$, however, there is a direction under an angle θ_C where constructive interference takes place and a wave front is formed. This can be seen in figure 2.10 for particles with $v < c_n$ (left) and $v > c_n$ (right). Using the traveled distance of light and the particle in the same time t, the relation between the particle speed and the emission angle θ_C can be computed: While the light covers a distance of $s_L = c_n \cdot t$, the particle range in that time is $s_P = t \cdot \beta \cdot c = t \cdot \beta \cdot c_n \cdot n$, where $\beta = \frac{v}{c}$ denotes the speed of the particle as a fraction of the vacuum speed of light. From a sole geometric consideration, one obtains for the Cherenkov emission angle with respect to the symmetry axis, along which the particle travels [KW16]:

$$\cos\theta_C = \frac{s_L}{s_P} = \frac{c_n t}{\beta c_n n t} = \frac{1}{\beta n} \tag{2.12}$$

This equation defines the opening angle of the so called *Cherenkov cone*. Due to the preserved azimuthal symmetry, the photons are emitted along the surface of a conic element, for which θ_C is the half angle. This formula provides a few important implications:

- **Threshold velocity:** Since the cosine has a valid range from -1 to 1, there is a minimum value for the velocity β for the Cherenkov effect to occur:

$$\beta^{\min} = \frac{1}{n} \tag{2.13}$$

  In that case the emission angle with respect to the momentum direction is as small as possible. The threshold velocity is a material constant and defined by the (wavelength

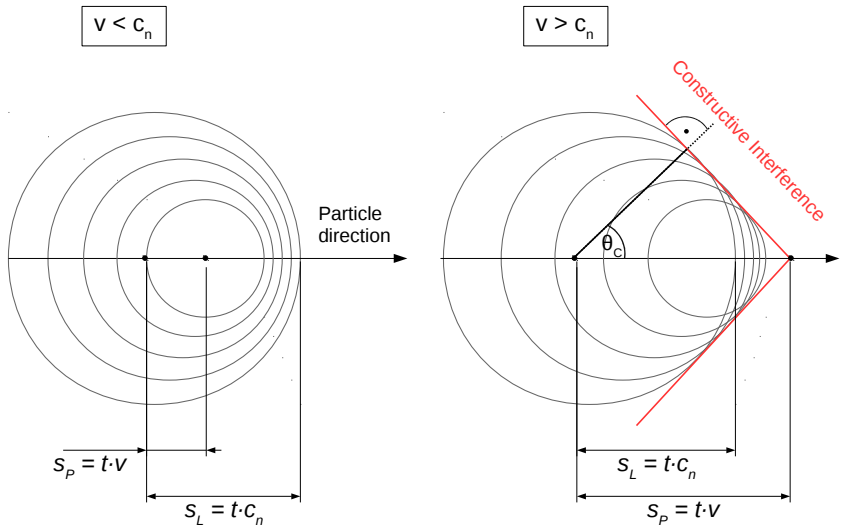

Figure 2.10.: Huygens principle of the interference of electro-magnetic waves: Constructive interference only happens for particle velocities larger than the speed of light in the medium. Otherwise, the effective contributions to the field intensity far from the particle are canceled out. Adapted from [KW16].

dependent) refractive index. In a wavelength range between 420 nm and 900 nm the refractive index of PMMA varies by 0.019 and lies between 1.504 (for the lower end of the wavelength range) and 1.485 (for the upper end) [Bea+15]. This implies a variation in the threshold value $\beta^{\min}$ between 0.673 (at 420 nm) and 0.665 (at 900 nm). For an electron for instance, the required minimum kinetic energy $E_{\text{kin}}^{\min}$ for the Cherenkov effect, therefore, lies between 173.21 keV and 179.87 keV. This constitutes a relative difference of $\Delta E_{\text{kin}}^{\min} = 3.7\,\%$.

- **Maximum opening angle θ_C :** Since the speed expressed as fraction of c cannot outstrip a value of 1, the maximum opening angle is given by:

$$\theta^{\max} = \arccos \frac{1}{n} \tag{2.14}$$

  In PMMA at a refractive index of 1.49, the maximum opening angle is 47.84°.

- **Mass influence:** As seen in formula 2.12, the mass of the particle has no influence on the opening angle of the Cherenkov emission. A proton and an electron of the same speed $\beta > \frac{1}{n}$ would create the same cone opening angle and – as will be shown later – the same number of emitted photons. Of course the required energy for these two particles to travel at that speed would be vastly different, due to the proton mass being magnitudes larger than the electron mass.

- **Wavelength dependence of the opening angle:** The opening angle has a wavelength dependence, simply because the refractive index is wavelength dependent. As

shown above the change of n is small in case of PMMA, so that the maximum opening angles only vary between 47.67° and 48.33°. A relative difference of 2.3 % can be calculated for the radii of the Cherenkov cones for these two extreme refractive indices at a maximum speed of $\beta = 1$ measured at a distance of 1 cm from the origin of the Cherenkov photons.

The minimum distance the particle travels must be significantly larger than the wavelength of the emitted radiation and the atomic distance of the medium. Otherwise, diffraction effects occur [MS69].

If a complete description of the effect is desired, the energy loss and the change of momentum of the electron due to the emission of Cherenkov photons would have to be taken into consideration as well [GS08]. A correction term is to be added in equation 2.12, effectively reducing the opening angle of the Cherenkov cone. However, the influence on θ_C is quite negligible, as one example shows: For electrons with an energy of 0.75 MeV passing through water ($n \approx 1.3$), the magnitude of the correction term is on the order of 10^{-6} [MS69]. In the scope of this thesis, the angular correction will not be taken into account and the energy loss through Cherenkov effect will only be considered for the computation of the number of photons that are created in the process. The energy loss per path element $\mathrm{d}x$ and frequency interval $\mathrm{d}\omega$ is described as follows:

$$\frac{\mathrm{d}^2E}{\mathrm{d}x\mathrm{d}\omega} = \frac{z^2e^2}{4\pi\varepsilon_0 c^2} \cdot \omega \cdot \left(1 - \frac{1}{\beta^2 n^2}\right) \tag{2.15}$$

Using $\alpha := e^2/(4\pi\varepsilon_0\hbar c) \approx \frac{1}{137}$, the fine structure constant, and $1 - \frac{1}{\beta^2 n^2} = \sin^2(\theta_\mathrm{C}\ )$ one can rewrite equation 2.15 in a more compact form:

$$\frac{\mathrm{d}^2E}{\mathrm{d}x\mathrm{d}\omega} = \frac{z^2\alpha\hbar}{c} \cdot \omega \cdot \sin^2(\theta_\mathrm{C}\ ) \tag{2.16}$$

Integration over a frequency interval ω_1 to ω_2 corresponding to a wavelength interval λ_1 to λ_2 yields:

$$\frac{\mathrm{d}E}{\mathrm{d}x} = \frac{z^2\alpha\hbar}{2c} \cdot \sin^2(\theta_\mathrm{C}\ ) \cdot (\omega_2^2 - \omega_1^2) \tag{2.17}$$

The number of photons per path element can be obtained by dividing 2.17 by the mean energy of one photon $E = \hbar\overline{\omega} = \frac{1}{2}\hbar(\omega_1 + \omega_2)$ [Jel58]:

$$\frac{\mathrm{d}N}{\mathrm{d}x} = \frac{1}{\frac{1}{2}\hbar(\omega_1 + \omega_2)} \cdot \frac{\mathrm{d}E}{\mathrm{d}x} = \frac{z^2\alpha}{c} \cdot \sin^2(\theta_\mathrm{C}\ ) \cdot (\omega_1 - \omega_2) \tag{2.18}$$

Substituting the frequency with the corresponding wavelength $\omega = 2\pi c/\lambda$ one obtains

$$\frac{\mathrm{d}N}{\mathrm{d}x} = 2\pi z^2\alpha \cdot \sin^2(\theta_\mathrm{C}\ ) \cdot \left(\frac{1}{\lambda_2} - \frac{1}{\lambda_1}\right) \tag{2.19}$$

Here, λ_2 is the shorter wavelength, corresponding to the higher frequency ω_2. Assuming a constant velocity β over a traveled distance L, one can compute the total number of emitted photons along the track:

$$N = 2\pi z^2\alpha \cdot \sin^2(\theta_\mathrm{C}\ ) \cdot \left(\frac{1}{\lambda_2} - \frac{1}{\lambda_1}\right) \cdot L \tag{2.20}$$

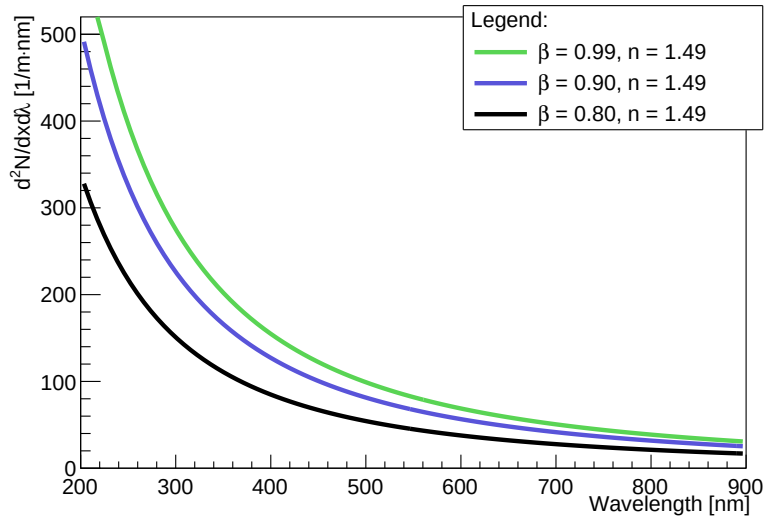

Figure 2.11.: Differential Cherenkov photon spectrum $\frac{\mathrm{d}^2N}{\mathrm{d}x\mathrm{d}\lambda}$. The emission increases towards the near UV range. The graph represents equation 2.19 differentiated with respect to the wavelength.

Figure 2.11 shows the differential Cherenkov photon spectrum $\frac{\mathrm{d}^2N}{\mathrm{d}x\mathrm{d}\lambda}$ for the example of electrons with $\beta = 0.8$, 0.9 and 0.99 traversing PMMA with $n = 1.49$. It represents equation 2.19 differentiated with respect to the wavelength. One obtains that the emission increases towards the near ultraviolet (UV) range, however, there is no extension of the emission into the X-ray range, since $n < 1$ [Jel58]. For $\beta = 0.8$, the total number of emitted photons is 528 per cm traveled distance, using the above stated values and assuming a wavelength range from 200 nm to 900 nm and neglecting energy losses of any kind of the electron in the medium. This number increases both with increasing velocity and refractive index. Furthermore, for a detection of Cherenkov photons, the efficiency of the photon detectors must be high especially in the near UV range. Of course, also the material used to create the Cherenkov radiation must be transparent for these wavelengths.

The wavelength range of Cherenkov light emission is however limited [MS69]. In dispersive media, the emission is restricted to wavelength bands for which the refractive index is larger than $1/\beta$. Figure 2.12 shows the dispersion curve (n versus λ) for a typical transparent dispersive medium for a wavelength range from X-ray to the radio waves. In the X-ray region, where $n(\lambda) < 1$, radiation is always forbidden.
Figure 2.13 shows the number of emitted Cherenkov photons per cm traveled distance for particles in PMMA versus particle velocity in $\beta = \frac{v}{c}$. Different wavelength ranges are used for the graph. The influence of the increasing Cherenkov emission spectrum towards the near-UV is rediscovered: Changing the lower wavelength boundary from 400 nm to 200 nm has a much higher influence on the number of emitted photons than changing the upper limit by the same amount.
Figure 2.14 shows basically the same using the kinetic energy of the particle – which in this case is an electron – on the abscissa. The graphs saturate already in the very low MeV range, which is why the total Cherenkov light yield in the MeV range and above is

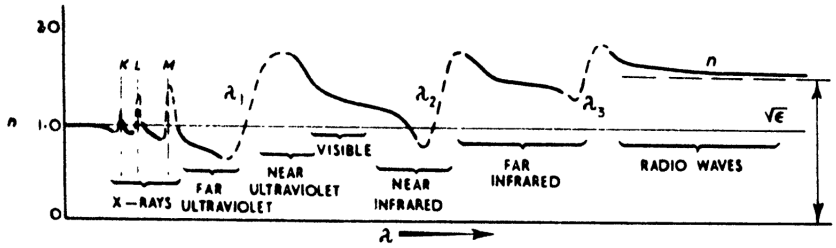

Figure 2.12.: Dispersion curve for a transparent medium shown for wavelengths of the whole electromagnetic spectrum. Radiation of Cherenkov photons is restricted to areas with $n(\lambda) > 1/\beta$. [Jel58].

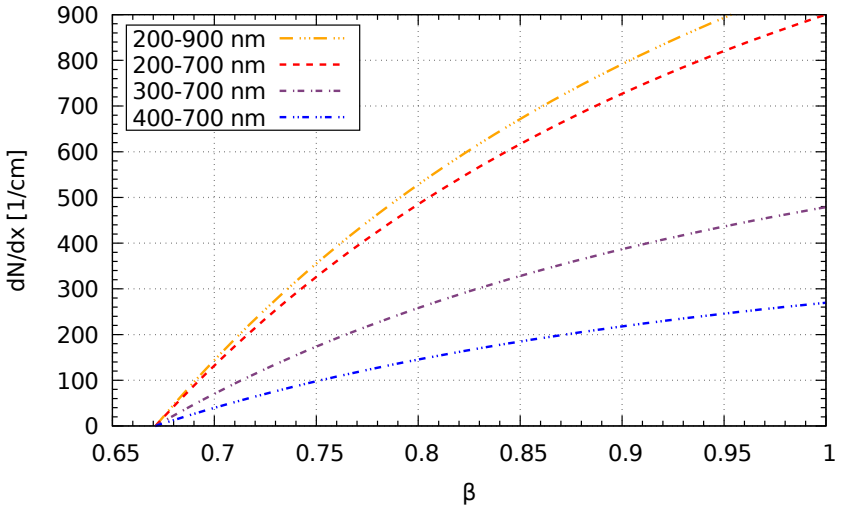

Figure 2.13.: Number of emitted Cherenkov photons per cm traveled distance in PMMA depending on the particle speed given as fraction of the speed of light $\beta = \frac{v}{c}$. Different wavelength ranges are plotted.

determined by the traveled distance. In general, one can conclude, if the speed of a particle is close to c, the emitted number of photons per distance is constant, independent of the energy.

Comparison to other photon emission processes:
The instantaneous nature of its emission differentiates Cherenkov radiation from scintillation light, which follows a decay law with a certain time constant usually on the order of nanoseconds up to microseconds [Bir64]. Also, due to its emission under a specific angle, Cherenkov radiation can be clearly distinguished from Bremsstrahlung [MS69].

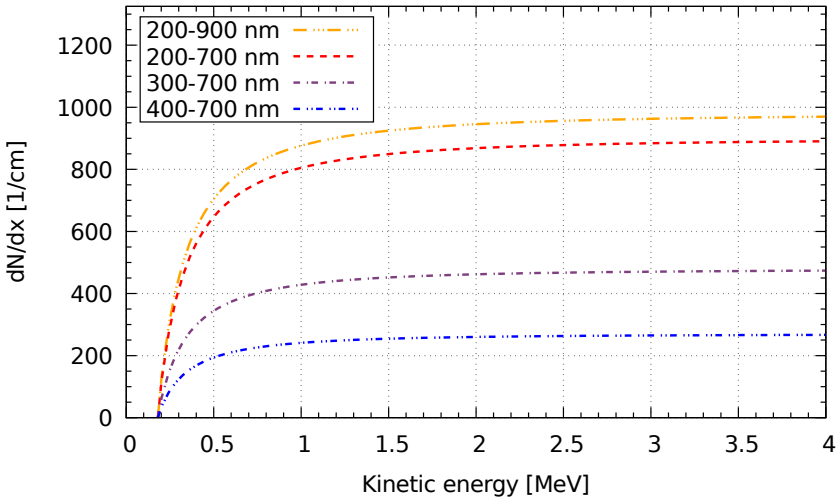

Figure 2.14.: Analogous to figure 2.13 this graph shows the number of emitted Cherenkov photons per cm traveled distance of an electron in PMMA depending on its kinetic energy. Again, different wavelength ranges are plotted. A saturation for higher energies is observed, as $\beta > 0.99$ above kinetic energies of $E \approx 3.2\,\mathrm{MeV}$.

2.2. Photon Interactions in Matter

The origins of photons and gamma rays are manifold[1] and their energies cover an enormous range. Starting in the optical range of a few hundred nanometers, this thesis deals with photon energies up to the MeV region. Higher energetic photons can be created as by-product of beta-decays into an excited state of the daughter-nucleus, the de-excitation of which is accompanied with the emission of a photon. Other very common gamma sources are the annihilation of positrons with electrons in a medium or nuclear reaction processes like fission, where the photon is created in the strong field of the nucleus and where the highest gamma energies are achieved. When fast electrons travel through media with high atomic number, Bremsstrahlung is radiated, and when they are bent in a circular orbit, a certain fraction of their energy is carried away in every cycle through Synchrotron radiation. Lastly, X-ray radiation is emitted after the excitation and de-excitation of atoms. The energy of the emitted radiation reflects the energy differences between individual electron shells and is characteristic for every atom.

In contrast to charged particles, which slow down continuously though interactions with many atoms, the behavior of a photon traveling though matter is of entirely different nature. The photon does not lose energy continuously but in distinct scattering or absorption events. In one or several interactions the photon either disappears transferring its energy to an electron or nucleus or it scatters under a significant angle. The three main interaction mechanisms of photons in matter, which are *Photo effect*, *Compton scattering* and *pair production*, are subject of this chapter. All of them cause an attenuation of a beam of photons incident upon matter, and the level of this attenuation depends not only on the photon's energy

[1] The words *photon* and *gamma ray* or simply *gamma* are often used synonymously as in [Kno10] and [NR91]. This thesis will stick to the conterminous use of *photon* and *gamma*. It will be explicitly mentioned, if other kinds of photons like optical or Cherenkov photons are referred to.

but on the quality of matter itself [Kno10]. A link between the Compton effect and the Compton scattered electron and its angular and energy distribution will be created. The physical requirements for the measurement of Compton electrons through the Cherenkov effect – requiring a minimum electron energy – will be given.

2.2.1. General Remarks on Photon Interactions

2.2.1.1. Attenuation of Photon Beams

A beam of photons traversing though matter experiences attenuation through absorption and/or scattering of individual photons. These processes remove photons from the beam causing an attenuation of the initial intensity I_0 [Dys93]. The rate of this photon removal is proportional to the number of photons in the beam, which is why the intensity of the beam depending on the traveled distance x can be described with an exponential law:

$$I(x) = I_0 \, \exp(-\mu_l \, x) \tag{2.21}$$

Here, μ_l is the *linear attenuation coefficient*, which depends amongst others on the particle energy and the density of the material [NR91]. The ratio of the attenuation coefficient to the density of the material is nearly a constant for all materials. Equation 2.21 allows to draw conclusions on the average traveled distance of a photon before interacting with a material with given properties. It is expressed in terms of the *mean free path* as follows:

$$\lambda_l = \frac{1}{\mu_l} \tag{2.22}$$

Based on equation 2.21, an absorber thickness of $L = \lambda_l$ for instance produces an attenuation of the intensity to a level of $1/e \approx 37\,\%$ of its initial value.
The attenuation coefficient is proportional to the electron density P, since gammas interact primarily with atomic electrons. The ratio of electron density to mass density ρ is a constant Z/A for a given material, with Z being the atomic number or proton number and A the atomic mass number. The ratio Z/A is a constant throughout most elements except for hydrogen and the heavy elements. Thus, the attenuation coefficient mostly depends on the density ρ. Because of this density dependence, the linear mass attenuation coefficient is usually not tabulated. For example, water and ice – both having the exact same atomic and nuclear constituent – show different attenuation for gamma rays. A density independent quantity called *mass attenuation coefficient* μ is introduced, characterizing the beam attenuation inside a material independent of its physical state or, more generally, its density. It can be calculated using the linear attenuation coefficient divided by the density $\mu = \mu_l/\rho$ and has therefore units $^{\mathrm{cm}^2}/_{\mathrm{g}}$. Thus, one might think of it as a cross section per unit mass so that the mass attenuation coefficient can be rewritten [Sel96]:

$$\mu = \frac{\sigma}{u\,A}, \tag{2.23}$$

where σ is the total cross section for an interaction by the photon, frequently given in units of b/atom (barns/atom), where $b = 10^{-24}\,\mathrm{cm}^2$. $u = 1.66 \cdot 10^{-24}\,\mathrm{g}$ is the atomic mass unit.

μ is independent of ρ and therefore quantifies the gamma ray interaction probability of an *element*. Equation 2.21 can be rewritten using μ:

$$I(x) = I_0 \exp(-\mu \rho x) \tag{2.24}$$

In cases, where a compound material consists of several different elements, one can compute the mass attenuation coefficient using the sum of the constituents μ_i weighted by their relative mass contribution to the compound w_i:

$$\mu = \sum_i \mu_i w_i \tag{2.25}$$

Exemplary, the mass attenuation coefficient of NaI (sodium iodide) is computed in the following. NaI is a common scintillator material employed in particle detection set-ups and amongst others used for gamma ray interaction. It will also become important in the third part of this thesis. The atomic mass of sodium (23.0 u) and of iodine (126.9 u) give the weight fractions $w_{\mathrm{Na}} = 0.153$ and $w_{\mathrm{I}} = 0.847$, respectively. Using the mass attenuation coefficients from the NIST Standard Reference Database 126 [Sel96], one obtains:

$$\mu = 0.153 \cdot \mu_{\mathrm{Na}} + 0.847 \cdot \mu_{\mathrm{I}}$$

μ is dependent on the photon energy. For a photon energy of 1 MeV, the mass attenuation coefficient for sodium is $6.100 \cdot 10^{-2}\,\mathrm{cm^2/g}$ while iodine has a value of $5.841 \cdot 10^{-2}\,\mathrm{cm^2/g}$. At that specific energy, the density independent mass attenuation coefficient of sodium iodine is $5.881 \cdot 10^{-2}\,\mathrm{cm^2/g}$. Based on equation 2.22 a photon of that energy has a free mean path of

$$\lambda_l = \frac{1}{\mu \cdot \rho} = \frac{1}{5.881 \cdot 10^{-2}\,\mathrm{cm^2/g} \cdot 3.67\,\mathrm{g/cm^3}} = 4.63\,\mathrm{cm}$$

The mass attenuation coefficients for NaI, lead and PMMA are shown in figure 2.15 for energies between 1 keV and 10 MeV. The relevant energy region for this thesis lies in the range of several hundred keV up to several MeV. The mass attenuation coefficients were again taken from the NIST Standard Reference Database 126 [Sel96]. With increasing energy up to the MeV range, the material's ability to attenuate an incoming beam of photons decreases, before nuclear effects occur (see section 2.2.4 on pair production). The edges with the step-like increase in attenuation originate in the photo effect, further discussed in section 2.2.2. At this point the photon's energy matches the binding energy of an electron in its atomic shell giving rise to the interaction cross section via photo effect and therefore increasing the mass attenuation coefficient according to equation 2.23.
Multiplying μ by the density of the corresponding material and taking the inverse results in the mean free path, which is depicted in figure 2.16. Density values of $3.67\,\mathrm{g/cm^3}$ for NaI, $11.342\,\mathrm{g/cm^3}$ for lead and $1.09\,\mathrm{g/cm^3}$ for PMMA were taken. The higher the photon energy, the larger the average distance it can travel through the material before undergoing scattering or absorption. [NR91; Kno10; Dys93]

2.2.1.2. Interaction Probability

As mentioned, three major processes determine the interaction probability of a photon in a medium, which are explained in sections 2.2.2, 2.2.3 and 2.2.4. The probability of their

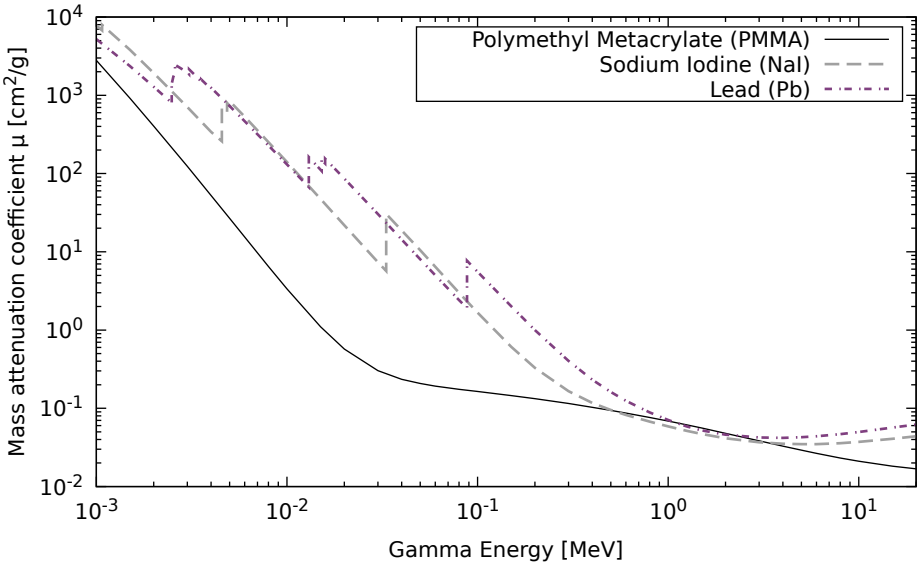

Figure 2.15.: Mass attenuation coefficient μ of photons in lead, sodium iodine and PMMA as a function of their energy. The absorption edges with suddenly increasing coefficients occur for photon energies close to the binding energy of an electron in its corresponding atomic shell, where a new channel for the photon effect opens up (see section 2.2.2).

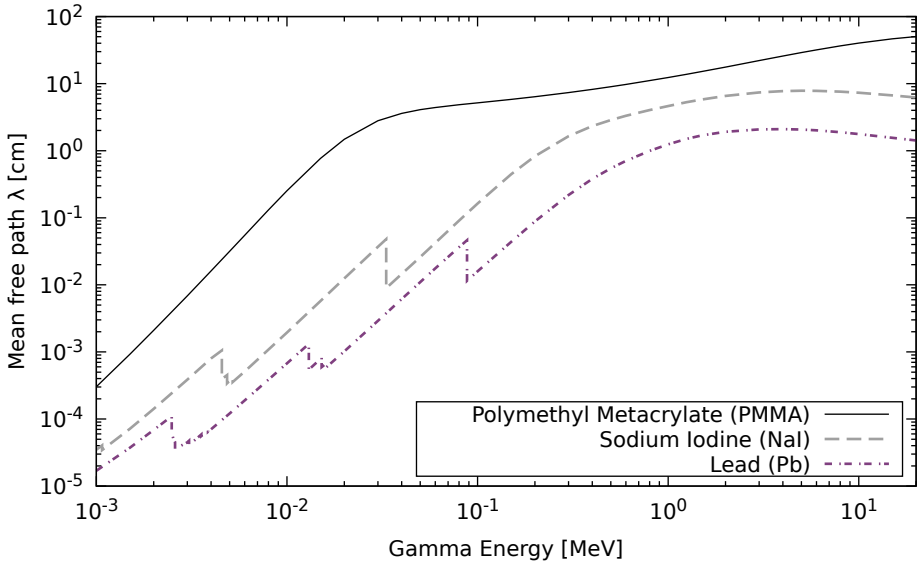

Figure 2.16.: Mean free path λ_l of photons in lead, sodium iodine and PMMA plotted versus energy. The edges with rapidly dropping λ_l originate in the photo effect (see section 2.2.2).

occurrence influences the attenuation for a photon beam of a certain energy. Therefore, the mass attenuation coefficient μ consists of three different components according to the aforementioned processes, which occur dominantly at different photon energies. μ is then the sum of the individual interaction probabilities, expressed in terms of the attenuations given in $^{\mathrm{cm}^2}/_{\mathrm{g}}$:

$$\mu = \mu_\gamma + \mu_C + \mu_{e^-e^+} \tag{2.26}$$

Here, the indices denote photo effect (γ), Compton scattering (C) and pair production (e^-e^+) respectively. The relative importance of the three processes is demonstrated in figure 2.17. It shows the energy regions, in which photo effect, Compton scattering and pair production are dominant. The lines in the graph indicate the points of equal interaction probability via photo- and Compton effect (left line) and via Compton effect and pair production (right line).

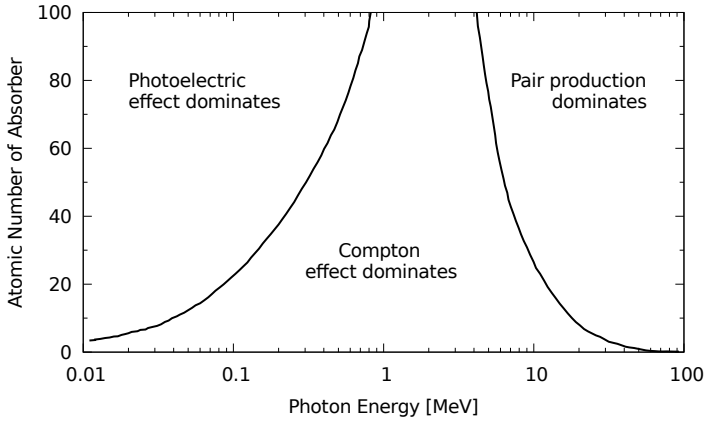

Figure 2.17.: Relative importance of the three major photon interaction types. At the lines the cross sections of the two neighboring effects are equal. Digitized from [Eva55].

In case of NaI with a mean atomic number of 38.5, the point of equal photo and Compton effect lies at an energy value of about 200 keV [Kno10], while for lead (Z=82), this point is about 500 keV higher [KW16]. PMMA, however, which solely consists of low-Z elements, does not show dominating photo effect, until energies below the keV range. For photons with an energy of 511 keV – which will play an important role later in this thesis in section 12 – Geant4 simulations predict a photoelectric fraction of only $(0.37 \pm 0.06)\,\%$ [Bä20b].
Independent of the exact process, the interaction probability of higher energetic [2] photons ($E \geq 100\,\mathrm{keV}$) inside a medium plays an important role in this dissertation, as it determines the required type and thickness of the material to achieve a sufficient interaction efficiency for the photons to be detected. The probability for a photon interaction within a given distance is investigated in the following.

[2] The meaning of *higher energetic* is ambiguous: In high energy physics, particles in the keV-range would very likely be considered low-energetic, while the same energy range would be considered very high in the field of solid-state physics for instance.

Based on equation 2.21 one can calculate for a single photon the probability $\overline{P(L)}$ to not have interacted within a distance L, i.e. to survive after passing through a material of thickness L:

$$\overline{P(L)} = \exp\left(-\frac{L}{\lambda_l}\right) \tag{2.27}$$

Obviously, the probability to not have interacted after zero traveled distance must be equal to 1:

$$\overline{P(L=0)} = 1 \tag{2.28}$$

The probability for a photon to have interacted within a distance L and therefore being absorbed or scattered is:

$$P(L) = 1 - \overline{P(L)} = 1 - \exp\left(-\frac{L}{\lambda_l}\right) \tag{2.29}$$

Since λ_l is energy dependent, the cross section and, thus, the interaction probability changes with energy as well. Using the example of PMMA this dependency is shown in figure 2.18 for different photon energies. Lower energetic photons are more likely to be absorbed or scattered within a PMMA sample of given thickness L than higher energetic ones. This does not come as a surprise, since especially in radiation protection, thick absorbers are used to attenuate gamma radiation emitted by radioactive sources. Lead with its high atomic number of $Z = 82$ is very convenient for shielding purposes of such kind, as can be learned from figure 2.19: For a fixed energy of 1 MeV, photon interaction probabilities for various materials are plotted versus the traveled distance L within that material. Highly dense materials with high Z can be used to attenuate gamma radiation. While for PMMA the interaction probability after a distance of 10 cm is only about 30 %, a photon of the same energy in lead would have interacted with a probability of 99.97 %.

Consequently, for the detection of gamma rays in the MeV range, either very dense or very thick absorber materials must be used. Otherwise, the interaction efficiency of the photons inside the detector material is small and – depending on the application – could limit energy and time resolution or reduce the signal to noise ratio.

2.2.2. Photoelectric Effect

The photoelectric effect (or short photo effect) describes the disappearance of a photon after the interaction with an electron in an atomic shell. An energetic electron is emitted by the atom from one of the bound shells [Kno10]. Due to momentum conservation, photo effect can only take place with the atom as a whole and not with free electrons [GS08].
The electron receives a significant part of the photon energy $h\nu$, reduced only by the binding energy of the electron in its shell E_{Bind}:

$$E_e = h\,\nu - E_{\text{Bind}} \tag{2.30}$$

Given binding energies in the eV range, the electron carries away almost the entire photon energy. Since the atom is left behind in an ionized state, an electron from a higher atomic

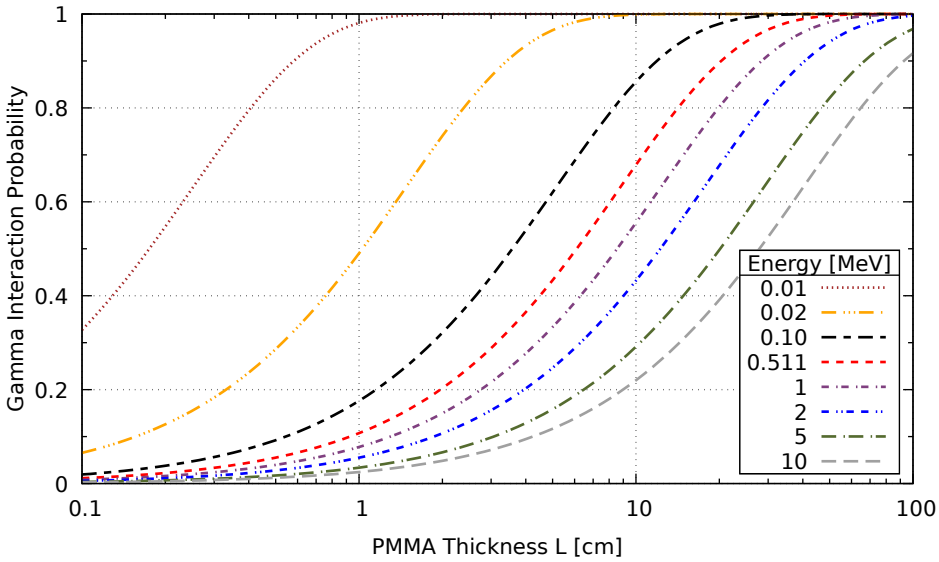

Figure 2.18.: Gamma ray interaction probability within a PMMA sample of thickness L. Curves are drawn for various photon energies. In this energy range, less energetic gamma rays are attenuated stronger than higher energetic ones.

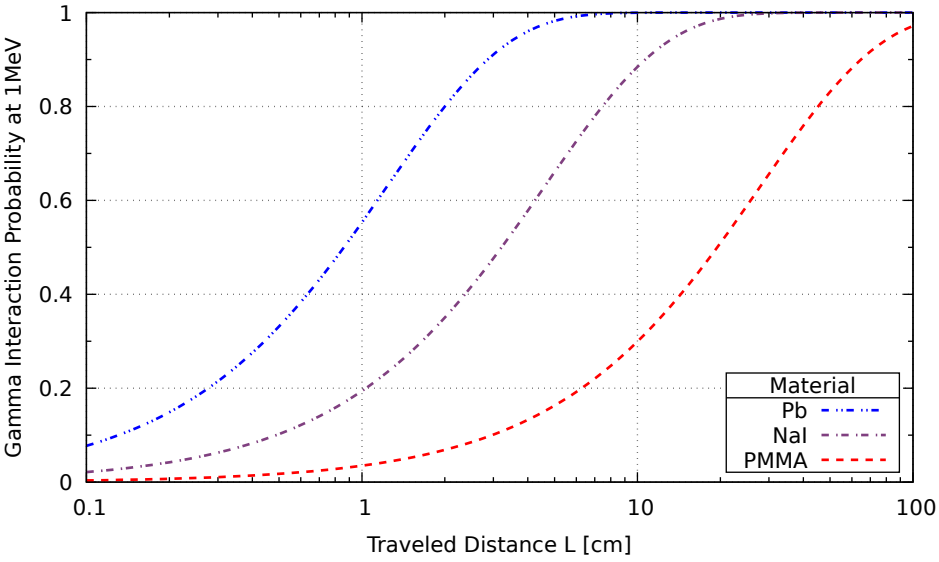

Figure 2.19.: Gamma ray interaction probability within a traveled distance L for different materials and fixed photon energy (1 MeV).

shell fills the vacancy under emission of characteristic X-ray radiation. In most cases the emitted X-ray photons are re-absorbed close to the initial interaction site. The atomic shells are traditionally denoted with letter K, L, M, etc., the K-shell being the closest to the nucleus and with the highest binding energy for the electron. If a photon does not interact with an electron from the K-shell, photo effect with the higher shells is possible as well under emission of lower energetic X-rays.

The photo effect is the predominant interaction of low energetic photons (compare figure 2.17), but it is also material dependent, especially on Z, the atomic number. The process is enhanced for higher Z. The attenuation μ_γ of a photon beam through interactions via photo electric absorption per atom in the non-relativistic range can be approximated with the non-relativistic Born approximation [GS08] and is proportional to the atomic number of the power of 5 and the photon energy to the power of 3.5:

$$\mu_\gamma \propto const \cdot \frac{Z^5}{(h\,\nu)^{3.5}} \tag{2.31}$$

The strong dependence on Z indicates that the photon does not interact solely with an electron from an atomic shell, but with the whole atom. In fact, Z-dependent corrections make the cross section a more complicated function of Z and the exponent varies between 4 and 5 in the range of $0.1\,\text{MeV} \leq h\nu \leq 5$ MeV. The increased photo electric absorption for high-Z materials is another reason to chose lead ($Z = 82$) as shielding element against gamma radiation.
In the previous chapter (2.2.1) the mass attenuation coefficient was drawn for various materials (figure 2.15). Even though it also contains the attenuation through Compton and pair production, one can identify some significant discontinuities in the lower energy range, where photo effect dominates. At these steps the incoming photon energy matches the binding energy of the electron of the corresponding shell. The K-shell corresponds to higher binding energy than the M and L shells, as electrons closer to the nucleus are bound more strongly. Right above the binding energy, the absorption coefficient increases as the photon just has enough energy to knock that electron out of its shell. For photon energies just below such a binding energy value, the attenuation through photoelectric absorption drops abruptly. In the mass attenuation coefficient of lead, the K-, L- and M-shell are visible in the energy range above 1 keV. While NaI still shows two of the edges, PMMA has no discontinuities in that range. Because of its low-Z molecular components, which are hydrogen, oxygen and carbon, the binding energy of the electrons is far lower and the edges would only occur below the keV range.

In medical applications, the Z-dependence of the photo effect is fundamental for diagnostic radiology, where x-ray photons are used to image internal structures. The absorption of the photon through photo effect inside the body depends on density and atomic number at that point. This circumstance allows for a distinction in the image between more dense regions such as bones from those with less density like tissue. Usually, a wide energy range of X-ray photons is favored. Due to its strong energy dependence, the cross section spreads out over a wide range as well. This can be used to probe both light absorbing and strongly absorbing anatomical features with high efficiency and contrast. In clinical practice, photon energies

are limited to about 90-100 keV to limit the influence of Compton scattered photons in the image. Compton scattering, which becomes the dominant process at higher energies, would give scattered radiation and would inevitably reduce contrast and visibility of features.

2.2.3. Compton Effect

Since the Compton effect is of fundamental importance for the gamma detection concept presented and investigated in this dissertation, a closer look at this scattering process will be given in this chapter. Explanations on the process itself are provided, including considerations of the energy transfer in the process as well as the angular distributions of photon and electron. Especially energy and momentum direction of the scattered electron released in this process is of great importance for a detection using Cherenkov light and will be investigated. For a detailed explanation on the concept of Compton electron detection using Cherenkov light, see chapter 5.

2.2.3.1. Process Description

The Compton effect received its name by its discoverer Arthur Holly Compton, who was later awarded the Nobel Prize of Physics in 1927 [Nob20a]. The effect describes the wavelength shift of electromagnetic radiation due to incoherent scattering on atomic electrons [MS69]. A photon with an initial energy $E_i = h \cdot f_i$ traversing a medium interacts with an electron at rest. The electron can be described as *quasi-free* as its binding energy is much smaller than the energy of the incoming photon and can therefore be neglected in calculations in good approximation. The photon transfers energy to the electron resulting in an increased wavelength of the photon leaving the scattering vertex. The photon scatters under an angle θ with respect to its original momentum direction, while the electron recoils under the angle ϕ. [LR09] For a graphical representation of the Compton effect see figure 2.20. The effect was first observed and described by Compton in 1922 who gave the effect its name and provided a first explanation based on the early corpuscular photon concept of electromagnetic radiation according to quantum ideas [MS69].

2.2.3.2. Energy Transfer in Compton Scattering

The wavelength change of a photon can be described in terms of the scattering angle θ of the initial photon with respect to the original momentum direction before the scattering took place [KW16]:

$$\Delta\lambda = \lambda_f - \lambda_i = \frac{h}{m_e\, c}(1 - \cos\theta) \tag{2.32}$$

Here, the index f stands for final and index i denotes the initial state of the photon. The quantity $\Delta\lambda$ is called *Compton Wavelength Shift* and can be computed using energy and momentum conservation [LR09]. The factor in front of the brackets reads

$$\frac{h}{m_e\, c} = \frac{6.626 \cdot 10^{-34}\,\mathrm{J\,s}}{9.109 \cdot 10^{-31}\mathrm{kg} \cdot 3.0 \cdot 10^{8}\,\mathrm{m/s}} \approx 2.425 \cdot 10^{-12}\,\mathrm{m} \approx 0.002425\,\mathrm{nm} \tag{2.33}$$

This value is also called *Compton wavelength* and NIST data base gives the value as $2.4263102367(11) \cdot 10^{-12}\,\mathrm{m}$ [SN14]. The maximum change in wavelength is reached when

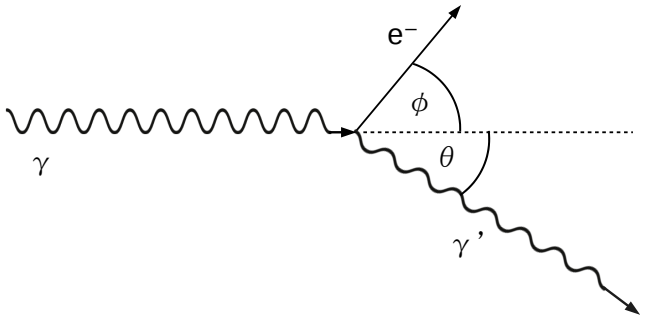

Figure 2.20.: Compton scattering of an incident photon by a quasi-free electron at an angle θ. The electron recoils at an angle ϕ. Adapted from [MS69].

the photon is back-scattered ($\theta = 180°$) and the cosine becomes -1. Equation 2.32 then becomes:

$$\Delta\lambda_{\max} = \frac{h}{m_e c} \cdot 2 = 0.004849\,\text{nm} \tag{2.34}$$

This means that in Compton scattering the photon can undergo a change in wavelength no more than the above stated value of 2 times the Compton wavelength of an electron. There is an inverse relation between the wavelength and the energy of a photon:

$$E = h \cdot f = \frac{h\,c}{\lambda} \tag{2.35}$$

In case of Compton scattering, this relation implies that a shift in energy depends on the absolute value of the initial wavelength of the photon. Using equation 2.35, the energy loss of the photon – which equals the energy transfer of the photon to an electron – can be expressed as follows:

$$\Delta E = h \cdot \Delta f = h \cdot (f_i - f_f) = h\,c \left(\frac{1}{\lambda_i} - \frac{1}{\lambda_f}\right) = E_i - E_f, \tag{2.36}$$

with $\lambda_i \leq \lambda_f$. The smaller the initial wavelength λ_i the larger is the energy transfer from the photon to the electron. Now, one can make use of equation 2.32 to find an expression for λ_f and substitute it into the equation for the energy shift:

$$\Delta E = h\,c \left(\frac{1}{\lambda_i} - \frac{1}{\frac{h}{m_e\,c}\,(1 - \cos(\theta)) + \lambda_i}\right) \tag{2.37}$$

The goal is to express the energy transfer ΔE onto the electron in terms of the initial photon energy E_i and scattering angle θ. Therefore, λ_i is written as hc/E_i according to equation 2.35. The expression from above therefore reads

$$\Delta E = h\,c\left(\frac{1}{\frac{h\,c}{E_i}} - \frac{1}{\frac{h}{m_e\,c}\left(1-\cos(\theta)\right) + \frac{h\,c}{E_i}}\right) \tag{2.38}$$

$$= E_i\left(1 - \frac{1}{\frac{E_i}{m_e\,c^2}\left(1-\cos(\theta)\right)+1}\right). \tag{2.39}$$

Often, the change in photon energy is expressed via the finial energy of the photon as a fraction of the initial energy, which can be obtained by rearranging the equation from above:

$$\frac{E_f}{E_i} = \frac{1}{1 + \frac{E_i}{m_e\,c^2}\cdot\left(1-\cos(\theta)\right)} \tag{2.40}$$

The energy transfer onto the electron, thus, only depends on the initial energy of the incoming photon and the scattering angle. Figure 2.21 shows a plot with the angular-dependence of the energy transfer for various initial energies. Due to energy conservation the energy of the electron saturates with a maximum at $\theta = 180°$. Saturation is reached at smaller angles the higher the energy of the initial gamma.
In Compton scattering the electron can never get the full energy of the incoming photon and the maximum transferred energy depends on the energy of the incoming photon. This can be expressed as follows:

$$\Delta E_{\max} = E_i\left(1 - \frac{1}{\frac{E_i}{m_e\,c^2}\cdot 2 + 1}\right), \tag{2.41}$$

The maximum transferred energy increases with E_i. The graph shows the relative energy transfer $\Delta E/E_i$ for various photon scattering angles. Higher photon scattering angles result in higher energy transfer to the electron as shown in figure 2.22. This circumstance becomes relevant for the detection of the Compton electron using Cherenkov light (see chapter 5 for explanations on the principle). The Cherenkov light yield increases with electron energy, which is why large photon scattering angles giving high energy transfer are beneficial for this detection concept. However, forward scattering of the photon plays a predominant role in Compton effect, as will be shown in the next section.

2.2.3.3. Angular Distributions of Compton Scattered Photons and Electrons

The electron scattering angle ϕ with respect to the direction of the incoming photon can be described in terms of the initial photon energy E_i and the angle θ of the scattered photon [LR09]:

$$\tan(\phi) = \frac{1}{1 + \frac{E_i}{m_e\,c^2}}\cdot\cot\left(\frac{\theta}{2}\right) \tag{2.42}$$

Figure 2.23 shows that relation for different energies of the incoming photon. The higher the scattering angle of the photon the smaller the electron scattering angle and vice versa. That means that when the photon is scattered in forward direction (i.e. at small angles), the

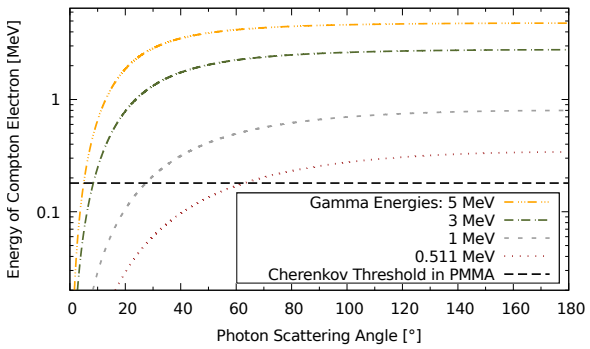

Figure 2.21.: Transferred energy to the Compton electron depending on the scattering angle of the incoming gamma for different initial energies. The energy threshold for the Cherenkov effect in PMMA is indicated as constant line at about 0.18 MeV.

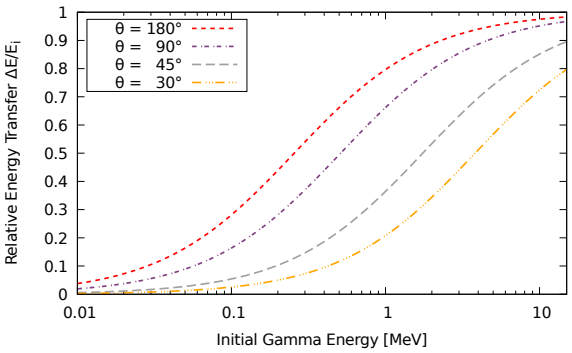

Figure 2.22.: Energy transfer to the Compton electron depending on the initial energy E_i of the incoming gamma shown for different photon scattering angles θ. The maximum transferred energy $\Delta E_{\max}$ occurs at an angle of 180°. The curve shows the relative energy with respect to the initial energy E_i.

electron angle tends to be high, which means the electron is scattered to the side. According to equation 2.38 these electrons have lower energies than those that were scattered under a smaller angle with respect to the initial photon momentum direction. Electron scattering angles larger than 90° are not possible.

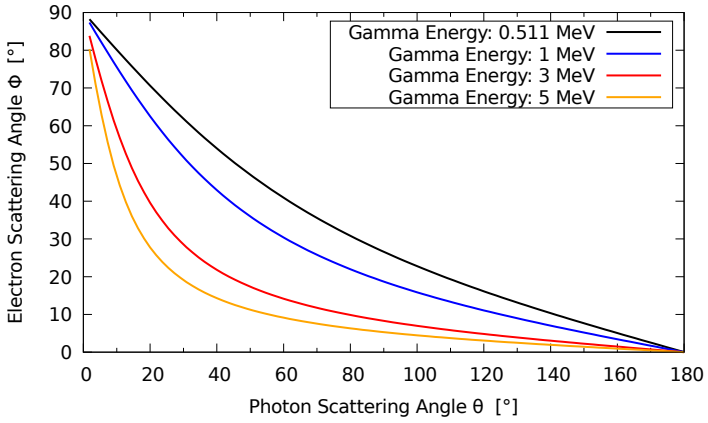

Figure 2.23.: Electron scattering angle versus photon scattering angle for different energies of the incoming photon.

For the detection of Cherenkov photons from Compton scattered electrons, small electron scattering angles and, thus, large electron energies are preferred. As an example, let's assume in a fictitious set-up, the electron angle must not be larger than 20° for a detection to be successful. Equation 2.42 predicts that for a 5 MeV photon such electron scattering angles are created for a large angular range of the photon of 30° till 180°, while for an energy of 511 keV only backscattered photons with $\theta > 120°$ give that result. This immediately seems beneficial for the detection of electrons using Cherenkov light, however, the photon scattering angles

tend to decrease rapidly with increasing energy, resulting in large electron scattering angles. In the following the differential cross sections for both photon and electron will be shown, from which conclusions will be drawn on the occurrence of the preferably small electron scattering angles.
The distribution of Compton scattering angles of the photon can be described by the so called Klein-Nishina-formula [KW16; LR09]:

$$\frac{\mathrm{d}\sigma_C}{\mathrm{d}\Omega_\gamma} = \frac{r_e^2}{2} \cdot \left(\frac{f_f}{f_i}\right)^2 \cdot \left(\frac{f_f}{f_i} + \frac{f_i}{f_f} - \sin^2(\theta)\right) \tag{2.43}$$

One can use equation 2.40 and $E = f \cdot h$ to express the ratio f_f/f_i in the cross section formula in terms of the initial and final photon energies. Furthermore one can make the substitution $\varepsilon = E_i/(mc^2)$, which is often referred to as *reduced energy* of the incoming photon. Then equation 2.43 becomes

$$\frac{\mathrm{d}\sigma_C}{\mathrm{d}\Omega_\gamma} = \frac{r_e^2}{2} \cdot \frac{1 + \cos^2(\theta)}{(1 + \varepsilon(1 - \cos(\theta)))^2} \cdot \left(1 + \frac{\varepsilon^2(1 - \cos(\theta))^2}{(1 + \cos^2(\theta)(1 + \varepsilon(1 - \cos(\theta)))}\right). \tag{2.44}$$

This is the differential cross section per electron. It gives the number of photons scattered into unit solid angle at a mean scattering angle θ. It is depicted in figure 2.24 for various energies. One can see that for small energies the distribution follows the nature of Thomson scattering where forward and backward scattering are equally likely. Then, the cross section is independent of the photon energy and incoming and outgoing photon have approximately the same energy. This is then called the *classical Thomson differential cross section* [LR09]. This symmetric distribution is more and more distorted for higher energies, with a preference for forward scattering (i.e. small photon scattering angles). This results in rather large electron scattering angles as seen in figure 2.23 and equation 2.42, which according to equation 2.38 creates only low-energetic Compton electrons.
Integration of 2.43 over all scattering angles will result in the total collision cross section giving the probability for a scattering taking place for a photon energy E_i.
For forward scattered photons ($\theta \to 0°$) the differential Compton cross section converges towards a constant value independent of the photon energy [LR09]:

$$\frac{\mathrm{d}\sigma}{\mathrm{d}\Omega_\gamma} \approx {r_e}^2, \tag{2.45}$$

while for backward scattered photons ($\theta \to 180°$) the cross section becomes

$$\frac{\mathrm{d}\sigma}{\mathrm{d}\Omega_\gamma} \approx {r_e}^2 \cdot \frac{(2\varepsilon^2 + 2\varepsilon + 1)}{(1 + 2\varepsilon)^3}. \tag{2.46}$$

It is worth noticing that in case of small scattering angles the differential cross section is an energy independent constant, meaning the probability for a photon to scatter in forward direction is energy independent. On the other hand, backscattering under 180° is not energy independent and is furthermore increasingly suppressed for higher energies.
The Klein-Nishina formula can also be visualized in polar coordinates giving a better impression of the scattering angle into the solid angle Ω measured in steradian (sr). This is

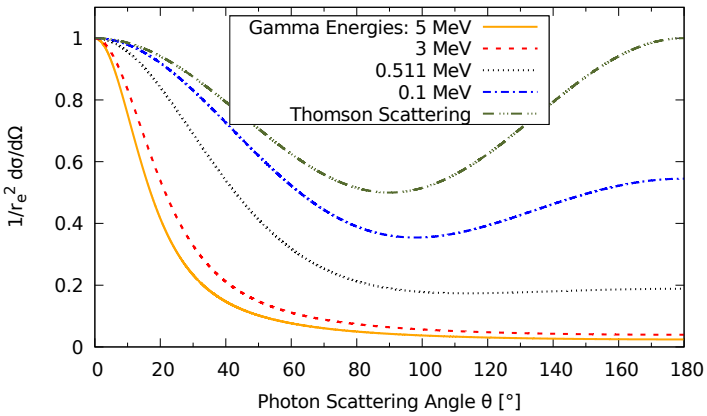

Figure 2.24.: Angular distribution of Compton scattered photons represented by the normalized differential cross section on free electrons. For small energies the Thomson-limit is reached. For higher energies, forward scattering is preferred.

shown in figure 2.25 for different photon energies expressed by the reduced photon energy $E_i/(m_e c^2)$.
For this thesis, the emission angle of the electron is of great importance, which is why an expression for the differential Compton cross section for the recoil electron is required. This differential cross section can be derived using the photon cross section and an appropriate solid angle factor [Dav68]:

$$\frac{\mathrm{d}\sigma_C}{\mathrm{d}\Omega_e} = \frac{\mathrm{d}\sigma_C}{\mathrm{d}\Omega_\gamma}\frac{\mathrm{d}\Omega_\gamma}{\mathrm{d}\Omega_e} = \frac{(1+\varepsilon)^2 \cdot (1-\cos(\theta))^2}{\cos^3(\theta_e)}\frac{\mathrm{d}\sigma_C}{\mathrm{d}\Omega_\gamma} \tag{2.47}$$

Figure 2.23, showing the relation between electron and photon scattering angle, and figure 2.24, showing the photon angle distribution, could only give limited insight on the angular distribution of the recoil electron. Figures 2.25 and 2.26 however, prove that with increased photon energy, both the electron and the photon tend to be scattered in forward direction preferably. For the Compton camera, where the Compton scattered electron is created by a high energetic gamma in the lower MeV range, forward scattered electrons are preferred.

2.2.4. Pair Production

If the initial energy of the photon exceeds a certain energy threshold, *pair production* is possible. This interaction happens in the electromagnetic field of the nucleus of an atom, where the photon disappears and an electron-positron-pair emerges. Therefore, the energy threshold is given by the rest mass of two electrons [Kno10]:

$$E_i \geq 2 \cdot m_e\, c^2 + E_{\mathrm{n.r.}} \tag{2.48}$$

$E_{\mathrm{n.r.}}$ describes the nuclear recoil energy on the nucleus of the atom. However, since in general the mass of the nucleus is much larger than that of the electrons ($m_{\mathrm{nucleus}} \gg 2m_e$) the recoil energy is negligible. The minimum energy of the photon is therefore usually stated with 1022 keV, which corresponds to twice the electron mass. In case the photon possesses

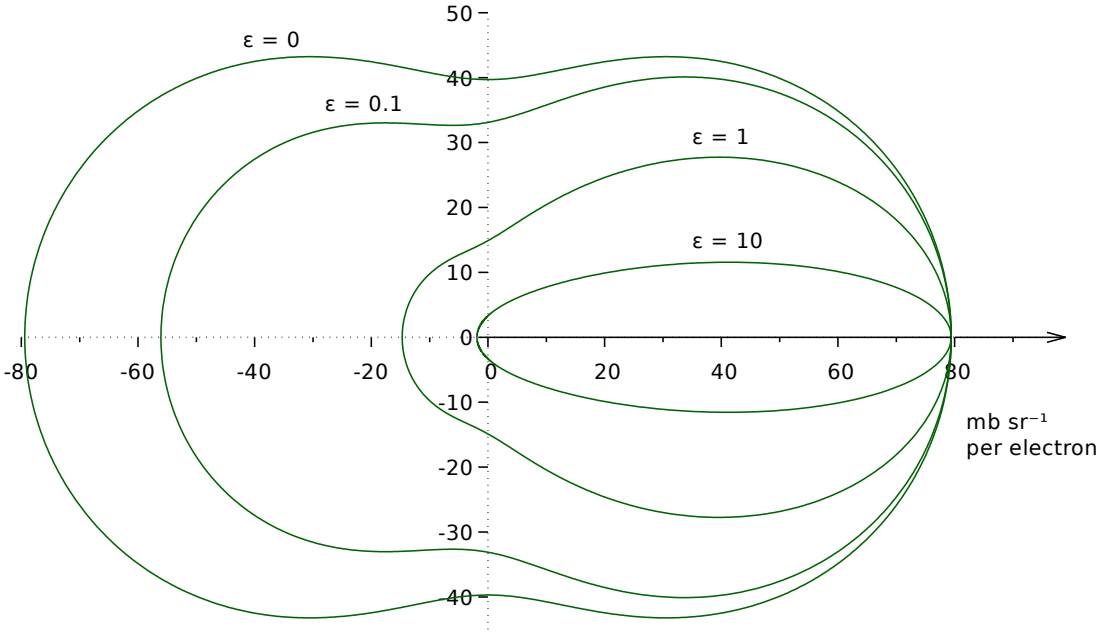

Figure 2.25.: Polar representation of the angular dependence of the differential cross section for the Compton scattered photon according to equation 2.43.

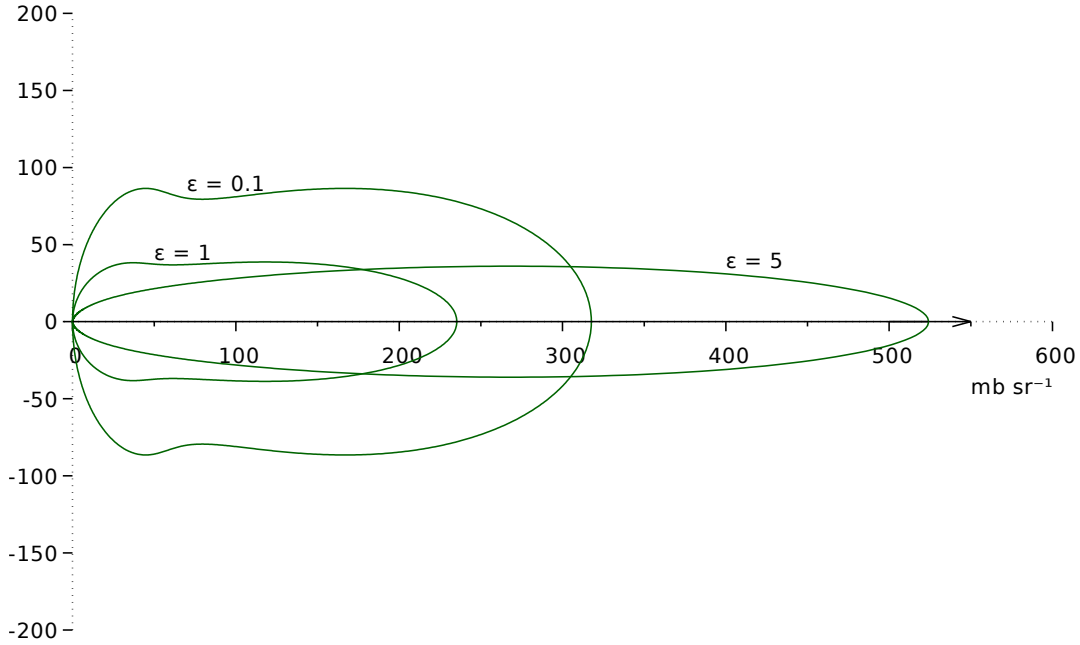

Figure 2.26.: Polar representation of the differential cross section for the Compton scattered electron recoiling at an angle ϕ according to equation 2.47.

more initial energy than required, the remaining energy of the photon is transfered to the electron-positron-pair in form of kinetic energy. After thermalization of the positron and annihilation with an electron from the medium, two photons of the energy of 511 keV are emitted in opposite directions. In gamma-ray measurements, the fate of the annihilation products have an impact on the detector response. The probability of photon interaction via pair creation is relatively small in the lower MeV range. An expression for the pair production cross section $\sigma_{e^-e^+}$ does not exist, but it approximately varies with the atomic number squared. For very large photon energies, $\sigma_{e^-e^+}$ saturates and converges towards an energy independent, Z-dependent constant.
It is also possible for pair production to take place in the Coulomb field of an electron, then the energy of the photon must be larger by a factor 2, this is, however, strongly suppressed compared to pair production in the field of the nucleus [GS08].

3. Photon Detection in Medical Applications

Contents

3.1 Introduction **45**
3.2 Gamma Ray Detection in Particle Therapy **48**
3.2.1 Particle Therapy Treatment 49
3.2.1.1 Introduction and Overview 49
3.2.1.2 Physics of Proton Therapy 51
3.2.1.3 Range Uncertainty in Proton Therapy 53
3.2.2 In vivo Proton Range Verification 54
3.2.3 Prompt-Gamma Detection 57
3.3 The Compton Camera **60**
3.3.1 General Concept 60
3.3.2 Resolution and Limitations 61
3.3.3 Potential Improvement Through Electron Tracking 62
3.3.4 Current Research Status 62

3.1. Introduction

This introduction is, in a way, divided into two categories, which are basically characterized by the considered energy range. Nuclear imaging and emission tomography requires photon detectors efficient in the energy range of up to a few hundred keV. However, there is an increasing demand for the detection of higher energetic photons, which in the following will also be referred to as *gammas* or *gamma rays*. The modest purpose of this introduction is to shed some light on each of the two ranges by exclusive examples without any claim of comprehensiveness or completeness.

Emission Tomography
The probably most prominent example for an emission tomography technique is Positron Emission Tomography (PET) – an imaging technique based on the detection of two time-coincident photons emitted in opposite directions by a positron-emitting radio-isotope. The working principle is based on the physical effect of the annihilation of a positron with an electron and the subsequent emission of two photons in opposite direction. Each photon has

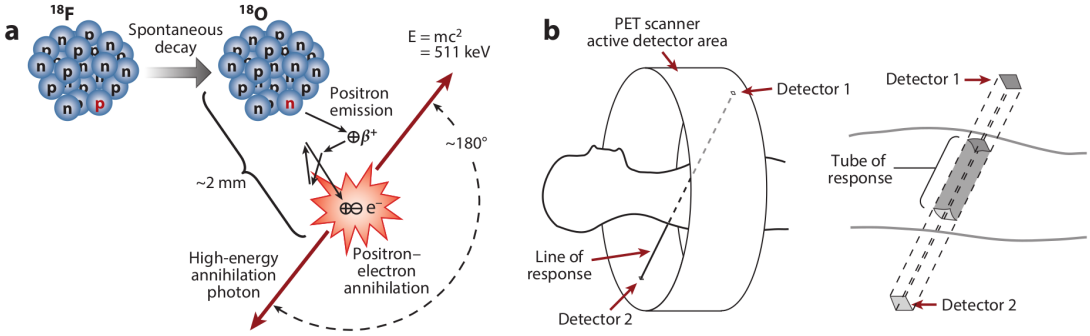

Figure 3.1.: Principle of Positron Emission Tomography (PET) demonstrated on the example of ^{18}F. **a** Demonstration of the annihilation of the emitted positron with an electron from the tissue and subsequent radiation of two 511 keV photons in opposed direction. **b** Coincident measurement of the photons on a ring of scintillation detectors. The origin of the photons can be confined to lie on the LOR between the two detectors. [VK15]

an energy of 511 keV corresponding to the rest mass of an electron or positron respectively. The two photons are detected in coincidence using scintillators and photomultipliers, each equipped with amplifiers and energy discriminators. The coincident detection allows for a localization of the annihilation event to lie on a line connecting the two detection channels – the so called line of response (LOR). In practice, many detectors are located on a ring all around the patient. [SK06] The general principle is schematically drawn in figure 3.1 and demonstrated on the example of positron emitting isotope ^{18}F.

PET has the unique capability of having high sensitivity and estimating the concentration of the radio tracer in the patient accurately. This imaging modality is found in cardiovascular, oncological and neurological applications. [VK15] In oncology, radiopharmaceuticals labeled with positron emitters can be applied to detect the altered metabolism in tumor cells. The tumor has the biochemical characteristic of having a preferential consumption of glucose. Labeling glucose molecules with the typical PET isotope ^{18}F is common practice in tumor imaging.

However, the signal to noise ratio is limited by confounding physical effects like false coincidences due to Compton scattering of one or both of the photons, false identification of coincidences from two different annihilation processes or the loss of events. Furthermore, patient movement, respiratory or organ motion must be compensated for. [VK15]

A currently investigated attempt for an improvement in the signal to noise ratio and the rejection of false signals is the use of the time of flight (TOF) information of the photons. Basically, the measurement of the difference in the arrival time of the two photons on the detector channels allows for a further confinement of the origin of the annihilation on the LOR. A PET system with this upgrade to the detection process is usually referred to as time-of-flight PET (TOF-PET) and constitutes an idea dating back to the 1980s [Sur15]. Since very fast light signals in the scintillators are used to achieve time resolution far below 1 ns, either fast scintillators or the Cherenkov light signal of the photo-electron created inside the scintillator must be used. Due to its instantaneous nature, it could potentially improve the time resolution compared to the conventional use of scintillation signals only. [Kor+13]

PET is a promising diagnostic tool for the prediction of biological and physiological changes on molecular level with the potential to future applications including stem cell research. [SK06]
A first full-body PET scanner has been finalized very recently where not only a ring of detectors but a full tube surrounding the whole patient has been installed. As a part of the EXPLORER total-body PET project, a predecessor for human brain and animal whole body images achieved a spatial resolution of 2.6 mm. [Lyu+19]

Of course there are many other important and well researched techniques in the photon energy range of a few hundred keV, more notably Single Photon Emission Computed Tomography (SPECT). As the name suggests, it realizes imaging using only one high energetic photon emitted from the patient – unlike PET, where two photons must be emitted and detected in coincidence. [VA+15]
Another photon detection technique for this energy range was presented in 2015 by Thirolf et al., which might at first come across like a hybrid system of PET on the one hand and a gamma camera or a single photon detector on the other hand: highly-sensitive PET-based imaging with coincidences of a beta emitter and an additional gamma emission was proposed. It would enable the use of further PET isotopes where, additionally to the positron, a higher-energetic photon is emitted from an excited state in the daughter nucleus. When compared to conventional PET, less reconstruction would be required and sub-millimeter resolution could be achieved. Monte Carlo (MC) studies showed first promising results. [TLP15]

Sources of Higher Energetic Photons

The focus of this thesis lies on the detection of electrons in a Compton camera (CC), which is a proposed imaging device for higher energetic photons in medical applications. In contrast to photon energies used in nuclear medicine and emission tomography like PET or SPECT, which are in the range of up to several 100 keV, the CC focuses on the detection of higher energetic photons in the range of up to several MeV. The CC is only one possible concept to realize such a measurement device. The rising interest in these higher energetic photons (or gamma rays) is represented by the increasing demand for detector systems capable of measuring photons in that energy range and in the large variety of developments throughout the last decades [HG+16].
The sources of these photons are nuclear reactions, for example by the decay of radioactive isotopes brought into the human body for treatment purposes, in whose decay chain gamma emission occurs. This stands in contrast to the isotopes used for imaging in PET, which are beta emitters. A second possible origin of nuclear reactions lies in external excitation of the tissue's nuclei through irradiation with charged particles like protons. Subsequent to the irradiation, the emission of higher energetic gamma rays occurs. This effect and especially the detection of these so called prompt gammas (PGs) is one possible method to determine the range of the proton beam inside the patient. Proton therapy will be summarized in section 3.2.1 and the importance of range verification is outlined in section 3.2.1.3.

As mentioned, there is gamma emission subsequent to the decay of radioactive isotopes purposely injected into the body for treatment measures as it is performed in targeted alpha therapy for cancer treatment. The goal of any cancer therapy is to create the ability to

target only malignant cells while sparing healthy tissue. Targeted alpha therapy seeks to achieve this goal by carrying alpha-emitting isotopes to specific sites in the body using so called vectors. Alpha particles have the great advantage that their energy deposition per unit distance is over 500 times higher than that of electrons or positrons. Due to the high stopping power, they have limited range. An alpha particle with an energy of 5 MeV traversing through tissue-equivalent plastic with a density of $1.127\,\mathrm{g/cm^3}$ has a range of only $3.2 \cdot 10^{-3}$ cm. The value was calculated using *stopping power and range tables for helium ions (ASTAR)* [Ber+99]. This circumstance enables targeting selected malignant cells with minimal effect on normal tissue and constitutes a highly controlled therapeutic modality. Some isotopes currently under investigation are for example ^{212}Bi, ^{227}Th, ^{212}Pb or ^{223}Ra. [BYB13]
In order to monitor this treatment process, the detection of the partially high energetic gamma rays emitted in the decay of the isotopes could be used. One isotope under investigation is ^{212}Pb [Tan+12], which has a half life of 10.64 hr and decays to ^{212}Bi under beta emission, which itself has a half life of 60.55 min. With a 35.94 % probability ^{212}Bi undergoes alpha decay. The decay product ^{208}Tl, with a half life of only 3 minutes, decays to ^{208}Pb, which is accompanied by the emission of a high energetic gamma ray with the energy of 2.615 MeV. [CEF99]

Independent of the specific application, the detection of higher energetic photons in the MeV range for medical purposes in clinically applicable systems is highly challenging, which will be demonstrated with the example of prompt-gamma detection in section 3.2.3. The following chapter summarizes the physics and problematics behind proton therapy (section 3.2.1) as well as the range uncertainty problem. The detection of gamma rays emitted subsequent to the irradiation of tissue with charged particles is one prominent range verification method, but other techniques are summarized briefly as well in section 3.2.2. The creation of gamma rays and some of the existing or envisaged detection concepts will be outlined (3.2.3) followed by an introduction to the concept of the CC (3.3).

This introduction to the topic has shown a small example of the vast number of applications for photon detectors in medicine and nuclear imaging and demonstrates the demand for research in this field. One specific type of photons – higher energetic prompt gamma – is the subject of investigation in the next section. Since this thesis addresses the detection of higher energetic photons in the MeV range, extended focus will be put on the origin of this type of radiation, novel and established detection concepts as well as the importance for and applicability in medical physics.

3.2. Gamma Ray Detection in Particle Therapy

The detection of higher energetic gamma rays of up to several MeV plays an important role in addressing the so called range uncertainty problem in particle therapy. The following chapter 3.2.1 provides an outline of particle therapy and explains the importance of verifying the beam range inside the patient as requirement for profound treatment planning and successful therapy outcome. An overview over the available imaging modalities for range verification will be given together with the most prominent techniques attempting to realize them (section

3.2.2). A special focus is put on prompt gamma detection (section 3.2.3), for which the CC is one possible concept.

3.2.1. Particle Therapy Treatment

3.2.1.1. Introduction and Overview

Already in 1946 Robert Wilson noticed that charged particles hold a potential advantage for cancer therapy in comparison with gamma rays and x-rays due to their advantageous dose distributions [Wil46]. Proton beam interactions in the body are characterized by the lower deposited energy (i.e. dose) in the entrance channel in front of the tumor and a strong increase and rapid fall-off towards the end of the range, which lies ideally inside the tumor. [Smi06; Joh17] This therapy modality promises highly conformal dose delivery to the tumor, improved therapeutic outcome and reduced toxicity, which is especially important for the treatment of pediatric tumor [PP18]. However, from the first treatment of a human with proton beams at Lawrence Berkely Laboratory in 1954 [NZ15] it took decades until in 1990 the first treatment facility for hospitals was installed in Loma Linda, California, USA [HG+16]. In 2001 finally the first commercial proton treatment system was implemented after overcoming considerable difficulties. In comparison to the already established technique of using high energetic photons for tumor treatment, the adaptation of proton beams for treatment was very slow, mostly due to the more severe technical difficulty and higher costs for installing and maintaining such a treatment facility [NZ15]. Nevertheless, today more than 200000 patients per year are treated worldwide using particle beams, mostly with protons [Gro19].

The great potential of protons lies in the way the dose is deposited inside the body: The energy loss per unit path length varies almost inversely with the kinetic energy of a non-relativistic particle. Therefore, most energy is deposited towards the end of the track resulting in an accumulated ionization shortly before the particle is stopped. This is the so called *Bragg peak*. With sufficient knowledge of the specific ionization (proton stopping power) of the tissue and the tumor it is possible to tune the energy of the proton beam so that the ion stops inside the tumor. Fine tuning of the proton beam energy results in minimal dose proximal to the tumor (meaning in front of it as seen from the proton beam direction) and almost no dose distal to the tumor (behind it). Robert Wilson also proposed the idea of range modulation to create a spread-out Bragg peak (SOBP) as shown in figure 3.2. It can then uniformly cover a larger target volume than non modulated proton beams. In practice a SOBP is realized in the so called *intensity modulated proton therapy* (IMPT) either by physical devices like filters or modulation wheels or by modulating the accelerator and variable weighting of each individual Bragg peak. Figure 3.2 demonstrates schematically the dose distribution along the trajectory of proton beams of several different energies in a water phantom forming the SOBP [NZ15]. The proton SOBP shows much better conformity to the tumor target than the photon dose distribution [Smi06]. In principle protons can also deliver higher doses to the tumor than conventional (x-ray) photon treatment [KL13].
A key aspect of evaluating proton therapy is not only the effectiveness in destroying the tumor but also in terms of how small the effect on the rest of the body is [Joh17]. A comparison of

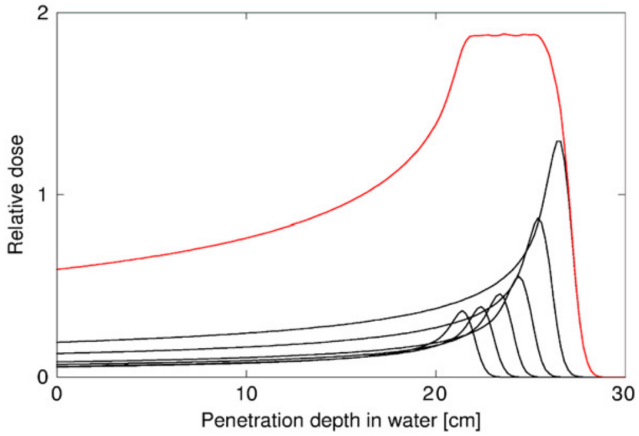

Figure 3.2.: Dose distributions of protons of different energy in water phantoms forming the spread-out Bragg peak (SOBP). Its clinical application for proton treatment has the potential for higher conformity to the tumor volume. [NZ15]

treatment with proton beams and higher energetic photons as well as the range uncertainty problem is addressed in detail in section 3.2.1.3.
In contrast to protons, tumor treatment using photons does not provide the advantage of sharp distal fall off. The only way to limit the dose to other organs is to irradiate from different angles and to distribute the dose over a large tissue volume. There are, however, some disadvantages proton therapy has, when compared to photon treatment: Firstly, there are the already mentioned higher costs for construction and clinical operation. Secondly, there is still a lack of clinical studies proving the success of the method and its superiority over photon treatment and, thirdly, there is the range uncertainty principle [HG+16]. The latter is subject to intense research up to this day.
In order to take full advantage of this treatment method, the treatment process needs to meet certain requirements. Firstly, the size of the beam needs to match the morphology of the cancerous tissue and the incident proton kinetic energy must be controlled independently at each location. The deposited dose must conform to the depth of the tumor and the tissue quality in front of it. The goal of any radiotherapy technique is always to deliver a dose distribution precisely to the tumor volume while affecting the surrounding healthy tissue or critical organs as little as possible [Joh17].
Collimators that are customized for each patient are used to control lateral size of the proton beam. Overall energy – and therefore the interaction depth – can be controlled by adjusting the accelerator or (in cases where this is not possible) by using a special mask in front of the tumor. It serves as degrader.
Knopf and Lomax define two different approaches to deliver the proton beam to the patient [KL13]:

1. Passive scattering: Scatter foils broaden the narrow proton beam extracted from the accelerator into a broad beam suitable for therapy. It is then shaped to the geometry of the target by apertures (for lateral dose conformation). Lateral variation in energy can be achieved by passing the beam through a plastic compensator with different thicknesses. It is thicker in regions where less penetration is desired and vice

versa. [Joh17] Range compensators controlling the overall energy – and therefore the interaction depth – are applied for distal conformation. In that case, either the proton accelerator is adjusted (which is not possible in every facility) or the beam is passed through degrader materials. Additional to that a range modulation device is applied to broaden the Bragg peak and form a plateau (Spread-out Bragg peak SOBP). The disadvantage is that patient-specific hardware is needed (degrader and aperture suiting the geometry of the target).

2. Active scanning: A narrow and quasi mono energetic beam (*pencil beam*) is magnetically scanned across the target in addition to a step-wise change of the energy for depth control of the Bragg peak. Within this method further distinctions could be made regarding the exact delivering mode. The advantage of this method lies in the greater target dose conformity and less neutron contamination. It also offers the possibility to deliver intensity modulated proton therapy (IMPT), which could include treatment from multiple directions [Joh17]. This gives better control of the dose distribution, and thereby greater success in sparing critical organs from harmful radiation doses. Pencil beams in air can have a diameter as small as 7 mm full width at half maximum (FWHM) [Smi06]. The major disadvantage is the high technical difficulty to produce narrow pencil beams and maximize the lateral dose fall-off. Furthermore, scanning is extremely sensitive to organ motion during the treatment or in between two treatment fractions.

After decades of research, proton therapy is still controversial, because of its high cost relative to x-ray facilities. Furthermore, clinical random trials are still lacking significance. From a physics point of view, however, proton therapy is expected to be beneficial because of the fact that the radiation can be localized better than in x-ray treatment. [Joh17]

3.2.1.2. Physics of Proton Therapy

Energetic protons used for therapeutic measures passing through tissue will undergo various interactions. The governing processes protons undergo inside an object are summarized in the following list [KL13; NZ15]:

- Energy loss according the Bethe-Bloch equation
  The protons continuously lose energy due to Coulombic interactions with electrons of the target material. The rate of loss increases with decreasing energy of the particle. This loss in a medium with density ρ is described by the stopping power $S(E) = \rho^{-1} \cdot \partial E / \partial z$, where E is the energy of the particle and z parametrizes the traveled distance in one dimension. For details see section 2.1 on particle interactions in matter. For charged particles with masses much larger than the electron mass, $S(E)$ can be analytically described with the Bethe-Bloch formula. For protons in the MeV-range, the stopping power scales approximately with the inverse square of the particle's velocity $S(E) \propto 1/v^2$. The statistical nature of Coulomb interaction gives contributions to a low plateau in the depth dose curve and the aforementioned velocity relation results in a steep distal peak (Bragg-peak).

- Multiple Coulomb scattering
  Coulomb interactions of the proton with atomic nuclei are called Multiple Coulomb

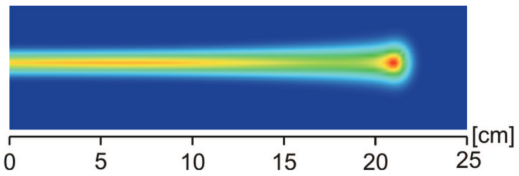

Figure 3.3.: Cross-section through a 177 MeV proton pencil beam entering from the left demonstrating the influence of Multiple Coulomb Scattering (MCS). The colors indicate the amount of deposited energy by the protons. Increased scattering can be seen in the halo around the end of the range. [Lom09]

Scattering (MCS). Deflection (or even repulsion) occurs due to positive charge of both nucleus and proton. Due to MCS the width of the beam at the Bragg peak increases by about 2 % of the beam range in water. Figure 3.3 demonstrates the effect of MCS on a cross-sectional plot of a 177 MeV proton pencil beam. The protons enter from the left and the deposited amount of energy is indicated by the colors. The scattering increases towards the end of the range close to the Bragg peak where the energy loss per distance increases. Additionally, a deflection through Coulomb interaction between the proton and an electron can occur. However, since the proton is about 1832 times heavier than the electron, this effect can essentially be neglected.

- In-elastic nuclear interactions
  In-elastic interactions directly with the nucleus causes the proton to be lost (in-elastic collision). After a projectile proton enters the nucleus, a proton, deuteron, triton, or heavier ion or one or more neutrons can be emitted as well as gamma rays. In this case the characteristics of the nucleus are changed as well and (usually short-lived) radio-isotopes can be formed, for example ^{15}O or ^{11}C, which both emit positrons. Another example would be the excitation of a ^{12}C nucleus with the subsequent relaxation to the ground state under the emission of a 4.4 MeV prompt gamma [HG+16].

  On the one hand about 1 % of protons are lost per cm in water due to in-elastic collisions, on the other hand one can make use of these created isotopes to directly extract information on the particle range in vivo[1]. In case of created positron emitters, PET can be used to monitor the beam range while gamma cameras can be employed to detect emitted prompt gamma radiation (see section 3.2.3).

  The third example to mention is the creation of neutrons by nuclear interactions. They give rise to the risk of radiogenic late effects in the patient, since they are high energetic and extremely penetrating [NZ15].

For the sake of completeness one should mention that proton Bremsstrahlung is possible as well. However, at proton beam energies used for tumor treatment (on the order of 200 MeV) this effect is negligible [NZ15].
Due to the statistical nature of these charged particle interactions, statistical variations affect the following quantities of the proton beam [PAE15]:

- The lateral position at a given penetration depth

[1] *in vivo*: within the living body [Wik17]

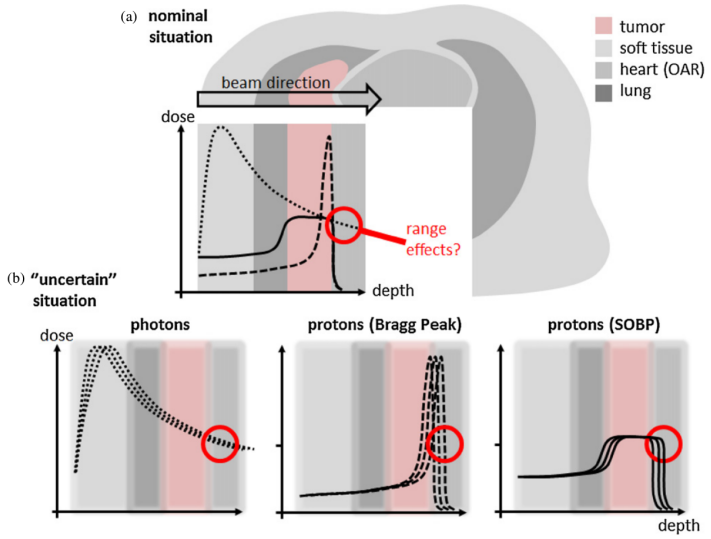

Figure 3.4.: (a) Comparison of photon treatment (dotted line) and mono-energetic proton beam including the Bragg peak (dashed line). Shown as well is the so called spread-out Bragg peak consisting of several proton energies to cover the whole tumor volume. (b) Demonstration of the influence of range uncertainties on the delivered dose distribution. [KL13].

- The proton direction at a given penetration depth
- The energy at a given depth
- The stopping depth at a given initial energy, which is also called *range straggling*

The last quantity is subject of the following section addressing the range uncertainty problem in particle therapy.

3.2.1.3. Range Uncertainty in Proton Therapy

Problem description:
A well defined range with a sharp fall-off is the greatest advantage of protons for radiotherapy. However, the large dose gradient at the distal edge of the Bragg peak bears a risk: uncertainties in determining the range of the protons can cause significant differences in the actually applied dose distribution compared to the calculated prediction or expectation. This uncertainty limits the ability of proton therapy to spare healthy tissue. To overcome the problem, improved knowledge of the proton range in vivo is required.
Figure 3.4 a) shows the difference of the dose distribution of photons compared to protons. The steep distal fall-off of the dose in case of protons can be used to protect organs at risk (OAR) like the heart. However, uncertainties in the range result in a larger difference in distributed dose inside the body compared to photon treatment.
Due to the sharp fall-off at the Bragg peak the temptation exists to aim directly at critical structures or organs lying behind the tumor. But range uncertainties and the potential overshoot of the distal gradient give rise to the possibility of overdosing these distal structures. Figure 3.4 b) demonstrates that effect for either photons and protons. If density variations within the patient are ignored, the dose changes on the order of a few percent in case of

photons. However, using a proton beam the dose at the distal edge of a SOBP could fall off by almost 100 % due to the sharp gradient. Range uncertainties, therefore, have a significant effect on proton therapy treatment and a successful dose delivery to the tumor.

Sources of Range Uncertainty:
The dose deposition curve and the proton range strongly depend on the stopping power of the tissue. Profound knowledge of the patient's anatomy is therefore crucial. Computed tomography (CT) data sets are the basis of range calculations and treatment planning. Usually analytical pencil beam models are used to calculate range. Algorithms calculate range straggling and beam broadening due to MCS, which are in good agreement with measurements at least in water. But the accuracy is limited due to the complex density heterogeneities. Since treatment plans are based on CT images, the range calculation/prediction is limited by inherent limitations of CT image acquisition. Image noise, volume effects, reconstruction artifacts and especially beam-hardening effects affect the precision of the calculation. The term *beam-hardening* describes the attenuation of lower energetic wavelengths in a polychromatic X-ray beam passing though an object. This causes an increase ("hardening") of the mean energy of the beam that contributes to the image. [Pes+13] In total, it is assumed that range uncertainties based on a well calibrated CT of sufficient quality are of the order of $\pm 3\,\%$ [Moy+01].
Further sources for uncertainty are changes in the delivered proton energy on a day-to-day basis (usually less than 1 %) and range changes due to variations in patient positioning relative to the beam. Especially the latter can cause quite substantial range uncertainties. Finally, anatomical changes in the body during or in between treatments can have an influence. Patient's weight loss (or gain) or tumor shrinkage as well as changes in the filling of inner cavities like the bladder or the rectum can contribute to range uncertainties. Finally, respiratory motion, the patient's heart beat and movements in the abdomen need to be taken into account.

Successful range prediction, monitoring and on-line correction paves the way for new beam directions using the steep distal fall-off to be able to protect organs directly behind it. Improvements in dose conformity to the target and reduction of the irradiation of normal tissue are further advantages. This would also potentially allow for an increase in dose and subsequently a reduction of treatment time while still sparing healthy organs. Furthermore, a reduction of safety margins could be achieved. These margins around the tumor are currently still required to obtain a robust treatment plan but they also limit the advantages of the dose profile of protons compared to photons. Ergo, there is a need for accurate verification of proton range in vivo.
[KL13; HG+16]

3.2.2. In vivo Proton Range Verification

Throughout the last 2 decades multiple concepts for experimental devices were proposed with the aim to measure the particle range and even the dose profile, preferably on-line during the treatment [HG+16]. The following part gives an overview of some of the most prominent and wide-spread methods and categorizes them based on their measurement characteristics.

Knopf and Lomax categorized the detection methods for the proton beam range using the following aspects:

- *Directness:* A distinction is made between methods where the range is measured directly and those where the range is implied from another secondary signal.
- *Timing:* On-line methods allow to measure the range during or immediately before the treatment starts. Off-line methods can only perform a range verification after the treatment has ended
- *Dimension:* 1-dimensional methods with only single point measurements, 2-dimensional imaging methods and 3-dimensional volumetric measurements are distinguished.

A brief overview of the currently investigated concepts and their potential will be given in the following list:

- **Prompt Gamma Detection:**
  One of the most prominent and most extensively researched concepts to track the proton beam is the detection of prompt gammas (PGs) emitted subsequent to nuclear interactions of the protons with the nuclei of the patient's tissue. Since the detection of PGs is the key subject of this thesis, a thorough introduction to this range verification method is given in a separate section (see 3.2.3).
- **Positron Emission Tomography (PET):**
  As mentioned earlier, β^+-active nuclei are produced as byproduct through nuclear fragmentation reactions caused by irradiation with protons. The subsequent emission of two 511 keV photons in opposite directions can be used to reconstruct the proton beam intensity and the range. Typically, the half lives of these isotopes are in the range of μs up to several minutes. Therefore, range verification with PET is an on-line as well as an off-line imaging modality. 3-dimensional images can be produced. Since the PET signal is created by secondary emission, this technique is an indirect method. Challenges lie in the low counting statistics, which is orders of magnitude lower than for tracer imaging in emission tomography. Also, organ motion and physiological washout of the produced PET-isotopes decreases the image quality. [PP18; KL13]
- **Proton Radiography and Tomography:**
  This ion transmission imaging technique uses protons themselves to create images of the tissue and the tumor for treatment planning while the patient is in the same position as for the treatment itself. Protons must pass entirely through the patient to use them for radiography (2-dimensional image) and tomography (3-dimensional). Therefore, they must have significantly higher energies than the protons used for the treatment. Not all existing accelerators can provide the required energy. Proton radiography might provide better density resolution and tissue contrast than conventional x-ray imaging, which is crucial for robust treatment planning. Since the protons themselves are detected, this concept is a direct range verification method and can be applied on-line right before the treatment of the tumorous tissue takes place. Position sensitive detectors are placed before and after the imaging object and the tracking of the protons is synchronized with the residual energy or range measurement of a calorimeter behind the object.

Thus, the stopping power of the protons along their trajectory inside the body can be determined and used for planning, range prediction and verification. Disadvantages are the influence of Coulomb scattering in the proton beam, which limits the achievable position resolution. On the other hand higher contrast is expected compared to X-ray imaging and, additionally, it is mostly artifact free. [Joh17; KL13; PAE15; PP18]

This technique has not yet reached clinical application and Schulte et al. [Sch+03] define the following requirements for this to happen: A spatial resolution of 1 mm and a density resolution of 1 % need to be achieved. Furthermore, the acquisition time needs to be less than 5 min while the patient is exposed to a dose of not more than 50 mGy, which is about the same as in an X-ray scan today.

- **Iono-accoustic range verification:**
  The very basic work by Hayakawa et al. (1995) proposed the detection of an acoustic pulse that is generated inside the patient during the treatment with pulsed proton beams. This so called *ionoacoustic effect* was used for range measurement of proton beams in water by Lehrack et al. (2017) [Leh+17]. The detection of the ultrasound waves was performed using a sensitive hydrophone. A comparison with range data from a calibrated range detector set-up gave an agreement of better than 1 mm at a Bragg peak dose of 10 Gy. Measurement of the ionoacoustics pulse is a direct range verification method in 2 dimensions happening on-line during the treatment and could potentially be combined with ultrasound tissue imaging.

- **Magnetic resonance imaging (MRI):**
  MRI can be used to make changes in tissue constitution visible that arise subsequently to radiation with charged particles. These changes provide an opportunity for off-line observation of the delivered dose distribution in vivo. The big advantages of this 3-dimensional imaging technique are its very high resolution, the lack of additional dose to the body during imaging and the availability in a large fraction of facilities. However, visual inspection of MRI images alone is not sufficient for range verification, since the signal intensity gradient in MRI does not correspond to the gradient of the delivered dose. Thus, a dose to signal intensity relationship is required. Another challenge is the temporal evolution of the magnetic resonance signal. Since tissue conversion happens only after the irradiation, MRI imaging only allows for a retrospective range check. [KL13]

- **Neutron tracking:**
  During the particle treatment, additional dose occurs along the beam path towards the target. Neutrons are especially dangerous, as they can travel over a significant distance and deposit their energy far away from the tumor volume giving rise to post-treatment development of cancerous, malignant tissues. Since 2018, the MONDO project (MOnitor for Neutron Dose in hadrOntherapy) aims for a detection and characterization for these secondary ultra-fast neutrons with 20-400 MeV energy. [Fis+18] There is, however, also a proposal for the use of secondary neutrons for on-line range verification in particle therapy. The NOVO (NeutrOn detection for real-time range VerificatiOn) project is based on the detection of secondary neutrons produced in nuclear interactions during proton therapy. A MC feasibility study by Ytre-Hauge et al. (2019) investigated this

on-line modality. One challenge lies in the dependency of production rate and energy of the neutrons on the initial beam energy. The production cross section for the creation of neutrons decreases with reduced proton energy along the beam path, which makes a clear representation of the Bragg peak difficult and only a range landmark can be determined to be correlated to the proton beam range. Although the study only looked at 1D distributions of neutron production positions in a water phantom, an extension to up to 3 dimensions using tracking detectors is envisaged. [YH+19]

- **Implantable markers:**
  For on-line in vivo point measurements in 1 dimension implantable markers with wireless readout became available. Although, the initial purpose was the dosimetry in photon therapy, investigations have been initiated to apply this technique to proton range verification. These markers allow for a range check before, during and after the beam delivery. But, so far, no time-resolved dose measurement is possible. [KL13]

3.2.3. Prompt-Gamma Detection

The use of prompt gamma (PG) rays as range verification modality was first proposed by Jongen and Stichelbaut in 2003 [SJ03]. Shortly after, in 2006 Min et al. provided the first experimental evidence of this method [Min+06]. Since then, various groups have actively investigated this option. There are several reasons why PG detection is a promising technique: The spatial emission distribution of PGs follows the dose deposition of the proton beam in the patient. The proton range is obtained by matching the observed PG distribution to CT scans, the treatment plan and nuclear physics models. PG detection is therefore an indirect measurement of the proton range.
PGs originate in proton-nuclear interactions all along the beam path inside the patient. Many of the most abundant atoms in the body have reaction channels with incoming protons, which result in excited nuclei and subsequent prompt gamma emission when the residual nuclei de-excite. The emission spectrum lies in the range of 2-15 MeV and contains a number of discrete gamma-lines from specific nuclear de-excitations. Discrimination of the dose fall-off at the Bragg peak is more successful for higher energetic gammas as they undergo less scattering inside the patient [KL13].
The time scale of the emission is on the order of 10^{-11} s giving prompt gammas their name and allowing for real-time range monitoring during the treatment. In contrast, some PET isotopes created through proton interactions have half lives of up to several minutes and can be used for off-line monitoring after the treatment or in between treatment fractions. [KL13].
In order to make PG detection clinically applicable, the following requirements need to be fulfilled [HG+18]

- Sufficient detection efficiency allowing for millimeter spatial resolution
- Accurate knowledge of the relation between proton dose deposition and measured gamma ray emission (the correlation between proton dose distribution and gamma ray emission depends on the tissue quality and the energy of the emitted gamma radiation)
- Adaptability to varying count rates (occurring in pencil beam scanning for example)

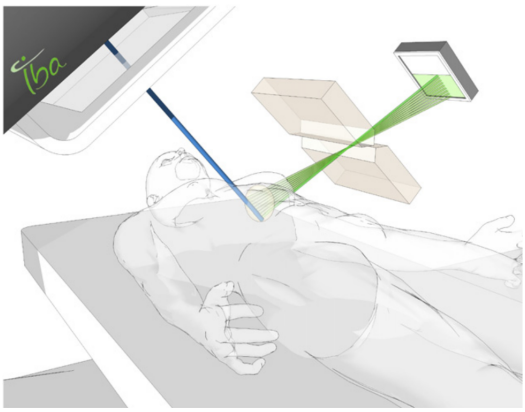

Figure 3.5.: Slit Camera for proton beam range measurement using prompt gamma (PG). [Sme+12]

- Operability of the detection and image reconstruction during the beam delivery in order to not prolong the treatment process for the patient

One major challenge lies in the high proton rates that are produced during the treatment. This can be demonstrated using the example of the proton beam at the University Proton Therapy Dresden: In pencil beam scanning mode about 1-2·10^8 protons are shot at the tumor within 10 ms. This results in a rate of 10^{10} protons per second, which equals a typical beam current on the order of 2 nA. Assuming a production yield of 0.1-0.3 PGs per proton, one expects 1-3·10^7 gammas per pencil beam spot and a total production rate of 1-3·$10^9\,s^{-1}$ emitted in 4π. There are more than enough prompt gamma (PG) available for imaging, however, the time for their measurement is very short. [Pau+18]
Besides, the so called neutron background plays an important role: gammas emitted by neutron interactions or after neutron capture in the surrounding material give false signals and increase the signal to noise ratio in the image.
From a solely clinical aspect, the designed detector must not interfere with either the patient or the treatment. An extension of the treatment time due to PG detection is also not acceptable as the clinics have to deal with a large patient throughput to compensate for operational costs and maintenance.
Already existing gamma cameras cannot be used as PG imaging devices due to the high count rates, the neutron background, the high gamma energies, and their polychromatic energy spectrum. Larger and more expensive collimators and detectors would be needed to absorb higher energetic gammas in the MeV range. In comparison, photons used for imaging in diagnostic and nuclear medicine are in the range of 80-511 keV (e.g. PET). Alternative concepts are needed, one of which is the *Compton camera* explained in chapter 3.3. [HG+16; HG+18; PP18].

Potential Implementations and Realizations of Prompt Gamma Detection:
Clinical applicability of prompt gamma (PG) detectors for proton range verification has failed so far, mostly because no commercially available detector solution exists yet. Existing photon detectors like Single Photon Emission Computed Tomography (SPECT) are not feasible because of the high energy of the prompt gamma emissions making impractically

thick collimators necessary. Hence, alternatives have been conceptualized and investigated throughout the last years. [KL13]

A collimated PG camera is the most straightforward approach, however, neutron background requires thick collimators and therefore reduces the efficiency. An improvement to the collimated concept and an attempt to overcome its challenges is made by the slit camera. This technique was proposed in 2012 [Sme+12] and its feasibility was investigated in a MC study as well as with a prototype set-up. The concept is to use a slit collimator to obtain a one-dimensional projection of the beam path on a scintillation detector. The study confirmed the potential of the concept for real-time range verification and achieved millimeter accuracy when using pencil beams. A schematic depiction of this gamma imaging modality is shown in figure 3.5.

A modification to this concept is the idea of prompt gamma timing for range verification: The use of the time of flight signal to differentiate the PG from the background makes bulky shielding unnecessary [KL13]. The concept uses the elementary effect that an incoming proton requires some time to be stopped, which is usually on the range of a few nanoseconds. This transit t_p time increases with the range of the proton. Also, the emitted PG requires a time $t_{\gamma\text{ToF}}$ to reach the detector. Measurement of the duration from the proton entering the body and the arrival of the produced prompt gammas (with assumed instantaneous emission) allows for an estimation of the proton range in the patient's body. [Gol+14]. Figure 3.6 shows the principle.

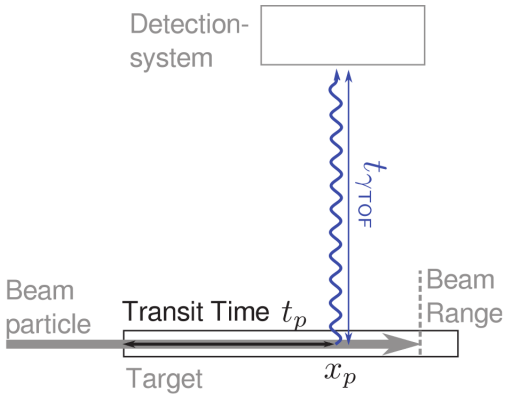

Figure 3.6.: Principle of prompt gamma timing measurements for range verification: A detection system measures the time difference between the time of the particle entering the target and the arrival time of the PG at the detector. [Gol+14]

Although, there have been clinical trials with promising results for some approaches (for example the slit camera [Xie+17]), none of the concepts introduced above have reached clinical applicability yet. Another project called PAPRICA (PAir-PRoduction Imaging ChAmber) attempts the detection of PGs using the production of an electron positron pair due to gamma interaction inside the detector. So far, no published results are available yet.

3.3. The Compton Camera

3.3.1. General Concept

First proposed by Todd et al. (1974) [TNE74], the principle of a Compton camera (CC) makes use of the predominantly occurring photon interaction in the MeV energy range: Compton Scattering. The principle is displayed in the sketch in figure 3.7. An incoming gamma with the energy $E_{\gamma,1}$ undergoes Compton scattering in a first detection layer creating an energetic Compton electron with energy E_e. The energy transfer E_e from the gamma to the electron equals the difference between the energy of the incoming and the absorbed gamma $E_e = E_{\gamma,1} - E_{\gamma,2}$. The scattered photon of energy $E_{\gamma,2}$ is then absorbed in a second layer. The Compton scattering angle can then be obtained using the following relation:

$$\cos\theta = 1 - m_e c^2 \frac{E_{\gamma,1} - E_{\gamma,2}}{E_{\gamma,1} \cdot E_{\gamma,2}} = 1 - m_e c^2 \frac{E_e}{E_{\gamma,2}(E_e + E_{\gamma,2})} \tag{3.1}$$

which can be derived by rearranging equation 2.40.
The Compton camera concept requires a coincident measurement of the energy of both electron and absorbed gamma as well as the positions of the gamma and the Compton scattering vertex. This allows to reconstruct the source location of the incoming gamma to lie on the surface of a cone – the *Compton cone*. The gamma source location can be obtained by intersecting many of these cones. [Roe+11; Dra+18]

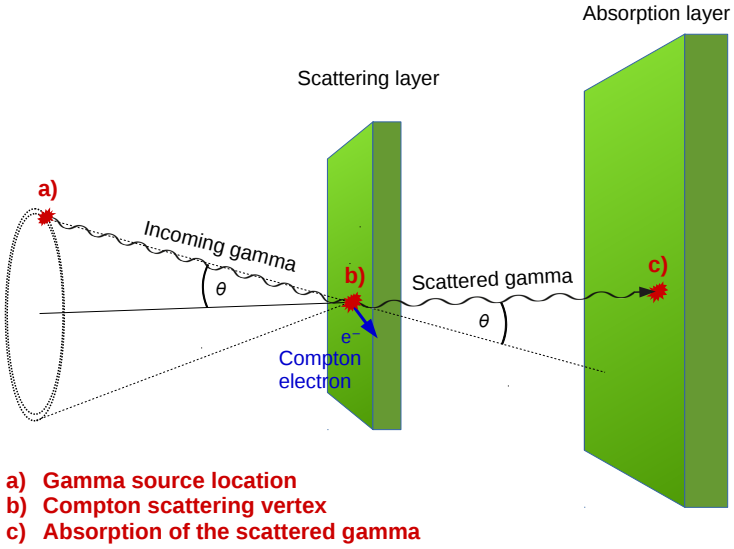

Figure 3.7.: Compton Camera working principle: An incoming gamma undergoes Compton scattering in a first layer creating a high energetic Compton electron and being absorbed in a second layer. Measurement of energy and position of both electron and absorbed gamma allows to reconstruct the source location of the incoming gamma to lie on the surface of a cone – the *Compton cone*.

3.3.2. Resolution and Limitations

The Compton camera is an electronically collimated detection system [Roe+11] with the main advantage of an increased efficiency of potentially up to two orders of magnitude compared to collimated gamma-cameras, which use performance-limiting absorbing collimators [KL13]. There are, however, limiting factors a CC suffers from, which will briefly be explained in the following part.

The obtained spatial resolution on the source location is defined by the precision $\Delta\theta$ of the measurement of the opening angle: $\Delta z = \Delta\theta \cdot d$, where d is the distance from the scattering layer to the source. The uncertainty on the opening angle $\Delta\theta$ is determined by the energy resolution of the detector and by the energy of the incoming gamma ray itself. Higher energies of the incoming gamma result in smaller uncertainties on the angle and, thus, better spatial resolution. Another influence on the spatial resolution arises from the uncertainty on the vector connecting the scattering vertex in the first layer with the position of absorption in the second layer. The latter of which depends on the position resolution of the absorber detector. [Nur+15].

If the energy of the incoming gamma is unknown – which is the case in an application to PG detection – it can in general be deduced from the measured energies E_e and $E_{\gamma,2}$ of Compton electron and absorbed gamma respectively. However, in a significant fraction of events, no full energy-deposition in the detector takes place making a correct reconstruction of the opening angle θ of the Compton Cone impossible. One reason for this is the low photon absorption cross-section in the second layer causing the photon to deposit only a part of its energy via Compton scattering. For these cases, a system with three detection stages might constitute a work-around, however, the detection efficiency would be relatively low making a clinical application questionable. [Roe+11] Additional to incomplete energy deposition, influences on the imaging capabilities can moreover be found in Non-Compton-scatter events: these are false coincident detections of separate gammas as well as interactions of neutrons or other secondary particles in the individual detector layers within the coincidence time window. The consequence is a reduction of spatial resolution and increased image noise. [Dra+18]

The overall efficiency ϵ_{tot} can be factorized as follows [Nur+15]:

$$\epsilon_{\text{tot}} = \frac{\Delta\Omega_1}{4\pi}\epsilon_1 \cdot \frac{\Delta\Omega_2}{4\pi}\epsilon_2 \tag{3.2}$$

The quantities ϵ_1 and ϵ_2 are the interaction efficiencies in the scattering layer and absorption layer respectively while $\Delta\Omega_1$ describes the solid angle between the source and the scattering layer, while $\Delta\Omega_2$ denotes the effective solid angle, at which a scattered photon from the first layer hits the absorption layer. Thus, the sensitivity increases for large $\Delta\Omega_1$ and $\Delta\Omega_2$. Since the impinging photons distribute more or less evenly over the entire opening angle, parallax errors can occur. This implies a complication for any good CC design and constitutes a coupling of resolution and detection efficiency. [Nur+15]

3.3.3. Potential Improvement Through Electron Tracking

Measuring the electron momentum in the scattering layer yields a significant improvement of the detection concept. Firstly, the reconstruction efficiency would be enhanced by the ability to reconstruct the Compton cone also for those photons that did not deposit their full energy in the detector. Secondly, for fully absorbed gammas, the source location could be confined to the arc of a cone. Figure 3.8 shows the reconstructed cones from one, two and ten simulated events using Geant4. The results for a detector being capable of electron momentum tracking are compared to the original design concept, where only the gamma is tracked [Lan15]. In both cases, the reconstruction requires a deconvolution process based on back-projection of the cone with angle θ and a symmetry axis defined by the scattering vertex and the absorption point. [Nur+15]

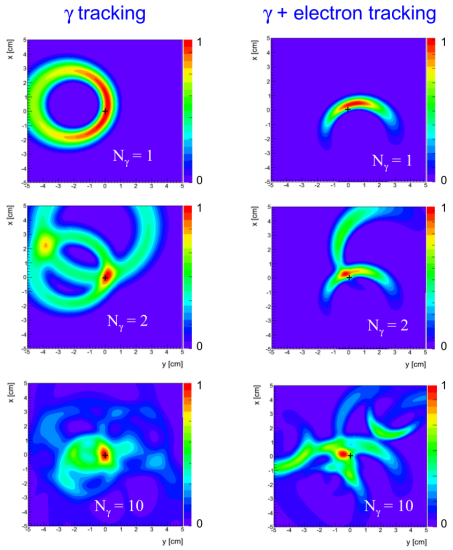

Figure 3.8.: Reconstructed Compton cones for gamma tracking only (left) and additional measurement of the electron momentum direction (right). One, two and ten events were simulated using Geant4. [Lan15]

The detection principle for the Compton scattered electron presented in this thesis aims to achieve the measurement of all three electron quantities: Scattering vertex position, energy and momentum direction. The concept will be explained in section 5.

3.3.4. Current Research Status

In 2016 Thirolf at el. [Thi+16] presented a Compton camera prototype for prompt gamma medical imaging. An angular resolution on the order of 2° was achieved in Geant4-based simulation studies and an image reconstruction efficiency of $10^{-3} - 10^{-5}$ for gamma energies from 2-6 MeV. The system was capable of tracking the electron using 6 double-sided silicon strip detectors acting as scatterer. A monolithic scintillation crystal $LaBr_3(Ce)$ with a mulit-anode Photomultiplier Tube (PMT) as light detector acted as absorption layer. Characterization of the detector components revealed a position resolution of the absorber detector between 2.9 mm and 3.4 mm [Lip18]. First tests with prompt-gamma events from 20 MeV

protons shot at water and PMMA targets have already been performed, and a full performance characterization of the imaging system's capabilities is soon expected to be performed.

In 2016 Solevi at al. [Sol+16] presented a first on-beam test of the MACACO Compton telescope based on $LaBr_3(Ce)$ crystals and Silicon Photomultipliers (SiPMs). This multi-layer Compton camera achieved a position resolution of 3-5 mm for a point like gamma source with energies between 2 and 7 MeV. Bragg peaks of 150 MeV proton beams in a PMMA target were reconstructed and peak shifts within 10 mm could be observed proving the potential of this Compton camera. [Sol+16]

The concept of single plane Compton imaging (SPCI) stands in contrast to the event-by-event reconstruction of photon angles and energies from individual coincidences in the two detection planes of a two-layer Compton camera. In SPCI, activity distributions are reconstructed from accumulated energy spectra [Pau+16]. Coincident energy depositions take place in a single layer consisting of a pixel matrix of scintillators with individual photon readout. Compton scattering of the incoming photon and subsequent absorption happen – preferably – in neighboring pixels. The energy distribution in the pixels yields information on the incident angle of the photon, while its energy is the sum of the deposited energies in the pixels. To increase the rate of valid events for low energetic photons, the scintillator pixels have different charge number Z and are arranged in a chessboard pattern. A Sketch of the set-up of this concept is shown in figure 3.9 next to a reconstruction of two different gamma source positions in figure 3.10.

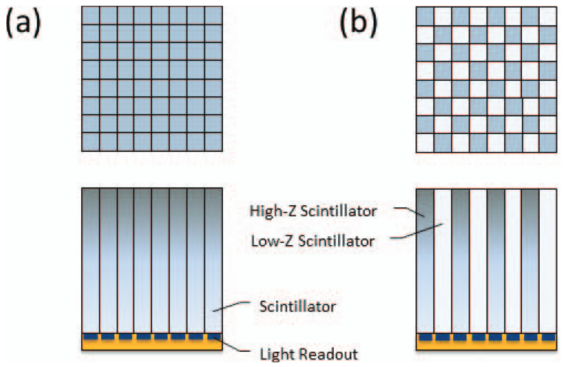

Figure 3.9.: Pixel matrix of SPCI. (a) Slabs of high-Z scintillator materials with individual photon readout form the detection layer. (b) High- and low-Z materials are used to increase the detection rate for low energetic photons. [Pau+16]

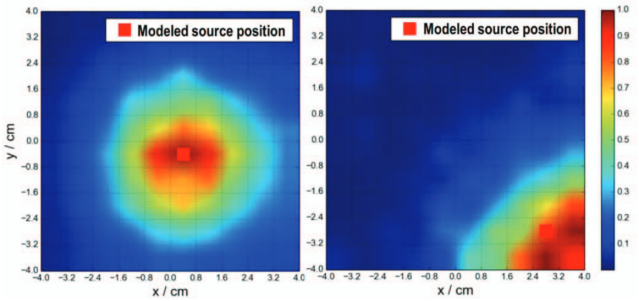

Figure 3.10.: Gamma source reconstruction using single plane Compton imaging. A single point source at two different positions was used. The original source position is indicated with a red square. [Pau+16]

Another single layer Compton camera based on Timepix3 technology – a hybrid single photon counting pixel detector – was introduced by Turacek in early 2020 [Tur+20]. An angular resolution on the order of a few degrees could be achieved.

There have also been tests of CCs in a clinical treatment environment [PP18]. One investigated design concept consists of a two-stage CC mounted on the underside of the treatment couch.

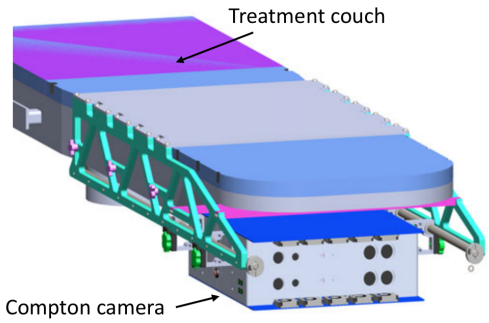

Figure 3.11.: A Compton camera mounted on the underside of the treatment couch. 3D prompt gamma imaging and a detection of beam range shifts with an accuracy of down to 3 mm is possible. [PP18].

The device can be moved along the underside of the couch allowing for 3D image creation with the ability to detect shifts in beam range as small as 3 mm as demonstrated by Draeger et al. in 2018 [Dra+18]. The design is shown in figure 3.11.

Today, the design of a Compton camera for prompt gamma detection for range verification in particle therapy is still a challenge. Results from experiments with clinical proton beams are limited to 2 MeV gammas or otherwise the beam current was far below the clinical standard. Technical complexity, electronics expense and high computational effort are not the only problems. Future research must address low coincident efficiency, large detector load due to high beam current and the subsequent PG emission rate, radiation background from scattered neutrons and random coincidences limiting the signal-to-noise-ratio. These hurdles complicate the realization of a Compton camera with a prospect of clinical application. [HG+16]

4. Single Photon Detectors

Contents

4.1 Semiconductor Detectors **65**
4.1.1 Introduction 65
4.1.2 Thermal Excitation and the Origin of Dark Count 66
4.1.3 The pn-junction 67
4.2 Photodiodes **69**
4.2.1 PN and PIN Diodes 69
4.2.2 Avalanche Photodiodes 70
4.3 The Silicon Photomultiplier (SiPM) **72**
4.3.1 Physical Principle 72
4.3.2 Properties and Characteristics 74

The detector concept presented in this thesis is based on the feasibility of the detection of single photons. The Silicon Photomultiplier (SiPM) was the chosen photon detector to achieve this goal, which is essentially a reverse biased semiconductor detector. This chapter gives a brief introduction to semiconductor detectors in general and the so called pn-junction. The PN/PIN photodiode and the avalanche photodiode (APD) are presented, the latter of which constitutes the center piece of the working principle of the SiPM. Finally, the SiPM is outlined, including its properties.

4.1. Semiconductor Detectors

4.1.1. Introduction

Semiconductor detectors are essentially ionization chambers: incoming radiation ionizes individual atoms to form electron-hole (e-h) pairs [Spi05]. An applied field enables the separation of the charge carriers and drifts them towards electrodes where they induce a signal. The required minimum ionization energy is equal to the band gap energy between valence and conduction band. In a typical semiconductor, this gap is in the range of 1-5 eV. As comparison, the ionization energy in gases is on the order of 30 eV.

Mostly used semiconductor elements are Silicon (Si) and Germanium (Ge), which are group 4 elements having 4 valence electrons. When combined in a lattice, the discrete energy states

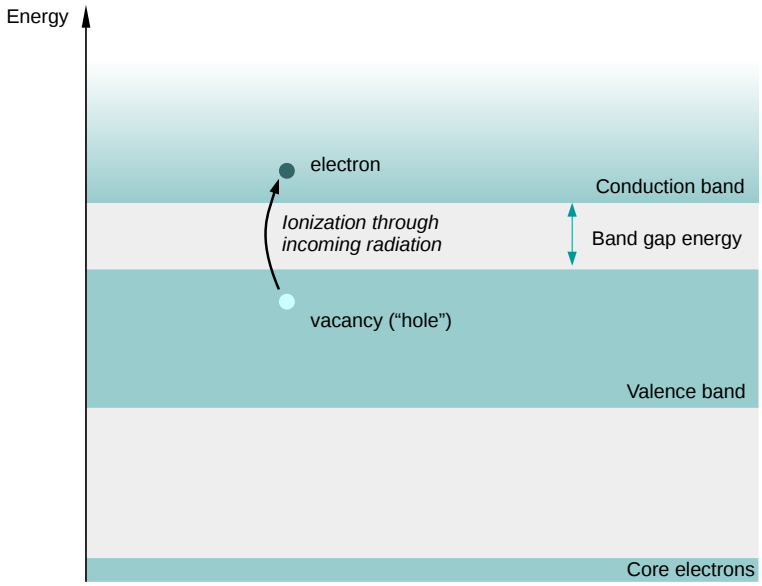

Figure 4.1.: Band structure of a semiconductor and electron-hole creation. Valence and conduction band are separated by a forbidden band gap. Due to incident radiation an electron from the valence band can receive enough energy to reach the conduction band leaving a vacancy (hole) behind. Adapted from [Spi05].

of the individual atomic shells broaden and form bands. The electrons from the outermost shells overlap to form the valence band, which is separated from the conduction band by a forbidden band gap. Without additional energy, no higher state can be occupied by a valence electron. If, however, energy is imparted to electrons via incident radiation, an electron can be excited to the conduction band leaving a vacancy (typically called *hole*) behind. This is shown schematically in figure 4.1.

The electron can move freely in the conduction band. Holes move as well, as the vacancy is filled up by an electron from a neighboring atom. They can be seen as positive charge carriers, but their speed is much lower than that of electrons in the conduction band. This movement of the e-h pair can be guided by an external electric field. Thus, semiconductors act as an ionization chamber and the minimum detectable quantum of energy is determined by the band gap energy between valence and conduction band. [Spi05] Table 4.1 lists a few semiconductor materials and their corresponding band gap energy values. SiPMs are made of silicon with a band gap energy of about 1.1 eV.

4.1.2. Thermal Excitation and the Origin of Dark Count

The thermal energy of electrons at room temperature is on the order of $\frac{1}{40}$ eV, which is much less than the band gap energy. Intuitively, one would not expect electrons to reach the conduction band without incident radiation providing them with sufficient energy. However,

Semiconductor	Band gap energy [eV]
Silicon (Si)	1.1
Germanium (Ge)	0.7
Gallium Arsenide (GaAs)	1.4
Diamond	5.5

Table 4.1.: Band gap energies of some semiconductor types [Spi05].

electrons are fermions. Thus, the probability of occupying an energy state in the conduction band for an electron with energy E is given by the Fermi distribution:

$$f_e(E) = \frac{1}{e^{(E-E_F)/kT} + 1} \tag{4.1}$$

where E_F is the Fermi level in the middle of the band gap. T is the temperature and $k = 1.38 \cdot 10^{-23}\,\mathrm{J/K}$ is the Boltzmann constant [Tie+19]. This implies that at temperatures close to 0 K, semiconductors act as insulators, while at higher temperatures there is substantial conductivity depending on the band gap. On the contrary, natural insulators have a high enough band gap energy so that the concentration of charge carriers in the conduction band is negligible at usual operating temperatures of interest. In case of semiconductors as sensor material, however, thermal excitation leads to a continuous current flow. The band gap has a major impact on the dark current, as a higher gap reduces the number of thermally excited electrons, but also lowers the sensitivity to incoming radiation and the number of charge carriers contributing to a signal. On the other hand, background current increases exponentially for narrower band gaps. The range of band gaps suitable for practical radiation sensors is quite limited and dark current is a key characteristic of semiconductor detectors. [Spi05]

4.1.3. The pn-junction

For successful radiation detection, the created *e-h* pairs need to be drifted towards electrodes with a sufficiently high field. To form a high field region with low thermally induced leakage current, a reverse-biased *pn*-junction can be used. To that end, impurities are brought into the material to control the conductivity. This procedure is called *doping*.

- **n-doping:** atoms that have one valence electron more than the semiconductor elements are implanted into the crystal lattice during the manufacturing process. Typically used elements with 5 valence electrons are phosphor (P), arsenic (As) or antimony (Sb) and are also referred to as *donator*. The bound level of the unpaired additional electron from these impurity atoms is just below the conduction band so that at room temperature electrons are introduced into the conduction band.

- **p-doping:** in this case atoms with one less valence electron are used for doping, which are amongst others boron (B), aluminum (Al), gallium (Ga) or indium (In). These impurities borrow an electron from the semiconductor and are therefore also called

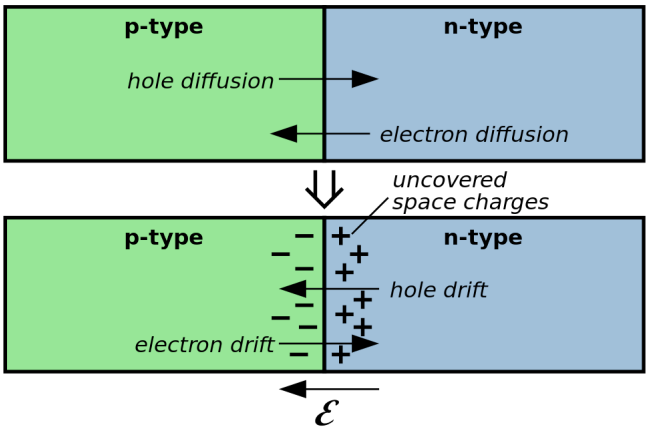

Figure 4.2.: Visualization of the processes occurring at a pn-junction. When the two doped regions are joined together, electrons move towards the p-doped regions via thermal diffusion leaving positive space charges behind, while holes move to the n-type region. A potential is formed at the junction. Electrons lifted into the conduction band can now be drifted towards the n-region. [Ind07]

acceptor. The electron is bound by the acceptor in an energy level just above the valence band in the forbidden band.

When p- and n-doped semiconductor materials are brought together to form a pn-junction, charge separation occurs. The effects were measured and described by Shockley, Sah and Noyce already in 1957 [SNS57]. Figure 4.2 demonstrates the processes happening at a pn-junction.
Both materials are actually neutral when separated, but when joined together, electrons and holes will cross the junction via thermal diffusion. Electrons leaving the n-doped area are accepted in the p-doped region and will leave the donors behind as uncovered positive space charges. A positive space charge acts on the electrons that moved to the p-region and, thus, a potential is formed. The diffusion depth of the electrons into the p-region is however limited: The movement stops when the energy required for thermal diffusion becomes smaller than the space charge potential that has evolved between the two regions. Right at the junction between the two doped areas, a region free of mobile charge carriers is formed. It is called *depletion region*.

The pn-junction forms a diode with asymmetric current flow for positive and negative bias voltage. In forward bias the potential between the p- and n-doped region is reduced and the current flow is increased. In reverse bias the depletion region is increased in connection with a growing electric field potential at the junction.

The reverse-biased diode:
The pn-junction can be seen as capacitor, since the depletion region is a charge-free volume and the p- and n-regions serve as electrodes. With an applied reverse voltage, the electric field is capable of moving charge carriers to the electrodes quickly. That way, an ionization chamber is formed with depletion regions on the μm-scale. Typical applications of reverse-biased diodes can be found in strip and pixel detectors.

4.2. Photodiodes

In contrast to charged particle and X-ray detectors, photodiodes have only a small absorption length. The devices discussed in this section are solely silicon-based photon detectors. The absorption length of photons in silicon depends strongly on the wavelength. At 400 nm the absorption length is of order 100 nm, whereas at 700 nm it is about 5 μm [HB19]. In silicon photodiodes, quantum efficiencies for the creation of an e-h pair are on the order of 80 % and sensitivity down to 200 nm is possible [Spi05].

4.2.1. PN and PIN Diodes

The PN diode is in principle the realization of the reverse-biased pn-junction that has been explained in the previous section. It shows efficiency for the absorption of photons in the optical wavelength range up to 1100 nm, which corresponds to the band gap energy in silicon (1.1 eV). An incoming photon creates an e-h pair with the electron reaching the conduction band to be drifted towards the cathode at the end of the n-doped layer. The signal is, therefore, proportional to the intensity of the incoming light. Speed and spectral response are determined by the doping-concentration of the pn-junction. [Din13]

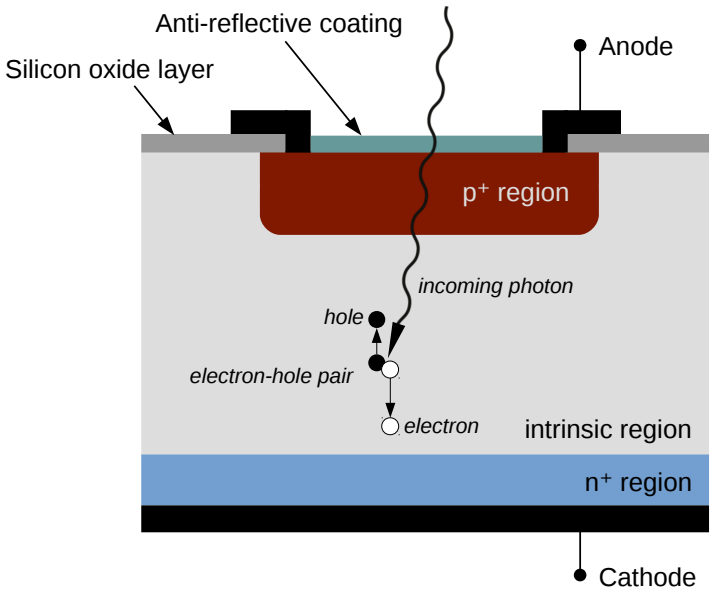

Figure 4.3.: PIN diode structure. An intrinsic layer is sandwiched between two highly doped regions. Ionizing radiation creates charge carriers that are drifted towards the electrodes. Adapted from [RL09].

An improvement of the PN diode is the PIN diode. The basic design is schematically shown in figure 4.3. This photon diode has an additional intrinsic, high-ohmic piece of semiconductor between highly doped (n^+ and p^+) regions. A field is produced across the intrinsic layer

(i-layer) to separate charge carriers and drift them towards the electrodes for detection [GH20]. Most incoming photons are absorbed in the i-layer and can contribute to the photo current at the electrodes. The undepleted p-layer on top must be transparent to incoming light. Its thickness is on the order of 1 μm [Din13]. The active area of the diode is often covered with an anti-reflective coating to reduce reflection of light of a specific wavelength. Passive areas are usually coated with silicon oxide. Sometimes protective layers are used, which cut off detection of incoming light at 290 nm - 320 nm.

The advantage of PIN diodes is their simplicity and reliability. In comparison to PN diodes, they show a more efficient collection of charge carriers and larger quantum efficiency. Also, their capacitance is lower and therefore a higher detection bandwidth is possible.
However, just like the PN diode, the PIN diode also has no internal gain. Therefore, PIN diodes are only sensitive to a minimum photon number of 200-300. Complex read-out electronics including charge-sensitive amplifiers and low band filters are needed for detection of low light level signals. Due to filter time constants on the order of 1 μs, signals tend to become slow and high signal rates cannot be processed.

4.2.2. Avalanche Photodiodes

The Avalanche Photodiode (APD) is another step towards the development of a single photon detector. APDs exploit avalanche charge multiplication as internal gain mechanism. When the field at the pn-junction is increased by applying a higher bias voltage, electrons gain enough energy to create secondary *e-h* pairs and the total amount of charge carriers per incident photon is increased. This process is called *impact ionization*. Only electrons create secondary charge carriers, while holes do not have enough energy. With an APD the minimum detectable number of photons is on the order of 10-20, while a bandwidth in the MHz range is possible [RL09].
If the voltage is increased even more above the so called *breakdown point*, holes also create secondary *e-h* pairs. The field is high enough so that a single charge carrier in the intrinsic layer can trigger a self-sustained avalanche. This is the regime of a Single Photon Avalanche Diode (SPAD) or also called Geiger-mode APD. The avalanche in the diode is stopped with help of a quenching resistor causing the bias voltage to drop below the breakdown point. The diode recharges afterwards for further detection. A Geiger-mode APD is capable of single photon detection, but works in binary mode and the signal does not contain information on the intensity of the incoming light.

The breakdown process was first studied in the 1960s and '70s for example by Haitz [Hai+63]. The first APD operated in Geiger-mode was introduced in the '80s by McIntyre, amongst others [McI85]. Figure 4.4 shows the three regimes of operation in a photodiode: The PN/PIN diode without any gain, the APD with linear gain and the Geiger-mode APD with exponential multiplication in a self-sustained avalanche process. The different photodiode types and their characteristics are listed in table 4.2.

The direction from which the photons impinge on the diode has an influence on the efficiency for different wavelength ranges. SPADs that are built with the p-doped side facing the

Diode type	Gain response	Detectable number of photons	Bandwidth
PN/PIN	none	200-300	few 100 kHz
APD	linear	10-20	MHz - few 100 MHz
Geiger-mode APD	exponential	1	MHz - few 100 MHz

Table 4.2.: Characteristics of PIN diode, APD and Geiger-mode APD.

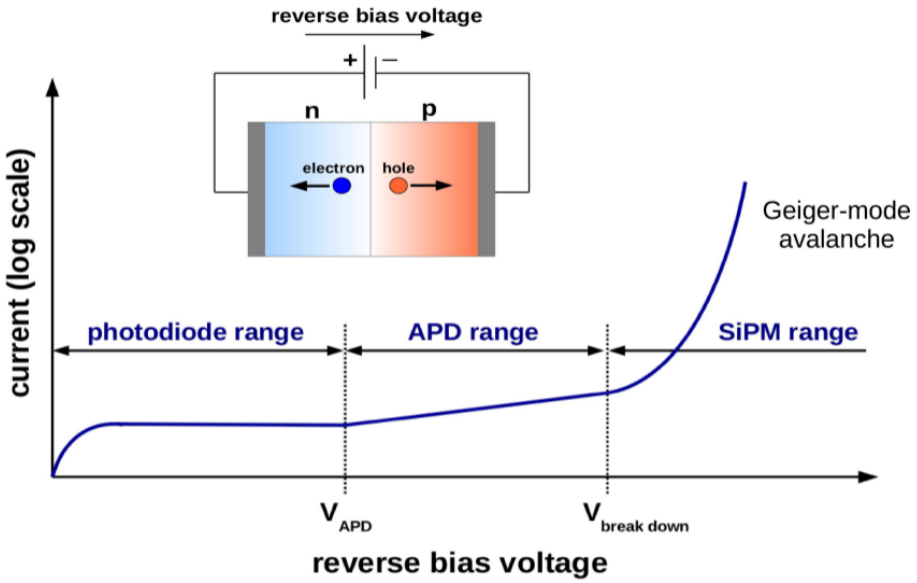

Figure 4.4.: The three operational regimes of a photodiode depending on the applied reverse-bias. PN and PIN diodes work without gain (left regime), while APDs have linear gain (center regime). Above a certain voltage, breakdown occurs and the gain response is exponential forming a Geiger-mode avalanche (right regime). [GH20].

entrance window (p-on-n-doped diode), are more sensitive in the blue part of the wavelength spectrum, whereas n-on-p-doped diodes are optimized for the detection of longer wavelengths.

Equivalent Circuit:
The Geiger-mode APD can be modeled as internal series resistance R_s of the space charge region and the capacitance C_d of the inner depletion layer in parallel [GH20]. Figure 4.5 shows the equivalent circuit of the diode with the integrated quenching circuit consisting of a resistor R_q and a parasitic capacitance C_q in parallel. The detection of a photon and the creation of an avalanche is modeled by closing the switch. The pixel capacitance C_d discharges almost exclusively over R_s since $R_s \ll R_q$. The time constant of this discharge is given by $\tau = (C_q + C_d) \cdot R_s$. With closing the switch, the parasitic capacitance C_q is being charged via R_d. The maximum voltage drop at the internal node between C_d and C_q is given as the operating voltage minus the breakdown voltage $V_{op} - V_{br} = V_{over}$. Here, V_{over} denotes the overvoltage of the APD.

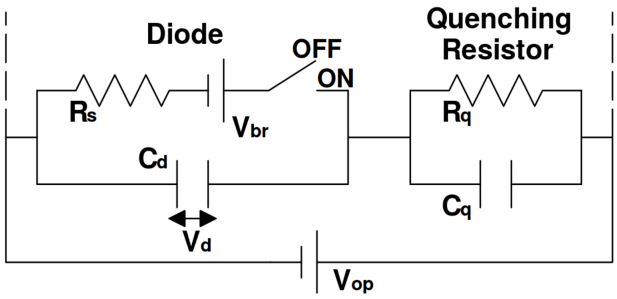

Figure 4.5.: Equivalent circuit of a Geiger-mode APD [Oto+08].

The discharge of the diode causes an exponentially decreasing current through R_d. When this current falls below the threshold value required to get a self-sustained avalanche process, the discharge stops. After the avalanche is quenched the diode recharges with a time constant $\tau_{recover} = R_Q \cdot (C_d + C_q)$, called *recovery time*.

The current flowing through the quenching resistor can be measured via a load resistor connected in series with the diode. The potential across this resistor is proportional to the current [Din13]. A charge sensitive amplifier can be used to amplify the signals before further processing.

4.3. The Silicon Photomultiplier (SiPM)

4.3.1. Physical Principle

Geiger-mode APDs are binary devices and their signal does not contain information on the number of impinging photons. To overcome this drawback, APDs can be arranged in a matrix structure consisting of a large number of micro-cells, which are connected in parallel. Every individual cell is a Geiger-mode APD in series with a quenching resistor. This constitutes the basic design of a Silicon Photomultiplier (SiPM) [Din13] and is shown in figure 4.6.
The parallel connection is enabled through a silicon substrate on the rear-side of the SiPM and a metal grid on the front. The size of the micro-cells [1] is on the order of 15-100 μm. An anti-reflecting coating on top of the matrix increases the transmission for impinging photons. This design is shown in figure 4.7.
All signals work together on a common load resistor where the voltage drop is tapped for signal read-out. Thus, the signal is a sum of all signals from the individual micro-cells. The measured output signal is proportional to the number of incident photons on different cells. This is shown in figure 4.8 on an oscilloscope graph. The measured voltage signal has discrete heights corresponding to the different detected photon numbers. This allows for counting the number of photons detected by the SiPM either by determining the peak height or by measuring the deposited charge. This is shown in the charge spectrum in figure 4.9. Each peak corresponds to a certain number of photoelectrons or photon equivalent (p.e.) signals.

[1] Often the cells are also referred to as *pixel*, which is also sometimes used as synonym for a *channel* in an array of SiPMs. To prevent confusion, the term *pixel* is entirely omitted in this thesis.

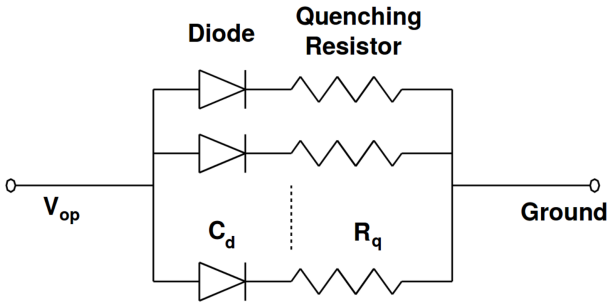

Figure 4.6.: Equivalent circuit of Geiger-mode APDs connected in parallel, which constitutes the basic design of an SiPM. [Oto+08]

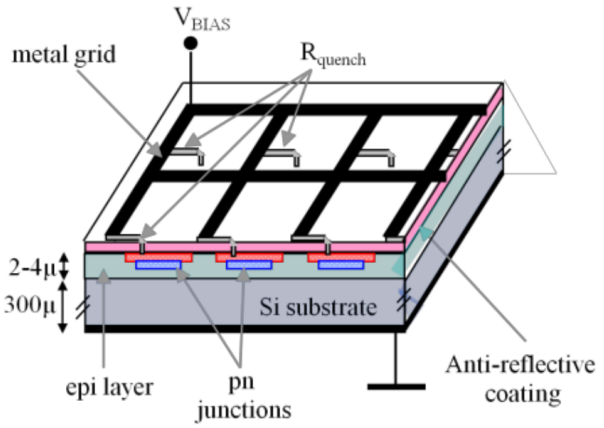

Figure 4.7.: Schematic drawing of an SiPM. The pn-junctions and quenching resistors are interconnected via a silicon substrate and a metal grid. Anti-reflective coating increases the transmission. [Din13]

The presence of a peak at zero photons originates in the specific measurement method and corresponds to events where no photon was detected [Eck+10]. The dynamic range is limited by the probability of 2 photons hitting the same cell and by the number of cells in total. Single photon sensitivity is possible and the maximum number of photons equals the number of micro-cells in the device.

Some devices show two time constants in their waveform, which can also be seen in figure 4.8. The short one creates a steep decrease of the signal right after the peak. It originates in the parasitic capacitance parallel to the quenching resistor, as explained in the previous section on APDs. The large time constant forms the long decay slope of the signal and is determined by the capacitance of the micro-cell.

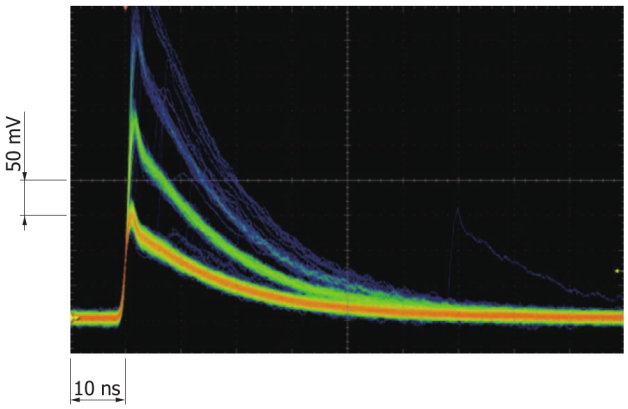

Figure 4.8.: Oscilloscope graph showing waveforms of an SiPM of type S13360-3050 by Hamamatsu. The discrete signal height represents the number of detected photons [Ham16].

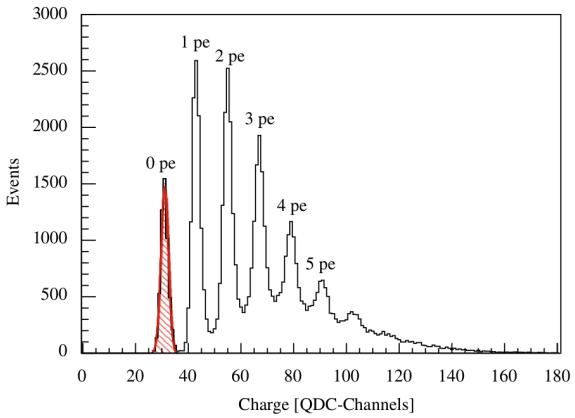

Figure 4.9.: Single photoelectron spectrum recorded using charge integration with a Hamamatsu SiPM. Each peak corresponds to a certain number of photons. [Eck+10]

4.3.2. Properties and Characteristics

This section introduces the most important characteristics and properties of SiPMs. Some of them have also been measured in the scope of this thesis to characterize the detector that has been used in the different set-ups (see chapters 6 and 9). Especially temperature dependencies proved to be important for the optimization of the detector performance.

Breakdown voltage:
The voltage above, which Geiger-mode avalanche multiplication occurs, is called the *breakdown point* or *breakdown voltage* V_{bd}. Since the required bias voltage V_{bias} for SiPM operation needs to be above this value, it has direct impact on the SiPM properties. It defines the applied overvoltage as $V_{over} = V_{bias} - V_{bd}$, which, in turn, influences other quantities like dark count rate, probability for optical cross talk (OCT) and the detection efficiency, all of which are explained in the scope of this chapter. The breakdown point increases for higher temperatures. This shift varies for different devices and typically lies in a range between $20\,\mathrm{mV/^\circ C}$ and $60\,\mathrm{mV/^\circ C}$ [GH20].

Photon detection efficiency (PDE):
The SiPM's efficiency for the detection of photons is defined by the number of detected photons divided by the number of impinging photons on the detector area. It can be calculated as follows:

$$\mathrm{PDE}(V_{over},\, \lambda) = \mathrm{QE}(\lambda) \cdot p_A(V_{over}) \cdot \epsilon_{geo} \tag{4.2}$$

where $\mathrm{QE}(\lambda)$ describes the wavelength dependent quantum efficiency. It is the probability for a photon to be transmitted into the sensitive volume through the entrance window or anti-reflective coating and then to be absorbed in the valence band of the silicon with the subsequent creation of an *e-h* pair. $p_A(V_{over})$ denotes the avalanche trigger probability, which depends on the overvoltage. This value quantifies the chance of an *e-h* pair to trigger an avalanche and, thus, a measurable signal. Finally, the geometric efficiency or fill factor ϵ_{geo} determines the fraction of the detector's front face that is sensitive to incoming light. The metal frame and quenching resistors as well as trenches in between micro-cells limit the area where photons can be detected. Depending on the cell size, this value can reach up to 80 %. Smaller cells limit the geometric efficiency due to larger dead space, but a larger number of cells is possible, which increases the dynamic range of the SiPM.
The photon detection efficiency (PDE) is independent of temperature changes as long as the overvoltage is kept constant, meaning any temperature-related shift in breakdown voltage is compensated for by adjusting the bias voltage. The PDE increases for higher overvoltage.

Signal response and dynamic range:
The SiPM is an intrinsically non-linear device due to the recovery time of every micro cell and the finite number of cells. This causes the number of fired micro cells N_{mc} (including cross talk and after pulses) and the number of photo electrons N_{pe} that are created inside the detector to differ. Their relation can be described by the following response function:

$$N_{\mathrm{mc}} = N_{\mathrm{tot}} \cdot \left(1 - \exp\left(-\frac{N_{\mathrm{pe}}}{N_{\mathrm{tot}}}\right)\right) \tag{4.3}$$

Here, N_{tot} denotes the maximum number of fired cells in an SiPM. This formula does not take the PDE into account as it uses the number of photo electrons instead of the number of impinging photons.
Expression 4.3 implies that for low photon numbers the device's response can be very well approximated with a linear function, however, for higher photon numbers, the assumption of a linear response would lead to an overestimation of the number of fired cells. For example, for a signal equivalent to 80 % of the total number of micro cells, only 55 % of the cells actually fire. This behavior has been measured with fast laser pulses of 40 ps using SiPMs with different numbers of micro cells [Gar11]. Graph 4.10 shows the results.

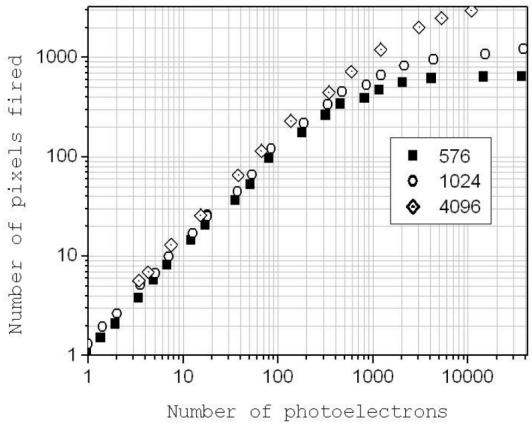

Figure 4.10.: Non-linear response of SiPMs with different numbers of micro cells. The number of fired pixels is plotted versus the number of photo electrons created in the detector. [Gar11]

The graph demonstrates a feature not described by the response formula: in the lower range of the graph, the number of fired pixels can be higher than the number of photo electrons due to OCT and after pulses. In the higher range the limited number of cells and the recovery time saturate the response, which consequently limits the dynamic range of the detector. The maximum number of fired pixels is equal to the total number of micro cells. [Gar11]

Gain:
The number of charge carriers that are created during an avalanche discharge process of a micro-cell and that contribute to the signal, defines the gain of the detector [Din13]. Using the capacity of a micro-cell C_D, the electron charge e and the applied overvoltage, the gain can be calculated [Oto+08]:

$$G = \frac{C_D \cdot V_{over}}{e} \tag{4.4}$$

The gain increases with the applied overvoltage V_{over}. Just like the PDE it is independent of the temperature as long as V_{over} is constant [GH20]. The gain strongly depends on the capacitance C_D and therefore varies especially for different cell sizes [Ham16]. Typical values are on the order of 10^6 [Eck+10].

Dark count rate (DCR):
The number of produced output pulses per second in total darkness is called *dark count rate* (DCR). Its origin has already been explained in section 4.1.2 and can probably be summarized best with the term *thermally generated charge carriers*. A second process contributing to dark count is band-to-band tunneling of electrons in the semiconductor band structure. The dark count rate (DCR) increases strongly with temperature and shows linear increase with applied overvoltage [Ram08; Sot+13].
The rate of dark counts is especially important for coincidence measurements between two or more SiPMs. Dark count contributes to false coincidences and gives rise to the background in a measurement. The choice of an appropriately narrow coincidence time window (CTW) together with cooling of the device can help reduce this influence.
The following two characteristics are commonly referred to as *correlated noise sources*. The term indicates that this type of noise is a follow-up product of a primary event – may it be a detected photon or a dark event. Figure 4.11 gives an impression of these different types of signals as they will be discussed in the following.

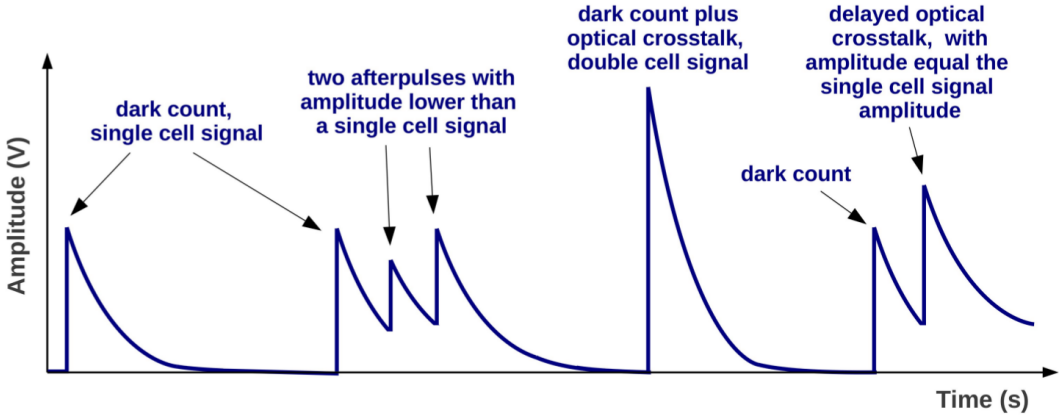

Figure 4.11.: Waveform sketches of SiPM signals together with explanations on the different types of correlated noise signals. [GH20].

Optical cross talk (OCT):
A secondary photon can be created in an avalanche and can subsequently enter one of the neighboring cells and induce a second avalanche. This process is called optical cross-talk and it can occur both for dark signals and actual photon induced signals. The likelihood for an avalanche to create another signal via emission of a secondary photon into a neighboring cell is called cross talk probability and is on the order of a few percent. Exact values mostly depend on the applied overvoltage. A quadratic dependency on the overvoltage has been reported by Soto et al. [Sot+13] and Eckert et al. [Eck+10]. For constant overvoltage, cross talk is independent of temperature [Din13].
Per 10^5 carriers there are on average 3 photons emitted isotropically that have sufficient energy to create a *e-h* pair [RL09]. Possible explanations for the light emission in an avalanche are bremsstrahlung or a multi-mechanism scenario including indirect and direct inter-band and intra-band transitions [RL09].

Since this process takes place on time scales of not more than a few hundred picoseconds [GH20], the two signals appear as one larger signal twice the size.
Different types of cross talk are distinguished [GH20]:

- *Direct cross talk* describes the direct emission of a photon into the neighboring cell.
- *Delayed cross talk* is the emission of a photon into the undepleted region of a neighboring cell. The created charge carrier can reach the multiplication region via diffusion to trigger a delayed avalanche. The diffusion takes some time so that the created secondary signal can be separated from the primary event in this case.
- *External cross talk* is the third type, where the photon leaves the cell through the active side of the SiPM and can then be reflected by the glass window or epoxy resin covering the surface. A fraction of these photons enter a different cell to create OCT.

The three types of cross talk are illustrated in figure 4.12.
OCT depends on the architecture of the SiPM as its intensity increases for smaller distance between the cells. Introducing trenches in between the individual micro-cells can help block the photon's way to the next neighboring cell. That way cross talk can be reduced but not entirely prevented.

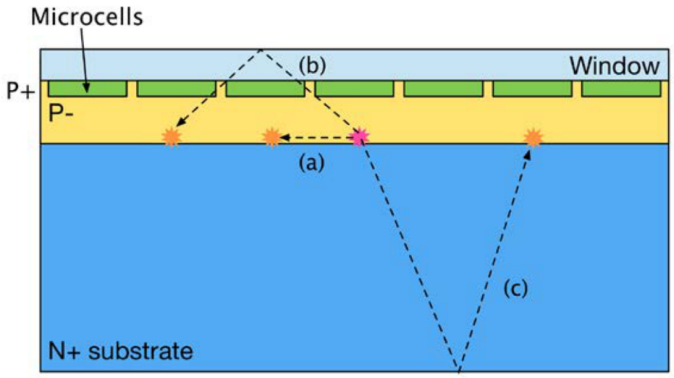

Figure 4.12.: Representation of the three types of optical cross talk: (a) direct, (b) external and (c) delayed cross talk. [Sem18]

After pulse:
An electron that is released in an avalanche can get trapped in material defects or impurities and released again after some time. This electron can then create a second signal in that same cell. The time delay between primary signal and after pulse is on the order of nanoseconds up to microseconds. The charge Q_{AP} of the pulses depends on the recovery state of the cell and can be expressed in terms of a single p.e. charge signal:

$$Q_{AP} = Q_{1\,pe} \cdot \left(1 - \exp\left(-\frac{t}{\tau}\right)\right) \tag{4.5}$$

Here, τ denotes the recovery time constant of the SiPM. For small times t, the height of the after pulse is smaller than that of a 1 p.e. signal. After pulses are illustrated in figure 4.11 as signals that are smaller than the 1 p.e. peak. For large time delays between the primary signal and the after pulse, the standard avalanche signal is triggered. Then, no distinction from delayed cross talk or a dark or single photon event is possible.

Part II.

Concept and Proof of Principle

5. Detection of Electrons Using Cherenkov Light

Contents

5.1 Detection Principle **82**

5.2 Requirements **84**

5.3 Challenges **85**

5.4 Towards a Proof of Principle **87**

This chapter introduces the novel concept of electron detection in a two-layer Compton camera (CC) using Cherenkov light – emitted in an optically transparent radiator material. The principle was first proposed by T. Peterson, A. Walenta and A. Brill in 2012 [PBW12].

In general, Compton detectors should provide high interaction probability for the initial photon by Compton effect, which effectively implies the use of high density materials. A majority of these detectors uses scintillators to detect the scattered gamma. In addition, concepts are required to reduce the influence of parallax effects for inclined incoming gamma ray momenta and multiple Compton scattering vertices. Detection of the scattering vertex involving imaging in three dimensions could help resolve this issue. Even though depth-of-interaction-measurements are commonly applied with scintillators, a vertex reconstruction seems far out of reach [PBW12]. Using Cherenkov light instead of scintillation constitutes a possible approach to realize Compton scattering vertex detection. Cherenkov light, emitted under a characteristic opening angle, provides a strong weighting of the signal to the beginning of the Compton scattered electron track. Furthermore, its instantaneous nature allows for excellent time resolution and for appropriate fast read-out, making it an attractive application for an electron detector in a CC set-up for prompt gamma detection or other medical applications.

The following sections explain the principle of detecting Cherenkov light from Compton scattered electrons and its use for a reconstruction of the scattering vertex as well as the electron energy and momentum direction. The requirements the detector and set-up components have to fulfill will be laid down together with the limitations of this principle, which can mostly be narrowed down to multiple scattering of the electron and scarcity of emitted Cherenkov photons.

5.1. Detection Principle

The concept for an electron detection in a CC investigated in this dissertation is based on the measurement of Cherenkov photons emitted in an optically transparent radiator material. A sketch of the principle is shown in figure 5.1. The incoming high energetic photon ($\geq 1\,\mathrm{MeV}$) scatters inside the radiator spawning a Compton electron. This electron emits Cherenkov radiation when traveling faster than the speed of light in that medium ($c_n = \frac{c}{n}$). Depending on the incident photon energy and the scattering angle, the electron carries energies between several hundred keV and a few MeV. The Cherenkov photon emission occurs under a characteristic opening angle, which is only dependent on the refractive index n of the material and the speed β of the electron. Assuming high electron energies with $\beta \approx 1$, a measurement of the resulting circle or ellipse formed by Cherenkov photons on a photo-sensitive detection plane can be used to reconstruct information on the electron as follows:

- The position and size of the ellipse allows reconstruction of the Compton scattering vertex. The larger the ellipse the farther above the photon detection plane the scattering interaction happened and vice versa.
- The eccentricity of the ellipse allows for a momentum direction reconstruction of the electron. The pattern of the incident Cherenkov photons on the optical read-out plane can be used to reconstruct an ellipse and, thus, the Cherenkov cone in three dimensions. A reconstructed cone can be bound to a unique electron momentum direction.
- The number of detected Cherenkov photons yields information on the electron energy. Starting with an offset due to the Cherenkov threshold, the number of emitted photons scales linearly with the electron energy. The threshold depends only on the refractive index n of the radiator material. In case of PMMA for example – which is one of the materials tested in this thesis – the threshold lies just below 180 keV, as shown and discussed in section 2.1.4.

The concept only measures position and kinetic quantities of the *electron*, such that for an application in a CC, a position- and energy sensitive absorber detector for the scattered *photon* would be required.
Originally, the principle has been proposed as a detection concept for only the momentum and vertex of the Compton electron for a *given* gamma energy [Wal+16]. The momentum of the electron carries necessary information to reconstruct the momentum of the incident gamma. However, the dependency of the number of emitted Cherenkov photons on the electron energy could be used to determine the electron energy. Thus, the energy transfer from the gamma to the Compton electron can be measured allowing to extend the principle to incident gammas of *unknown* energy.

In order for this principle to work the opening angle of the Cherenkov cone must be assumed roughly constant, which is true for electron velocities β close to 1.
Practically, the opening angle must be close to its maximum during a large part of the electron track and over a large range of the electron's energy. The opening angle for electrons in PMMA versus energy is shown in figure 5.2. The angle grows rapidly with increasing

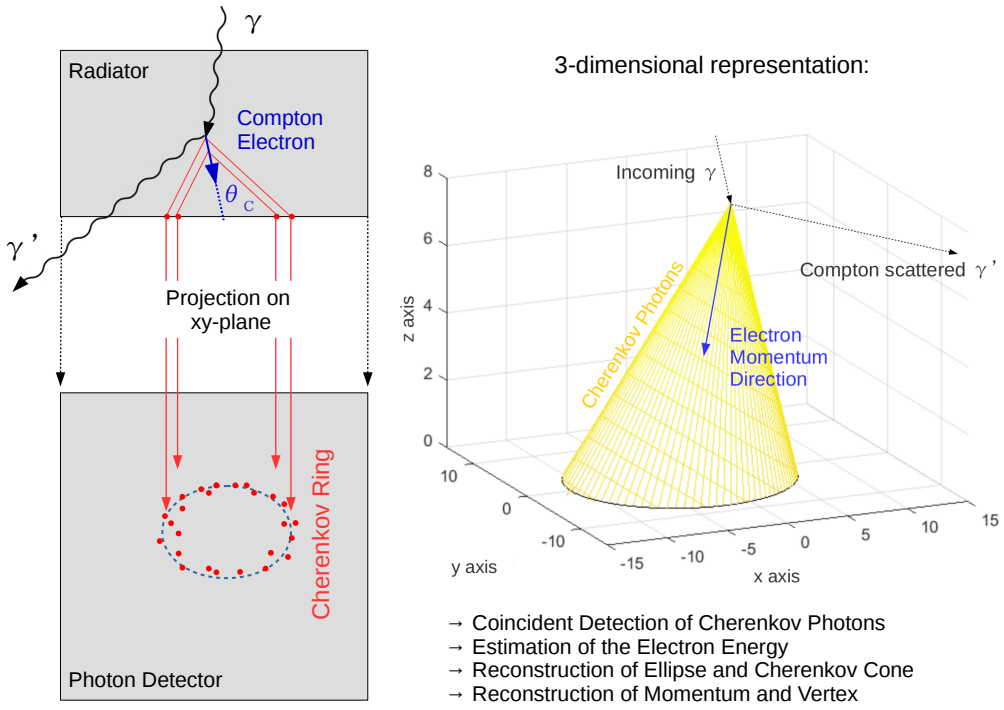

Figure 5.1.: Concept of Compton electron detection using Cherenkov cone reconstruction. Left: The incoming photon scatters releasing a higher energetic electron, which emits Cherenkov photons under a characteristic opening angle θ_C. Reconstruction of the Cherenkov cone allows for an estimation of scattering vertex, momentum information and energy of the electron. Drawn based on the concept in [Wal+16]. Right: three-dimensional representation of the detection principle. The Cherenkov cone (shown in yellow) intersects the read-out plane forming an ellipse pattern, which is subsequently used for the reconstruction of the information about the electron.

energy and converges towards its maximum. At 780 keV the angle has already reached 90 % of its maximum value ($\theta_{max} = 47.8°$). This behavior of constant opening angle is important for the envisaged reconstruction of the location of emission [PBW12].

The advantages of this electron detection modality are, amongst others, the good time resolution capabilities based on the instantaneous nature of the emission of Cherenkov radiation and, therefore, the potential fast read-out. For example, in case of a Compton electron with an energy of 1 MeV ($\beta \approx 0.94$) created inside PMMA with a calculated range of 0.49 cm, the emission of Cherenkov photons happens within a time window of approximately 17 ps. The excellent timing is particularly attractive for monitoring high PG rates in proton therapy treatment.

Another advantage is the suppression of the parallax effect via the measurement of the scattering vertex and thus the depth of interaction (DOI) of the incoming photon in the radiator material. MC simulations predict a DOI measurement for 2 MeV gamma rays with a precision better than 5 mm [Wal+16]. Finally, the possibility of estimating the momentum direction of the electron improves the reconstruction capabilities of a CC set-up, since the reconstructed Compton cone can be reduced to an arc (see section 3.3.3).

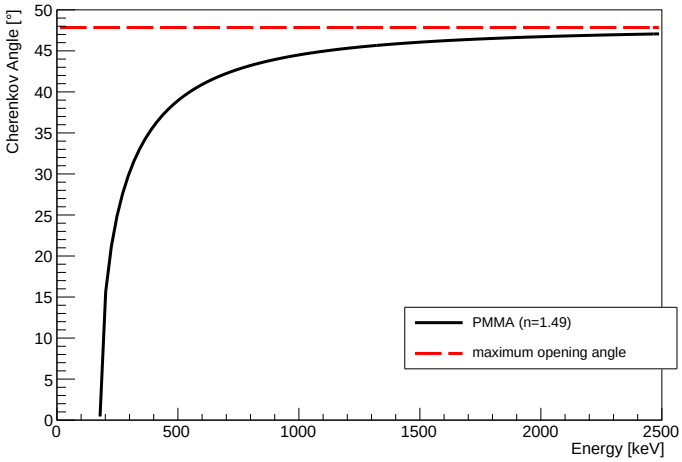

Figure 5.2.: Cherenkov cone opening angle versus electron energy in PMMA. The angle is close to its maximum (47.8°) for a large part of the energy range allowing for a reconstruction of the momentum and vertex information via measurement of the detected pattern of Cherenkov photons.

5.2. Requirements

The radiator material used to create Compton scattered electrons needs to fulfill specific requirements, some of which contradict each other and trade-offs need to be found. To enable high enough interaction probability for incoming photons in the MeV-range to interact inside the radiator, materials with high density are preferred. However, for two reasons higher density is detrimental for this detection concept: Firstly, the higher density is often connected to higher atomic number Z and, thus, higher probability for photo-effect, resulting in single-vertex events, unusable in a CC. In the MeV range, this influence can be considered small, since Compton scattering is the dominating process for all Z (see section 2.2.1.2). Secondly, higher density causes the electron track to be shorter and increases multiple scattering of the electron (see section 5.3 for more details). Since the number of emitted Cherenkov photons per traveled distance dx saturates quickly for increasing electron energy (as has been demonstrated in section 2.1.4, figure 2.14), the electron's total track length has a major impact on the number of emitted Cherenkov photons. Consequently, the density of the scattering medium implies a trade-off between Cherenkov light yield and gamma interaction efficiency.

Furthermore, the refractive index n influences the measurement for multiple reasons: It determines the maximum possible Cherenkov cone opening angle θ_C (see equation 2.12), which is desired to be rather large to achieve good resolution on the reconstructed size and eccentricity of the ellipse on the read-out plane. Also, the number of emitted photons increases with larger n according to equation 2.20. Another advantage of large n lies in the reduced threshold velocity for the Cherenkov effect. While in PMMA ($n = 1.49$), the threshold velocity is $\beta_{th} = 0.67$, in water ($n = 1.3$) a minimum speed of $\beta_{th} = 0.77$ is required. Unfortunately, materials with high refractive index are often those with high atomic numbers and high densities.

A sufficiently thick sample of low-Z material with rather low density and intermediate refractive index might incorporate all trade-offs. UV-transparent PMMA might be one candidate that has also been tested in the scope of this thesis.

Regarding its optical properties, the radiator needs to fulfill one more requirement, which is a high transparency especially in the near UV range. This is due to the increased emission of Cherenkov photons for smaller wavelengths (see equation 2.19). That implies for any photon detection device employed in this concept that the detection efficiency in that wavelength range is paramount. The pattern of coincident Cherenkov photons on the read-out plane is needed for the reconstruction of the Cherenkov cone, the electron momentum and the start vertex. Thus, a pixelated detector matrix in connection with fast read-out electronics is required. The signal rise time must be on the order of 1 ns to allow for good coincidence time resolution on the detector matrix and – for applications in a CC – between Cherenkov detector and absorber detector. Although, in general, more and smaller channels increase the position resolution, size and number of detector channels are subject of investigation and optimization of a detector set-up. Due to detector dark count and limited event rate of common read-out electronics, certain limits are apparent.

Fast read-out electronics – preferably equipped with on-line coincidence search – are required to allow for good time resolution. Sufficiently high event rates could be achieved with electronics based on ASICs in connection with field programmable gate arrays (FPGAs). Counting the number of detected Cherenkov photons per channel is required to gain information on the electron energy. This thesis explores the possibility of using the deposited charge as well as the width of the signals – which is encoded in the Time over Threshold (TOT) – to count the number of detected photons in each channel.

Finally, a pattern recognition algorithm needs to be implemented extracting information on momentum and vertex from the measured pattern of Cherenkov photons. Attempts have been made to use ellipse fits [Ben20] or Hough transforms [Wal+17], the latter of which has achieved a resolution on the photon's DOI inside the radiator of 4 %.

5.3. Challenges

Compared to scintillation, the light yield in Cherenkov effect is relatively small. While ten thousands of photons per incident electron can be emitted in a scintillator, only a few hundred Cherenkov photons are created along the trajectory of an electron in the lower MeV range. A 1.5 MeV electron emits only about 900 Cherenkov photons per centimeter in PMMA within the wavelength range from 200 nm to 900 nm. Considering an electron range of only about 7 mm, an estimated number of 630 photons are emitted in total. This is already an overestimation, since the slowing down of the electron has not been taken into consideration and the fact that the electron does not undergo Cherenkov effect when its kinetic energy falls below 180 keV. More exact values are calculated in section 7 where the continuous energy loss along the trajectory is taken into account as well as geometric considerations of the radiator material. For a successful reconstruction of the Cherenkov cone and especially for sufficient energy resolution, the number of detected photons must be

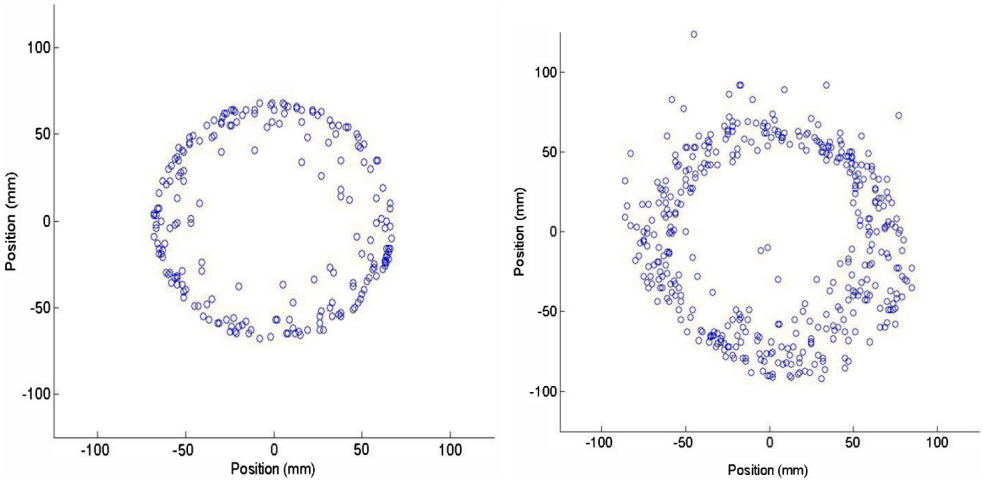

Figure 5.3.: Simulated coincident hits of Cherenkov photons from a single electron in PMMA on the detector plane. Left: No multiple scattering and only the slowing down of the electron is considered. Right: Multiple scattering deflects the electron and causes a diffusion of the Cherenkov cone. From [PBW12].

as high as possible. Any photon detector needs to have high detection efficiency, especially in the near UV range. Regarding energy resolution, another challenge lies in the number of created photons. Since the electron track length varies even for electrons of the same energy, the resolution on the energy by counting the number of photons might be limited already by the physics of electron interactions inside the radiator material.

A successful cone reconstruction relies on the distribution of Cherenkov photons on a ring or an ellipse forming the line of intersection between Cherenkov cone and read-out plane. Since the electron loses energy along its trajectory, a sharp ring is not to be expected. The opening angle of the Cherenkov cone shrinks towards the end of the track giving rise to photon contributions inside the ideally expected ring. This can be seen in projected photon hits from a MC simulation [PBW12] in the left picture of figure 5.3. A single electron event in PMMA is shown creating Cherenkov photons. The points where the photons hit the detector plane are depicted in this figure. Another reason for contributions inside the ring lies in the elongated electron track, which is why an extended circular ring is expected rather than only a discrete circumferential line. The width of this ring is determined by the length and direction of the trajectory.

A distinct ring can still be seen even with these two effects at play. A more severe influence originates in multiple scattering of the electron during its movement through the medium. This is shown in the right picture of figure 5.3. Multiple scattering causes random changes of the electron direction and consequently a diffusion of the cone. The scattering increases with decreasing electron energy and therefore is strongest towards the end of the track. Simulations have shown that the pattern created by photons from the first part of the electron track still shows a clear ring structure. Analysis algorithms attempting to reconstruct the ellipse need to be able to find the best adapted ellipse for example through a Hough transform [Wal+16].

The influence of multiple scattering and also the emission of Compton electrons under large angles (corresponding to small photon scattering angles) causes a significant fraction of Cherenkov photons to be emitted towards directions where they are lost for detection. This circumstance imposes another challenge to the detector set-up, which needs to be addressed by appropriate positioning and geometry of the photon detectors. As already suggested by Peterson et al. in 2012, photon detectors might also be put at the side walls of the radiator to increase light collection and reconstruction efficiency. However, a distribution of photons over a complex geometry of two or more planes complicates the reconstruction.

Although there is existing knowledge on Cherenkov cone detection in particle physics, the conditions in this application are vastly different and large efforts need to be made to develop a functioning electron detector based on Cherenkov light detection. The following section describes the very first simplified Cherenkov detection set-up capable of proving the concept on a smaller scale.

5.4. Towards a Proof of Principle

The first test set-up has the purpose of demonstrating the ability to detect Cherenkov photons from electrons in coincidence. A β-emitter as electron source is used to create photons in an optically transparent material and a position sensitive photon detection is performed. So, no Compton scattered electrons are used for this first test. The detector seeks to achieve a coincidence time resolution (CTR) on sub-nanosecond time scale. This section explains the detection principle of the test set-up while the individual components and their corresponding properties are discussed in full detail in chapter 6.
Figure 5.4 shows the basic idea for the set-up: electrons from a beta source are used to create Cherenkov light in an optically transparent non-scintillating material. In the scope of this work different sample types and thicknesses will be used and tested for their applicability. For the proof of principle, mostly PMMA with different thicknesses was employed. The use of different thicknesses mimics Compton electrons that are created at different hights above the detector area having an initial momentum direction perpendicularly to the SiPM surface. The properties of the samples – especially the refractive index and the wavelength dependent transmission behavior – are discussed in section 6.5.

An array of Silicon Photomultipliers (SiPMs) by Hamamatsu serves as photon detection device optically coupled to the radiator sample. This device enables light detection on single-photon level with a signal rise time of 1-2 ns. In the first tests a 4×4 detector matrix is used and two different types of read-out electronics are utilized. The first one is a sequential read-out of 4 channels at a time using a GHz-oscilloscope. An integrated measurement is performed and the average number of photons is being determined. The second one is an ASIC-based read-out capable of performing coincidence measurements on 16 channels at a time on sub-nanosecond time scale.

After the demonstration of a successful coincident Cherenkov light detection on a 16-channel SiPM array and a thorough comparison to theoretical expectations, measurements with an improved set-up with 64 channels will be explained in chapter 9. Finally, in the third part of

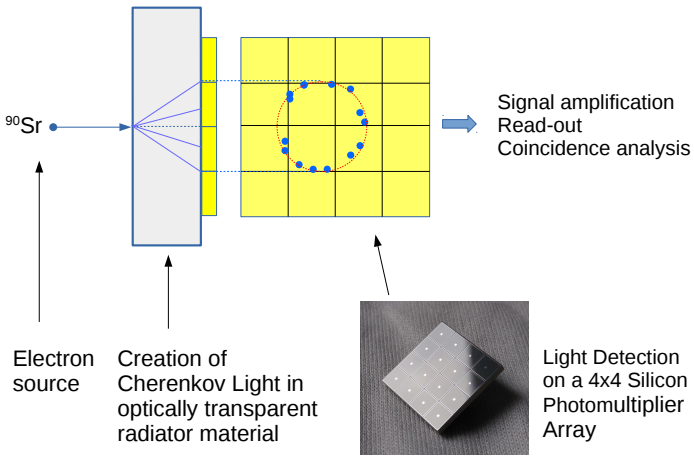

Figure 5.4.: Design of a first test set-up to prove the principle. An electron source is used to create Cherenkov photons in an optically transparent radiator material to be detected on a 4×4 array of Silicon Photomultipliers (SiPMs). Signal read-out and analysis will be performed in different ways as described in chapter 6.

this thesis, the concept will be applied to the detection of actual Compton scattered electrons created by photons with an energy of 511 keV emitted by a ^{22}Na source.

6. Set-Up and Detector Components

Contents

6.1 Overview **89**
6.2 Signal Read-Out Using an SiPM Timing Chip (STiC) **91**
6.2.1 Technical Layout and Design 93
6.2.2 Signal processing 93
6.3 Charge Sensitive Read-Out Using a 4 GHz Oscilloscope **96**
6.4 Silicon Photomultiplier Array **97**
6.4.1 Device Description 97
6.4.2 Key Characteristics 98
6.4.3 Temperature Dependencies 101
6.5 Radiator Materials **106**
6.5.1 Sample Preparation 106
6.5.2 Transmission Measurements 107
6.5.3 Discussion of Different Material Thicknesses and Types 110
6.5.4 Absorption Coefficient 112

6.1. Overview

The general idea for a set-up capable of successfully demonstrating the principle of electron measurement using coincident detection of Cherenkov photons has already been presented in chapter 5.4. All required components to build a set-up that can prove the concept are introduced and characterized in this chapter. The basic components of the design are the electron source, the transparent radiator material, in which Cherenkov photons are to be created, and the photon detector array. These fundamental parts will stay basically the same throughout the entire part II of this thesis. The variable and interchangeable components are the different types of read-out electronics, which basically constitutes everything that happens after the photons have been captured by the detectors. This also introduces a change in the exact measurement procedure and the required analysis algorithms, which are explained in chapter 8.

For these proof-of-concept measurements, electron source, radiator and detector were put into a large dark box, serving two main purposes: Firstly, external light could be shielded from the set-up, which would otherwise give rise to false signals and increased detector count rate even in the absence of an electron source. Secondly, the box was equipped with a ventilation

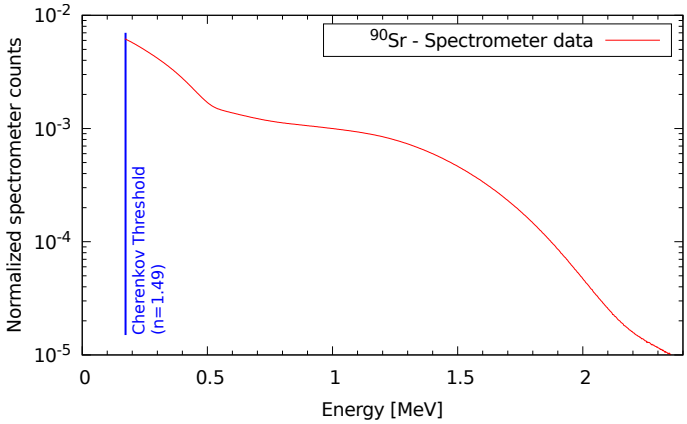

Figure 6.1.: Continuous spectrum of ^{90}Sr with a maximum energy of 546 keV together with the spectrum of its daughter nucleus ^{90}Y with a peak energy of 2.27 MeV. The Cherenkov energy threshold for a material with refractive index $n = 1.49$ (like PMMA) is indicated by the vertical blue line at about 180 keV.

system to keep the interior at a constant temperature and dissipate heat emitted by the individual components when powered.

The inside of the box contained the experimental set-up, while the power supplies and data-taking devices were located outside. One of the components inside was a ^{90}Sr source, which emits electrons via beta decay with a maximum energy of 546 keV within a half-life of 27.7 years. The daughter nucleus ^{90}Y undergoes beta decay as well, however, with a maximum energy of 2.27 MeV and a shorter half life of 64 hours [Kno10]. The source is therefore not mono-energetic but has a continuous energy spectrum as shown in figure 6.1. The energy threshold for the Cherenkov effect in a material with a refractive index of 1.49 (typical value for PMMA) is indicated by a vertical blue line. The spectrum has been measured with a Silicon-based semiconductor detector, in combination with a multi-channel analyzer to create a peak height histogram of the measured signals. Energy calibration was performed using a ^{207}Bi source.

The optically transparent radiator material was another essential component of the set-up and needed to fulfill a string of requirements regarding its optical properties and density as described in section 5.2. In order to find the most suitable material, an investigation of various different sample types regarding their transmission was performed using a spectrophotometer. The results are presented in this chapter in section 6.5.

The sample was coupled to the detector matrix – a 4×4 SiPM array by Hamamatsu of type S13361-3075AS. It had a $3 \times 3\,\mathrm{mm}^2$ channel size and a micro cell pitch of $75\,\mu$m. All parameters and characteristics of this detector type are presented and discussed in section 6.4.

The SiPM surface had a refractive index of 1.55 [Ham18], while the samples had an index between 1.4 and 1.55. Total reflection of Cherenkov photons could occur, if air is located between SiPM and radiator sample. To prevent light loss and to match the refractive index of the sample and the detector surface the optical grease BC630 from manufacturer Saint Gobain was used with a refractive index of 1.47 [Sai16]. A very thin layer was put in between SiPM and radiator sample, which were subsequently lightly pressed together for best optical interconnection. The resulting layer had a thickness $\ll 1\,\mathrm{mm}$, but an exact value cannot be

stated and might actually fluctuate in between measurements especially after samples have been exchanged.

Signal read-out was performed with two different set-ups:
The first one used a so called Silicon Photomultiplier Timing Chip (STiC) developed at the Kirchhoff Institute for physics, University of Heidelberg. It is an ASIC designed for the readout of SiPMs [Har+14]. Its intended application is the fast read-out of scintillator signals with sub-nanosecond time resolution for TOFPET systems. The chip itself is an ASIC able to process up to 64 channels with a time to digital converter (TDC) module for every channel. It is connected to an evaluation board housing an FPGA providing communication with the data taking device (measurement laptop). Details on its working principle and key characteristics are provided in section 6.2. An overview of this set-up is shown in figure 6.2 in the top picture.

The second read-out type used a 4 GHz mixed signal oscilloscope of type MSO 40404C by Tektronix and is also shown in figure 6.2 in the bottom picture. The signals of four Silicon Photomultipliers (SiPMs) at a time were fed into amplifiers with a gain of 50 and a rise time of 220 ps. Using the integral of the waveform within a certain time frame the deposited charge for each signal could be determined. Due to the linear dependency of the charge on the number of detected photons, the average number of detected Cherenkov photons per channel could be counted. The measurement procedure and the corresponding analysis is presented in section 6.3.

The following two sections explain the two read-out types in more detail. The working principle of the STiC board is outlined together with its key characteristics. Afterwards the measurement set-up using the oscilloscope is explained. The measurement procedures and analysis algorithms are not part of this chapter. The photon detector array is characterized in section 6.4. The most important properties like gain, PDE, DCR, cross-talk and after-pulsing probability are discussed. In section 6.5 the radiator materials are investigated regarding optical and physical properties and the applicability to coincident Cherenkov photon detection from higher energetic electrons is discussed.

6.2. Signal Read-Out Using an SiPM Timing Chip (STiC)

The original prototype of STiC was introduced in 2012 with the aim to provide SiPM read-out with optimal time resolution [She+12]. It was designed for TOF measurements in high energy physics and medical imaging applications. For the measurements in this thesis, the third version (STiC3) was used.
The main purpose of this read-out device in this case was to demonstrate the coincident measurement of Cherenkov light signals on the 16-channel SiPM array on sub-nanosecond time scale and to investigate the detected pattern of coincident hits on the array. Details on its working principle and key characteristics are provided in this section. The top picture in figure 6.2 shows the schematic representation of the set-up using this read-out modality. The SiPM bias voltage as well as the power for the evaluation board were applied from outside the box using a Keithley 2400 source meter and a Keysight E3648A power supply, respectively. A pulse generator served as high-frequency test signal for the calibration of

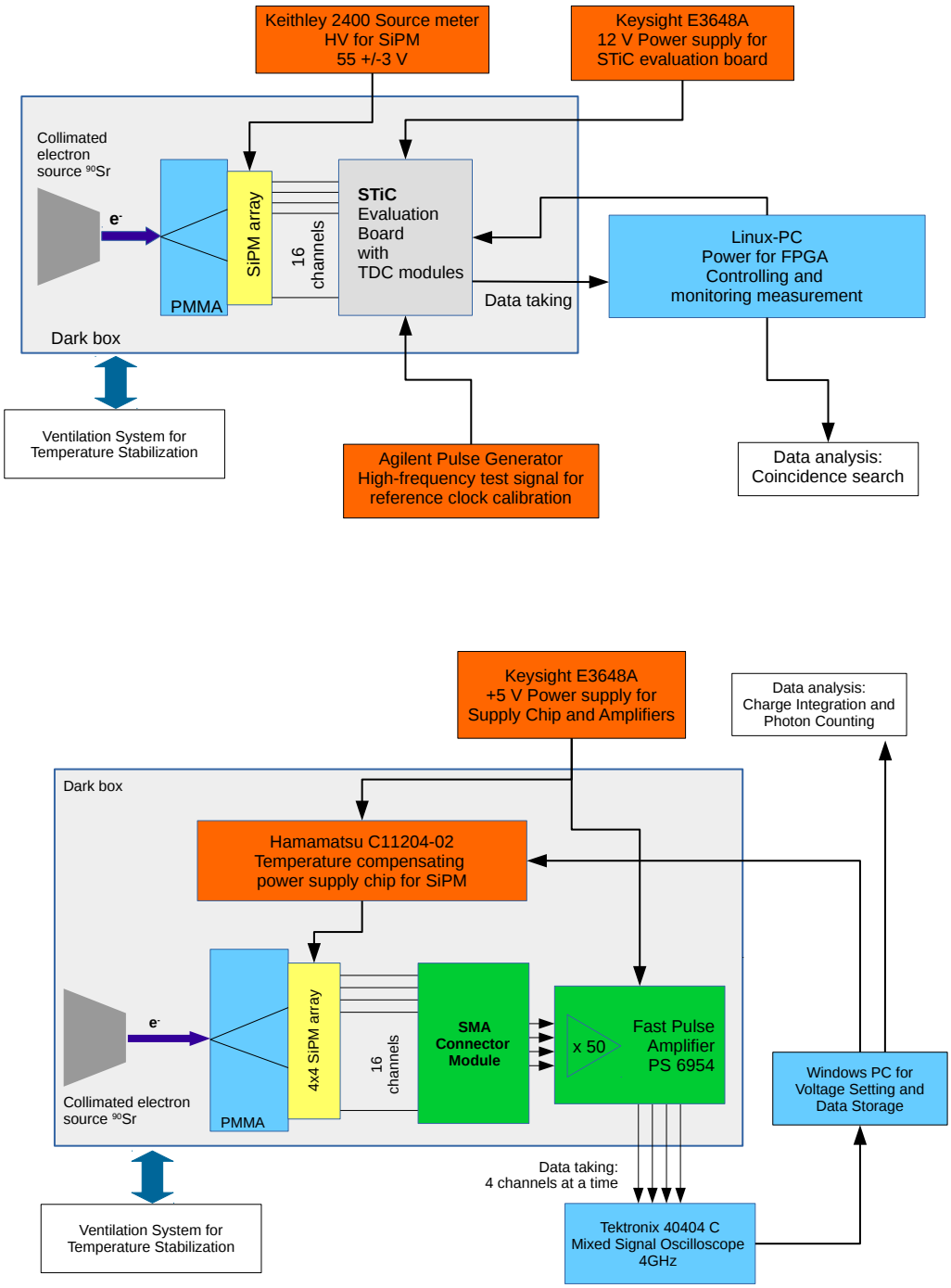

Figure 6.2.: Schematics of the set-up for the first proof of principle together with its two different read-out versions. Top: Signal read-out with a STiC enables a coincidence measurement on 16 channels. Bottom: Connection to a mixed signal oscilloscope allows to measure the deposited charge and use that for photon counting.

the reference clock on the FPGA. Data were sent to a Linux-based laptop via USB 2.0, from which the parameter setting was performed and the measurement process was controlled.

6.2.1. Technical Layout and Design

The chip is bonded on a small board, which is called cavity MCM module [YC]. It is installed on an evaluation board together with a power regulation circuit for the chip and an FPGA. The chip was capable of reading out 64 channels at a time, which could be connected to 4 sockets with 16 channels each. The SiPM array used in this work was plugged into one of the sockets using an appropriate connector board. Single-ended and differential connection of the detector is possible, the latter of which suppresses noise from the internal digital part and external sources and was therefore chosen for the measurements. Additionally to the externally applied bias voltage, an 8-bit digital-to-analog converter (DAC) fine-tunes the SiPM bias at the input stage of each channel in a range of 500 mV. This enabled compensation for differences in break-down voltage between individual channels [Har+14]. The whole evaluation board was enclosed in a metal box with a separate grounding cable and a fan for colling the STiC. The communication between FPGA and the measurement laptop happened via a USB 2.0 connection. A picture of the evaluation board with the STiC installed on it can be seen in figure 6.3.

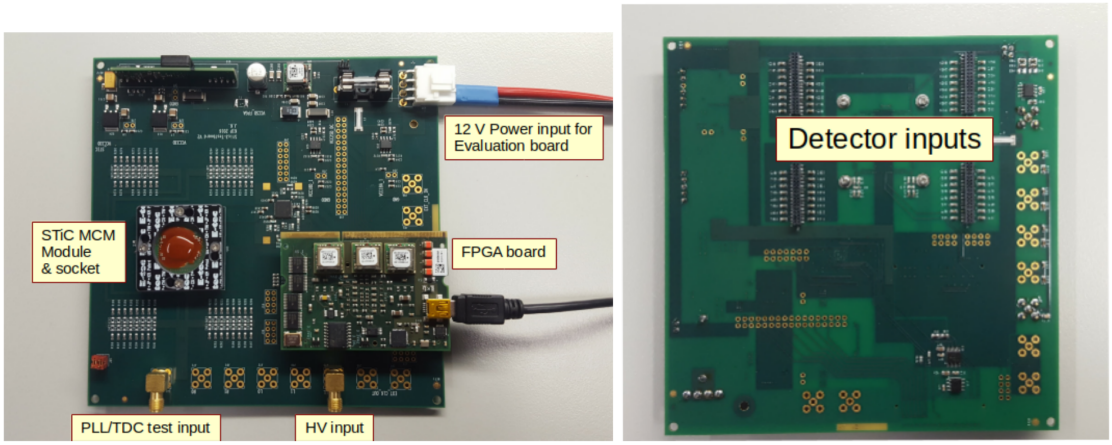

Figure 6.3.: The STiC board and its evaluation board. Left: Back side of the evaluation board showing the ASIC, the FPGA board and the inputs for power and reference clock calibration (PLL/TDC test input). Right: Top side with the four connector sockets for the SiPM. From [YC].

6.2.2. Signal processing

The SiPM signals are precessed by an analog input stage, which creates two branches for energy and time with their corresponding triggers. The two discriminator signals are encoded into one single trigger output by the hit logic unit. This allows to measure both energy and time of a signal in one TDC channel. Thus, every SiPM event receives two time stamps by the TDC, one for the arrival time of the signal and one corresponding to the energy of the

signal. The time stamps are further processed in the digital control logic and stored in a FIFO (first-in-first-out) buffer. Finally, data are transferred to the data acquisition (DAQ) system over a serial link with 160 MBit/s. [YC]. The settings for the SiPM bias, the TDC as well as the trigger levels can be configured with a serial peripheral interface (SPI). The data flow for the signal read-out can be seen in figure 6.4. The following paragraph provides more details on the above mentioned steps.

Details on the implementation of triggering, hit logic and data processing:
The analog signal is fed into two different branches. The T-branch for timing and the E-branch used to measure the energy of the signal. The arrival time is defined by the moment the signal exceeds the threshold on the T-branch. This threshold is set on a low level of a few photons to allow for good time resolution. The energy of the signal is encoded in the Time over Threshold (TOT) defined by the time difference between the aforementioned T-trigger and the moment the signal falls below the threshold of the E-branch: ToT $= t_D - t_E$. A hit logic unit combines the two triggers into one under the use of a XOR combination of the T-branch and a delayed E-trigger. The working principle of the hit logic is shown in figure 6.5. The XOR combination returns a rising edge when only one of the two branches is triggered and resets as soon as both or none of them are above the threshold. As a result, two pulses are created, one for the arrival of the signal and one for the moment it drops below the E-threshold. The rising edges of the output of the hit logic unit are then measured by the TDC unit.

The time base unit of the TDC is a Voltage Controlled Oscillator (VCO) consisting of 16 delay elements. The VCO creates a coarse counter clock with a period of $32 \cdot \tau_D$, where $\tau_D = 50.2\,\text{ps}$ is the fine counter clock period [YC]. The coarse counter therefore has a period of 1.6064 ns. τ_D also constitutes the time binning of the ASIC. The period of the VCO must be locked to a stable reference clock to prevent the clock frequency to vary due to fluctuations in power or voltage or due to changing temperature. Tuning and control of the VCO is performed with a so called Phase Locked Loop (PLL), which needed to be calibrated with an external reference signal from the pulse generator. [Har15]

The receiver unit stores the data generated by the TDC channels. A packet containing the time stamps and energy triggers is stored in a 64 word deep FIFO buffer to be transmitted as one frame every 6.4 μs. A serial link with 8/10-bit encoding is used. [Har+14]

Capabilities and Limitations:
Unfortunately, no single photon detection is possible with STiC [Har15]. Even though the T-trigger can be set on one photon level, the corresponding E-trigger has a more coarse step size and is not sensitive on single photon level. Thus, the thresholds for the measurements were set as low as possible where signals could still be acquired, but the exact value in terms of a p.e. level was unknown. There is, however, a measurement mode where the E-trigger branch is ignored and only the T-trigger is used. Since there is no trigger from the E-branch an event is completed when a new signal arrives that exceeds the T-threshold. the acquired energy value is then the time difference between consecutive events. This measurement mode is called *receive all mode* and is only applicable to dark count estimations and cannot be

used for the actual measurements. However, the dark rate is usually on the order of several hundred thousand counts per second and channel and the ASIC is overwhelmed and can not process all events. The observed maximum possible event rate was on the order of 230 kcps (kilo counts per second) for all channels. The thresholds were therefore set to a level, where no more than 10-12kcps per channel were measured in darkness. Judging by the dark count rate of each channel on the order of 500 kcps (see section 6.4), and assuming a drop of dark rate by one order of magnitude for every higher photon level, the thresholds were at a level of about three photons.
The achievable CTR according to the data sheet is 220 ps FWHM.

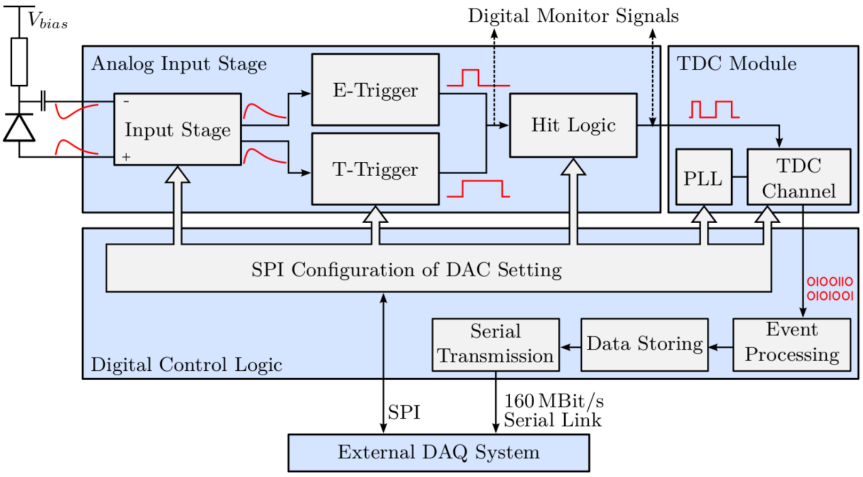

Figure 6.4.: Data flow of the read-out of SiPM signals in the STiC chip. From [YC].

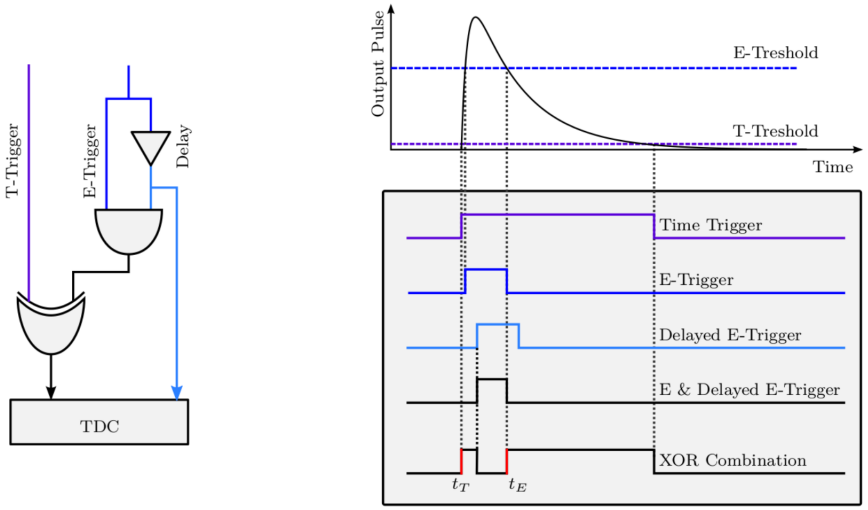

Figure 6.5.: Trigger merging procedure in the hit logic of the STiC chip. The T-trigger and a delayed E-trigger are combined to one trigger signals using a logical XOR combination. Two output pulses are created to be measured by the TDC unit. From [YC].

6.3. Charge Sensitive Read-Out Using a 4 GHz Oscilloscope

The detector array and the radiator materials were placed inside a smaller black box that served as shield from external light at a time when the large black box was not yet available. Some parts of the interior were tightly connected with the walls of the small box, and so the box was kept for further measurements. The small box is shown in figure 6.6. The electron source could be mounted directly on top of that box. The electron source was located inside a lead cylinder and additionally collimated using an aluminum collimator with an inner diameter of 1 mm and a length of 10 mm. The source was mounted on top of a plate, which could be fixed in several different positions. At each of these positions the electron source would be focused on a different location on the SiPM array. Thus the distribution of photons over the array for various electron source positions could be tested.
The SiPM array was placed on a printed circuit board (PCB) serving mainly as a connector between the SiPM channels and the read-out part. A second smaller PCB was mounted below the first one, which provided the power supply for the SiPM array. It contained a temperature compensating power supply chip of type C11204-02 by Hamamatsu, which provided the bias voltage for the SiPM channels. The chip was powered with 5 V. It measured the temperature inside the small box and adjusted the applied overvoltage with a correction of 50 $^{\mathrm{mV}}/_{\circ\mathrm{C}}$. The nominal temperature value was 22 °C room temperature. The bias voltage could be set using a Labview executable on a Windows PC connected to the power supply board via USB. The temperature correction factor could be defined there as well. Since the output of the USB induced noise into the channels, the USB connection was interrupted after the transmission of the settings. The 5 V for the supply chip were then provided by a Keysight E3648A power supply. The signal of each Silicon Photomultiplier (SiPM) channel was tapped over a 100 Ohm resistor versus ground and then fed into a D-Sub connector serving as feedthrough between the interior of the box and a SMA connector board on the outside. From there, one could select up to four channels and connect them to the input of fast amplifiers using coaxial cables. The amplifiers by Phillips Scientific (model 6954) provided a gain of 50.
The amplified signal of these four selected channels was then connected to the input of a 4 GHz mixed signal oscilloscope of type MSO 40404C by Tektronix. The limit of four channels originates in the number of available oscilloscope channels. One of these four channels served as trigger channel while the signals of the remaining three were used for further analysis. The exact measurement procedure for the read-out of all 16 channels in several runs is described in section 8.2.

Oscilloscope properties:
The device was equipped with a Windows 7 operating system and an oscilloscope software displaying the signal from the four analog input channels. Each channel had a 50 Ohm impedance. Digital signals as well as an external trigger signal could be fed into the device as well. The oscilloscope had a bandwidth of 4 GHz. The signal could be sampled with a maximum sampling rate of 25 Gs/s (Giga samples per second). This corresponds to a time difference of 40 ps between two data points of a sampled signal. The voltage of each data point was sampled in 8 bit. The maximum voltage resolution was 0.2 mV. Whole waveforms

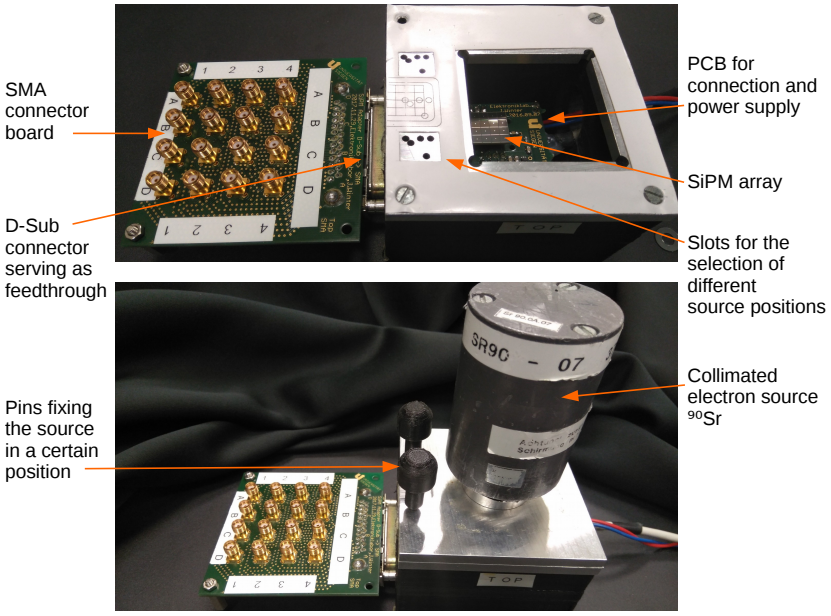

Figure 6.6.: Small black box containing SiPM array, radiator material and power supply board without (top) and with (bottom) electron source mounted on top of it. The signals were fed through the wall of the box with a D-Sub connector. Outside, a SMA connector board enabled the selection of the channels to be connected to the amplifiers and read out with the oscilloscope.

could be saved or information on the signals like area or widths calculated by the oscilloscope directly. In cases where the whole waveforms had to be saved, a sampling rate of 3.125 Gs/s was chosen, which provided a high enough time resolution while limiting the amount of data to be saved. The device was directly connected to a Windows PC via Ethernet providing a fast data link to the hard drive. Files were saved in ASCII-files format to be analyzed with a specifically designed C++ program.

6.4. Silicon Photomultiplier Array

6.4.1. Device Description

The photon sensitive detector array was the heart of the set-up. A Silicon Photomultiplier (SiPM) array of type S13361-3075AS manufactured by Hamamatsu was used. It consists of 16 channels arranged in a 4×4 matrix with $3 \cdot 3\,\mathrm{mm}^2$ channel size and a quadratic micro cell with an area of $(75\,\mu\mathrm{m})^2$ as indicated by the last four digits in the type number. Including the gaps between the channels and the frame around the array, the total side length of the quadratic device was 13 mm.
A technical drawing of the channels and their dimensions is shown in figure 6.7. A connector made by Samtec was located on the bottom of the array. This allows the array to be plugged in directly in the PCB in the small black box used together with the oscilloscope-based signal read-out, while a special connector was required to feed the signals into the evaluation board for the read-out with STiC.

The surface was made of silicon resin, for which a refractive index of 1.55 is stated in the data sheet for the device with a 50 μm cell size [Ham18]. There is no data sheet for the exact device used in this work, but there exists one for the predecessor version from the very similar S13360 series. There, a refractive index of 1.41 is given for the silicon resin surface [Ham16]. According to the statement by Hamamatsu in the data sheet for the S13361 series the main difference lies in a reduced probability for optical cross talk (OCT) compared to the S13360 version. Based on a comparison of the SiPMs with 50 μm cell size from both series it is assumed that the other key quantities of the 75 μm-device are the same or at least very similar in both versions.

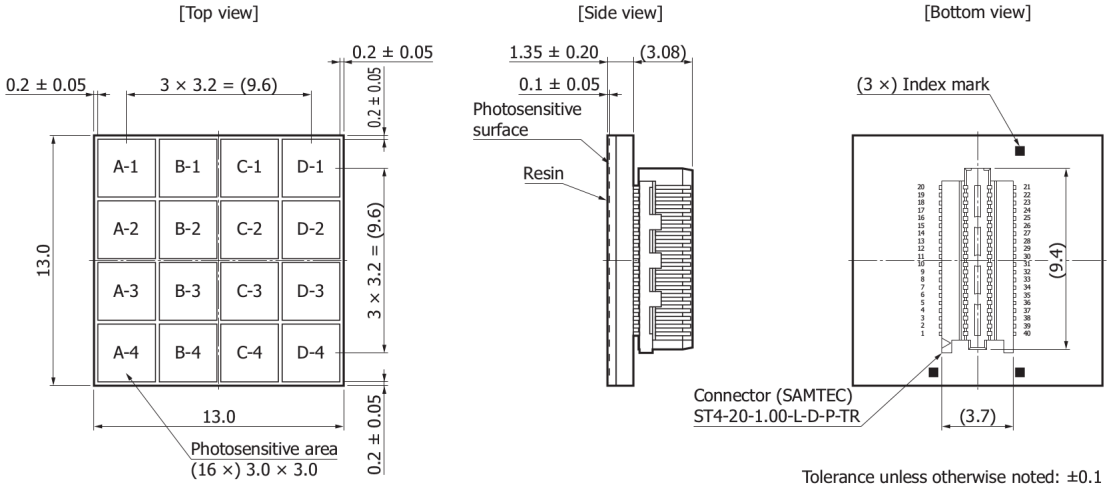

Figure 6.7.: Technical drawing including dimensions, valid for the SiPM S13361-3075AS by Hamamatsu. [Ham18]

Figure 6.8 shows two photos of the array. Each channel shows a small square in its center, which is called through-silicon via (TSV). It eliminates wiring on the side of the photo sensitive area and allows for a more compact design and reduction of dead-space [Ham18]. The close-up picture reveals the pixelated structure of the sensitive area of the SiPM .

6.4.2. Key Characteristics

Since no data sheet was available for the device used in this work, the key characteristics were taken from the data sheet for the predecessor version from the S13360 series. Table 6.1 shows the most important parameters. Some of these characteristics were also measured in the scope of this thesis. Especially the temperature dependence of some of the quantities is important. Temperature fluctuations during the measurement or active cooling impose a potential influence on the outcome of the experiment. This section gives a brief overview of the main characteristics of the devices used for the measurements like PDE, DCR and after pulsing, before in section 6.4.3 temperature dependencies of the breakdown point, the cross talk probability and the dark rate are discussed.

Photon detection efficiency (PDE), gain and optical cross talk (OCT)
The PDE is usually given as the peak value at a fixed overvoltage. The same applied to the

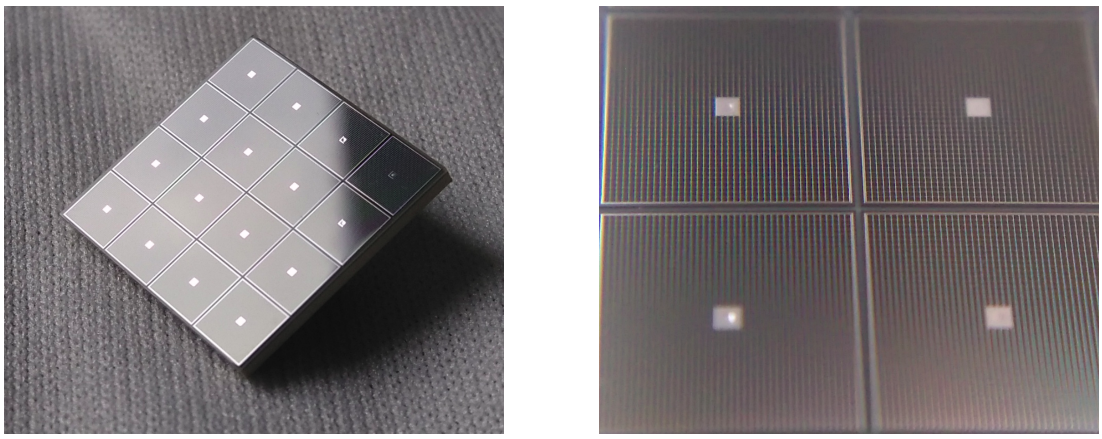

Figure 6.8.: The SiPM array S13361-3075 by Hamamatsu. The through-silicon via technology can be seen as small squares on each channel, while the close-up photo on the right hand side reveals the pixel-structure of the sensitive area.

optical cross talk and the gain. All these quantities significantly change with the applied overvoltage. Figure 6.9 shows the change of PDE, OCT and gain under a variation of the applied voltage. All three values increase for higher bias and a trade off has to be found between increased efficiency and high OCT.
Figure 6.10 demonstrates, how the PDE changes with wavelength. One can see that the efficiency extends down to about 270 nm due to the use of silicon resin as window material. Devices with an epoxy window show a cut off in sensitivity already above 300 nm [Ham16]. High PDE in the near UV range is beneficial for the detection of Cherenkov light, the emission spectrum of which increases towards smaller wavelengths.

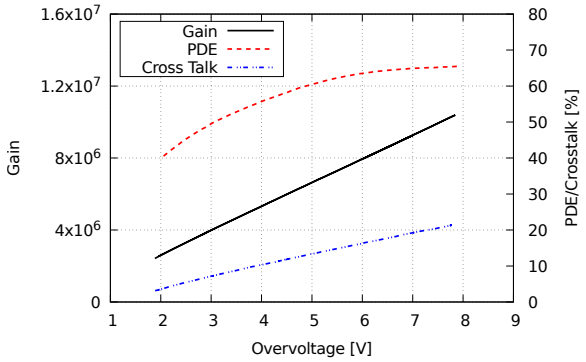

Figure 6.9.: Voltage dependence of gain, PDE and optical cross talk for the SiPM model S13360-3075 by Hamamatsu. Digitized from [Ham16].

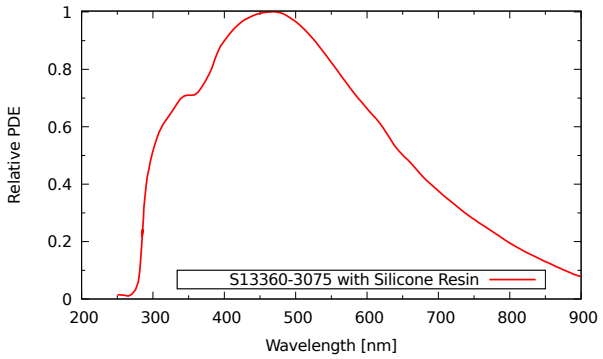

Figure 6.10.: Relative PDE of the SiPM model S13360-3075 by Hamamatsu. Digitized from [Ham16].

The gain increases linearly with the applied overvoltage. At 4 V, a gain of $5.30 \cdot 10^6$ is given in the data sheet. The gain has also been measured at room temperature to compare to the manufacturer's statement. The average deposited charge of a 1 p.e. signal was measured to that end using the oscilloscope for the read-out of amplified SiPM signals. Five different over

voltages were applied between 3.2 V and 6.2 V and the gain was determined. The results are shown in the graph in figure 6.11. The gain increases with voltage by $1.67 \cdot 10^6$/V. At an overvoltage of 4 V, a gain of $6.67 \cdot 10^6$ was calculated in contrast to a value of $5.30 \cdot 10^6$ in the data sheet for SiPM S13360-3075. Deviations could first of all originate in the fact that the tested device is from a different series (S13361). Other influences are the accuracy of the overvoltage setting as well as potentially different measurement conditions compared to the ones performed by Hamamatsu.

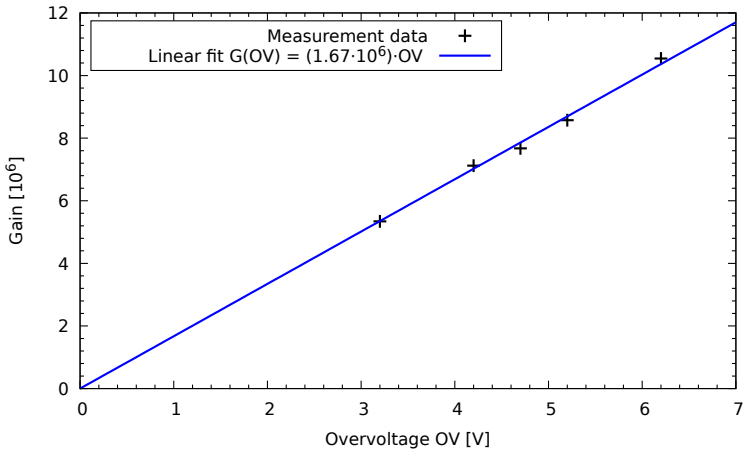

Figure 6.11.: Gain versus overvoltage of SiPM S13361-3075AS by Hamamatsu measured with charge integration technique using the oscilloscope.

Parameter	Value	Unit	Comment
Micro cell size	75	μm	-
Number of micro cells	1600		-
Fill factor	82	%	-
Breakdown voltage	53±5	V	-
Overvoltage	3	V	recommended value
Peak PDE	50	%	at 450 nm and 3 V overvoltage
Dark count rate per channel	500	kcps	at 3 V overvoltage
Gain	$4.0 \cdot 10^6$		at 3 V overvoltage
Cross talk probability	7	%	at 3 V overvoltage
Temperature coefficient	54	mV/°C	at 3 V overvoltage

Table 6.1.: Parameters and values for the SiPM type S13360-3075 by Hamamatsu, which is the very similar predecessor version of the SiPM used in this work. Numbers taken from [Ham16]. Values for the DCR, cross talk and breakdown point are given for conditions at room temperature.

The OCT probability is on the order ot 10 % percent at an overvoltage of 4 V. The value has to be treated with care, though, as the data refer to the S13360 series. The device used

in this thesis belongs to the S13361 series, for which a lower OCT probability is assumed. However, no exact value is available.

Dark Count Rate
Another quantity strongly increasing with the applied voltage is the DCR, potentially overwhelming the read-out electronics and in general slowing down data taking and analysis procedure. The rate of SiPM signals without a light source depends on the applied overvoltage and the chosen photon level. The temperature dependency is discussed in the next chapter. In general, the dark rate drops by about one order of magnitude when the trigger threshold is increased by one photon level. But DCR also depends on the applied overvoltage. Soto et al. (2013) report a linear relation between DCR and overvoltage in their study of Hamamatsu SiPMs for the GlueX experiment [Sot+13]. For the measurements with the STiC board at room temperature, where an overvoltage of 4.2 V was applied, a DCR of 500-600kcps per channel on single photon level was obtained. The trigger threshold was set to a level, where the STiC would not be overwhelmed with dark count. However, the exact threshold in terms of a photon level could not be determined with this read-out device. For the measurements with the oscilloscope, an overvoltage of 3.8 V was chosen, resulting in a similar dark count rate per channel. The threshold was again set well above the 1 p.e. level.

6.4.3. Temperature Dependencies

Some important characteristics of an SiPM change, when the temperature of the device is varied. Such temperature changes can occur due to heating up during the measurement or active cooling of the device. Understanding the behavior of the detector under temperature variation helps adjust measurement settings to account for temperature-dependent performance differences.

Breakdown voltage
Since the applied overvoltage has major impact on OCT probability, rate of dark signals and detection efficiency, knowing the break-down point V_{BD} is vital for a successful and reproducible measurement. The change of V_{BD} with temperature is described by the temperature coefficient of the SiPM given in $^{\mathrm{mV}}/_{^{\circ}\mathrm{C}}$ and can be used to adjust the overvoltage according to the temperature. Thus, a measurement method has been developed for the estimation of the temperature coefficient. Measurements were carried out with the help of Ayesha Ali, master student in the group of Prof Ivor Fleck, who published the results in her thesis [Ali18]. A voltage was applied to a single SiPM channel of the array and scanned in steps of 0.01 V in an interval of $2 - 4$ V around the suspected position of the breakdown point. The current was measured with the highly sensitive ampere meter Keithley 2400. Thus, a so called IV-curve (current-voltage curve or current-voltage characteristic) was created, from which the breakdown point could be determined.
The measurements were carried out in a light tight climate chamber able to regulate the temperature and – within certain boundaries – also the humidity. Since the chamber's dehumidification function could only be used down to a temperature of 10°C, no negative temperatures were used to not freeze water on any of the electronic devices. Figure 6.12 shows the measured IV-curves for temperatures between $T = 5$°C and $T = 40$°C. The breakdown

voltage is characterized by the sharp increase in the current. For increasing T, the curves shift towards higher voltages representing a corresponding shift in breakdown point towards higher voltages as well.

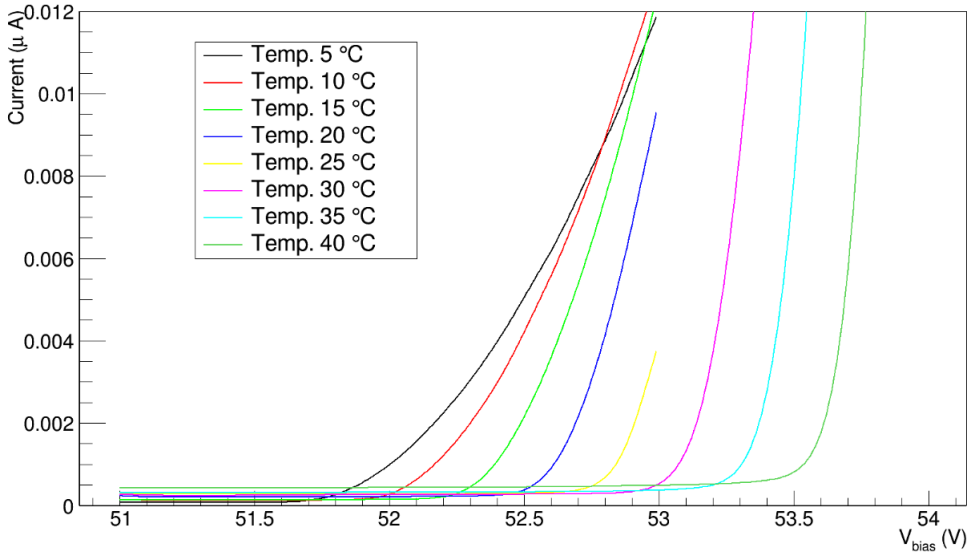

Figure 6.12.: Current-voltage characteristics for the SiPM type S13361-3075AS measured at different temperatures. A shift towards smaller voltages is obtained for decreasing temperature. From [Ali18].

To obtain V_{BD} from the IV-curves, the method of the inverse logarithmic derivative (ILD) was used, which has been proposed and successfully tested in 2017 [Chm+17]: A numerical derivative was applied to the logarithm of the data points and then the inverse value of the result was plotted. The ILD reads

$$\mathrm{ILD} = \left(\frac{\mathrm{d} \ln |I|}{\mathrm{d}V} \right)^{-1} \tag{6.1}$$

where the absolute value $|I|$ is needed to compensate for fluctuations in the current, which potentially results in negative values, for which the logarithm is not defined. Below the breakdown point V_{bd}, the ILD curve scales with $-(V - V_{bd})$, while above V_{bd}, an increase proportional to V_{over} is observed. The minimum of the curve is the desired breakdown point. Figure 6.13 shows an example of an ILD curve with the corresponding breakdown point marked in it.

V_{BD} for all temperature values was calculated in that way. A linear relation between V_{BD} and T was found (see figure 6.14), which could be used to obtain the temperature coefficient:

$$V_{BD}(T) = c_T \cdot T + V_{BD}^0 \tag{6.2}$$

Here, V_{BD}^0 denotes the breakdown point at zero degrees and c_T is the temperature coefficient. The following results were obtained: $C_T = (0.0535 \pm 0.003)\,\mathrm{mV/^\circ C}$ and $V_{BD}^0 = (51.515 \pm 0.009)\,\mathrm{V}$.

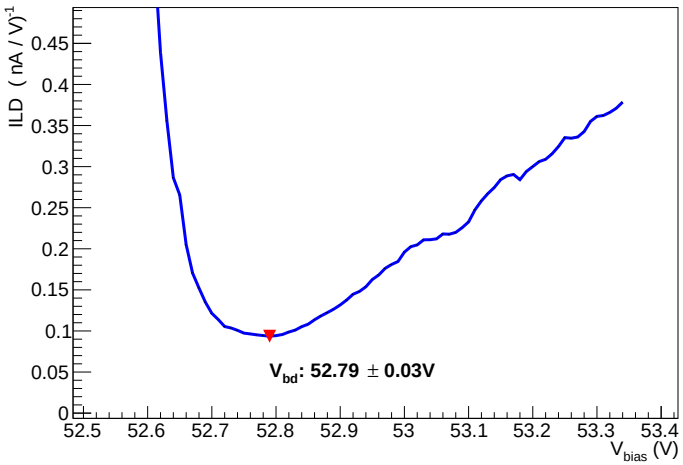

Figure 6.13.: Inverse logarithmic derivative for one channel of the SiPM S13361-3075AS. The breakdown point is the minimum of the curve and is marked as a red triangle. Measurements and results taken from [Ali18].

Dark count rate

To estimate the influence of temperature on the SiPM's DCR, two different measurement set-ups were used, both of which were placed in total darkness inside the climate chamber:
At first, an analog measurement set-up was employed consisting of the SiPM connected to the amplifier, the discriminator and a high frequency counter of type HM 8021-2 by Hamag Instruments[1]. The SiPM overvoltage was set to 4 V for all DCR measurements in this paragraph. The discriminator threshold was scanned through a certain range starting just above noise level and reaching up to a level of 4-5 photons. The rate of dark events was measured using the counter. These measurements were performed at temperatures between 5°C and 35°C in steps of 5°C. An example of a measurement using the discriminator set-up at two different temperatures is shown in figure 6.15. Measurements performed at all other temperatures can be found in the addendum in figure A.1.
The data points in the graph form plateaus, each representing a trigger threshold on a certain photon level. In the graph below the data points, a schematic representation of an amplitude spectrum is displayed showing the distribution of the photon peaks[2]. A plateau with almost constant DCR is formed for threshold values between the noise level (also called *pedestal*) and the level equal to the amplitude of a 1 p.e. peak. On this plateau, the DCR contains all contributions from all peak heights that are above noise level – meaning roughly above 15 mV in the present case. When the threshold is further increased and exceeds the amplitude of a 1 p.e. signal, then, single photon signals do not contribute to the dark rate any more and a significant drop in DCR is measured (at about 50 mV). The same principle can be applied to

[1] This measurement method has been developed in the scope of this PhD thesis, but some of the measurements have been conducted by Ayesha Ali and published in her thesis [Ali18].
[2] This peak spectrum does not originate from a measurement, but is rather a sketch with the purpose of explaining the features of the graph above like the steps and plateaus.

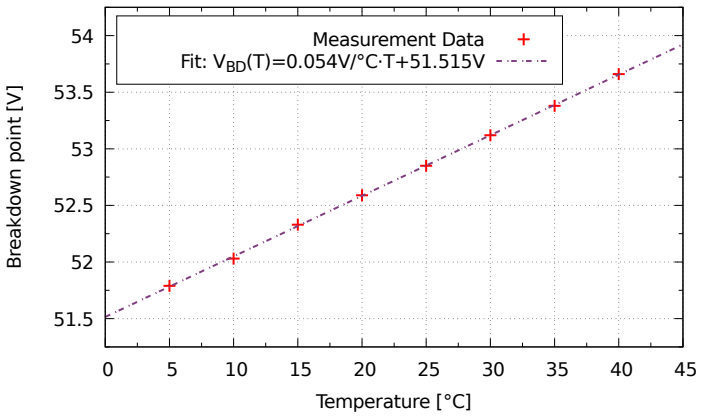

Figure 6.14.: Measured breakdown points of the SiPM S13361-3075AS by Hamamatsu at different temperatures. Measurements and results taken from [Ali18].

the 2 p.e. and 3 p.e. level as well, but the steps appear increasingly smeared out mostly due to noise and after pulses.
Triggering on 1 p.e. level means to chose a discriminator level between noise level and the one photon peak amplitude. This enables to capture all SiPM signals starting on single photon level but minimizing the contribution from noise level. In this measurement, the 1 p.e. level would be triggered by setting the discriminator to about 30 mV. This level is sometimes also called 0.5 p.e. level [Eck+10], as it is ideally in the middle of the plateau between pedestal and 1 p.e. peak.

The positions of the steps are independent of the temperature. The rate at one photon level was taken as SiPM dark count rate at that temperature. The DCR was calculated using the mean value of the data points between noise level and the step between one and 2 photon level. The steps between the p.e. levels were identified by calculating the slope between the data points and identifying the maximum values.

For comparison, the STiC was used in the aforementioned *receive all* mode, where the time difference between consecutive dark signals was saved instead of the TOT information of a single signal. The distribution of time differences between events follows an exponential decay. The time constant of this exponential is the desired DCR [YC]. The DCR at a certain trigger threshold was calculated in that way. The threshold was scanned through the available DAQ range and the 1 p.e. level was identified. The measured rate at that level was taken as the DCR of that channel. These measurements were performed at the same temperatures as the discriminator and counter measurements.
All results are listed in the appendix in table A.1 and are also shown in figure 6.16 in this chapter. An exponential increase of the dark count rate with temperature is observed, indicating the importance of cooling for the limitation of DCR. Since for single photon detection, large signals are preferred and the overvoltage for the measurements is chosen fairly large, the dark count rate rises as well. Cooling leads to a reduction of dark count

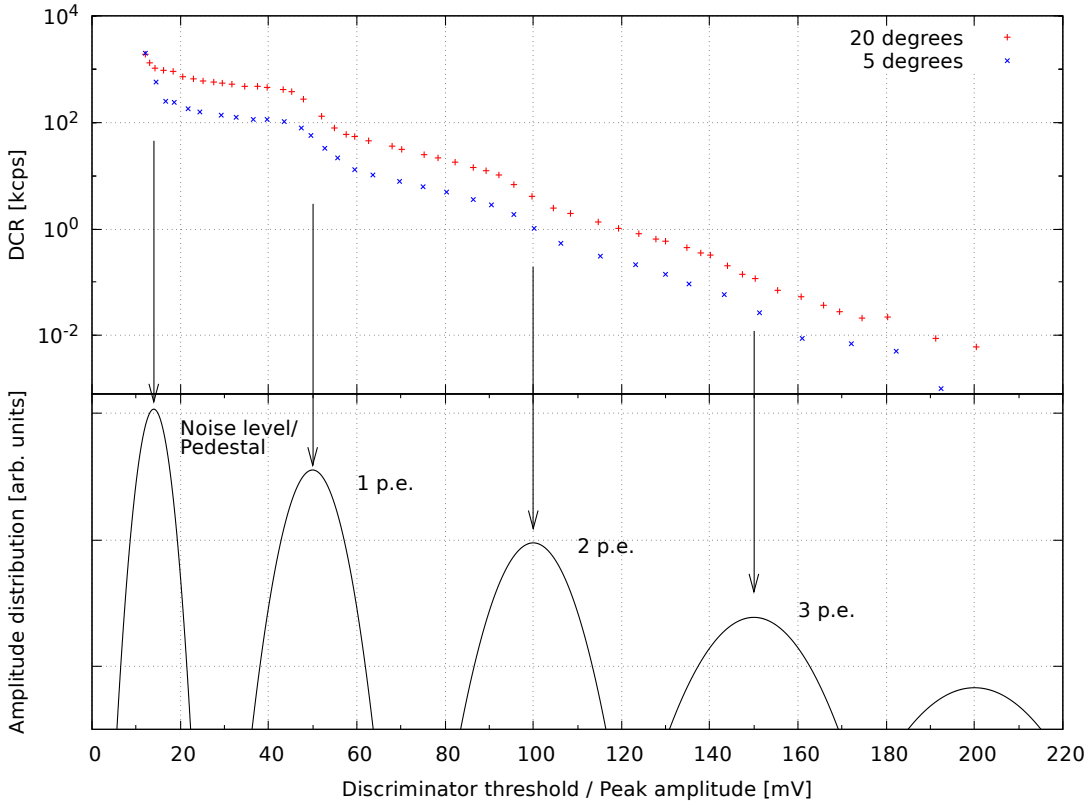

Figure 6.15.: Measured dark count rate versus discriminator threshold for two different temperatures. The rate at one photon level is used to define the dark count rate of the SiPM at a given temperature. In the graph below the amplitude distribution is shown schematically. It does not originate from a measurement but is a sketch that helps visualizing the position of the discriminator threshold relative to the photon levels.

while leaving the height of the signal unchanged. With the analog read-out a temperature decrease by 22.14°C caused a drop in DCR of one order of magnitude. With the STiC a required temperature change of 20.02°C was obtained for the same effect on the DCR [Ali18]. The implementation of cooling is not discussed until section 9, but as a prospect it shall be said that temperatures below zero were achieved pushing the DCR far below 100 kcps per channel.

Cross talk probability

This quantity can be calculated by dividing the DCR on 2 p.e.level by the DCR on 1 p.e.level [Eck+10]. The measurements from the analog read-out with the discriminator and counter were used to that end. The average OCT probability for temperatures between 5°C and 25°C and an overvoltage of 4 V lies at 2.76 %. The results are also shown in table A.1. For room temperature and below, no change within the uncertainty of the measurement were obtained. For higher temperatures, the calculated OCT probability increases, which could originate from an uncertainty of determining the one and two photons levels. The steps become less pronounced for higher temperatures. These measurements are only valid for the applied overvoltage of 4 V, because the OCT probability increases for higher voltages. An

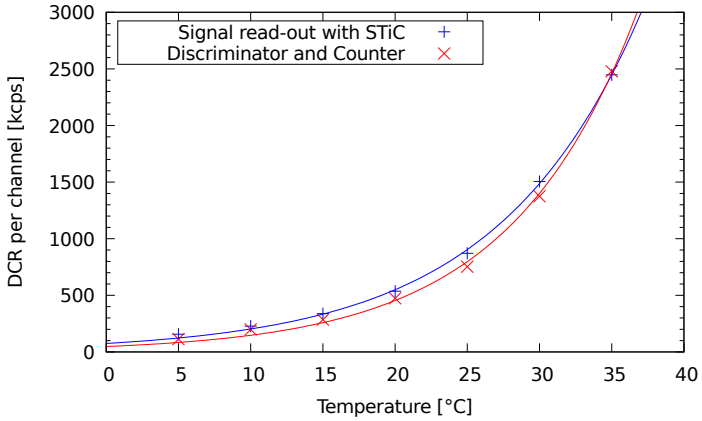

Figure 6.16.: Dark count rate per channel versus temperature. The graph compares the measured values from an analog read-out method using a discriminator and a counter with an ASIC-driven method using STiC. Values from [Ali18].

investigation of the voltage dependent OCT is performed in the scope of the development of the improved set-up using a different ASIC (see section 9).

Final remark
In the scope of these temperature dependent measurements it became clear that cooling the detector was not possible for the actual measurements. The SiPM and parts of the read-out devices – especially the STiC – were located inside the climate chamber, which did not allow for dehumidification at low temperatures and the risk of water condensing on the devices was too high. Therefore, the measurements as they are described and analyzed in section 8 took place at room temperature. The set-up inside the dark box described in sections 6.2 and 6.3 was used.

6.5. Radiator Materials

The most significant quantities that define the applicability of a radiator material to the creation, propagation and detection of Cherenkov photons are the density ρ, the refractive index n and the transmission T. Especially in the near UV range and up to the peak efficiency of the SiPM at 450 nm high transmission is required. To find the optimal material for the use in the experiment, transmission measurements have been performed for all available samples. The measurement preparation and procedure as well as the analysis are described in this section.

6.5.1. Sample Preparation

Quite a large number of different transparent plastic materials by various manufacturers were available: LURAN 358, NAS 30, TOPAS 5103, TOPAS 8007, TPX R18, commercial PMMA, UV-transparent PMMA and ZEONEX 330. The samples were available in different thicknesses and dimensions and at first the area of the samples had to be trimmed to an

appropriate size. Samples with quadratic areas between $15 \times 15\,\mathrm{mm}^2$ and $40 \times 40\,\mathrm{mm}^2$ were created in the mechanical workshop. This variety of sample areas allowed for a use in the 16-channel set-up as well as in the updated 64-channel version described later. Since most materials were only available as thin samples between 1 mm and 4 mm, some of the samples were glued together to artificially create a thicker sample. The optically transparent, single component, UV-curing adhesive named Lens Bond Type SK-9 was used.
Finally, from all samples and thicknesses, small pieces with an area of $9 \times 9\,\mathrm{mm}^2$ were made to be investigated in a spectrophotometer. This device was used to measure the wavelength dependent transmission of the materials.

6.5.2. Transmission Measurements

The Varian Cary 50 Bio UV vivible spectrometer was used to scan the transmission of the samples in a range between 200 nm and 900 nm [Agi20]. The working principle is as follows: A light beam from a Xenon lamp is sent through a monochromator to select the wavelength and to enable scanning through the whole wavelength range. The accuracy of the wavelength was ± 0.5 nm at 541.94 nm [Agi20]. The beam is then split up into a reference beam of intensity I_0 and a beam sent through the sample. Both beams are detected with silicon diode detectors. The intensity I of the beam after the sample is compared to the intensity of the reference beam.

The measured quantity was the *optical density* A, also called *absorption*. It is in close relation to the transmission T, which describes the fraction of the incoming light that leaves the sample on the other side. It is calculated as follows:

$$T = \frac{I}{I_0} = e^{-\ln(10)\cdot A}, \tag{6.3}$$

where I_0 denotes the incident intensity of the light and I is the transmitted intensity. The above equation is based on the definition for the optical density given by D. Bower [Bow03]

$$A = \log_{10}\left(\frac{I_0}{I}\right) = \log_{10}\left(\frac{1}{T}\right) \tag{6.4}$$

It has proven to be reasonable and has been used by others performing optical studies on PMMA blends like R.M. Ahmed [Ahm09] or spectrophotometric analyses of UV-irradiated PMMA like J.H. Nahida [Nah12]. The transmission T will in the following be given in percent.
The results of these measurements are shown in figure 6.17. The transmission is plotted versus wavelength. The most distinct difference between the various samples occur in the lower wavelength. At higher wavelengths all samples show a saturation in transmission. As there is always some light loss due to surface reflections when the beam enters and exits the sample, the saturation is at around 90 %.

To compare the transmission of the samples, the mean values in the range from 270 nm to 450 nm was calculated. This range was chosen since at the SiPM has a detection efficiency that cuts off at 270 nm and has its maximum at 450 nm. The higher wavelength range is less relevant due to the decreasing Cherenkov light emission at higher wavelengths. The mean

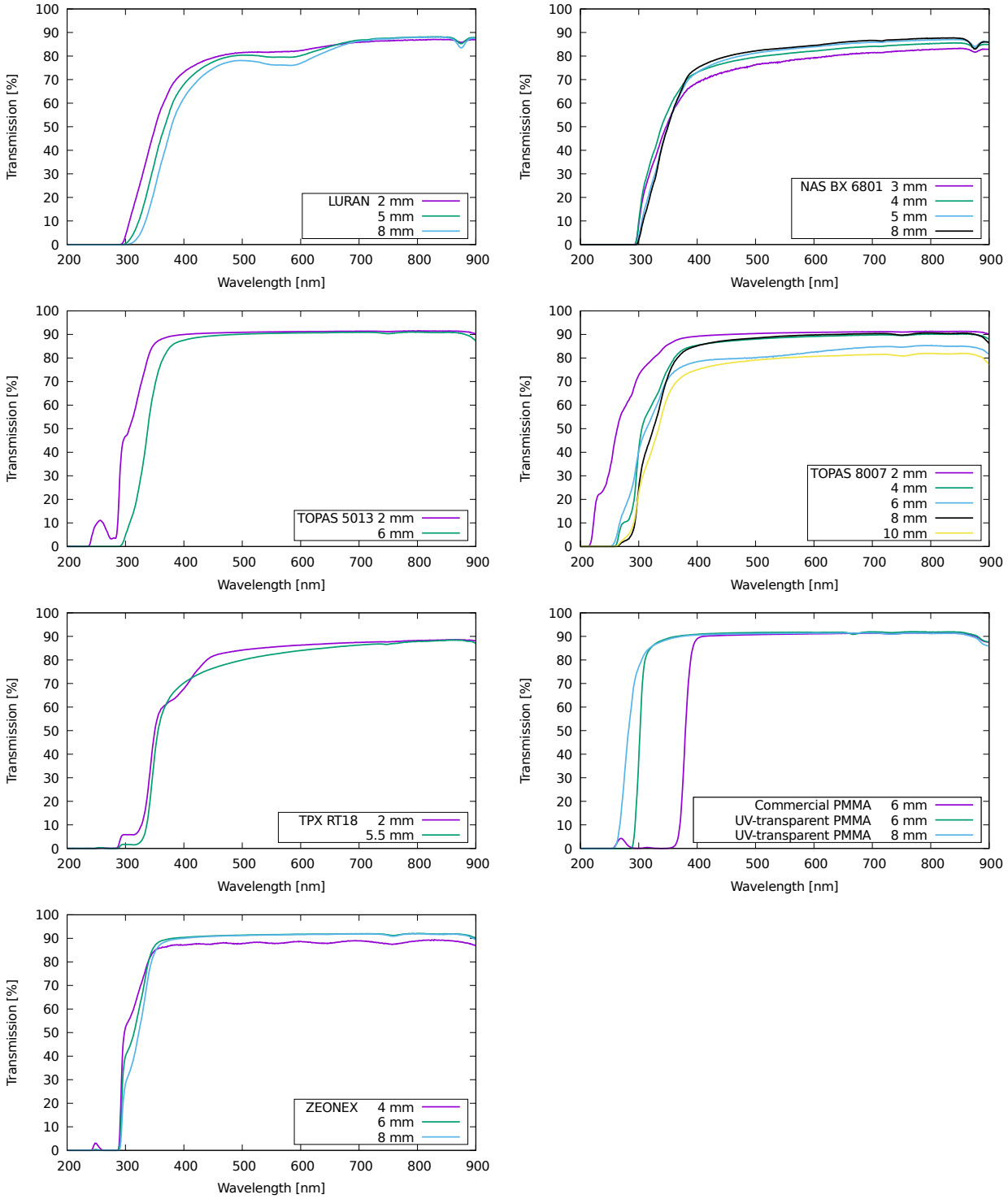

Figure 6.17.: Transmission of various potential radiator materials of different thicknesses measured with a spectrophotometer.

transmission in this range is shown in table 6.2. The table states the name of the material as given by the manufacturer and the thickness of the sample that was used in the measurement given in millimeters. The mean transmission in the aforementioned range is given in the third column.

Material	**d [mm]**	$\overline{T}$ [%] [270 nm; 450 nm]	ρ [g/cm³]	n
LURAN 358 [(a)]	2	46.64	1.08	1.57
	5	39.62	1.08	1.57
	8	34.13	1.08	1.57
NAS 30 [(b)]	3	46.83	1.09	1.56
	4	50.33	1.09	1.56
	5	47.09	1.09	1.56
	8	47.29	1.09	1.56
TOPAS 5013 [(a)]	2	71.60	1.02	1.53
	6	56.52	1.02	1.53
TOPAS 8007 [(a)]	2	82.24	1.01	1.53
	4	66.93	1.01	1.53
	6	63.00	1.01	1.53
	8	61.94	1.01	1.53
	10	54.77	1.01	1.53
TPX RT18 [(c)]	2	43.07	0.83	1.46
	5.5	40.18	0.83	1.46
TPX RT18 with Holder	5.5	39.20	0.83	1.46
Commercial PMMA [(d)]	6	35.71	1.09	1.49
UV transp PMMA [(d)]	6	74.24	1.09	1.49
	8	82.84	1.09	1.49
ZEONEX 330R [(a)]	4	69.83	0.95	1.51
	6	69.17	0.95	1.51
	8	66.00	0.95	1.51

Table 6.2.: List of all samples and thicknesses together with their mean transmission in the range from 270 nm to 450 nm. The density ρ and refractive index n are displayed as well. [(a)]on-line data base for material properties [Mat20], [(b)][Ine16], [(c)] [Mit18], [(d)][Bea+15].

It was found that a 2 mm sample of TOPAS 8007 from the second batch as well as the UV-transparent PMMA samples show very high transmission in that range. The former is too thin for an application to Cherenkov light detection, since the resulting cone intersecting the optical read-out surface would be smaller than the size of the SiPM channels. This circumstance would make a reconstruction of the Cherenkov cone impossible. UV transparent samples of 8 mm constitute a promising material. Unfortunately, this material was not available until the improved set-up was installed, so that for the measurements with STiC and oscilloscope-based read-out, the commercial PMMA as well as TPX were used. Also,

LURAN, NAS, TOPAS 5013 and 8007 as well as ZEONEX were at that time only available as thin samples of maximum 4 mm. The thicker stacked and glued versions were only created for the scope of these transmission measurements and were not available for the first proof of concept set-up.
In the case of TPX RT18, two different measurements were performed, the first one using a holder and the second one where the sample was just placed standing in the beam path of the Spectrophotometer. No significant difference in the result could be found.
Apart from the transmission also the density is important to judge if a material is optimal for the use in a Cherenkov detector. Even if the transmission is very high, the light yield can be limited if the density is too low and the electron range is shortened. The density is displayed in the fourth column of table 6.2.
For all samples there was more than one thickness at hand, for which the absorption was measured. Commercial PMMA was available in thicknesses of 2.2 mm, 3 mm, 4 mm, 4.9 mm, 5.9 mm, 7.8 mm, 10 mm and 15 mm. A transmission curve was only available for the 6 mm sample.
In the following, inconsistencies in the transmission curves for different thicknesses will be discussed and different sample materials will be compared.

6.5.3. Discussion of Different Material Thicknesses and Types

Physical intuition predicts that the transmission decreases when using increasing sample thicknesses of the same material. The samples named NAS, TOPAS 8007, ZEONEX and UV-transparent PMMA show inconsistent transmission with respect to their thickness. It can be seen that only for LURAN and TOPAS 5013 the transmission drops with increasing thickness. All other samples show irregularities.
The difference might originate in different surface properties, like scratches or dust. All samples were cleaned with gas from a nitrogen pistol before the measurement, but the environment was not entirely dust-free. Another influence on the measurement lies within the fact that some samples where glued together using thinner sample thicknesses. This glue, although transparent in the near UV-range, might cause additional light losses, especially when the glue was not distributed equally over the whole area when drying out.

Promising samples of different type were compared. Figure 6.18 shows UV transparent PMMA together with commonly available commercial PMMA, TOPAS 8007 and ZEONEX 330R. Samples of similar thickness were chosen for this comparison. UV PMMA had a thickness of 8 mm and commercial PMMA 6 mm. The samples TOPAS and ZEONEX both had a thickness of 8 mm. One obtains that the UV transparent PMMA has the highest transmission in that range.
The aforementioned different surface structures can also be observed in figure 6.18 by a comparison of TOPAS 8007 and ZEONEX 330R: The height of the plateau above wavelengths of 400 nm is different. This indicates different surface qualities since the reflections at perpendicular beam incidence are roughly equal for all materials and both samples had the same thickness. In order to compare different materials, only the light loss *inside* the sample should be considered, since Cherenkov light is created inside the material and does not enter

from outside like in the case of the spectrophotometer beam. One way to express light loss inside a medium is encoded in a material property called *absorption coefficient* and is defined in the next section 6.5.4.

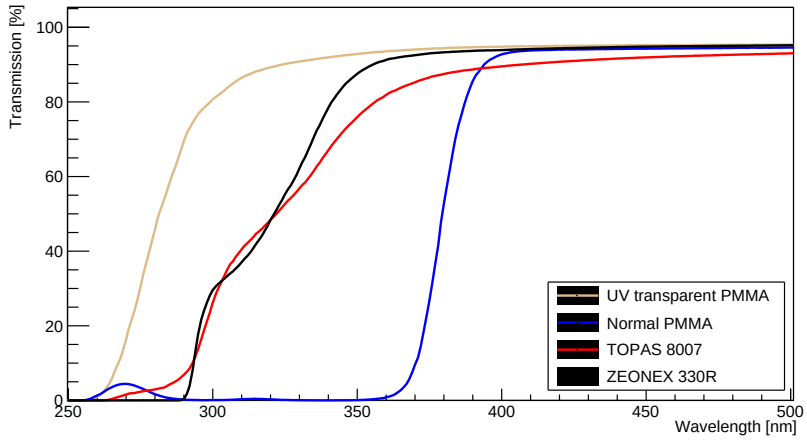

Figure 6.18.: Comparison of transmission curves for four different sample types.

Finally, the transmission of TPX was compared to the curves from the data sheet [Mit18] showing that the sample that was investigated had far lower transmission in the relevant range. Judging by the data sheet, TPX was actually thought to be promising but the sample at hand was not as good as the data sheet suggested (see figure 6.19). The measurement suggests that the UV-transparent PMMA sample shows better transmission property than the TPX sample.

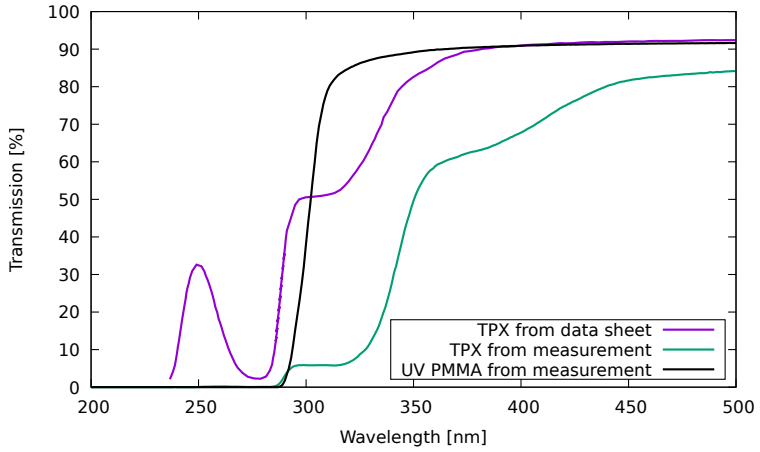

Figure 6.19.: Comparison of the transmission of TPX with the data sheet [Mit18]. A significant difference is obtained making the available TPX sample less promising than indicated by the data sheet. The transmission of UV-transparent PMMA is shown for comparison.

6.5.4. Absorption Coefficient

Surface independent light loss inside a medium can be expressed in terms of a material property called *absorption coefficient* and will be introduced in this chapter. This quantity can help clarify the question if differences between the samples reside in the surface properties or if the composition of the materials themselves are different. A difference in the composition would also give an explanation why for some samples the transmission does not decrease for increasing thicknesses but rather shows inconsistencies as can be seen for UV-PMMA for instance.
The absorption coefficient has another important application: To use the absorption properties of the samples in calculations predicting the number of detected photons per electron (see section 7), a thickness independent quantity is preferred. In these calculation, the fraction of detected Cherenkov light created inside a sample is being calculated. Cherenkov photons are created all along the track of the electron, which is usually in the range of several millimeters in these types of materials. This implies that the probability of such a photon to reach the read-out plane does not only depend on its wavelength but also on its distance from the detector's surface in the moment of its creation. The farther away from the surface the higher the absorption probability.
A quantity independent of the thickness is the so called *absorption coefficient* α, which allows to rewrite equation 6.4 as follows:

$$T = e^{-\ln(10)\cdot A} = e^{-\alpha\cdot d} \tag{6.5}$$

where d is the distance the photon has to travel through the medium. The absorption coefficient creates a link between absorption and thickness of the medium:

$$A = A_0 + \frac{\alpha \cdot d}{\ln(10)}, \tag{6.6}$$

A is the measured absorption or optical density. A consists of two terms: the first one is the constant A_0 that can be described as a default absorption for all wavelengths due to reflection and scattering losses at the surface of the sample. In this case A_0 is treated as constant and therefore wavelength independent. A_0 is the height of the plateau that each transmission curve describes above 450 nm. It can be determined using the mean value of the measured optical density A in a range from 450 nm to 900 nm and define this as the default absorption A_0 due to surface reflections or absorption by dust and scratches. The second term on the right side of equation 6.6 describes the absorption of light *inside* the medium. Since A and A_0 can be determined in the measurement and d is the known thickness of the investigated sample, the absorption coefficient can be calculated:

$$\alpha(\lambda) = \ln(10) \cdot \frac{A(\lambda) - A_0}{d} \tag{6.7}$$

For the same type of material, α is independent of the thickness of the sample and can be used to calculate the absorption losses of light of wavelength λ inside the sample traveling a given distance. It is pointed out that α is a wavelength dependent quantity as already indicated in equation 6.7.
As an example for a direct comparison the absorption coefficients for TPX R18, NAS 30 and TOPAS 8007 are shown in figure 6.20. TPX shows the highest transmission in the near UV

below 220 nm but the SiPM does not have any efficiency in that wavelength range and also the absorption coefficient is still quite high: It fluctuates around a value of 1.3/mm. This means that after a distance of $(1/1.3)\,\mathrm{mm} \approx 0.77\,\mathrm{mm}$ the intensity has dropped to $1/e \approx 0.37$ of its initial level. This coefficient only treats light propagation inside a material and losses at the surface are not taken into account.

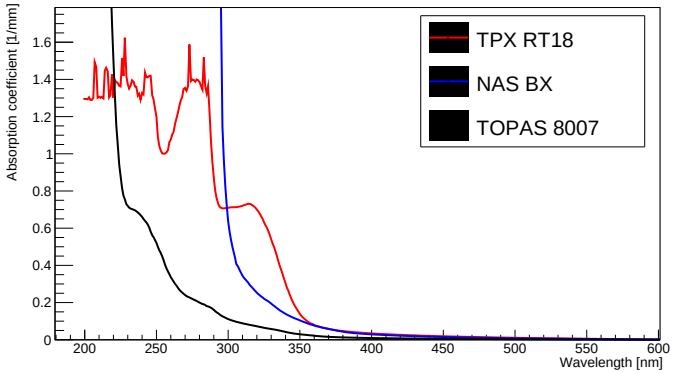

Figure 6.20.: Absorption coefficients $\alpha(\lambda)$ for TPX R18, NAS 30 and TOPAS 8007.

An overview of all absorption coefficients can be found in figure 6.21. The graph with the PMMA samples demonstrates that the two different samples of UV-transparent PMMA are indeed not only different with respect to their thickness, but also their internal optical properties. The absorption coefficient for the 8 mm sample stays below a value of 0.5/mm within the wavelength range down to 260 nm, while the 6 mm sample cuts off already at 290 nm. Since surface properties and thickness are compensated for when using the absorption coefficient, there must be an inherent difference in the materials, i.e. different chemical composition.

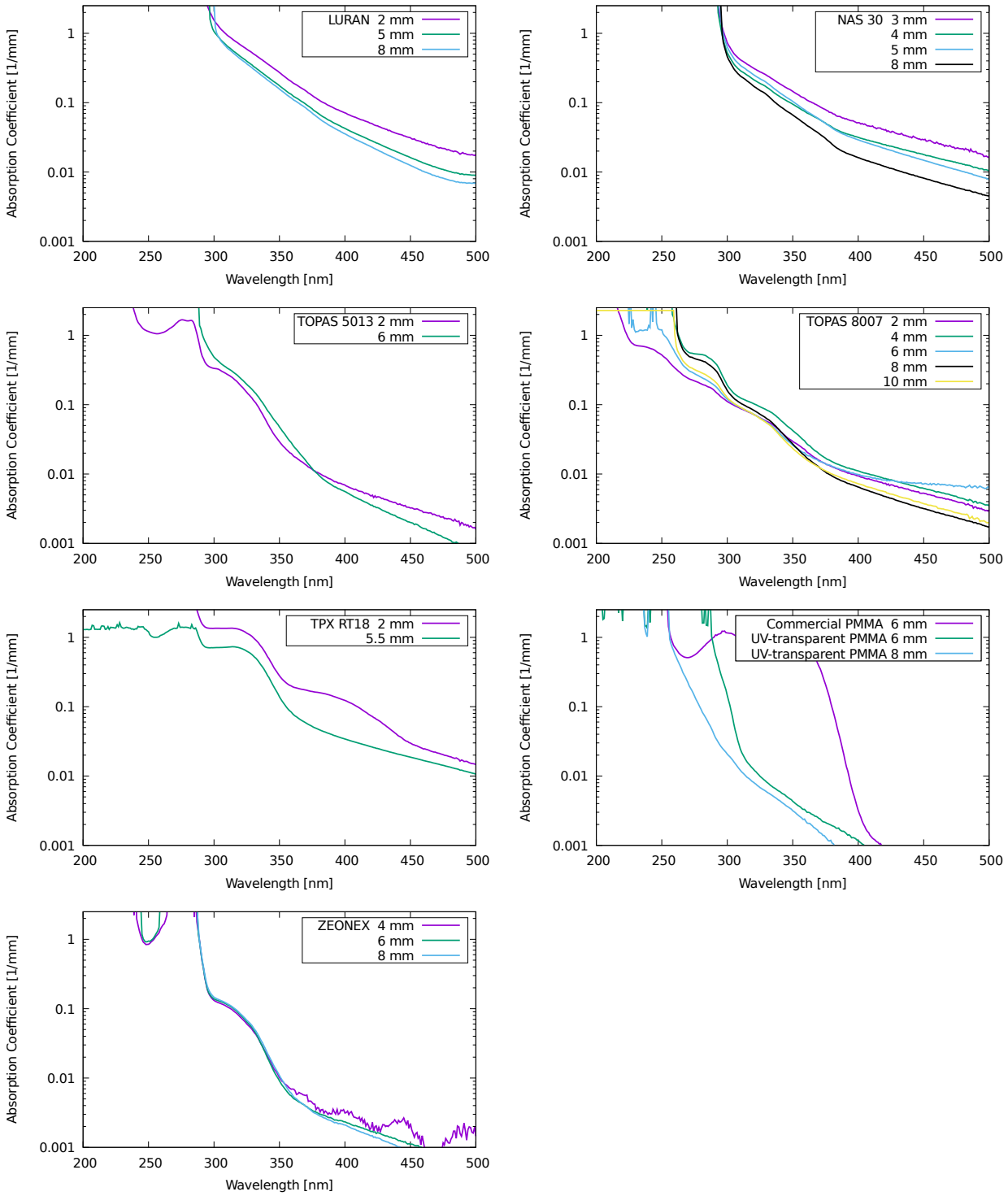

Figure 6.21.: Absorption coefficients of various potential radiator materials of different thicknesses measured with a spectrophotometer.

7. Theoretical Expectations

Contents

7.1 Estimation of the Number of Generated Cherenkov Photons **115**
7.2 Estimation of the Number of Detected Photons **118**
7.3 Applications **123**
7.3.1 Number of Detected Photons Versus Electron Energy 123
7.3.2 Threshold on the Minimum Number of Detected Photons 123
7.3.3 Photon Spectrum 124
7.4 Discussion **126**

The purpose of this chapter is the estimation of the number of generated and detected Cherenkov photons under consideration of the physical and geometrical properties of the set-up. The theory of the Cherenkov effect according to section 2.1.4 as well as tabulated electron range values were employed for the calculation of the number of emitted photons. Detector properties like radiator material and thickness, detector area, photon detection efficiency and cross talk probability were incorporated into the computation algorithm. The underlying code has been written in C++ and using the data analysis toolkit ROOT.
At first the calculation of the number of generated Cherenkov photons is described. The estimation of the number of detected photons is then presented in the second part of this chapter. Finally, the algorithm's accuracy, limitations and potential improvements are discussed in the last part.

7.1. Estimation of the Number of Generated Cherenkov Photons

All calculations relate to the test set-up described in sections 5 and 6 with a collimated electron source focused perpendicularly on a transparent radiator material. The basic idea of the algorithm was the stepwise calculation of the number of emitted photons based on the electron energy in the current step. Therefore, the trajectory of an electron with a certain starting energy E was subdivided into small steps Δx, for which the number of Cherenkov photons was calculated. The algorithm takes the slowing down of the electron along its trajectory into account and, therefore, also the changing number of emitted Cherenkov photons per traveled distance $\mathrm{d}N/\mathrm{d}x$.

The calculation used the *Stopping Power and Range Tables for Electrons* provided by NIST. A material can be chosen from a data base or generated by stating its chemical components and density. The data base then provides a table of electron energies and corresponding stopping power $\mathrm{d}E/\mathrm{d}x$ of electrons in that medium. Choosing a small enough step size ΔE, one can assume the stopping power to be approximately constant along that step. Then the distance Δx that the electron travels between two energy steps can be calculated:

$$\Delta x = \frac{\Delta E}{\mathrm{d}E/\mathrm{d}x}$$

The number of emitted Cherenkov photons within a wavelength interval $[\lambda_1, \lambda_2]$ per traveled distance of the electron is described by equation 2.19:

$$\frac{\mathrm{d}N}{\mathrm{d}x} = 2\pi z^2 \alpha \cdot \sin^2(\theta_\mathrm{C}\ ) \cdot \left(\frac{1}{\lambda_1} - \frac{1}{\lambda_2}\right) = 2\pi\alpha \cdot \left(1 - \frac{1}{\beta^2 n^2}\right) \cdot \left(\frac{1}{\lambda_1} - \frac{1}{\lambda_2}\right) \tag{7.1}$$

with $z = 1$ and $\lambda_1 < \lambda_2$ [1].
Assuming the refractive index to be constant within the wavelength range of interest, the number of photons generated within each step $(\Delta x)_i$ could be computed by integrating equation 7.1:

$$N_i = \int_{(\Delta x)_i} \frac{\mathrm{d}N}{\mathrm{d}x} = 2\pi\alpha \cdot \left(1 - \frac{1}{\beta^2 n^2}\right) \cdot \left(\frac{1}{\lambda_1} - \frac{1}{\lambda_2}\right) \cdot (\Delta x)_i \tag{7.2}$$

For the calculations a wavelength range from 200 nm to 900 nm was chosen. The total number of emitted Cherenkov photons along the whole electron track was the sum of all partial photon numbers N_i from all steps $(\Delta x)_i$:

$$N_\mathrm{tot} = \sum_i N_i \tag{7.3}$$

Figure 7.1 shows the total number of produced Cherenkov photons as a function of initial electron energy. This estimation was performed for different thicknesses of the radiator material PMMA. The summation was conducted until the total sum of all steps $\sum_i (\Delta x)_i$ had reached the thickness d of the PMMA sample. The number therefore saturates at a certain energy, above which the electron track length would be larger than the thickness of the sample. The solid curve shows the number of emitted photons in an infinitely thick sample. For all mentioned calculations the assumption was made that the electron track is a straight line and multiple scattering (which deflects the electron) happens mostly at the end of the track, where the electron does not have enough energy to maintain the Cherenkov effect.

For example, for a 10 mm thick sample of PMMA, the expected number of emitted Cherenkov photons created by electrons with an energy of 1.5 MeV was 504. This value does not contain

[1] The careful reader may notice that in the theory part (section 2.1.4) λ_2 was stated as the smaller wavelength corresponding to the higher frequency ω_2. The reason was to preserve consistency in the derivation of the formula. This chapter will stick to the more commonly used convention of choosing λ_1 as the smaller wavelength.

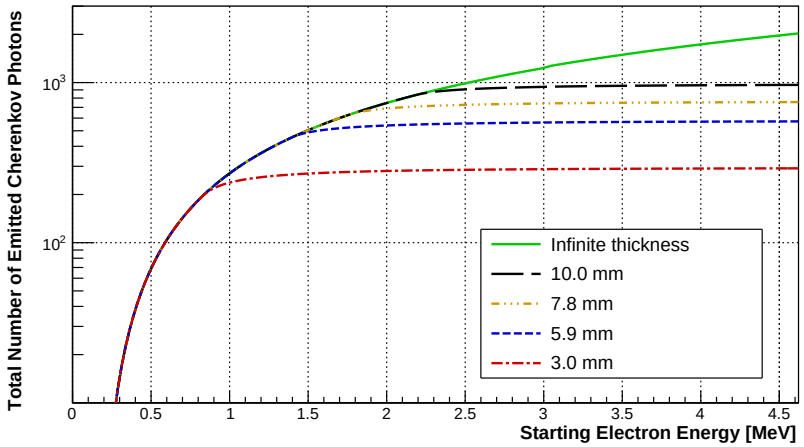

Figure 7.1.: Calculated number of generated Cherenkov photons within a wavelength range between 200 nm and 900 nm as a function of the initial electron energy. Results are shown for different thicknesses of PMMA. Thinner samples limit the range of the electron and therefore the light yield, causing the number of created photons to saturate.

information on the distribution of the number of emitted Cherenkov photons. Due to multiple scattering of the electron, the total range can vary causing significant fluctuations of the number of emitted Cherenkov photons and giving rise to the width of the distribution. A simulation of 10^6 electrons in PMMA with an energy of 1.5 MeV performed in Geant4 results in a standard deviation of 69.3 [Bä20a]. A mean value of 461.4 was found, which is smaller than predicted by the calculation. The distribution is shown in figure 7.2.

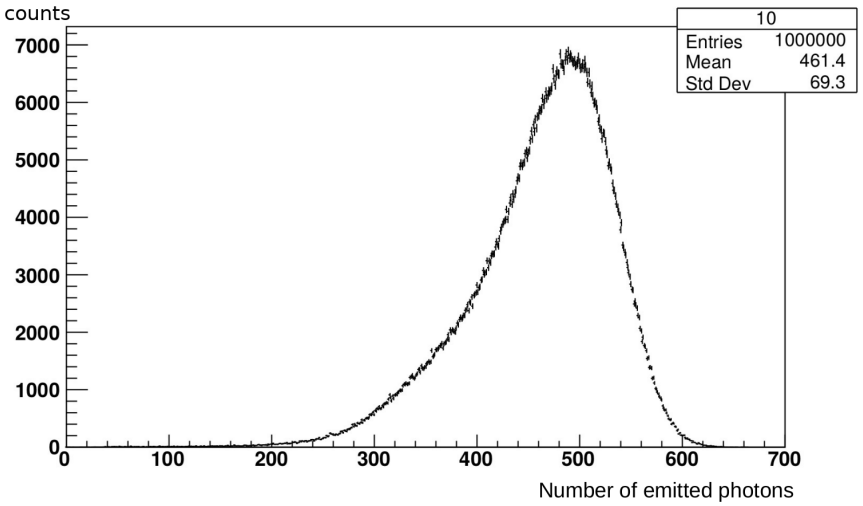

Figure 7.2.: Simulated number of emitted Cherenkov photons for a 1.5 MeV electron in a PMMA sample with a thickness of 10 mm. 10^6 events were simulated. A broad distribution was obtained with a mean value smaller than the calculated one. [Bä20a]

This distribution contains photons from events where the electron was back-scattered and only a small number of photons was created inside the sample. This explains the long tail towards smaller photon numbers.

In the experiment a ^{90}Sr electron source was used, which has a continuous energy spectrum up to about 2.4 MeV. The goal was to calculate an expectation value for the average number of generated – and later also detected – photons per measurement. Therefore, to compare results from measurements to the calculation, the above algorithm was repeated for all electron energies in the spectrum with a step size of 293 eV and the mean value on the number of created Cherenkov photons was calculated. The measured spectrum is shown in figure 6.1 in section 6.1 and contained 8192 values. Finally, the expectation value of the photon number was computed using the weighted mean of all results:

$$\langle N \rangle = \sum_j \omega_j \cdot N_{\text{tot}}^j$$

where ω_j denotes the relative occurrence of the j-th energy bin from the spectrum.

7.2. Estimation of the Number of Detected Photons

For a calculation of the expected number of detected Cherenkov photons per electron with given energy E the following quantities must be taken into consideration:

- Transmission properties of the sample: depending on its wavelength and the location of its creation, a Cherenkov photon is only transmitted through the medium with a certain probability. The quantity to describe the transmission of photons is the absorption coefficient.
- The geometry of the detector array: the side length of the array has an influence on the light collection efficiency. For large sample thicknesses the Cherenkov cone can exceed the boundaries of the array and the emitted photons would not reach the sensitive area.
- The detector's photon detection efficiency (PDE): depending on the applied overvoltage, the SiPM array is only capable of detecting a certain fraction of impinging photons. The PDE depends furthermore on the photon wavelength.
- Cross talk probability: for each detected photon, a second signal with the size of a p.e. signal could be created due to cross talk. This effect essentially increases the number of photons registered by the read-out electronics and the analysis algorithm.

To include the above list into the algorithm of section 7.1 additional functions were implemented into every step of the computation. The full algorithm can be retraced step by step using the flow chart in figure 7.3.
After the calculation of the number of generated photons in a step, the transmission probability for these photons was computed as follows: based on the emission spectrum of Cherenkov

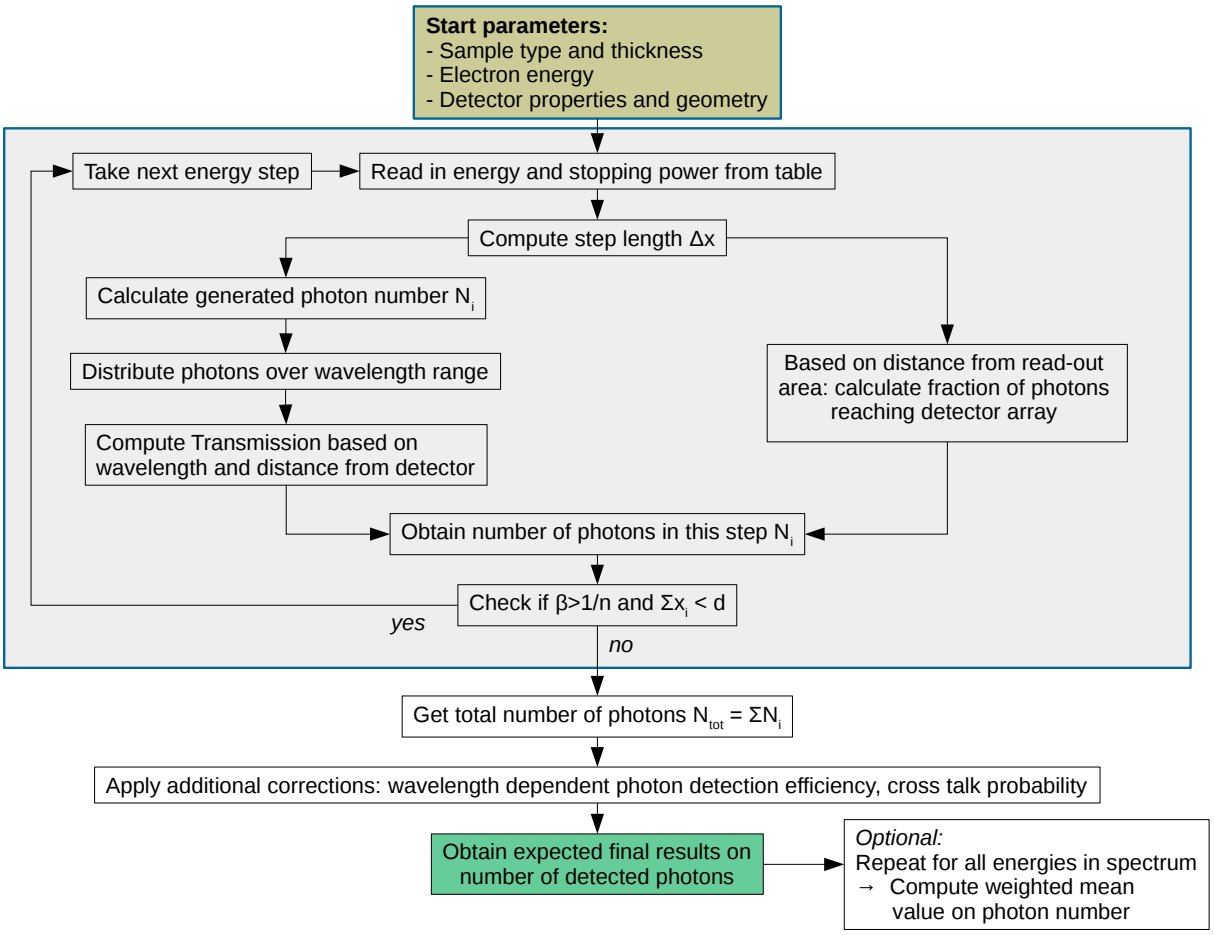

Figure 7.3.: Flow chart of the algorithm for the computation of the number of expected Cherenkov photons per electron. The algorithm takes the initial electron energy, type and thickness d of the radiator material and the detector properties as start parameters. In a step-by-step fashion the number of generated and detected photons is calculated under consideration of absorption (left branch in the box), detector geometry (right branch), PDE and cross talk (at the bottom).

photons discussed in section 2.1.4, the number of generated photons was distributed over the wavelength range following a $1/\lambda$ relation. A step size of 5 nm was chosen for this distribution. Essentially, the computed number of photons was entered into bins of a histogram with 5 nm bin width and in accordance with a $1/\lambda$-relation. The green curve in figure 7.4 shows the wavelength dependency of emitted Cherenkov radiation. In the graph the number of generated photons from an 1.5 MeV electron in PMMA is shown versus wavelength. In total 504 Cherenkov photons were generated.
The transmission T of the photons of each wavelength bin was calculated based on equation 6.5 using the wavelength-dependent absorption coefficient $\alpha(\lambda)$:

$$T = \exp\left(-\alpha(\lambda) \cdot s\right)$$

Here, s is the distance the photon has to travel through the medium to the read-out plane based on the location of its emission and the opening angle θ_C of the Cherenkov cone. This

procedure was repeated for each electron step Δx and the wavelength bins were added up accordingly. This part of the computation algorithm is shown in the left branch of figure 7.3. Figure 7.4 shows an example of a transmission curve for photons in a sample of PMMA. As an example, the graph shows the transmission for a step taking place 10 mm above the detector array. The farther away from the SiPM surface, the smaller the transmission and vice versa.

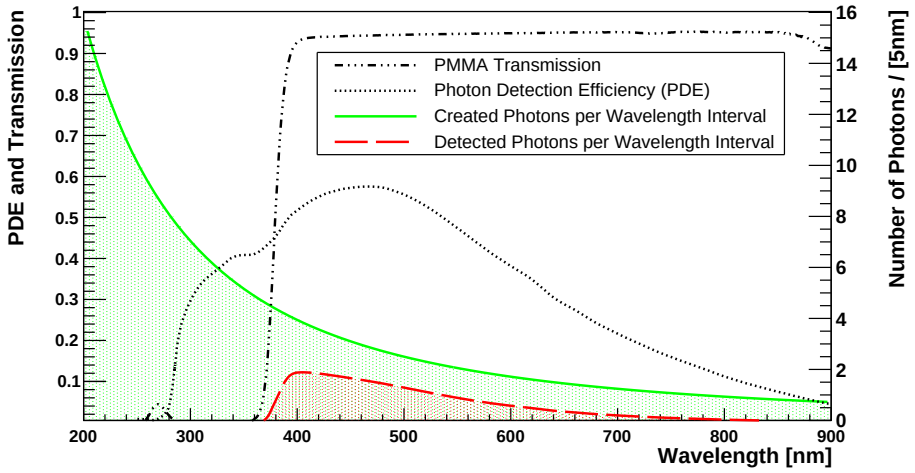

Figure 7.4.: Theoretical estimations of the number of detected Cherenkov photons (red dashed curve) from a 1.5 MeV electron in a PMMA sample of 10 mm thickness under consideration of wavelength-dependent transmission, bias-dependent detection efficiency and geometric boundaries of the SiPM array. The solid green curve shows the number of generated Cherenkov photons per 5 nm wavelength interval.

The right branch represents the calculation of the fraction of photons that can reach the read-out area. This fraction depends on the size of the Cherenkov cone and on the distance h above the array, where the photons are created. The sketch in figure 7.5 demonstrates this. For large enough SiPM arrays geometry effects do not play a role. However, in the actual experimental set-up the size of the array was limited to $12.6 \times 12.6\,\mathrm{mm}^2$, or $26.5 \times 26.5\,\mathrm{mm}^2$, respectively (used in an extended and improved set-up, see chapter 9).[2]
A sharp, well-defined Cherenkov ring on the read-out plane is considered for photons emitted within a step Δx at a distance h above the surface. From geometric considerations, one can deduce that the fraction f_{out} of photons, which arrived outside the sensitive area and would not be detected, can be written as

$$f_{out} = \frac{4}{\pi} \cdot \arccos\left(\frac{a}{2\,r}\right), \tag{7.4}$$

with a, the side length of the array and r the radius of the circle created by the intersection of the Cherenkov cone and the detector plane:

$$r = h \cdot \tan(\theta_{\mathrm{C}}\,) = h \cdot \tan\left(\arccos\left(\frac{1}{n\,\beta}\right)\right)$$

[2] These dimensions include all gaps between channels according to the technical drawing in figure 6.7. The dimensions of the extended array are discussed in chapter 9 in detail.

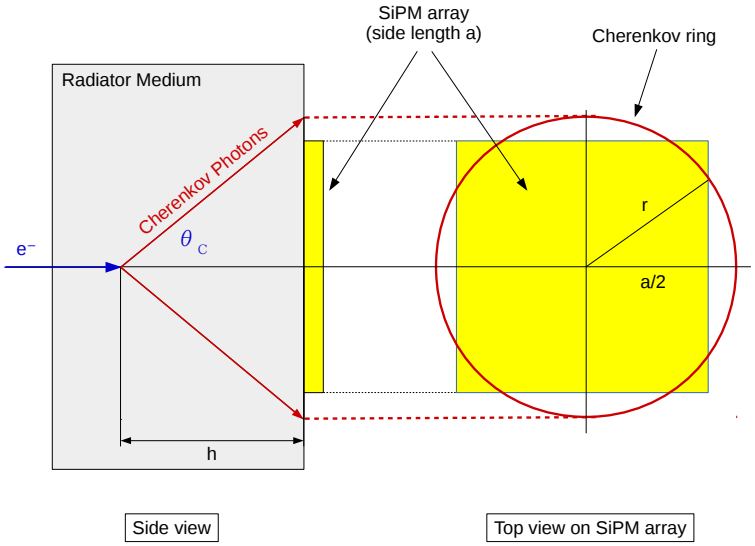

Figure 7.5.: Sketch for the visualization of the fraction of photons leaving the sensitive area of the detector. The Cherenkov cone (red) can exceed the boundaries of the array (yellow) depending on the thickness of the sample, the opening angle θ_C and the distance above the SiPM array.

Equation 7.4 is only valid for $\frac{a}{2} < r < \sqrt{2}\frac{a}{2}$. For $r < \frac{a}{2}$ the value for f_{out} is automatically set to 0 by the algorithm, while for $r > \sqrt{2}\frac{a}{2}$ it is set to 1. Thus, the fraction of photons impinging on the SiPM is

$$f_{in} = 1 - f_{out} \leq 1. \tag{7.5}$$

For each step, this factor was calculated and the number of emitted photons is multiplied with it. Thus, the geometry of the detector is taken into account. This calculation only holds for a collimated electron source focused on the center of the radiator sample.

The influence of the geometry on the result has been tested with different PMMA sample thicknesses. The expected mean value of the number of detected Cherenkov photons created by electrons from the ^{90}Sr source was calculated. Figure 7.6 shows the calculation with and without consideration of the geometric boundaries of the array. For the demonstration of the influence of the geometry, the absorption of photons was not considered. Results using a realistic SiPM with a side length of 12.6 mm (red) are compared to the values obtained with an artificial, infinitely large array, where all Cherenkov photons would be captured (blue). Both sets of data points show growing values for small sample thicknesses due to increasing electron range. The thicker the sample, the larger the fraction of electrons that can travel over their full range and attain their full light yield. However, only the red points decrease at larger sample thicknesses. Above a peak value at about 6 mm, the expectation values for the realistic geometry start dropping again, as the Cherenkov cone exceeds the detector area. The amount of photons that are lost outside the sensitive area increases with growing thickness.

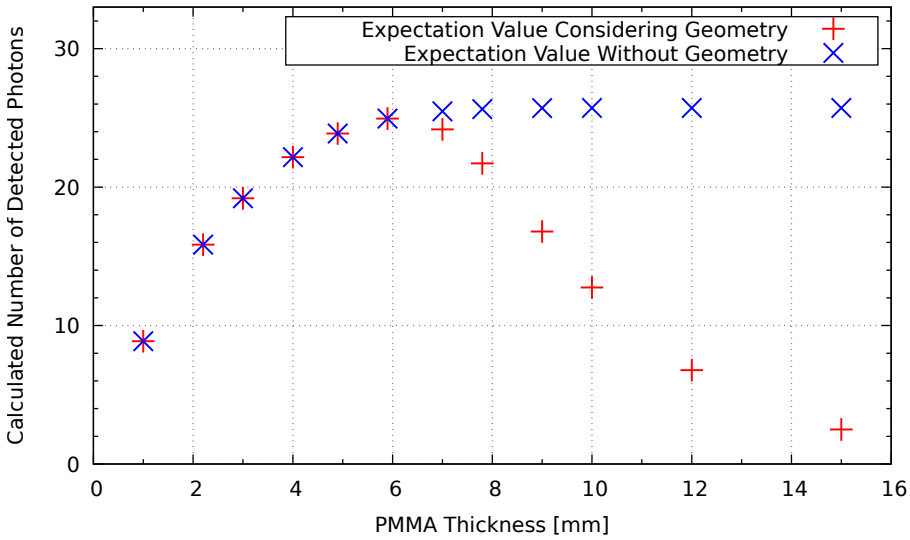

Figure 7.6.: Calculated average number of detected Cherenkov photons with (red) and without (blue) consideration of the detector geometry. The calculations have been performed for electrons in PMMA samples of different thicknesses. For growing thickness, the Cherenkov cone exceeds the boundaries of the array causing the number of detected photons to shrink.

In the next part of the algorithm, the number of photons that are actually detected, was calculated. That happens after the total number of Cherenkov photons from all steps has been calculated including absorptive and geometric considerations. This part of the algorithm takes place outside the box in the flowchart of figure 7.3.

The number of photons in each wavelength interval was multiplied by the PDE of the detector within that interval. The PDE increases with applied detector voltage. This voltage dependency was implemented using the manufacturer's statement about the change of the peak PDE with bias voltage [Ham16]. The PDE of each wavelength interval was scaled accordingly. Afterwards, the total number of detected photons was calculated as the sum of all numbers of photons from all wavelength intervals.

The red curve in figure 7.4 shows the number of detected photons for the aforementioned example of a 1.5 MeV electron in a PMMA sample of 10 mm thickness. Under consideration of PDE and absorption as well as the size of the SiPM array, 76 out of 504 generated photons were detected in the end.

In this case, the transmission of PMMA is the limiting factor for the number of detected photons, as it already cuts off at about 360 nm, while the SiPM was capable of detecting photons with wavelengths as short as 270 nm. For the measurements with the set-up described in chapter 6, only commercial PMMA was available. UV transparent PMMA samples were used only in the improved set-up presented in chapter 9.

Finally, optical cross talk (OCT) was incorporated into the computation. The probability of optical cross talk is voltage dependent and values were taken from the measurements shown in section 6.4.3. The photon number from the step before was multiplied by a factor of $(1 + P_{\mathrm{CT}})$ to obtain the final results on the expected number of detected Cherenkov photons.

For a OCT probability of 3 % at an overvoltage of 4 V, the final result for the number of detected Cherenkov photons in a 10 mm sample is 78.

7.3. Applications

7.3.1. Number of Detected Photons Versus Electron Energy

The number of detected Cherenkov photons created by electrons in PMMA was calculated for various electron energies. The same thicknesses as used in the actual measurements were employed in the calculations and compared to one another. The results are depicted in figure 7.7. The influence of various effects can be observed. First of all, the electron track length is limited by the thickness of the sample, which subsequently reduces the Cherenkov light yield. Therefore, for all samples the number of detected photons saturates. For thinner samples the saturation occurs at lower energies and the maximum number of detected photons is smaller as well.

The depicted results also demonstrate the influence of the detector geometry on the outcome of the calculation: In case of thinner samples, the Cherenkov cone does not exceed the geometric limitations of the array and all photons impinge on the detector. However, for thicker samples, photons emitted at the beginning of the electron trajectory can leave the boundaries of the array and are lost for detection. The data points for 10 mm show this effect by their less steep increase at lower energy values than the points of any other data set. The higher the energy, the longer the electron range and the larger the fraction of photons emitted towards the SiPM array. Thus, the data points are able to "catch up" with the other sets for higher energies.

A trade-off is required to find the optimal thickness giving the highest expectation value for the number of detected photons. It can be deduced from the results shown in figure 7.6 that for the given detector size, a sample thickness of about 6 mm shows the highest expectation value. If larger arrays are being used, this maximum value shifts towards larger thicknesses.

7.3.2. Threshold on the Minimum Number of Detected Photons

For a more thorough comparison to the actual measurement, no single energies, but the whole ^{90}Sr spectrum was used for the calculations. The calculated number of detected photons is the mean value of the photon numbers of all energy values weighted by their relative occurrence in the spectrum. This computation was again performed for different sample thicknesses of PMMA.
To make the calculation more realistic, a minimum threshold on the number of detected photons was set. In an actual measurement, coincident signals on a certain minimum amount of channels is required for a detection of Cherenkov light – for example 3 in case of STiC. Thus, a photon number smaller than the minimum number of channels cannot possibly be detected. That number is in this thesis referred to as required number of coincident channels (rnocc). The use of such a requirement rejects certain events with small photon numbers and essentially constitutes a lower energy limit for the electron energy. Electrons

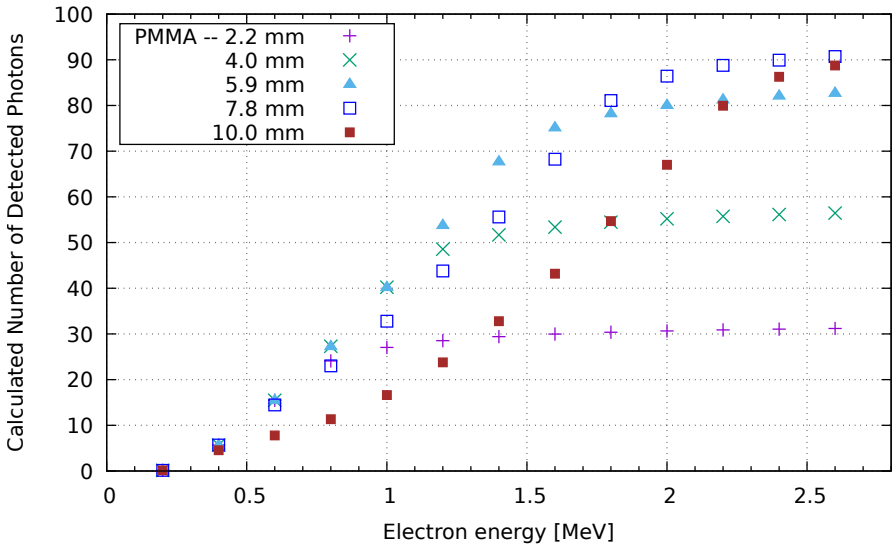

Figure 7.7.: Calculated number of detected Cherenkov photons versus electron energy. Different sample thicknesses are compared in the graph and the detector geometry was taken into consideration.

with smaller energies are less likely to be detected, since the number of detected Cherenkov photons does not fulfill the requirement.
This behavior was investigated for a minimum required amount of 1, 3 and 5 photons. Figure 7.8 shows the results. All three data sets show essentially the same behavior: the rising values at the beginning represent the increase in electron range for growing sample thickness. There is a maximum value at about 6 mm thickness until the exceeding Cherenkov cone causes the mean values to decrease again.
The difference in the three data sets is seen in the changing mean value, when the required number of detected photons is increased. For higher rnocc, more events are rejected in the detection that have low photon numbers. Therefore, the mean value increases for larger rnocc.

7.3.3. Photon Spectrum

The number of detected Cherenkov photons for each energy value from the ^{90}Sr spectrum has been filled into a histogram with a bin width of 1. Thus, a spectrum of the calculated number of detected photons is created. Figure 7.9 shows the spectrum for three different thicknesses, 10 mm (red line), 5.9 mm (green) and 3 mm (blue).
All three thicknesses show a large contribution from small photon numbers and higher photon numbers occur less likely. For a thicker sample, the contribution from smaller photon numbers is greater, as seen by the red curve for 10 mm. This represents the Cherenkov cone exceeding the SiPM boundaries causing light loss and effectively reducing the number of detected photons compared to thinner samples. Towards higher numbers, a pile up is observed, which corresponds to the limited electron range reducing the Cherenkov light yield. For thinner samples this pile up effect is visible at lower photon numbers, as the trajectory is more limited than for a thicker sample.

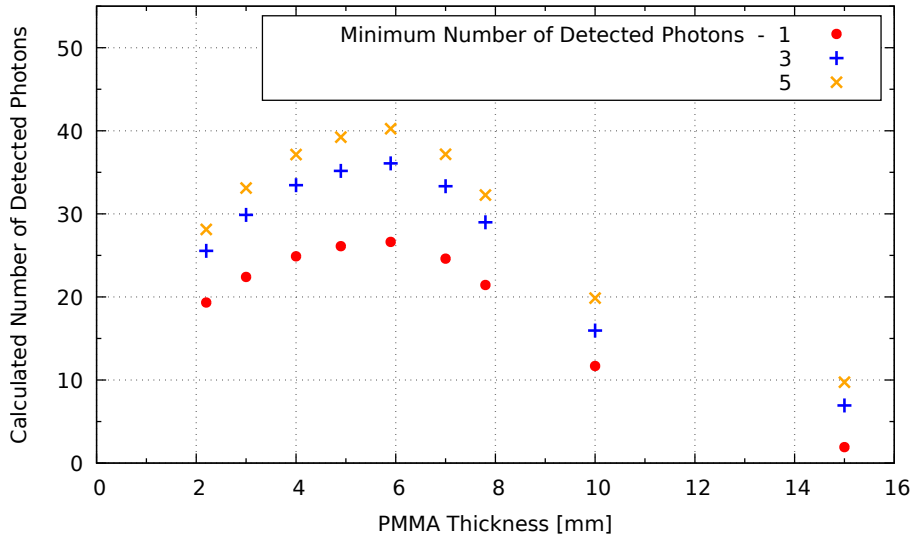

Figure 7.8.: Mean value of the number of detected photons for various PMMA thicknesses. The graph compares different minimum required numbers of detected photons and contains all effects that were implemented into the algorithm: geometric considerations, wavelength dependent absorption and PDE as well as OCT.

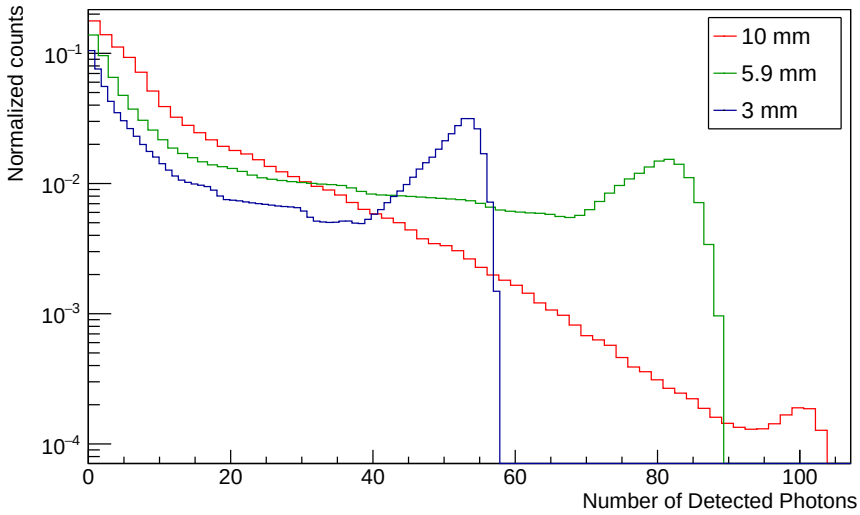

Figure 7.9.: Calculated Cherenkov photon spectrum for three different thicknesses. The histogram contains the number of detected photons for each energy value from the ^{90}Sr spectrum.

7.4. Discussion

The described algorithm is capable of calculating the number of detected Cherenkov photons created by electrons in transparent radiator materials. Material properties and detector geometry are taken into account as well as bias-dependent detection efficiency and cross talk probability. The calculation of an expectation value for the number of detected photons created by electrons from a non-mono-energetic source was implemented. The computations are able to make valuable predictions on the outcome of measurements. Limitations of the algorithm are discussed in the following paragraphs.

First of all, no multiple scattering of the electron has been considered. This statistical process causes the electron to change direction multiple times and photons are emitted towards the side where they are lost for detection. Neglecting this effect gives rise to an overestimation of the number of detected photons in the calculation. This has already been demonstrated by means of the distribution of the number of emitted Cherenkov photons from simulated events (see figure 7.2).
Light losses at the boundaries between radiator and detector surface were neglected. This also gives rise to an overestimation.
Reflections of photons off the side walls of the radiator material were neglected as well. The number of photons reaching the detector array might therefore have been underestimated in the calculation.
Another neglected geometric influence resides in the channel structure of the array: the gaps in between the individual channels were not considered. Photons impinging on these areas could not be detected. This overestimates the light collection efficiency. Also, in the measurements, the minimum requirement was set on the number of channels fired, since it was more practicable. In the calculation, however, the minimum was set on the number of detected photons. This circumstance neglects the probability of two photons hitting the same channel.
The electron range was considered a straight line between start point and thermalization. Due to multiple scattering, the electron range fluctuates, as demonstrated in Geant4 simulations. This gives rise to uncertainties on the traveled distance and, therefore, on the number of created photons and, consequently, on the number of detected photons.
Furthermore, values like PDE and cross talk probability are of statistical nature. The same counts for the Cherenkov emission light yield and the distribution of the photons over the wavelength range. Thus, no exact calculation is possible and only expectation values can be given.

Additionally to that, a realistic Cherenkov ring has a slightly different opening angle for different wavelength ranges. No sharp ring can be expected in reality. This limits the accuracy of the prediction on the fraction of photons reaching the array. As a matter of fairness, however, it should be mentioned that this influence on the accuracy of the calculation is relatively small compared to other limitations described in this section.

8. First Measurements to Prove the Principle

Contents

8.1 Coincident Detection of Cherenkov Photons **127**
8.1.1 Method Description 128
8.1.1.1 Measurement Procedure 128
8.1.1.2 Coincidence Search Algorithm 128
8.1.1.3 Correction of Inherent Time Differences 130
8.1.2 Measurements 131
8.1.2.1 Coincidence Time Resolution 131
8.1.2.2 Distribution of Coincident Photon Hits 132
8.1.2.3 Light Yield Quantification Using Time over Threshold . 133
8.2 Photon Counting Using Charge Integration **135**
8.2.1 Calibration 135
8.2.2 Measurement Procedure 138
8.3 Results **139**
8.3.1 Measured Light Intensity and Number of Detected Photons . . . 139
8.3.2 Quantification of the Occupancy of the Detector Array 141
8.3.3 Reconstruction of the Electron Source Location from Accumulated Events 142
8.4 Conclusion on the Proof of Principle **142**

8.1. Coincident Detection of Cherenkov Photons

The purpose of these first measurements was to prove the ability to detect Cherenkov photons from electrons in optically transparent radiator materials in coincidence using a Silicon Photomultiplier (SiPM) array.

8.1.1. Method Description

8.1.1.1. Measurement Procedure

This section contains the data taking procedure and the parameter settings for both measurement and analysis. The set-up in general as well as the read-out electronics have already been described in chapter 6.
A coincidence measurement of photons on 16 channels was performed using a Silicon Photomultiplier Timing Chip (STiC). Different radiator types of various thicknesses were coupled to the 4×4 SiPM array and data was taken for 60 s with each sample. A motorized source-holder was employed for the measurements to choose various electron source locations with respect to the surface of the sample or the detector matrix respectively. The electron source could be moved in 3 dimensions in steps of approximately 0.2 μm. A picture of this device is shown in figure 8.1.
The SiPM breakdown voltage at room temperature was at 52.8 V and an overvoltage of 4.2 V was chosen. The trigger levels of each channel were set to a level of 2-3 p.e. resulting in a dark count rate (DCR) of 1-10 kcps per channel. The STiC recorded every signal from every channel that exceeded the trigger threshold. An off-line coincidence search was performed after the measurement.

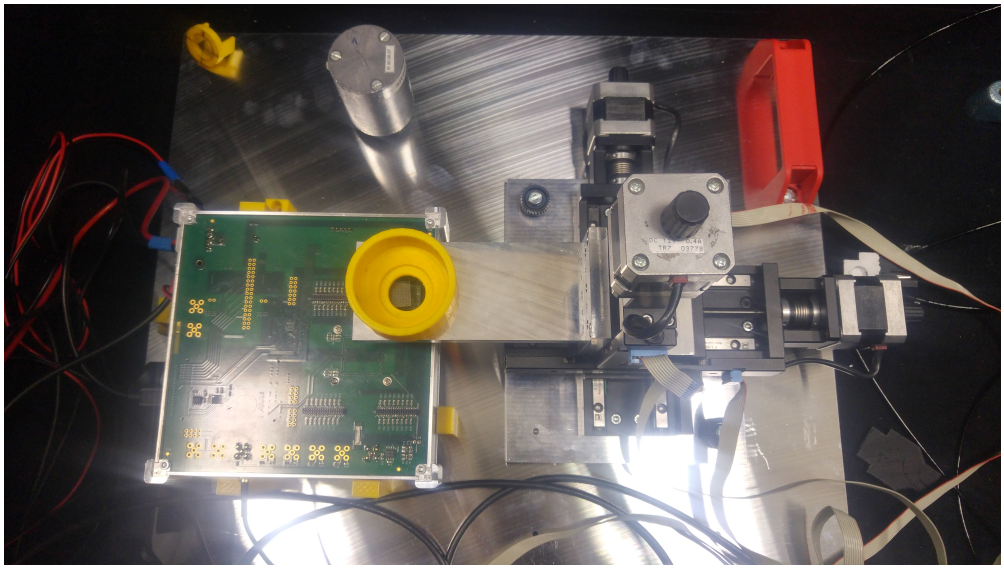

Figure 8.1.: Motorized source holder for varying the source location with respect to the surface of the sample or the detector array, respectively. The electron source could be mounted in the yellow holder and moved in 3 dimensions in a step size of approximately 0.2 μm. The green colored STiC evaluation board is seen on the left.

8.1.1.2. Coincidence Search Algorithm

The data written to file during a measurement contain not only valid signals from Cherenkov photons but mostly dark count from the semiconductor material of the SiPM itself. An on-line coincidence search or pre-selection of certain frames with a minimum number of

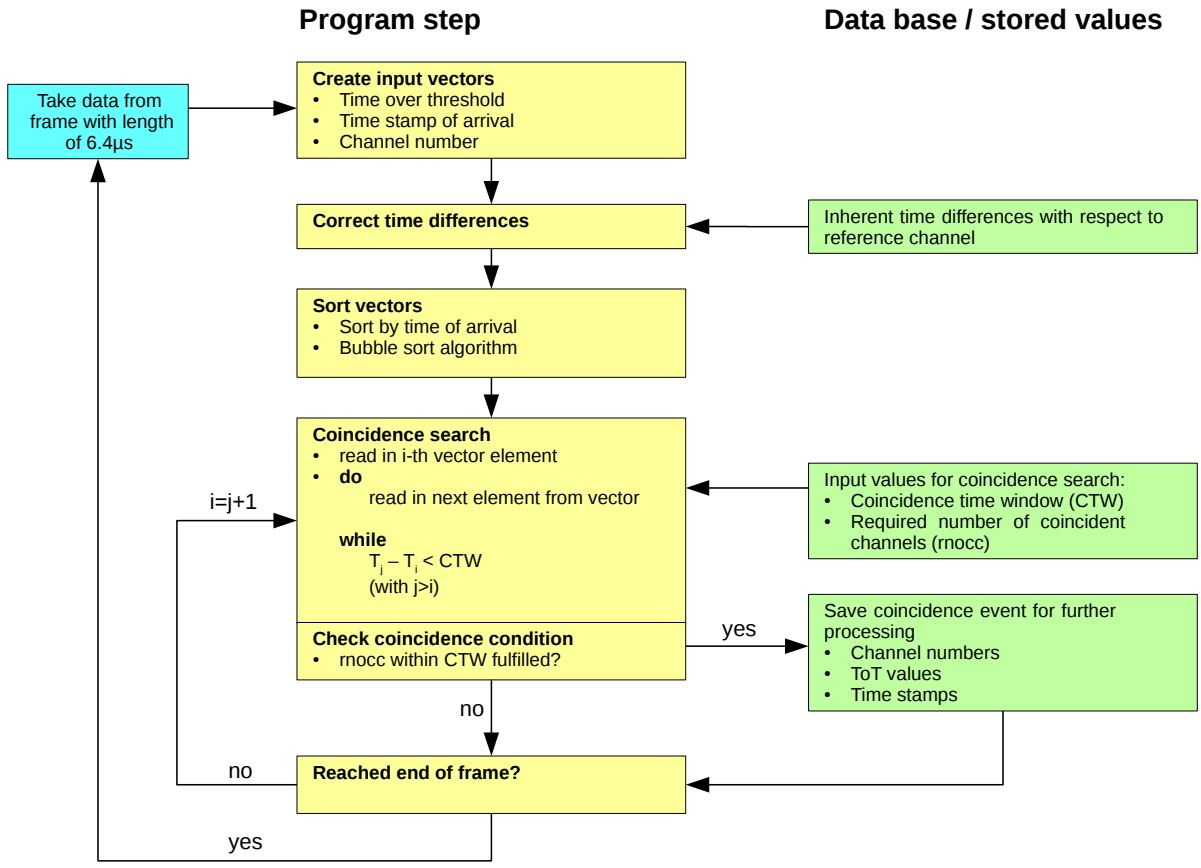

Figure 8.2.: Flow chart describing the coincidence search algorithm in STiC.

signals was not possible. Thus, an off-line coincidence search algorithm was developed using the data analysis framework ROOT [R B96] in the programming language C++. A flow chart with the coincidence search algorithm is depicted in figure 8.2.

The measurement data taken with STiC are stored in frames of a total length of 6.4 μs containing an unsorted list of all signals including the time of arrival, energy (TOT value) and channel number. The first step was to read these events into vectors for further processing. Then, the time stamps of the arrival times had to be corrected for inherent time differences between individual channels. These time differences had to be measured separately and stored in a data base to be used on the analysis. A description of the measurement is given in section 8.1.1.3. Afterwards, the unsorted vector was sorted by increasing time of arrival using a bubble sort algorithm.

Then, the coincidence search was performed. Here, parameters like the coincidence time window (CTW) and the required number of coincident channels (rnocc) were needed, which could be entered at the start of the analysis program. Typical values were on the order of $800 - 1600$ ps for the CTW and 3 for the rnocc. In general, the algorithm started at element i and read in signals from the vector as long as the time difference between the first signal i and the current signal j is smaller or equal to the coincidence time window: $T_j - T_i \leq$CTW.

Once the first signal is further away in time, the coincidence condition is checked: if at least the minimum required number of channels has been read in, the event is considered *a coincident Cherenkov signal* and all important information on the event is stored. That is, energy (saved as TOT value), time stamp and channel number of each signal involved. This information is used later in the program to plot the distribution of coincident hits or to calculate the coincidence time resolution.
After a coincident event with $(j - i + 1)$ coincident channels had been found the algorithm started again with the first element in the vector that was not involved in the latest coincident event: $j+1$. In case the coincidence search did not find a coincidence, the algorithm continued at element $i + 1$. A continuing analysis of the same frame was only performed if there were enough signals available for a potential coincidence. Otherwise the next frame was read in and the algorithm started again.

8.1.1.3. Correction of Inherent Time Differences

The ASIC's TDC provides a time stamp for the time of arrival for every signal above the threshold. However, there are some inherent time differences in the ASIC, resulting in unequal time stamps on different channels even for coincident light signals. These inherent time differences need to be measured and compensated for to obtain optimal coincidence time resolution.
To that end a light source needed to be employed that provided coincident light signals on the channels. Due to its instantaneous nature, Cherenkov light from electrons in a 10 mm thick sample of commercial PMMA was used. The sample had an appropriate thickness such that the Cherenkov cone could also cover the corners of the array.
A measurement of 180 s was performed. Then, one fixed reference channel was chosen, which in this case was channel 3. For every other channel i a histogram with the time difference $T_i - T_{ref}$ with respect to this reference channel was created. The mean value of a gauss fit was taken as the inherent time difference of channel i with respect to the reference channel. Figure 8.3 shows an example of the measured time differences of one channel with respect to the reference channel. The mean value for this channel was at 183.1 ps, with a sigma of 180.8 ps.
To test the result of this correction under the same conditions, the time differences were measured again and the correction was applied. Figure 8.4 shows the measured time differences for all 16 channels before (in red) and after (blue) the aforementioned correction was applied. For channel 3, no value is shown, as this was the reference channel with a time difference of 0 ps by default. After the correction had been applied, a clear improvement was observed for every channel: the measured time difference after the correction is on the order of the time binning of the TDC, which was 50.2 ps.
Finally, the influence on the coincidence time resolution (CTR) is tested. A measurement under aforementioned conditions was taken for a period of 180 s and the CTR was calculated. It is here defined as the average time difference of every coincident channel with respect to the first channel involved in that coincident event. A histogram of these time differences is shown in figure 8.5. The same set of data was analyzed with and without applying the time difference correction. The CTR for this measurement was found to be 374 ps without the correction of inherent time differences, while applying this correction gave a value of 271 ps. This constitutes an improvement of 27.5 %.

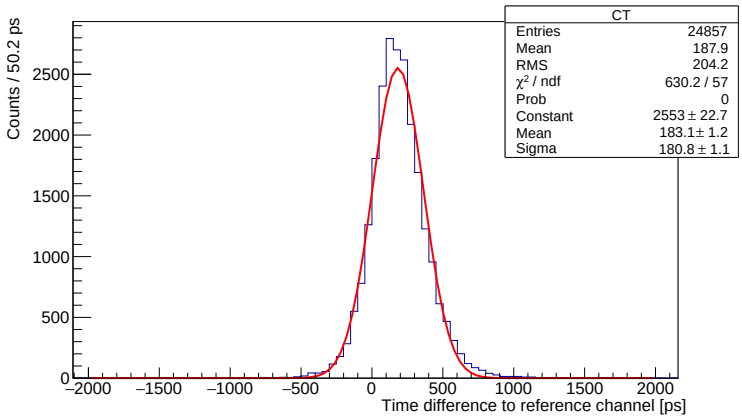

Figure 8.3.: Example of a time difference histogram between channel 0 and reference channel 3. The mean value is taken as inherent time difference between these two channels.

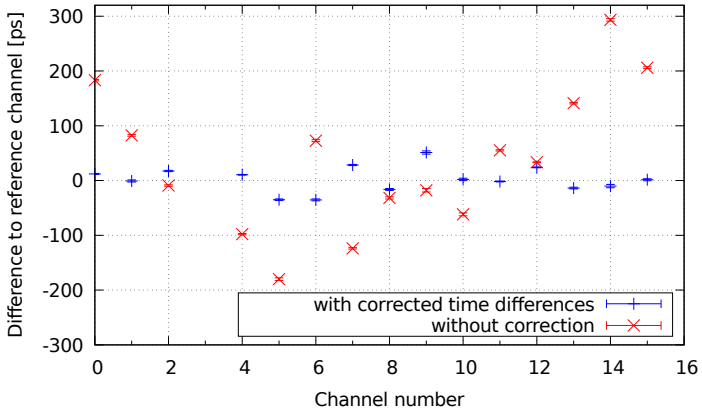

Figure 8.4.: Inherent time differences of all channels with respect to reference channel 3 with (blue) and without (red) correction. After the correction has been applied, the time differences were on the order of the ASIC's time binning (50.2 ps).

8.1.2. Measurements

8.1.2.1. Coincidence Time Resolution

Using the described measurement method and analysis algorithm and employing the time difference correction, the coincidence time resolution (CTR) for the detection of Cherenkov light from electrons in PMMA was measured. The CTR was defined as the average time difference to first trigger. A 10 mm thick sample was used with a cross-sectional area of $15 \times 15\,\mathrm{mm}^2$. The CTW for this and all further analyzed measurements was set to a value of 800 ps. The obtained CTR was 242 ps, which is in good agreement with the timing resolution of 220 ps from characterization measurements for the STiC [YC]. The measurement was repeated for various sample thicknesses. The coincidence time was found to be independent of the thickness of the sample with fluctuations on the order of the bin width of the TDC. For the purpose of comparison, another measurement with a fast scintillator called Polyvinyl

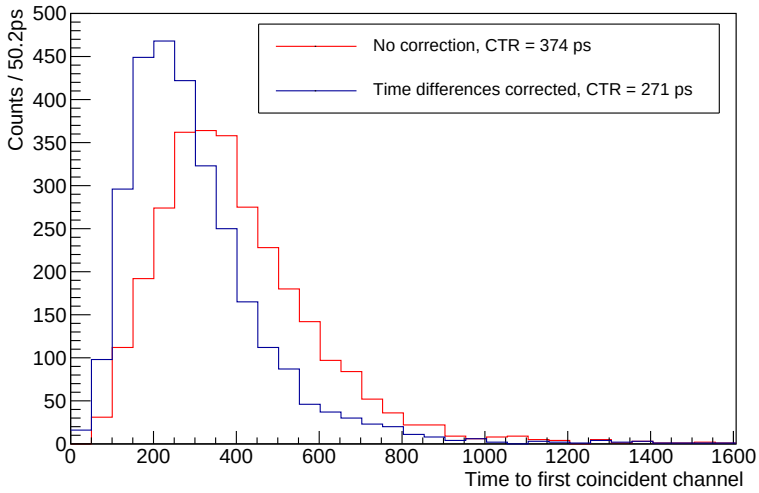

Figure 8.5.: Coincidence time resolution with (blue) and without (red) application of the correction of inherent time differences.

Toluene (PVT) with a decay time constant of 2.1 ns [Rex19] and a thickness of 9.8 mm was conducted. The scintillator material covered all channels of the array. Due to the non-instantaneous emission of light, the distribution is expected to be broader than for PMMA. A CTR of 492 ps was obtained. Figure 8.6 shows the histogram of time differences of every coincident channel with respect to the first channel involved in the event. The blue line represents the measurements with PMMA, while the red curve is the measurement with the scintillator. In some detector channels the signal from the scintillator contains also a small fraction of Cherenkov light, which gives shorter time measurements than scintillation light only. Still, one can make a clear distinction of scintillation light and Cherenkov light judging by the CTR.

8.1.2.2. Distribution of Coincident Photon Hits

The distribution of coincident hits of Cherenkov photons on the 16-channel SiPM array was investigated. To that end PMMA was chosen as radiator material in several different thicknesses between 2.2 mm and 15 mm. The electron source was pointed at the center of the array and data was again taken for 60 s for each thickness. A symmetric Cherenkov cone is expected in the middle of the SiPM array. Figure 8.7 shows the distribution of coincident hits for the example of 2.2 mm, 4.0 mm, 5.9 mm, 7.8 mm and 10 mm. The colors represent the number of occurrences of each channel in a coincident event. As expected, the width of the distribution increases with larger thickness, as the Cherenkov cone spreads out covering more channels. The measurement with the 2.2 mm sample shows mostly hits in the center of the array, while for larger thicknesses, also the outer channels are triggered frequently.

For a second set of measurements, the electron source was moved to the top right corner of the array. Figure 8.8 shows the results. One can see that the measured pattern of coincident hits on the array shifted with the electron source and the channels in the corner were most

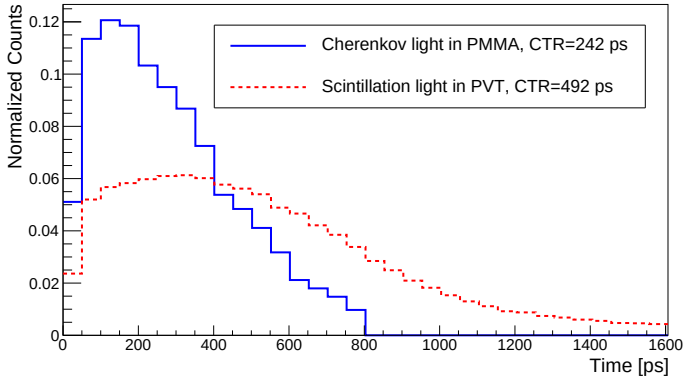

Figure 8.6.: Coincidence time resolution for the detection of Cherenkov light created in a 10 mm sample of PMMA (blue) and for the detection of scintillation light (red) in PVT. A clear distinction can be made between the two detected light signals.

frequently involved in coincidences. Again, increasing thickness of the sample causes the Cherenkov cone to spread out over the array.

Comparison to scintillator measurements:
The distribution of coincident hits over the array can be used to make another clear distinction between scintillation and Cherenkov light: While Cherenkov light is distributed according to the direction of the Cherenkov cone with its characteristic energy-dependent opening angle, scintillation light is emitted isotropically by the incident electron. The latter therefore shows an almost even distribution of hits over the array. This behavior was investigated using the 9.8 mm thick PVT scintillator. The isotropic nature of the emission of scintillation light can be seen in the occupancy plot in figure 8.9.

8.1.2.3. Light Yield Quantification Using Time over Threshold

The Cherenkov light yield on the SiPM array was quantified using the TOT information of the SiPM signal. The TOT of a channel increases with increasing signal height, which again is proportional to the number of photons that were detected by that channel. The step size for the TOT measurement with the STiC read-out was 1.6 ns, which was sufficiently small given an SiPM time constant on the order of 100 ns for the SiPM of type S13361-3075AS.
To measure the intensity of the Cherenkov radiation, the TOT information from each coincident channel per event was summed up. The mean value of the sums from all coincident events was taken as measure for the light intensity in arbitrary units. This procedure was repeated for all available PMMA thicknesses. The obtained TOT mean values allowed to draw conclusions on the number of photons detected for each sample thickness. Arbitrary units were used to quantify the detected light level, since measurement on single photon level was not possible and therefore a calibration for the photon number was not performed with this device. The behavior of the TOT values with changing sample thickness is shown and discussed in section 8.3.1 together with the results from the photon counting method using the oscilloscope.

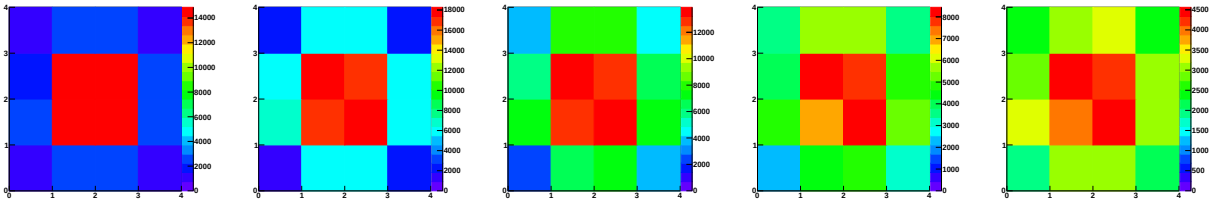

Figure 8.7.: Occupancy of the SiPM array for different PMMA thicknesses. The distribution of coincident hits is shown with the electron source centered above the array. The thicknesses of the PMMA samples were (from left to right): 2.2 mm, 4.0 mm, 5.9 mm, 7.8 mm and 10.0 mm. The Cherenkov cone radius increases with sample thickness.

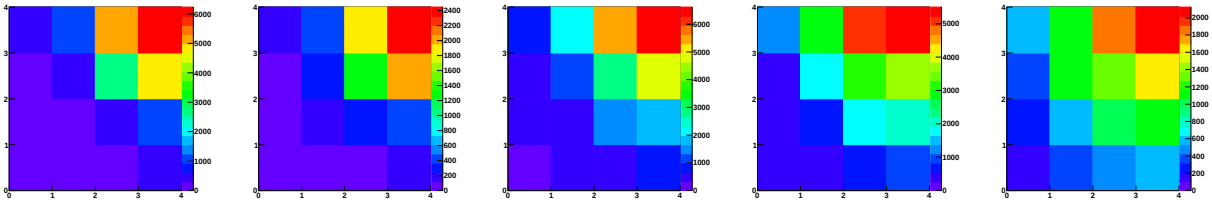

Figure 8.8.: Occupancy of the SiPM array for different PMMA thicknesses. The distribution of coincident hits is shown with the electron source centered above the channel in the top right corner. The measured pattern shifts with the source location. The thicknesses of the PMMA samples were (from left to right): 2.2 mm, 4.0 mm, 5.9 mm, 7.8 mm and 10.0 mm.

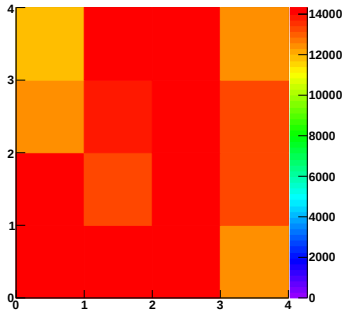

Figure 8.9.: Occupancy of the SiPM array with coincident hits from scintillation signals on 16 channels read out with STiC. The isotropic nature of the emission of scintillation light is represented by the even distribution of coincident photon hits.

8.2. Photon Counting Using Charge Integration

8.2.1. Calibration

The deposited charge in each SiPM channel is proportional to the number of detected photons. This circumstance can be used to count the number of detected Cherenkov photons. Integration of the voltage signal of a channel over a fixed time interval $[t_0, t_1]$ allows for a calculation of the deposited charge as follows

$$Q = \frac{1}{R \cdot G} \int_{t_0}^{t_1} V(t)\,\mathrm{d}t \tag{8.1}$$

where R denotes the resistance creating the voltage drop and G is the gain. The idea for the calibration was to calculate the integral over SiPM waveforms for different signals, corresponding to different p.e. levels. Thus, each obtained integral of a signal can be linked to a number of photons creating that signal and the channels can be calibrated.

Peak Integral Spectra:
Since counting of Cherenkov photons on single photon level was envisaged, low level signals were desired, with only a few photons per channel at a time. To that end, coincident Cherenkov photons created by electrons in a 10 mm sample of PMMA were used. The electron source was centered above the SiPM array, which was biased with 3.8 V overvoltage. Signals from the SiPM array were amplified and read out with the oscilloscope using the set-up described in section 6.3. One fixed trigger channel in the center of the array was chosen with a trigger threshold of 200 mV corresponding to a 3 p.e. level. The channel to be calibrated was only read-out and analyzed when there was a signal on the trigger channel. Thus, mostly coincident Cherenkov light signals were captured and just a small fraction was dark events.
For every triggered signal, the whole waveform of all four channels was saved within a time window ranging from 100 ns before the trigger position until 300 ns after the trigger. The sampling rate was 3.125 GS/s, which equals 320 ps between data points. The area under the waveform (peak integral) was calculated, which according to formula 8.1 was proportional to the number of photons. An integration window of 200 ns was chosen starting at 0 ns (time of trigger). Figure 8.10 explains the procedure on a waveform example. Fluctuations of the baseline cause the peak integral to be under- or overestimated. To compensate for this effect, the mean value of the data points in an interval of 100 ns before the trigger was calculated and used to correct the peak integral.
10000 triggered signals were analyzed that way and a peak integral histogram was created. An example for one channel is shown in figure 8.11. The peak integral value is given in nVs (nano volt seconds) and the bin width is 0.2 nVs. The first peak corresponds to the so called pedestal, which is the 0 p.e. peak, where no photon was detected in that channel. Starting with the second peak and incrementing in integers, each peak represents a number of detected photons.

Calibration:
An algorithm was programmed to find the peaks in the obtained spectrum. A local maximum in the histogram was identified as peak, if its bin had the most entries within an interval of ± 3 bins. Especially at higher bin numbers every local maximum was a real peak in the

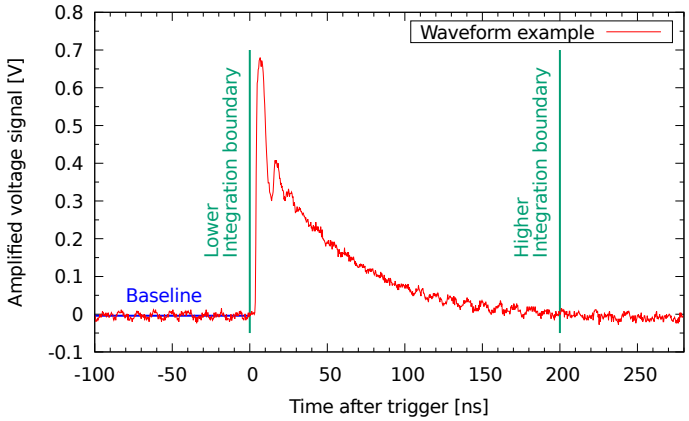

Figure 8.10.: Example of an amplified waveform read-out with the oscilloscope and analyzed with respect to the peak integral. The area under the curve was determined between 0 ns and 200 ns and the baseline was determined to compensate for fluctuations.

spectrum corresponding to a photon number. To not falsely identify a bin as peak, a certain threshold was defined: A bin had to contain more than 1 % of all entries in the histogram, which in the present case equals 100 entries. This rejects all peaks at higher integral values where the spectrum appears to be strongly smeared out.
At least 4 peaks had to be found in the spectrum to proceed with the calibration. A gauss fit in a range of ±3 bins around each valid peak was performed. The mean value of the fit was taken as the peak position. The fit was rejected if the uncertainty on the mean value exceeded half the fit range (i.e. 3.5 times the bin width). The linear relation between the integral value and the number of detected photons was then used to calibrate the channel with a linear fit function:

$$N(A) = s \cdot A + b$$

where the peak integral value is denoted with the letter A. s is the slope of the function in units of $^1/_{\mathrm{nVs}}$ and b is the offset. The graph in figure 8.12 shows the calibration fit function for the peak integral histogram of that same channel. In this case, the fit function for the number of photons $N(A)$ reads

$$N(A) = 0.93\,{}^1/_{\mathrm{nVs}} \cdot A + 0.39$$

This calibration was performed for all 16 channels of the array and the calibration data were used for all following measurements to compute the number of detected photons. The mean slope from the calibration of all channels was $0.91\,{}^1/_{\mathrm{nVs}}$ with a standard deviation of $0.14\,{}^1/_{\mathrm{nVs}}$. The spread of the slopes is shown in figure 8.13. The obtained values lie in an interval between $0.68\,{}^1/_{\mathrm{nVs}}$ and $1.19\,{}^1/_{\mathrm{nVs}}$.

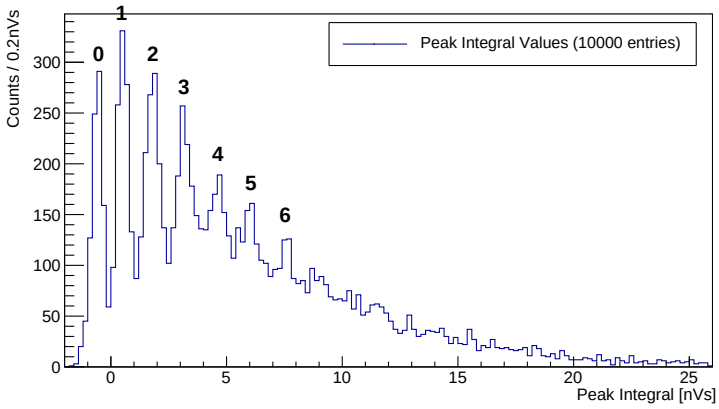

Figure 8.11.: Peak integral spectrum for a single amplified channel measured with an oscilloscope. Each peak corresponds to a number of detected photons.

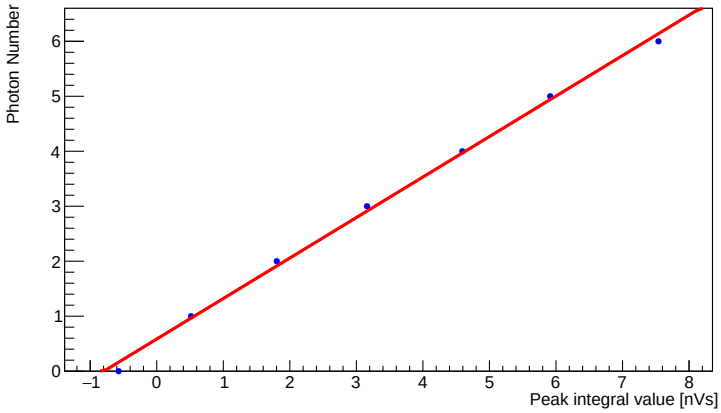

Figure 8.12.: Linear calibration curve converting the measured peak integral into a number of detected photons.

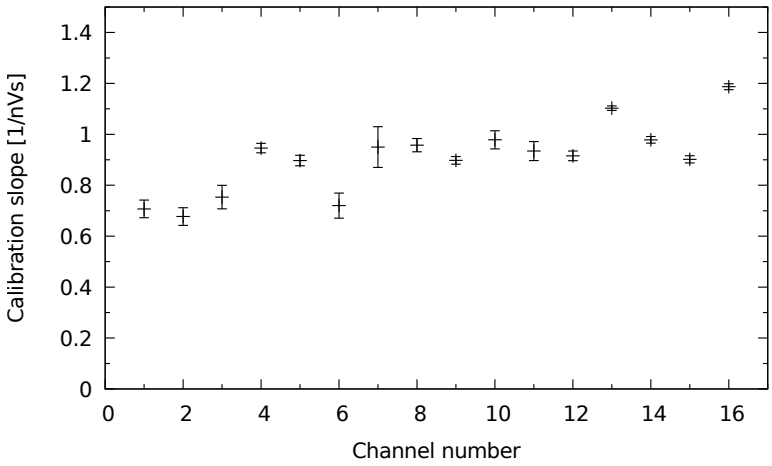

Figure 8.13.: Slope of the calibration curve from all channels of the 16-channel SiPM matrix. A mean value of 0.91 $^1/_{\mathrm{nVs}}$ was found with a standard deviation of 0.14 $^1/_{\mathrm{nVs}}$.

8.2.2. Measurement Procedure

The above described calibration was in the following used in measurements with different sample thicknesses of PMMA between 2.2 mm and 15 mm. The goal was to estimate the average number of detected Cherenkov photons for each thickness. To that end, 4 channels at a time were connected to the scope, one of which was the trigger channel. The trigger level was set to 200 mV. The three non-trigger channels were read-out for 10000 triggered events. Then, the next three channels were read-out leaving the trigger channel unchanged. The read-out channels were consecutively moved over the array until for all channels measurements had been taken. In a last measurement run, a different channel was used as trigger channel and the former trigger channel was read out. Thus, no coincident measurement with all 16 channels at a time was possible, but only the average detected number of photons per channel could be estimated with this method. Figure 8.14 shows the number of detected Cherenkov photons in each channel for a PMMA thickness of 7.8 mm. The electron source was centered above the sample.

The number of detected photons per channel was also measured in darkness. On average, 0.22 photons per channel were detected in 10000 events. Figure 8.15 shows the corresponding color map of coincident signals. Those values were subtracted from the average number of detected photons in the measurements with Cherenkov light in PMMA. The sum of the mean values from all channels was calculated for each sample thickness. The results will be shown in the next section together with the light intensity estimations using the TOT values from the STiC set-up.

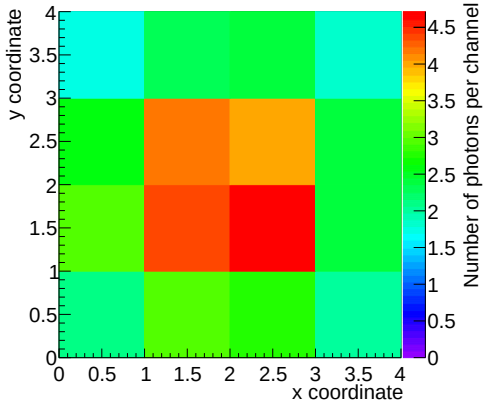

Figure 8.14.: Color map showing the average number of Cherenkov photons detected by each SiPM channel. The channels were read out in a consecutive manner with 3 channels at a time and a fixed trigger channel.

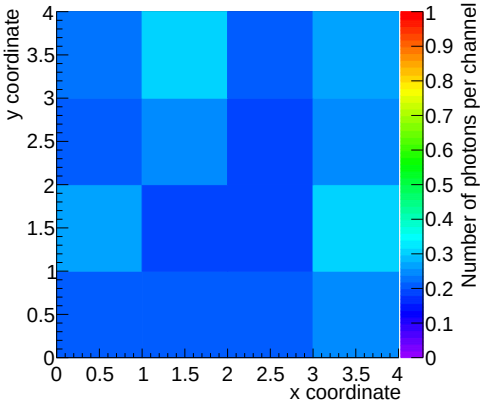

Figure 8.15.: Color map for a dark count measurement showing the average number of photons detected on average. Dark measurements were performed in the same way as the ones with electron source.

8.3. Results

The results presented in this section have also been published in [Bay+19a].

8.3.1. Measured Light Intensity and Number of Detected Photons

The results of the measurements described in section 8.2.2 are showns in figure 8.16 for all sample thicknesses. In that graph, the number of detected photons is compared to the light yield quantification using TOT information from the STiC measurements. A comparison to calculated values is shown as well and will be discussed later in this section. A list of all results can be found in table 8.1.

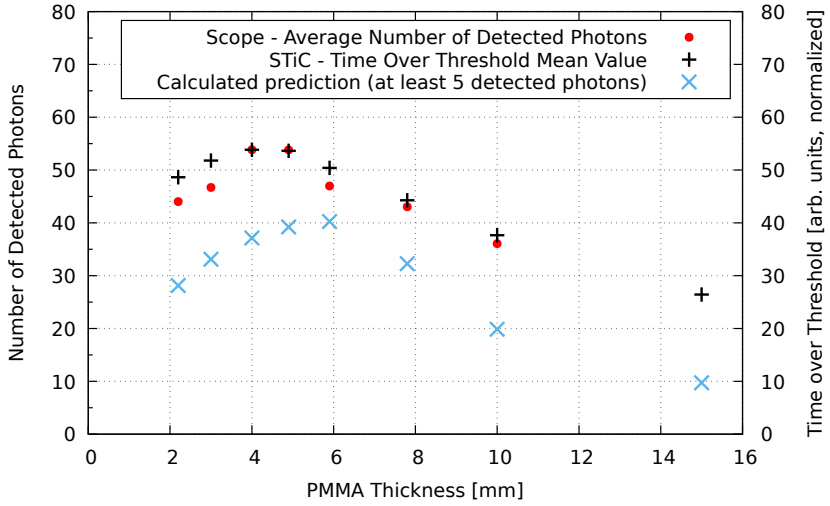

Figure 8.16.: Measured light intensity quantified with the TOT values from the STiC and detected number of photons measured with the oscilloscope. A comparison to calculations is shown, which only considers events with at least 5 detected photons.

In the graph, one can see the number of detected photons increasing with growing sample thickness, forming a plateau-like structure at 4–5 mm before a decline occurs above 5.9 mm. In the lower range the dominating effect is the limited electron range determined by the thickness of the PMMA, resulting in a reduction of the Cherenkov light yield. For the higher energetic fraction of electrons, this causes the Cherenkov effect to terminate before the Cherenkov energy threshold is reached. Therefore, the light yield is reduced. The thicker the sample, the less dominant is this reduction, which explains the increasing number of detected photons between 2.2 mm and 4.0 mm.
For larger thicknesses, a different process is responsible for the decrease in the number of detected photons. The maximum Cherenkov cone opening angle in PMMA is 47.8°. This means, above a certain thickness, the cone will exceed the boundaries of the SiPM array and photons will be lost for detection. The side length of the sensitive area of the array is 12.6 mm (compare figure 6.7), which implies that above a calculated thickness of 5.7 mm for the absorber the number of detected photons starts to decrease again. In reality, this effect is already visible at slightly smaller thicknesses due to multiple scattering.

The same behavior can be reproduced by the Time over Threshold measurements with STiC. As figure 8.16 indicates, the value increases for smaller thicknesses and starts dropping again for all samples thicker than about 5.7 mm.

The TOT measurement was also performed for a 5.5 mm thick sample of TPX RT18. The refractive index n, which is a key quantity for the number of created Cherenkov photons, was 1.46 and therefore smaller than in PMMA (1.49). This could reduce the number of detected photons. However, the influence of this change in refractive index is on the order of a few percent only: for example, for a 1.5 MeV electron in a material with $n = 1.49$ about 928 photons are created per centimeter traveled distance and for $n = 1.46$ the Cherenkov light yield is 894 photons per centimeter. This constitutes a reduction of the number of emitted photons of only 3.7 %. The higher transmission in the near UV range below 400 nm has much greater influence (see section 6.5) and an increase in the detected light intensity is expected. The TOT measurement revealed a light level 30.1 % higher compared to the one from the 5.9 mm sample of PMMA. Within the uncertainties of the measurements, this denoted a significant increase.

Comparison to theoretical expectations:
The measurement results were compared to the expected number of detected photons obtained with the calculation algorithm introduced in chapter 7. Both measurement types introduce a certain threshold on the number of detected photons (in case of the oscilloscope read-out) or number of coincident channels (in case of STiC). Therefore, in the calculation only those electron energies were taken into account for which at least 5 detected photons – not including cross talk or after pulses – were expected. The exact trigger threshold in both devices was unknown, and the choice of a minimum of 5 photons in the calculation was rather random and served the purpose of qualitative comparison.

The qualitative behavior of the measurement and calculation is the same: An increasing number of detected photons is observed in the range up to a thickness of 5.9 mm. Also, the decreasing number of photons is reproduced in the calculated prediction for thicknesses above 5.9 mm.

Absolute numbers, however, deviate significantly: while only 37.1 detected photons were calculated for a thickness of 4 mm, in the actual measurement 53.8 photons were detected. The most important contribution to this deviation originates in the threshold of the trigger channel. The trigger threshold was set above the level of 2 photons, in order to reduce the contribution of dark signals to the measurement. At this level the dark count rate is reduced by about two orders of magnitude. The trigger threshold induces a significant bias on the detection: Lower energetic electrons, producing a small number of photons, are less likely to be detected.

The electron energy spectrum of ^{90}Sr (figure 6.1) shows a strongly increased intensity towards smaller electron energies where fewer photons are generated. Therefore, in the calculation these energies have a large contribution to the average number of detected photons, while in the measurement these events are most likely not triggered.

Multiple scattering of the electrons, constitutes another reason for the discrepancy. It effectively changes the total range of the electron until being stopped by the SiPM's surface. Since according to equation 2.20 the number of emitted photons depends on the traveled distance of the electron, scattering also influences the number of detected photons. While

Material	Thickness	Number of Detected Photons	Time over Threshold
PMMA	2.2 mm	44.0 ± 0.4	48.6 ± 0.3
	3.0 mm	46.7 ± 0.5	51.8 ± 0.3
	4.0 mm	53.8 ± 0.5	53.8 ± 0.3
	4.9 mm	53.8 ± 0.5	53.7 ± 0.3
	5.9 mm	47.0 ± 0.5	50.4 ± 0.3
	7.8 mm	43.1 ± 0.4	44.3 ± 0.3
	10.0 mm	36.1 ± 0.4	37.7 ± 0.4
	15.0 mm	–	26.5 ± 0.7
TPX	6 mm	–	65.6 ± 0.4

Table 8.1.: Results for the detected number of Cherenkov photons from electrons in PMMA and TPX RT18 measured with the oscilloscope set-up together with the corresponding Time over Threshold values from measurements using the STiC.

in the calculation algorithm the range was used as given by the NIST data base, the actual track length in the measurement can fluctuate.

Furthermore, subsequent to the scattering of the electron the Cherenkov cone gets deflected and some fraction of emitted Cherenkov photons will not reach the active area of the detector, unless reflected from the side walls of the radiator sample. This fraction of lost photons could not be estimated with the calculation algorithm.

The degree of multiple scattering is strongly dependent on β and, thus, also on the energy of the electron, as could be demonstrated in section 2.1.3 in figure 2.8. Multiple scattering therefore affects especially electrons from the lower end of the spectrum and these energies hold the major contribution to the strontium spectrum. However, the number of photons created in that energy range is lower than for higher energies.

The influence of after pulses was not taken into account in the calculation, which is another explanation for higher photon numbers in the measurement compared to the calculations.

Finally, the statistical nature of the emission of Cherenkov light regarding photon number and wavelength as well as its distribution over the channel matrix in each event limit the accuracy of the calculation. Also, the surface properties and therefore also the reflection behavior of the surface of PMMA is unknown. Geant4 simualtions are required to create more precise predictions on the outcome of the measurements. They have been performed in the scope of a master thesis and will be presented and compared to measurement results in chapters 10.2 and 11.3.

8.3.2. Quantification of the Occupancy of the Detector Array

Additional to the number of detected photons, the radius of the intersection between the Cherenkov cone and the detector's surface changes with radiator thickness as well. This behavior has already been demonstrated graphically in the color maps of figures 8.7 and 8.8.

This implies that the width of the distribution of the photons over the array increases with thickness. This sample-dependent width was quantified as follows:
A two-dimensional gauss fit was applied to the data from the centered electron source position. The width of the distribution was then described using the fit parameter σ. Since the fit was chosen to be symmetric, the σ-parameter was the same in x- and y-direction. Also, since the source position was defined by the set-up the mean value was fixed as well and not used as fit parameter. Figure 8.17 shows the results of this analysis technique for different thicknesses of PMMA. Especially for a thickness of 15 mm the coarseness of the sampling with only 16 channels causes enhanced uncertainties. Nevertheless, the expected behavior for a continuous increase of the width with growing thickness could be reproduced.
In comparison to PMMA a sample of TPX RT18 with a thickness of 5.5 mm was used. A PMMA thickness of 5.9 mm was chosen for this comparison. For PMMA the σ-parameter was (4.56 ± 0.03) mm and TPX showed a value of (4.27 ± 0.02) mm. The difference in refractive index of TPX (1.46) compared to PMMA (1.49) causes the opening angle of the Cherenkov cone to be smaller inside the TPX sample according to equation 2.12. In PMMA a maximum opening angle of 47.8° is calculated, while in TPX the angle is 46.8°. The different opening angle and the fact that the TPX sample was thinner by 0.4 mm than the PMMA sample explains why the σ-parameter for TPX was found to be smaller than for PMMA.

8.3.3. Reconstruction of the Electron Source Location from Accumulated Events

The electron source was moved towards different positions using the step motor with sub-μm position resolution. The position was noted and data was taken in the same way as before using STiC with 60 s of measurement time. A gauss fit was applied to the two-dimensional histogram of the occupancy of the channels with the goal to reconstruct the mean value. Unlike in the previous section the mean values in x- and y-direction were not fixed anymore and rather used for a reconstruction of the various source locations. The results are shown in figure 8.18. A precise calculation of the source location was possible with an accuracy on the order of 1 mm, which is mainly influenced by the diameter of the source collimator of 1 mm. This result successfully demonstrates a spatial sensitivity for the electron source location using an accumulation of coincident Cherenkov photons.

8.4. Conclusion on the Proof of Principle

The first test set-up consisting of an electron source, a radiator material and a 16-channel SiPM array served the purpose of demonstrating the ability to detect Cherenkov photons in coincidence. The fast nature of Cherenkov light emission could be probed: using an ASIC based read-out a sub-nanosecond coincidence time resolution of 242 ps was achieved promising good applicability to medical imaging techniques like a CC. The distribution of coincident hits on the array was in good agreement with expectations and a sensitivity to the electron source location could be demonstrated using accumulated events. The number of detected photons could be counted using a 4 GHz oscilloscope and employing a charge-integrating analysis method. The number of photons yields information on the electron energy and plays an essential role in the reconstruction of the energy of a higher energetic gamma in a

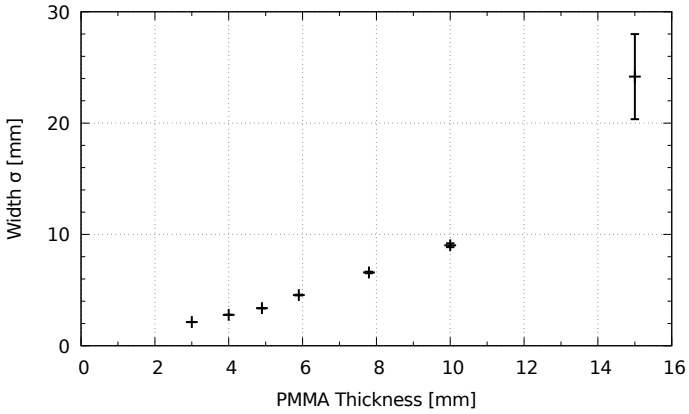

Figure 8.17.: Width of the Distribution of Cherenkov photons shown for various PMMA sample thicknesses. The sigma parameter of a two dimensional gauss fit to the distribution of coincident hits was used to parameterize the width.

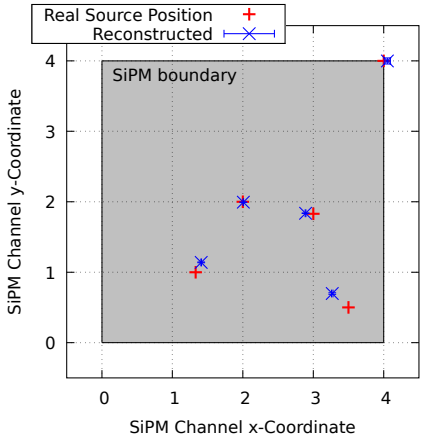

Figure 8.18.: Reconstructed electron source positions from accumulated events. An accuracy on the order of 1 mm was achieved.

Compton camera. These achievements constitute a first qualitative proof of the detection principle for electrons using Cherenkov light.
However, no Cherenkov light detection on single photon level was possible with either of the two set-ups discussed in this chapter. STiC did not allow for a TOT measurement on single photon level and with the oscilloscope the trigger channel had to be set to a level above 1 p.e. to minimize contributions of dark events.

To be able to apply this principle to the detection of Compton electrons and to reconstruct the scattering vertex, individual events need to be investigated. Larger arrays with more channels are required and the possibility of coincident detection and photon counting needs to be incorporated into one system. The next chapter 9 introduces such an improved detection modality including cooled detectors for reduced dark contribution, UV transparent PMMA samples for higher light yield and the ability to read out 64 channels at a time while counting the number of detected photons per channel starting on 1 p.e. level.

9. Improved Set-Up Using TOFPET2-ASIC

Contents

9.1 Design of the Set-Up **146**
9.1.1 Overview 146
9.1.2 Radiator Materials 147
9.1.3 Cooling System 147
9.1.4 Assembling 148
9.2 Signal Read-Out Using the PETsys TOFPET2-ASIC **149**
9.2.1 Technical Layout and Design 149
9.2.2 The TOFPET2 ASIC 151
9.2.3 Configuration, Calibration and Data Processing 151
9.3 Commissioning **152**
9.3.1 Threshold Setting 152
9.3.2 Characteristics of the Acquisition System at Low Temperatures . 153

The two set-ups presented in the previous part had significant disadvantages: while a coincidence measurement on 16 channels was possible with the STiC, no photon counting could be performed due to the TDC's lack of sensitivity on single photon level. Moreover, high dark count rate at room temperature limits the detectable signal rate and eventually overwhelms the read-out electronics. In case of the oscilloscope set-up, where photon counting was possible, only four channels at a time could be read out. In general, the resolution of the coincidence pattern on 16 channels is very limited and more detector channels would be beneficial.

The improved set-up described in this chapter attempts to provide solutions for the aforementioned drawbacks: a coincidence measurement on 64 SiPM channels was implemented using the TOFPET2 ASIC by PETsys Electronics. The SiPM array was cooled below zero degrees to significantly reduce the dark count rate. Photon counting beginning on 1 p.e. level was performed using the signal's TOT information.

This chapter will provide details on the set-up and its components. The TOFPET2 ASIC and the PETsys SiPM read-out system will be introduced together with investigations regarding the reduced DCR and the triggering possibility on single photon level.

9.1. Design of the Set-Up

9.1.1. Overview

The very basic principle of this measurement set-up is unchanged compared to the former ones: an electron source (^{90}Sr) is pointed at an optically transparent radiator material to create Cherenkov photons, which are detected by an array of SiPMs. However, some significant improvements were implemented, which are shown and explained in figure 9.1.
First of all, a larger SiPM array was used. In fact, four 16-channel arrays of type S13361-3075AS by Hamamatsu were placed next to one another to form one large 8×8 array. There was a 0.5 mm wide gap in between the four arrays, so that the total side length of the detector matrix was 26.5 mm. The signals were read out using the PETsys SiPM read-out system. This system is based on the high performance TOFPET2-ASIC optimized for processing SiPM signals in TOF PET applications [PET18d]. It sits on the Front End Module (FEM), which acts as interface between the SiPM signals and the digital read-out chain. A second board called Front End Board type D (FEB/D) is equipped with a field programmable gate array (FPGA), collects the data from the FEM and provides the link to the acquisition computer.
The PETsys system allowed for a coincident signal read-out from all 64 channels at a time and provided a trigger on single photon level. Furthermore, the TOT information of the signal could be used to calibrate each detector channel to enable photon counting (see chapter 11 for further explanations on this photon counting method). Details on the read-out system will be given in section 9.2.

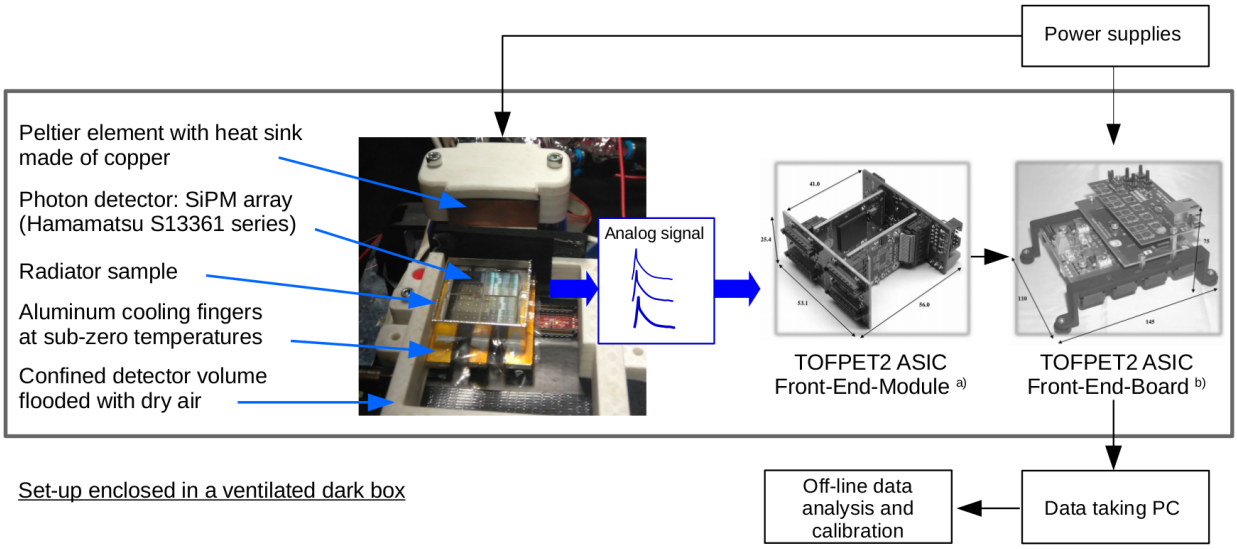

Figure 9.1.: General set-up design consisting of the 64-channel detector array with a radiator sample on top of it, a cooling system with a Peltier element and the ASIC-based read-out system. [a)] [PET18d], [b)] [PET18c].

Like the set-ups before, this improved system was placed inside a large ventilated dark box. Data was taken with a Linux-based computer and analyzed off-line to search for coincidences,

to compute photon numbers and to perform further analyses. The analysis procedure is described in section 10.1.

9.1.2. Radiator Materials

Due to its promising transmission properties, UV transparent PMMA was used for the measurements. This material type is transparent for photons from the UV spectrum down to a wavelength of about 260 nm. Figure 9.2 shows the wavelength dependent transparency of UV transparent PMMA together with the SiPM detection efficiency. In the same graph, the calculated number of generated and detected Cherenkov photons per 5 nm wavelength interval is depicted for an electron with an energy of 1.5 MeV creating Cherenkov light inside a 10 mm thick sample. An overvoltage of 4 V was chosen for the estimation. A similar graph has been shown in chapter 7 (figure 7.4) regarding commercial PMMA. One can see that for measurements with this radiator type, the limiting factor will be the PDE of the SiPM, which cuts off at 270 nm. For this example, calculations predict 504 created and 116 detected Cherenkov photons. The dimension of all radiator samples employed in the measurements were $35 \times 35\,\mathrm{mm}^2$. Different sample thicknesses were used and compared.

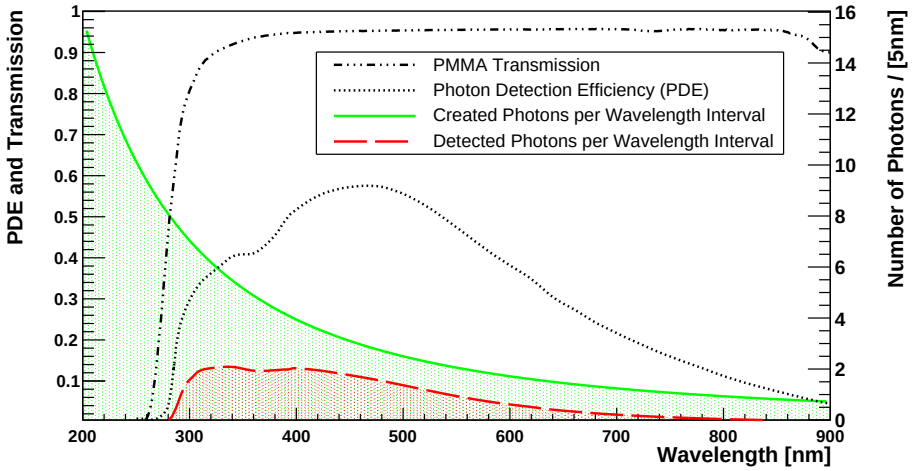

Figure 9.2.: Theoretical estimations of the number of detected Cherenkov photons (red dashed curve) from a 1.5 MeV electron in a UV transparent PMMA sample of 10 mm thickness. Wavelength-dependent transmission and PDE are shown as dashed and dotted curves, respectively. The solid green curve shows the number of generated Cherenkov photons per 5 nm wavelength interval.

9.1.3. Cooling System

An essential improvement compared to former set-ups was the implementation of a cooling system for the detector. To that end, aluminum cooling fingers were placed underneath the array. The aluminum fingers were coupled to a the cold side of a Peltier element. A maximum temperature difference of 65°C between hot and cold side was possible. The Peltier was operated at a voltage of 12 V with a current uptake of 8.5 A. The hot side of the Peltier

element was connected to a copper body, which was itself cooled by water being pumped through it. At the cooling finger, temperatures below zero degrees were measured using a platinum measuring resistor Pt-100. The temperature of the SiPM array might have differed from the value measured with the Pt-100 due to a difference in thermal coupling to the cooling finger: the Pt-100 was pressed onto the finger with a thin layer of heat sink compound in between, whereas the thermal connectivity to the SiPM was provided using the thermally conductive gap filler material SARCON 150X-Pe by Fujipoly. Uncertainties on the SiPM temperature of several degrees Celsius have to be assumed. For an uncertainty of $\Delta T = 10°\mathrm{C}$, the uncertainty on the breakdown point – and consequently the overvoltage – is 540 mV.

Due to negative temperatures, the detector array, radiator sample and cooling fingers were placed inside a small confined volume flooded with dry air. This was necessary to not freeze water from the air on the detectors, which would eventually cause severe damage to both detector and read-out device located underneath.

With this cooled system the dark count rate (DCR) of the SiPM channels could be reduced by at least one order of magnitude. At room temperature a DCR of more than 500 kcps was measured per channel at an overvoltage of $V_{\mathrm{over}} = 4\,\mathrm{V}$. In the cooled system, the rate dropped to values on the order of 60 kcps. A deviation in rate between individual channels originates from non-uniform cooling. Some channels are closer to the cooling fingers than others and also the quality of the thermal coupling might vary throughout the array. Nevertheless, cooling enabled to trigger on single photon level without overwhelming the read-out electronics with dark count or slowing down the analysis process. This is investigated further in section 9.3.2.

9.1.4. Assembling

Figure 9.3 gives some impression on the assembling process of the new improved set-up. The first picture shows the 4 SiPM arrays plugged into a connector board, which then feeds the channels into the front end module of the PETsys read-out system. The front end module consists of 4 PCBs housing the connector for signal input, the ASIC and a pre-processing unit transferring the data to the front-end board with an FPGA. In the set-up, the module is located below the cooling fingers. In the second picture of figure 9.3 the cooling fingers can be seen, which lie between the connectors. The ASIC was covered in thin plastic foil to prevent contamination with thermally conductive gap-filler or optical grease. The cooling fingers themselves were wrapped in insulating Teflon foil to prevent short-circuiting the SiPM channels. Picture 3 shows the 4 arrays after they have been plugged into the connectors. The gray material is the thermally conductive gap filler. Another layer of thin plastic between SiPM array and gap filler was used for protection.
Finally, picture 4 shows the whole assembled set-up including the electron source sitting on a cantilever mounted to the step-motor that has already been used in the previous measurements. The holder for the Peltier element and the copper and aluminum parts has green color in pictures 1, 2 and 3 but appears in white in picture 4. They are in fact identical 3D-printed parts that got damaged at some point and needed to be replaced explaining the change of color. The dry-air flooded detector volume can be seen as a closed box covered with black tape to prevent light pollution during measurements. To further improve the

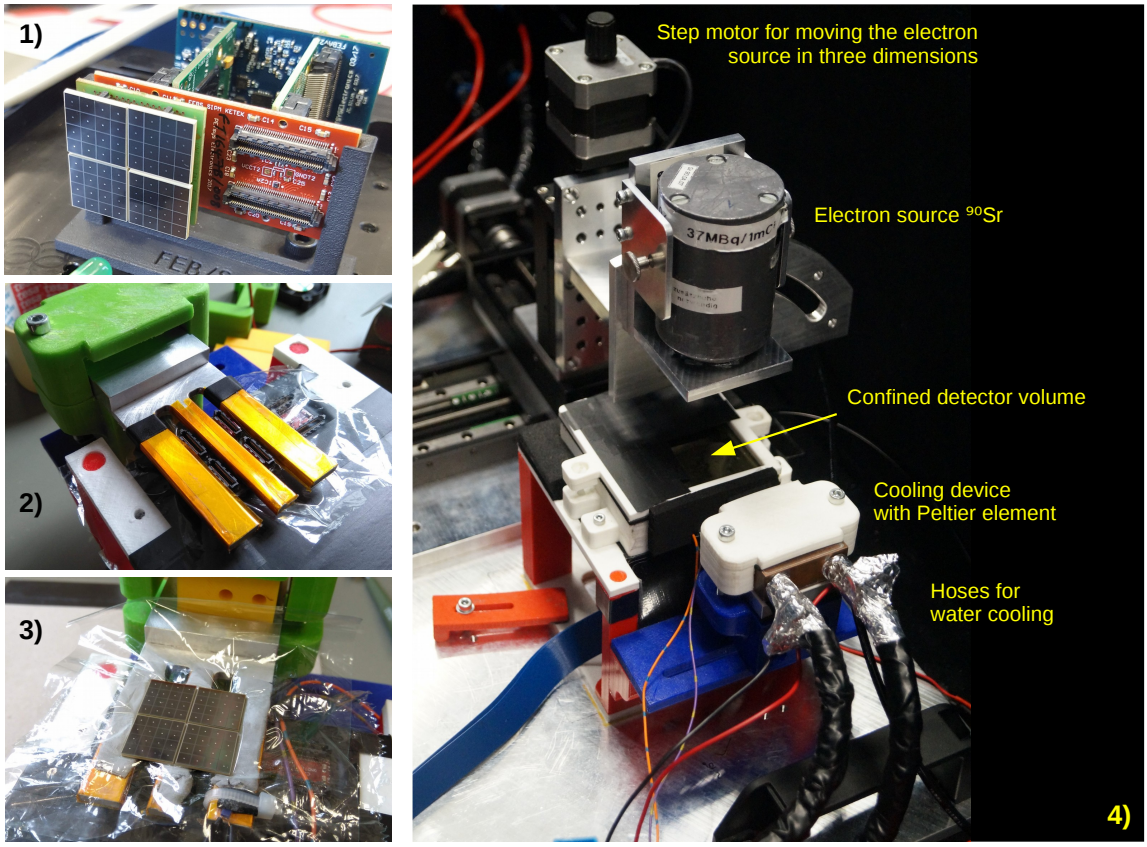

Figure 9.3.: Assembling of the improved PETsys-based set-up including an overall view. **1)** The four 16-channel SiPMs connected to the PETsys front-end board housing the ASIC. **2)** Aluminum cooling fingers between the connectors of the array. Thin plastic foil is used to prevent thermally conductive gap-filler or optical grease from contaminating the ASIC-board below. **3)** SiPM array plugged into the connectors and coupled to the cooling fingers using thermoelastic gap filler. **4)** Overall view of the set-up containing a step motor and the electron source.

shielding from external light, the side walls of the PMMA sample were covered with black tape and a piece of thin black foil was placed on top of the sample. Electrons were able to penetrate the foil with negligible energy loss.

9.2. Signal Read-Out Using the PETsys TOFPET2-ASIC

9.2.1. Technical Layout and Design

The PETsys SiPM read-out system is designed for high data rates and excellent timing as required for signal read-out in TOF PET applications. The center piece of the readout system is the High Performance TOFPET2 ASIC with a TDC module for each detector channel. The ASIC will be outlined in section 9.2.2. The system uses a modular design, which allows to build scalable data acquisition systems for tens of thousands of detector channels. The technical layout comprises an Front End Module (FEM) housing SiPM and

ASIC and a Front End Board type D (FEB/D) with an FPGA as communication and data transfer unit. The two devices are shown in figure 9.4 and 9.5, respectively, and will be briefly introduced below.

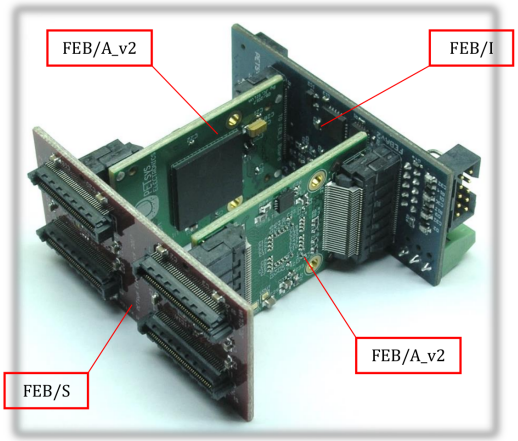

Figure 9.4.: Front End Module (FEM) of the PETsys read-out system with the interface board (FEB/I), two ASIC boards (FEB/A) and a passive connector board for the SiPM (FEB/S). [PET18d]

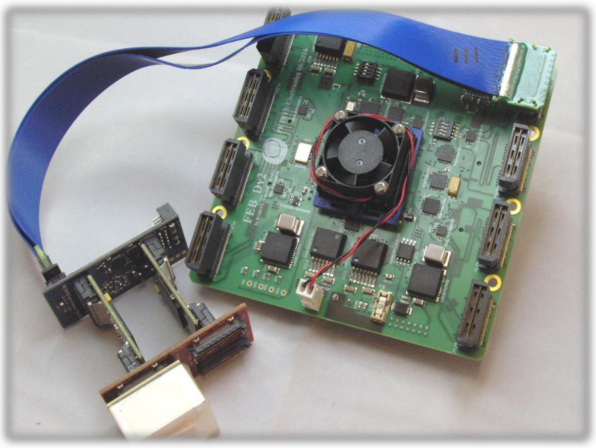

Figure 9.5.: Front End Board type D (FEB/D) of the PETsys read-out system with an FEM connected to it. It serves as data collection and communication unit between ASIC and DAQ unit. [PET18a]

Front End Module (FEM):
The FEM (figure 9.4) constitutes the interface between the analog signals from the SiPM and the digital read-out chain. It consists of three boards:

- FEB/S: This is a passive board, which serves as connector between the analog output of the SiPM channels and the input stages of the ASIC. This board can be specifically designed to match the individual application and can, therefore, be different for different SiPM arrays in use.
- FEB/A: There are two boards of this kind, each of which can carry an ASIC with 64 channels. So, an FEM can have up to 128 channels in total.
- FEB/I: This is the interface unit managing the data transfer and the communication with the FPGA on the FEB/D.

Temperature sensors on the FEB/A board could be used to supervise the temperature progression during the measurements. A warmed up system during operation would show an ASIC temperature between 30°C and 34°C. A ventilator close to the FEM prevents a further temperatures increase.

Front End Board type D (FEB/D):
The FEB/D houses a Kintex 7 FPGA, which implements the communication logic necessary to configure the ASIC and it provides the low jitter reference clock for the TDC with 200 MHz frequency. The FEB/D provides the power for the ASIC and the SiPM using a high voltage

digital-to-analog converter (HV DAQ). It furthermore implements the data read-out and transfer to the DAQ unit, which in this case is a Linux-based laptop. The FEB/D collects data from up to 8 FEMs, meaning it could process signals from up to 1024 channels. Its maximum output rate is 10^8 events per second. There is an option to scale the system up by connecting several FEB/Ds to a central DAQ board to increase the number of channels. In the scope of this thesis the use of one FEB/D was sufficient.
[PET18c; PET18d]

9.2.2. The TOFPET2 ASIC

The TOFPET2 ASIC is a low power, low noise read-out and digitization ASIC. Each channel has its own quad-buffered, analog interpolation TDC and a charge integration analog-to-digital converter (ADC), the latter of which was not used in this work. The TDC time binning is 30 ps.
Every incoming signal from the SiPM is amplified using a transimpedance amplifier. This type of amplifier is used to convert a current signal into a positive voltage signal [HH89]. The gain of the amplifier is thereby determined by the transimpedance resistor, or feedback resistor, R_f. The maximum transimpedance gain of the amplifier in this ASIC is given as $R_f = 3000\,\Omega$.
The ASIC has three different trigger thresholds: a low trigger for optimal timing, a second trigger for rejection of dark count and a third one for accepting an event and computing an "energy" value of the signal. This value is computed either as the integrated charge or the Time over Threshold (TOT) of the signal and, thus, is not a real energy value. However, the TOT or charge value can be used as a measure of the energy of the particle incident in a scintillator in the case of PET applications, which the TOFPET2 ASIC is often used for. The user can choose before each measurement whether TOT or charge is to be saved in the measurement. Every time a signal exceeds the threshold of a channel a record is created containing energy, time stamp and channel number. The trigger thresholds can be set for each channel individually, while only one bias voltage can be set for the SiPM array as a whole. A signal triggered on one channel does not cause dead time on the rest of the channels. However, after a channel has been triggered, it requires roughly 100 ns until it can detect further signals [Lui19]. The maximum hit rate per channel that the ASIC can process is 480 kcps.
[PET18b]

9.2.3. Configuration, Calibration and Data Processing

Configuration:
Before a measurement could be performed, the configuration had to be sent to the ASIC. This includes the bias voltage for the detector, the DAC values for the trigger thresholds and the step size of the discriminator.

Calibration:
To enable correct functionality of the read-out system the discriminators and the TDCs needed to be calibrated. PETsys provides calibration routines that have to be carried out

before the system is operable. The discriminator is calibrated by a scan of the discriminator levels with disabled bias in order to determine noise level and base line. This routine also performs a dark count scan with biased SiPM that helps find the 1 p.e. level (see section 9.3.1).
For a correction of the non-linearity in the correspondence between TDC codes and reference clock phase, a TDC calibration was performed. This routine sends internal test pulses to the ASIC to trigger the TDCs at different phases relative to the reference clock. The data is used to find a calibration function to map TDC codes and time.

Data Processing:
In the raw data of a measurement the arrival of a signal does not have the correct time stamp in seconds, but only the measured value by the TDC in DAC units. Thus, after every measurement, the TDC values of the events needed to be converted to time based on the functions obtained from the TDC calibration of each channel. PETsys provides processing applications to perform this conversion. It has been observed that this conversion process can take up 7 times as long as the measurement itself depending on the event rate. Pre-processing actions can be applied during this data conversion, like coincidence search between different ASICs or saving data in frames with a fixed length rather than as a list of all events from the measurement.
[PET18e]

For the measurements with the electron source, the so called raw-to-group application was chosen, which groups two or more events from different channels together in one frame if they occurred within 100 ns. The data were saved in a ROOT tree for further analysis, especially for the coincidence search.

9.3. Commissioning

9.3.1. Threshold Setting

The first step of the commissioning of the read-out system was to find the correct discriminator DAC value for every channel that corresponds to the 1 p.e. level. This procedure is described hereafter.
As mentioned above, PETsys provides a discriminator calibration procedure that scans the whole DAC range of the lowest trigger threshold in darkness and determines the base line for each channel. Furthermore, the program calculates the DCR for each discriminator step. The DAC values are inverted, so that a higher digital value corresponds to a lower physical threshold and vice versa. Therefore, the dark count rate increases for increasing DAC value due to a decreasing physical threshold. An example of such a scan is shown in figure 9.6 where for one channel the DCR is plotted against the discriminator DAC value. The steps in the graph occur whenever the threshold exceeds the amplitude of the signal corresponding to a certain photon number. Often this type of graph is referred to as *staircase function*. The first plateau corresponds to the 1 p.e. signals. In this graph the results for two different discriminator step sizes are plotted. The step size DAC value is given in least significant bit (LSB) units. An LSB value of 57 corresponds to a step size of 5.0 mV and an LSB of

60 corresponds to 2.5 mV. PETsys Electronics obtained these values by simulating the ASIC, not through an analytical expression [Lui20]. With a larger discriminator step size, the edges in the staircase function are drawn closer together, while the measured DCR remains unchanged. The 1 p.e. level can be best found by using a large LSB, thus a value of LSB=60 was used.
The goal was to set the threshold to a value at the 1 p.e. plateau. To that end a C++ program was developed that helped determine the steps in the graph. The program computed the slope between all data points. The DAC value, at which the maximum slope was obtained, was defined as the location of the jump between 1 and 2 p.e. level. The DAC value that lies in the center between that step and the base line computed by the discriminator calibration routine was used as the trigger threshold for that channel. For the example shown in figure 9.6 the step occurred at a DAC value of 37 and the base line was found at 58. Given a discriminator step size of 2.5 mV and a plateau length of 21 DAC units, the amplitude of the 1 p.e. signal inside the ASIC is 52.5 mV.

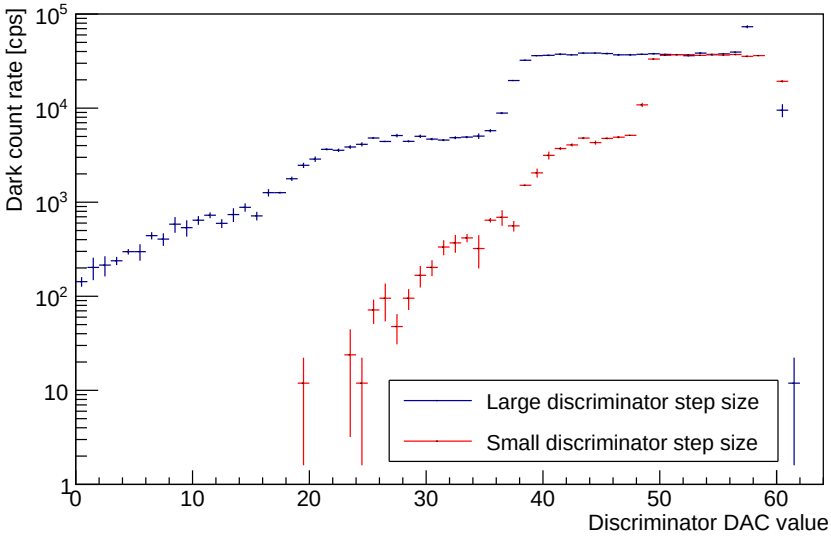

Figure 9.6.: Staircase function in darkness measured with the TOFPET2 ASIC for two different discriminator step sizes. The individual photon levels result in the same dark count rate, but the steps in between them appear for different discriminator DAC values.

9.3.2. Characteristics of the Acquisition System at Low Temperatures

For the following measurements the temperature of the cooled SiPM array was −6.0°C. The breakdown point at this temperature is 51.19 V, which is 1.40 V lower than at room temperature (20°C).
At room temperature the DCR was at least 0.5 Mcps per channel when triggered on 1 p.e. level. With the above stated maximum hit rate of the ASIC of 480 kcps per channel, the read-out system would be overwhelmed with dark count. Due to the cooling of the detectors the dark count rate was reduced and triggering on 1 p.e. level was possible without any event

loss. The dark count rate was measured at 1 p.e. and 2 p.e. level using the staircase graphs shown above. To that end the mean value of the data points on the one photon plateau was computed for each channel of the SiPM array. The same was done for the points on two photon level.[1] The mean value from all channels was then calculated and is plotted in figure 9.7 for different overvoltages. The cautious reader may notice that the overvoltages are not integers, but are slightly shifted towards smaller values. This is due to a false calculation of the breakdown point at the time of the measurement. A value of 51.00 V was assumed instead of the correct value of 51.19 V based on the temperature. The values were afterwards corrected and every data point was shifted by -0.19 V.

The DCR increases for higher overvoltages, but even at around 6 V, the rate is far below the limit of 480 kcps that the ASIC is able to process. At an overvoltage of 4 V – the value chosen for the measurements that will be presented in the next chapter – the DCR was on the order of 50 kcps. For voltages below 1.81 V, no dark count calculation was possible, since the signals were too small such that the steps in the staircase graph could not be clearly identified.

The obtained dark rates at 1 p.e. and 2 p.e. level were then used to determine the probability for a correlated avalanche – or optical cross talk (OCT). The results for various overvoltages are shown in figure 9.8. The probability was calculated by dividing the DCR on 2 p.e. level by the DCR at 1 p.e. level.

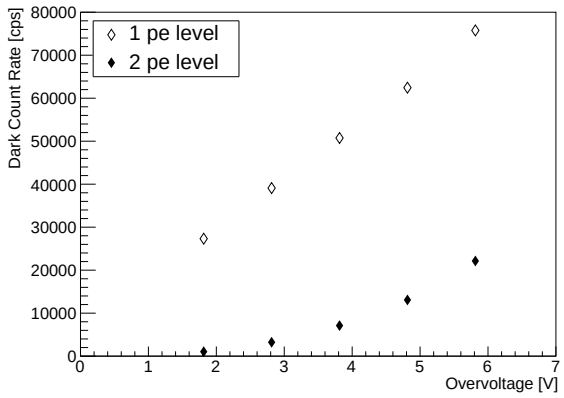

Figure 9.7.: SiPM dark count rate at −6°C measured with the TOFPET2 ASIC for various overvoltages. The rate was measured on 1 p.e. and 2 p.e. level for comparison.

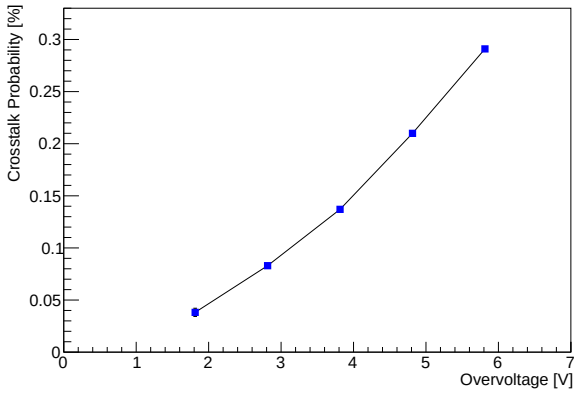

Figure 9.8.: Probability for optical cross talk (OCT) versus overvoltage measured with TOFPET2 ASIC. The measurements were carried out with cooled SiPM channels.

Table 9.1 summarizes the results from the dark count measurement and the calculation of the OCT probability. The obtained probabilities were used in the calculation program (chapter 7) and in Geant4 simulations of the cooled detector set-up (chapters 10, 11 and 12).

The OCT probabilities were calculated using the weighted mean value of all 64 channels, where each weighting is determined by the relative statistical uncertainty on the OCT proba-

[1] This procedure of identifying the one and two photon level is analogous to the one presented in section 6.4.3.

V_{over} [V]	DCR (1 p.e.) [kcps]	DCR (2 p.e.) [kcps]	Cross talk probability [%]
1.81	27.32 ± 0.17	1.04 ± 0.03	3.82 ± 0.40
2.81	39.09 ± 0.20	3.23 ± 0.06	8.30 ± 0.25
3.81	50.74 ± 0.23	7.11 ± 0.08	13.70 ± 0.20
4.81	62.45 ± 0.25	13.08 ± 0.11	20.99 ± 0.15
5.81	75.77 ± 0.28	22.14 ± 0.15	28.10 ± 0.11

Table 9.1.: Dark count rate on 1 p.e. and 2 p.e. level and OCT probability measured at −6°C and at 5 different overvoltages.

bility of the individual channel. Therefore, channels with larger uncertainty contribute less strongly to the mean value [Bar93] (More details on the calculation of weighted mean values is given in the addendum in section A.2.1.2). The statistical uncertainty on the OCT of the individual channel originates from the uncertainties on the measured DCR values. These errors are propagated using Gaussian error propagation.

The calculated OCT probabilities are higher than given in the data sheet (see figure 6.9). For example at 3.81 V a probability of about 10 % is stated [Ham16] whereas this measurement method gives a value of (13.08 ± 0.11) %, where the uncertainty is statistical only. Potential explanations for this deviation lie in inaccuracies inherent in the measurement method itself as explained below.

Due to the dead time of a channel, a small fraction of events will be missed, which causes an underestimation of the DCR. This effect can be considered small, since the probability for having two dark signals on the same channel within 100 ns can be neglected. Moreover, it influences the DCR on the 1 p.e. and 2 p.e. level in the same manner.

Another influence arises from a pile-up effect due to slow baseline recovery after a triggered signal, as investigated in [Rom+18]. A second dark event could occur on the falling edge of the first signal. This would cause the DCR on 1 p.e. level to be underestimated, since some of the piled up events would be missed. On the other hand, a 1 p.e. signal on a falling edge could be seen as a 2 p.e. signal and, thus, the DCR on 2 p.e. level is overestimated. The influence of the pile-up effect has been reported to be in the low percent range with a falling tendency for lower temperatures [Rom+18].

Finally, the accuracy on the temperature measurements could lead to a false estimate of the breakdown point and consequently of the overvoltage. Thus, obtained OCT probabilities might correspond to higher voltages than assumed, which in turn explains the deviation from the data sheet.

In summary, it should be pointed out, that the above calculated values only state the probability of *occurrance* of OCT for an initial real photon event. This quantity does not take the p.e. level of the OCT signal into account. Thus, it cannot give information on the number of additional triggered micro cells per OCT event or on the additional charge contribution that is measurement by the detection system. In this work the number of detected photons is of great interest. A cross talk correction of the number of detected photons is not precisely possible with this value, due to the aforementioned reasons.

The measurements presented in this chapter demonstrate the successful commissioning of the cooling system and the ASIC-based read-out electronics. The SiPM shows a massively reduced DCR compared to the operation at room temperature. This enables setting the trigger on single photon level, without overwhelming the read-out system. The calculated OCT probabilities can help optimize simulations and calculations, although with limited precision. The following chapter presents coincidence measurements with this improved set-up on single photon level. Afterwards, in chapter 11, the implementation of photon counting using TOT values will be presented.

10. Coincident Detection of Cherenkov Photons on 64 Channels

Contents

10.1 Measurement and Analysis Procedure **157**
10.2 Distribution of Coincident Cherenkov Photons **159**
10.2.1 Sensitivity to Sample Thickness and Source Location 159
10.2.2 Quantifying the Occupancy of the Array 162
10.2.3 Energy Dependence of the Measured Pattern 164
10.2.4 Reconstruction of the Electron Source Location from Accumulated Events 165
10.3 Timing Corrections **166**
10.3.1 Problem Description 166
10.3.2 Time Difference Compensation Using Time over Threshold 168
10.3.3 Implementation in the Analysis of Coincidence Measurements . . 170
10.3.4 Coincidence Time Resolution 170
10.4 Contribution of Random Coincidences **173**
10.4.1 Expectation 173
10.4.2 Measured Number of Random Coincidences 175

The measurements described in this chapter use the improved, extended and cooled set-up described in chapter 9. The goal was to detect Cherenkov light from electrons in transparent radiator materials on 64 SiPM channels. The investigations in this chapter regard the sensitivity to sample thickness and source location from accumulated events, a quantification of the measured patterns and the contribution of random coincident events to a measurement. The coincidence time resolution was calculated after compensation of time walk effects and inherent time differences between individual channels.

10.1. Measurement and Analysis Procedure

The detection method is very similar to the data taking and analysis procedure using the STiC evaluation kit described in chapter 8: every signal exceeding the threshold of this channel is saved and an off-line coincidence analysis is performed. This section, therefore,

only describes the trigger mode, summarizes the measurement parameters and gives further information on the analysis of PETsys read-out data.

Measurement parameters:
For all measurements an overvoltage of 4 V was chosen. That allowed for high gain and PDE while limiting contributions from OCT.
The temperature was measured right before data taking and the applied overvoltage at the SiPMs was adjusted accordingly. This took into account the shift of the breakdown point of a cooled detector, which for this SiPM drops by 54 mV per degree Celsius.

The measurements were performed with UV transparent PMMA samples, as this radiator type showed excellent transmission properties over a large wavelength range (see figure 9.2 in the previous chapter). Different sample thicknesses were used as well. Data was taken for 60 s in each measurement.

Trigger mode:
As pointed out in the previous chapter, the system possesses three different triggers, for timing, dark count rejection and energy. However, the step sizes of the two higher thresholds were too coarse and the charge integrator was not sensitive enough for a use on 1 p.e. level [Lui19]. As a workaround, the ASIC was operated in a trigger mode, where only the lowest threshold was used and the two higher ones were ignored. The threshold values were set on 1 p.e. level using the method described in 9.3.2. The TOT value was defined as the time in which the SiPM signal stayed above that threshold. The TOT values were eventually used for a calibration of every channel with respect to the number of detected photons (see chapter 11).

Measurement Goals:
Since a coincidence measurement was performed, the coincidence time resolution (CTR) is of great interest – especially with regard to a potential application of this electron detection principle in a Compton camera where good timing is crucial. Similar to the STiC and oscilloscope measurements the distribution of coincident hits from accumulated events was investigated and the response to a shift of the source location and a variation of the sample thickness was examined. Finally, the number of detected photons per channel and event was calculated using the TOT information of the SiPM signals. The results were compared to Geant4 simulations and calculations based on the algorithm introduced in chapter 7.

Analysis procedure:
The coincidence search algorithm is based on the analysis for STiC data described in section 8.1.1.2. The flow chart in figure 8.2 is valid also for data taken with PETsys read-out system. There are only two main differences, one of which is the frame length. The program (provided by PETsys) that was used to convert the raw data into usable events bundled the data in frames of 100 ns. In comparison, the STiC data were packaged in frames of 6.4 μs. The second difference was that the converted PETsys events contained the information on the number of events per frame. So, frames that did not have enough entries could be omitted, which reduced the total analysis time.

The key input parameters were the required number of coincident channels (rnocc) per event and the coincidence time window (CTW). Due to the larger amount of channels and the increased dark count per channel compared to the STiC measurements[1] the rnocc had to be set to a larger value than for the analysis of STiC data. Otherwise, random coincidences from dark count would contribute too strongly to the measurement. The rnocc was set to 5 as nominal value.
The CTW was set to values between 5 ns for most of the measurements performed in this chapter.
The influence of the CTW and the rnocc on the measurement was investigated with regards to random coincident events in section 10.4.
Inherent time differences between the channels were corrected and a compensation of time walk between coincident signals of different amplitude was performed. The procedure of time walk correction is explained in section 10.3.
The analysis program calculated the CTR of the coincidence measurement, provided a histogram of the number of coincident channels per event and created a photon hit map with all accumulated events of that measurement. The algorithm was also capable of calculating the number of detected Cherenkov photons per channel per event based on the TOT value of the SiPM signals. The calibration of the channels for photon counting using TOT values is described in chapter 11.

10.2. Distribution of Coincident Cherenkov Photons

This section covers the results of the investigation of the detected patterns of coincident Cherenkov photons. The response to sample thickness and electron source position are presented in section 10.2.1. Afterwards the occupancy of the array was examined and quantified. This is shown in section 10.2.2. Section 10.2.3 demonstrates the behavior of the detected coincidence patterns depending on the electron energy. Finally, the patterns from accumulated events were used to reconstruct the electron source position. This is shown in section 10.2.4.

The parameters for data taking and analysis are the same for all measurements presented in this chapter and are listed in table 10.1. The overvoltage was set to 4 V and a temperature of −6.5°C was measured at the cooling finger. Cherenkov light was produced in UV transparent PMMA samples of various thicknesses between 6 mm and 16 mm. The electron source was focused on the center of the array for all measurements unless explicitly indicated otherwise. Each data taking period was 60 s.
For the analysis an rnocc of 5 was used with a CTW of 5 ns. Deviating CTWs are explicitly stated.

10.2.1. Sensitivity to Sample Thickness and Source Location

This section focuses on the qualitative behavior of the observed patterns, while a quantified analysis is performed afterwards.

[1] Even though STiC was operated at room temperature, the measured dark rate per channel was lower, since the triggers were set to much higher thresholds.

Parameter	Value	Unit
PMMA cross-sectional area	35×35	mm^2
PMMA thickness	variable	mm
Overvoltage	4	V
Temperature	-6.5	°C
Measurement period	60	s
Required number of coincident channels	5	-
Coincidence time window	5	ns

Table 10.1.: Data taking and analysis parameters for the measurements using 64 SiPM channels and the PETsys read-out system.

The coincidence measurement was performed for 5 different thicknesses of UV transparent PMMA. However, only 6 mm and 8 mm were available as one piece, whereas the other thicknesses of 12 mm, 14 mm and 16 mm were created by stacking thinner samples together. This is why no measurements with a sample thickness smaller than 6 mm or with a thickness of 10 mm was performed. The layers were coupled with optical grease. Figure 10.1 shows the occupancy of the SiPM array with coincident hits. Every channel that was involved in a coincident event contributes to the corresponding bin in the histogram. The number of hits per channel is indicated in color code.

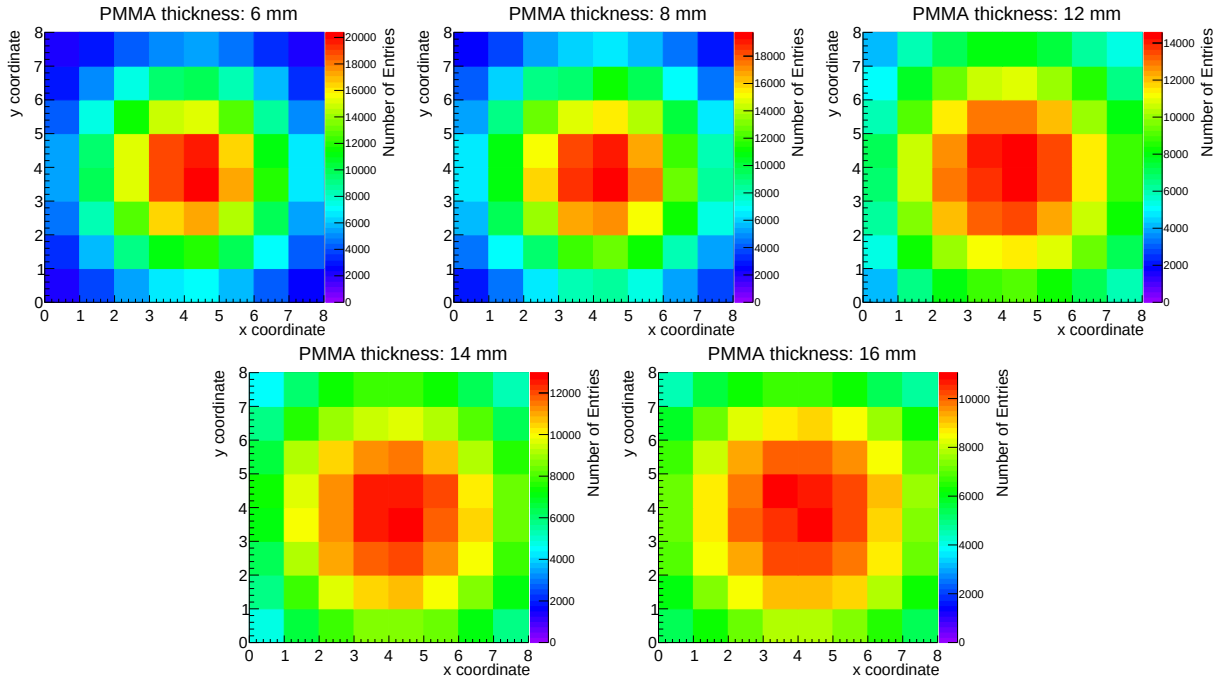

Figure 10.1.: Measured coincident events of Cherenkov photons created by electrons from a ^{90}Sr source in UV transparent PMMA samples of various thicknesses.

All patterns accumulate around the center of the array. One can see that the width of the patterns increases for larger thicknesses, which can easily be understood by considering an increasing diameter of the Cherenkov cone intersecting the array. Assuming an opening angle of the Cherenkov cone of 47.8° and an array side length of 26.5 mm, the cone would exceed the boundaries of the array above a PMMA thickness of 14.6 mm.

For the purpose of comparison and verification of the results, Geant4 simulations [Ago+03] were performed with the same parameters as in the measurements. Also a 10 mm PMMA sample was used. The electron energies were chosen randomly from the ^{90}Sr spectrum. Possible energies were restricted to values above the threshold energy for the Cherenkov effect to occur, which is why the minimum energy for a refractive index of 1.49 was at 177 keV. The coincidence pattern from 10000 accumulated electron events per sample thickness are shown in figure 10.2.

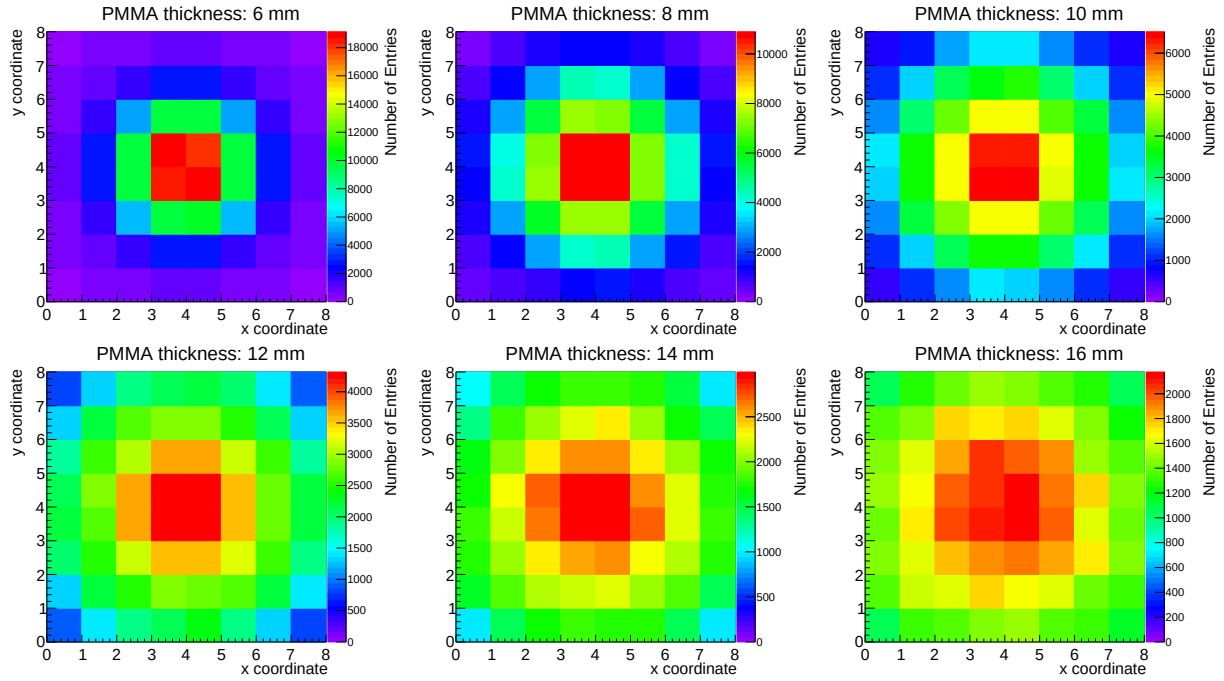

Figure 10.2.: Simulated coincidence events of Cherenkov photons created by electrons from a ^{90}Sr source in UV transparent PMMA samples of various thicknesses. 10000 events were simulated for each thickness. [Bä20a]

The general form of the patterns is in very good agreement with the measurement, however, the simulated distribution appears to be more peaked at the center of the array.
One possible reason for this discrepancy could be the divergence of the electron source, which had a collimator with a diameter of 1 mm. In the simulation a point source was used and the initial electron momentum direction was always perpendicular with respect to the sample. Another explanation for the deviations is the fact that some samples were glued together, which was not considered in the simulation. Contributions of reflections are neglected as well, as the side walls of the PMMA sample were defined as *back-painted* in Geant4, which would absorb incident photons. Even though the PMMA was covered in black tape and foil

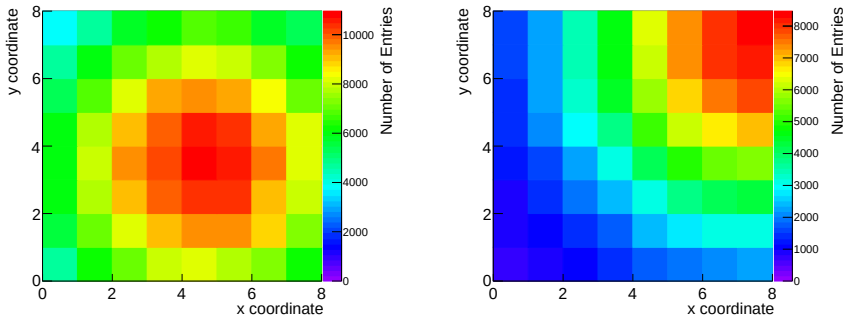

Figure 10.3.: Sensitivity of the occupancy of the SiPM array to a shift of the electron source using accumulated coincident events. A sample thickness of 16 mm was chosen.

on 5 sides, the exact contribution of reflections off the side walls in the actual measurement is unknown. A quantification and further discussion of the width of the patterns of both measurement and simulation is given in section 10.2.2 together with a comparison to the results obtained with the 16-channel array.

Figure 10.3 demonstrates the sensitivity of the measurement to a shift in electron position using accumulated coincident events. A sample thickness of 16 mm was chosen. In the left histogram the electron source was roughly centered and in the right one the source was moved by four channels in x- and four channels in y-direction towards the upper right corner of the SiPM array. A quantified reconstruction of the electron source location from accumulated events is shown in paragraph 10.2.4.

10.2.2. Quantifying the Occupancy of the Array

To describe the qualitative response of the patterns to a change of thickness, the width of the distribution was quantified. The same approach was used as for the analysis of the occupancy plot using measurements with STiC (see section 8.3.2): a two-dimensional gauss fit was applied to the data and the width of the distribution was described using the σ-parameter of the fit. The fit was chosen to be symmetric and the σ-parameter was identical in x- and y-direction.
The results for all thicknesses are shown in figure 10.4. The width of the distribution is plotted against the thickness of the sample (red pluses). As expected, the width decreases for thinner sample thicknesses. The results are also compared to simulations (green, filled diamonds) and the values obtained with the 16 channel SiPM array that were read out with the STiC board (blue, empty diamonds).

It could be observed that the measurement data and the simulation data have different slopes. Especially at 6 mm and 8 mm there are significant deviations between measurements on 64 channels and the corresponding simulation. There are several potential explanations for the discrepancies. The main reason is the divergence of the electron beam, which has not been taken into consideration in the simulation [Bä20a]. This can be visualized by comparing the occupancy for the thicknesses of 6 mm and 8 mm from measurement (figure 10.1) and

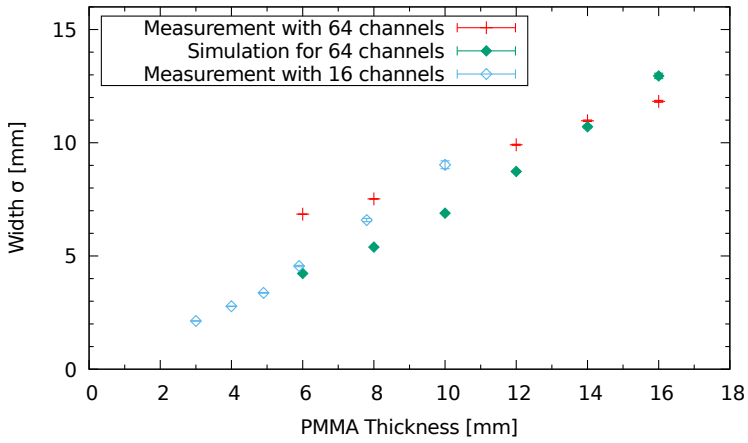

Figure 10.4.: Quantification of the width of the distribution of coincident Cherenkov photons. The width is expressed by the σ-parameter of a 2-dimensional gauss fit. Measurements on 64 channels are compared to simulations using Geant4 and former measurements using a 16-channel array.

simulation (figure 10.2). Due to the geometric boundaries of the array, this influence decreases for larger thicknesses as more photons are lost for detection.
As mentioned above, reflections off the side wall of the radiator sample contribute to a broadening of the distribution and therefore constitute another possible influence contributing to the difference.
Additionally, in the measurement the source positions might have been slightly misaligned from the center position. Due to the coarseness of the detector matrix, this could cause a change of the measured width of the gauss fit. Simulations with an electron source location shifted by 1 mm indicated an increase in the width on the order of only 0.1 mm. Thus, the influence of a misalignment of the source on the measured width is small.

The STiC measurements on 16 channels are in good agreement with the simulation at around 6 mm thickness and they seem to reasonably extend the simulated data points towards thinner sample thicknesses. Discrepancies between simulation and STiC measurement for thicknesses above 6 mm originate from the smaller number of channels in the STiC measurement. Patterns that outgrow the boundaries of the array make a quantification of the width of larger patterns less reliable.
The deviation between STiC and PETsys measurements for 6 mm is also quite pronounced. In general, one might want to argue that the measurements on 16 and 64 channels should give similar results, as the same electron source was used. However, using STiC, the trigger level was significantly higher, which also influences the width of the distribution from accumulated events. This can be explained as follows: It could be shown that the average number of photons a channel received when involved in a coincident event is larger for the channels in the center than it is for the rest of the array.[2] Channels in the center are, therefore, triggered more likely in a coincident event resulting in a narrower distribution of coincident hits on

[2] These results have not been presented up to this point in the thesis. They are discussed later in connection with the photon number investigations in chapter 11.

the array. This effect might be less prominent for thinner samples where the photons are distributed over a smaller number of channels in the first place.

In summary, due to the above listed influences, the comparability of measurements performed with different set-ups using different ASICs and different channel numbers is quite limited. Furthermore, simulation results appear to have limited accuracy and cannot perfectly represent the set-up, which manifests in discrepancies from the measurement. Nevertheless, all three data sets are capable of reproducing the growing intersection of the Cherenkov cone with the detector arrays for increasing sample thickness.

10.2.3. Energy Dependence of the Measured Pattern

The results presented in the previous two sections were produced with the continuous spectrum of the electron source ^{90}Sr. It incorporates events with electron energies up to 2.4 MeV. To investigate the energy dependence of patterns, simulations with single energies between 200 keV and 3 MeV were performed and the width of the distribution was investigated. The electron source was placed 10 mm above the surface of the PMMA sample, which was defined with a thickness of 8 mm. One goal was to determine whether the patterns from accumulated events show any sensitivity for the energy change. 10000 electrons were simulated for each energy and all hits of Cherenkov photons on the array were counted, thus, no coincidence condition of at least 5 channels at a time was applied. This was required to display events at low energies, where the number of created and detected photons was very scarce. These events would have been lost otherwise.

The patterns for four different energy values are displayed in figure 10.5. For 200 keV, the patterns are almost exclusively limited to the center of the array, representing the very small Cherenkov cone opening angle of 15.2° (top left graph). The pattern shows increased width for 300 keV electron energy, as the Cherenkov cone opening angle increases to 30.2° (top right). At 500 keV the angle is 38.9° and the width of the pattern increases as well (bottom left). Then, the energy is further increased to 2 MeV where the opening angle of the Cherenkov cone is 46.7° and is therefore close to its maximum value of 47.8°. Here, the pattern shows slightly decreased width, which is explained by the elongated electron trajectory inside the PMMA. Additional photons are created close to the SiPM array than for lower energies, thus, limiting the area covered by the Cherenkov cone. The result is an accumulation of hits in the center of the array and a narrower width in total.
Even though the angle increases for larger energies and the Cherenkov cone covers more channels, no clear ring is seen, but an accumulation in the center of the array. Multiple scattering of the electron causes a random deflection of the Cherenkov cone subsequently smearing out the ring structure to be detected on the array (compare visualization in chapter 5 figure 5.3). The average over many events explains the accumulation in the center of the array.

Figure 10.6 shows the quantification of the width of the distribution of coincident hits for various electron energies. A two-dimensional symmetric gauss fit was performed again like before, and the width was defined using the σ-parameter of the fit. The width increases strongly for small energies and reaches a maximum at around 700 keV-1000 keV. Above that

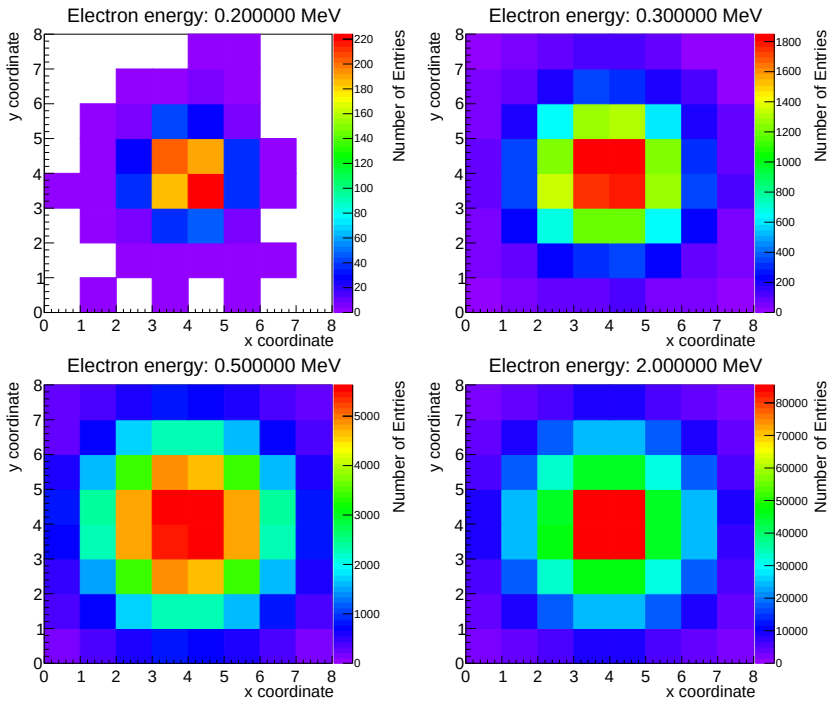

Figure 10.5.: Simulated distributions of coincident Cherenkov hits from electrons with fixed energy traversing through UV transparent PMMA. The distribution is shown for four different electron energies. Bins with zero entries are indicated with white color in the top left graph.

energy, the width decreases again representing the extended electron trajectory in the PMMA. The graph exhibits strong similarities to the relation between opening angle and electron energy in figure 5.2, chapter 5.

This observation has implications on the feasibility of the concept for the detection of Compton scattered electrons as well: the principle as described in chapter 5 foresees the reconstruction of the Compton scattering vertex via a measurement of the eccentricity and the size of the ellipse formed by the Cherenkov photons from individual events. Especially for lower electron energies up to about 0.75 MeV, the size of the ellipse is strongly energy dependent as indicated by the measured width from accumulated events. Thus, to obtain full information on the vertex and momentum direction of the electron, an energy measurement might be necessary to obtain the electron energy and, subsequently, the Cherenkov cone opening angle. The applicability of counting the number of detected photons to an energy measurement is discussed in the upcoming chapter 11.

10.2.4. Reconstruction of the Electron Source Location from Accumulated Events

The electron source was placed at six different positions above the array. A reconstruction of the electron source position was performed with the gauss fit in two dimensions. The

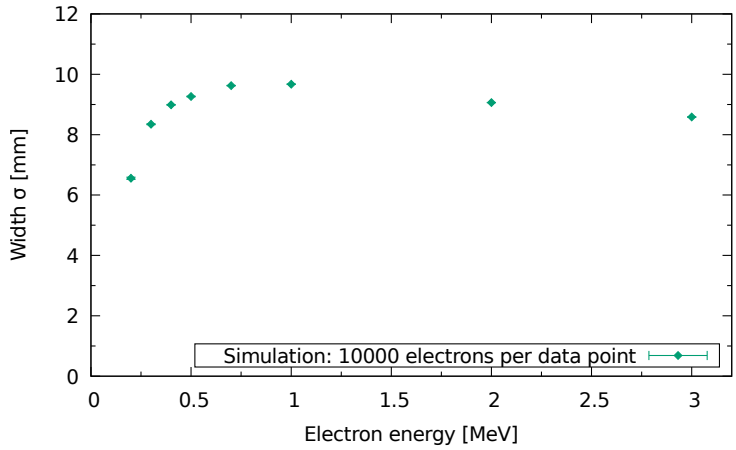

Figure 10.6.: Quantification of the width of the distributions of coincident Cherenkov photons from simulated mono-energetic electron events. The width is expressed by the σ-parameter of a 2-dimensional gauss fit.

obtained mean values μ_x and μ_y of the gauss fit were compared to the x- and y-coordinate of the source. The results are shown in figure 10.7.
The grey square indicates the sensitive detector area. The red markers indicate the real source location and the blue markers show the reconstructed positions. The positions could be reconstructed precisely with an accuracy of better than 1 mm. The only exception is the location at position (8,8), for which the reconstruction algorithm returned a value of $\mu_x = 8.70 \pm 0.05$ and $\mu_y = 8.61 \pm 0.05$. For this location, only about 25 % of the emitted Cherenkov photons reached the array, which limited the accuracy on the gauss fit.
Like the measurement with 16 channels and STiC, the results using PETsys successfully demonstrate a spatial sensitivity for the electron source location using accumulated coincident Cherenkov photons.

10.3. Timing Corrections

10.3.1. Problem Description

The coincidence time resolution (CTR) is the most important factor in coincidence measurements. It describes the smallest time interval that can be measured with accuracy [Leo87]. One method of determining this resolution is by measuring the time difference between exactly coincident signals. In an ideal detection system, this time difference would be zero resulting in perfect time resolution. However, noise on the signal, and fluctuations of the time relation between coincident signals impair the resolution.
With the present detector and read-out system there are several major reasons why coincident signals would not be detected with the exact same time stamp:

1. There is a time difference between individual channels of the SiPM array inherent in the ASIC. This might be caused by signal propagation delay in cables and connectors and in the slightly different response time of each detector channel, amplifier and

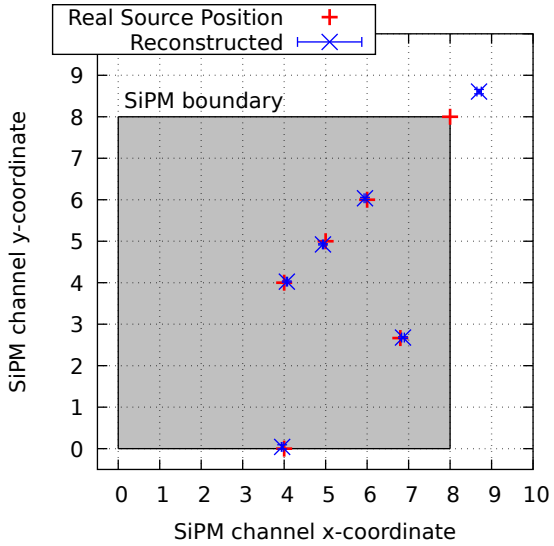

Figure 10.7.: Reconstruction of the electron source position from accumulated coincident events on 64 channels. The real position (red pluses) is reconstructed with good accuracy (blue crosses).

threshold discriminator. Measuring this time delay of every channel with respect to a fixed reference channel allows to compensate for these differences in the analysis of any further measurement.

2. The second influence on the time resolution is called *time walk* originating from different amplitudes of the SiPM signals depending on the number of detected photons. Since the rise time is mostly independent of the signal amplitude, coincident signals can exceed the threshold at different times. This is demonstrated schematically in figure 10.8. The time difference between coincident signals depends on the amplitude of the signals. Thus, a method is needed to compensate for these differences based on the signal amplitude or in this case the number of detected photons. Using PETsys, the only available measure for the light level in a channel is the Time over Threshold (TOT), which increases monotonously with the number of photons (see chapter 11 for details on the relation between TOT and photon number). The time difference is more prominent for smaller signal amplitudes than for higher ones. Therefore, a correction of time walk is of great importance for coincident detection of low intensity light signals like Cherenkov light.

3. There is a third influence on the timing resolution, which is called *timing jitter*. Random fluctuations of the signal cause the trigger time to fluctuate as well even for signals of same amplitude. The root-mean-square of the fluctuation of the time stamp when triggering a voltage signal with slope $\mathrm{d}V/\mathrm{d}t$ and noise level σ_n can be expressed as

$$\sigma_{\text{time}} = \frac{\sigma_n}{|\mathrm{d}V/\mathrm{d}t|}$$

The jitter decreases for lower noise and statistical fluctuations on the voltage signal and also decreases for greater slopes of the leading edge – i.e. shorter rise times. Therefore,

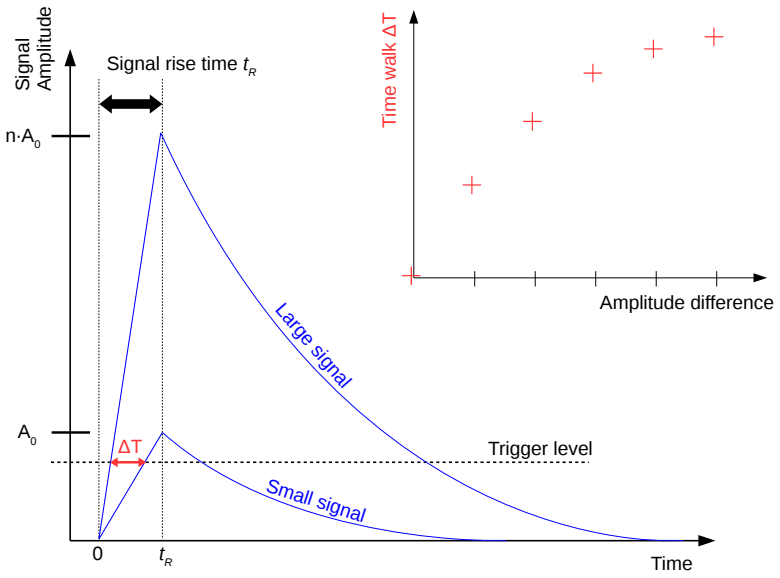

Figure 10.8.: Schematic description of the time walk effect. Two signals with the same rise time t_R but different amplitude exceed the trigger at different times, causing a difference ΔT between the time stamps. The larger the amplitude difference, the stronger the effect as the small graph in the top right corner demonstrates.

it is also correlated to the amplitude of a signal. But other than reducing noise and using detectors with a fast rise time, no method can be implemented to compensate for the influence of timing jitter. [Leo87].

The next section describes the method of compensating for TOT dependent time differences between individual channels in a coincidence measurement.

10.3.2. Time Difference Compensation Using Time over Threshold

The purpose was to implement a time difference correction for coincident signals depending on the measured TOT value. To that end, the time difference of a large number of coincident signals was measured. A variety of different amplitudes was required to cover a large TOT range.
To that end Cherenkov photons were used to provide coincident, low light level signals starting on single photon level. The photons were created in a UV transparent PMMA sample with a thickness of 8 mm using electrons from the ^{90}Sr source. Measurements were performed with the source located at 5 different positions in order to create a large variety of light levels per channel. The exposure at each position was 180 s. About $6 \cdot 10^5$ coincident events were recorded in total, each of which containing at least 5 triggered channels within a 5 ns CTW.

For the analysis, one fixed reference channel in the center of the array was defined and time differences were calculated with respect to that channel. For every channel i, a 2D-histogram

was created showing the TOT values of that channel and the reference channel on y- and x-axis, respectively. The bin width on each axis was 10000 ps = 10 ns. For every coincident event, where these two channels were involved, the time difference was computed as

$$\Delta T = T_{\text{ref}} - T_i \tag{10.1}$$

and sorted into the corresponding TOT bin in the histogram. Such a histogram is shown in figure 10.9. After all events were analyzed, the mean time difference of every bin was computed using a gauss fit to the distribution of time differences. Using color code, the measured mean time difference of each bin is indicated in the histogram. If there were less than 10 entries in a bin, the gauss fit was omitted and simply the mean value was calculated. If a bin was empty, its time difference value was set to zero.

In that way, a look-up table (LUT) was created for every channel of the array containing the time differences at given TOT values. The only exception was the reference channel, for which all time differences must be zero by definition. The LUT was saved as ROOT file to be accessed in the analysis of further measurement data.

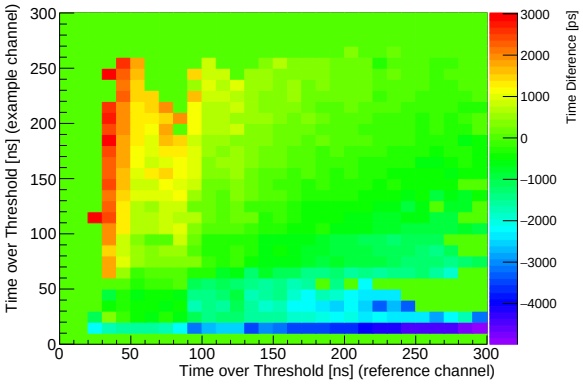

Figure 10.9.: Color plot of the TOT dependent time differences ($T_{\text{ref}} - T_i$) between an example channel and the reference channel. Larger signals tend to be detected earlier due to time walk.

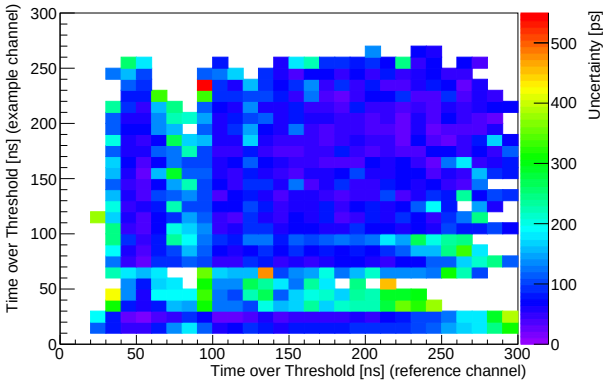

Figure 10.10.: Color map of the statistical uncertainty of the obtained time differences in every pair of TOT values. An average uncertainty of 106 ps was obtained.

The example histogram in figure 10.9 demonstrates how the time difference changes depending on the TOT value: if on average the reference channel was triggered first, the value in the corresponding bin is negative and vice versa. One can also see the tendency that the signal that comes first has higher TOT than the second signal. This represents the time walk of coincident signals of different amplitude.

Not all TOT bins were filled in the histogram. However, since the signals were created using Cherenkov light, it can be assumed that the map contains the most frequently occurring TOT values in an actual measurement.

Figure 10.10 shows the uncertainty of each entry in the histogram. The average uncertainty on the calculated time differences is 106 ps.

10.3.3. Implementation in the Analysis of Coincidence Measurements

The analysis procedure described in section 10.1 implements the time difference correction based on TOT values. For every signal the time difference value with respect to the reference channel is read out from the LUT based on the TOT values of the signal of that channel and that of the reference channel. The measured time stamp T_{meas} is corrected accordingly:

$$T_{\text{corr}} = T_{\text{meas}} + \Delta T \tag{10.2}$$

Of course the reference channel is not involved in every single coincident event. In such an event the time difference value is taken from the bin that corresponds to the same TOT value on the reference channel. For example, let us assume that the signal in a channel has a TOT value of 100 ns, which corresponds to bin number 10 on the y-axis (first bin has number 0). If no signal on the reference channel was detected in that event, the time difference value from the bin with coordinates (10, 10) is taken. By doing so, it is possible to compensate at least for the time difference inherent in the ASIC (bullet point 1 in aforementioned list).
In the next section the algorithm and correction method is tested with a coincidence measurement using Cherenkov light and the coincidence time resolution is calculated.

10.3.4. Coincidence Time Resolution

To show the applicability of the above presented compensation algorithm, a test measurement with about 120000 coincident Cherenkov events was performed using again a 8 mm thick sample of UV transparent PMMA. The electron source was centered above the array. The condition for a valid coincidence was set to 5 channels within a time window of 5 ns.
The CTR was obtained using a histogram of the time difference of every channel involved in a coincident event with respect to the reference channel. The result is shown in figure 10.11. One can see that the distribution is not strictly Gaussian but shows rather large tails on both sides of the peak. A possible explanation is the presence of two contributions to the histogram: firstly, the sharp peak is formed mostly by events that contained the reference channel and for which the TOT dependent time difference correction could be performed (corresponding to point 2 in the bullet point list of section 10.3.1). The broad tails on both sides resemble events that did not contain the reference channel and for which only the inherent time differences could be subtracted (point 1 in the list). To compute the CTR, the sum of two gauss functions was fitted to the histogram, representing the two contributions to the distribution of time differences. Both gauss functions reproduced the same mean value of 88.1 ps – yet with slightly different uncertainties of 1.1 ps in case of the sharp gauss and 2.2 ps for the broad gauss.
The width of the sharp gauss function was $\sigma_1 = (481.7 \pm 1.6)\,\text{ps}$, whereas the with of the broad gauss was given by $\sigma_2 = (1351 \pm 3.1)\,\text{ps}$. The smaller sigma parameter was used to define the CTR:

$$\text{CTR} := \text{FWHM} = 2.35 \cdot \sigma_1 = (1133 \pm 5)\,\text{ps} \tag{10.3}$$

Since the broad gauss contribution is ignored in this definition, one could say the smaller sigma determines the best possible coincidence time resolution.

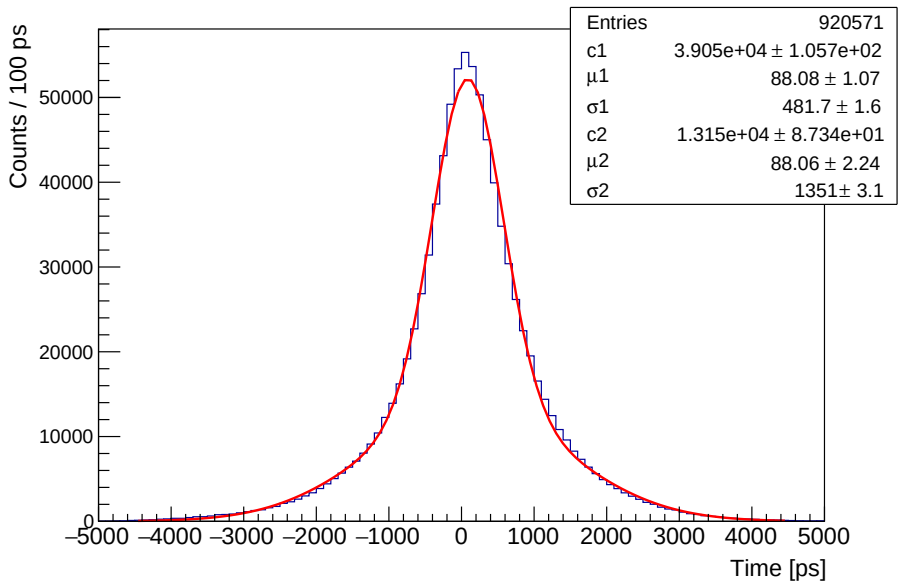

Figure 10.11.: Coincidence time resolution of the detection of Cherenkov light on SiPM channels. The histogram shows the time difference of every coincident channel with respect to the reference channel. Two gauss functions were used to model the distribution. The best possible coincidence time resolution is given by $\mathrm{FWHM} = 2.35 \cdot \sigma_1 = (1133 \pm 5)\,\mathrm{ps}$.

The fit was performed within an interval of ±4500 ps around the peak bin, which was at 0 ps. Clearly, the choice of the fit range constitutes a bias on the analysis, and therefore gives rise to systematic uncertainties on the result. This is why the fit was performed again for the intervals of ±4000 ps and ±5000 ps around the peak. A reduction of the range below ±4000 ps would cut away a too large fraction of the broad gauss fit and outside of a ±5000 ps interval, almost no entries were found. For a fit range of ±4000 ps (±5000 ps) a CTR of 1116 ps (1137 ps) was found. The smaller interval results in a stronger deviation from the nominal value calculated in expression 10.3, which is 17 ps. Thus, the final result on the CTR is given as:

$$\mathrm{CTR} = (1133 \pm 5^{\,\mathrm{stat}} \pm 17^{\,\mathrm{syst}})\,\mathrm{ps}$$

Single photon timing resolution (SPTR):
Finally, the timing resolution for a coincidence measurement of only single photon signals was computed. This quantity is usually called single photon timing resolution (SPTR). To that end, the test measurement from above was analyzed again with respect to the CTR. Only individual channels were investigated. The time difference of a coincident signal on a channel with respect to the reference channel was saved, if on both channels there was only one photon detected.[3] These saved time differences were drawn in histograms and, again, a gauss fit was used to determine the SPTR. Figure 10.12 shows such a histogram for the

[3] The cautious reader may notice that the calculation of the photon number using TOT values has not been introduced up to this point in the thesis. However, it was assumed reasonable to talk about SPTR in connection with CTR. The TOT based photon number calibration is explained in chapter 11.

channel that showed the best timing. This channel was located right next to the reference channel on the array.

The fit was performed in an interval of ±800 ps around the peak. For this channel an SPTR of (481 ± 7) ps was obtained defined as the FWHM of the peak. The choice of the fit range was considered a source of systematic uncertainty and therefore, the fit was repeated for ±600 ps and ±1000 ps. This resulted in an SPTR of (473 ± 6) ps and (482 ± 7) ps, respectively. The single photon timing resolution is

$$\mathrm{SPTR} = (481 \pm 7^{\mathrm{stat}} \pm 8^{\mathrm{syst}})\ \mathrm{ps}$$

It has already been pointed out that the above discussed channel had the best timing resolution. In fact, the average SPTR was 1170 ps with 1913 ps being the largest obtained value for one channel at the edge of the SiPM array.

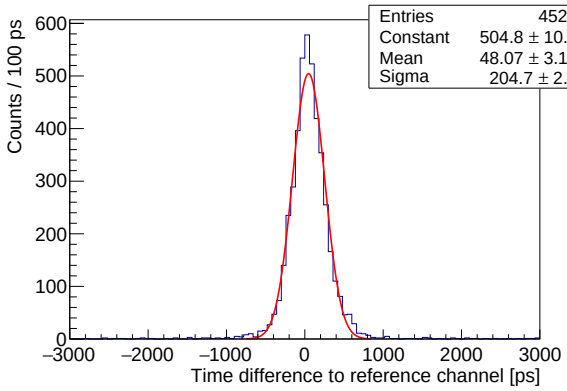

Figure 10.12.: Best single photon timing resolution that could be achieved with the PETsys read-out system. The time difference with respect to the reference channel is plotted and a gauss fit was performed to obtain the time resolution.

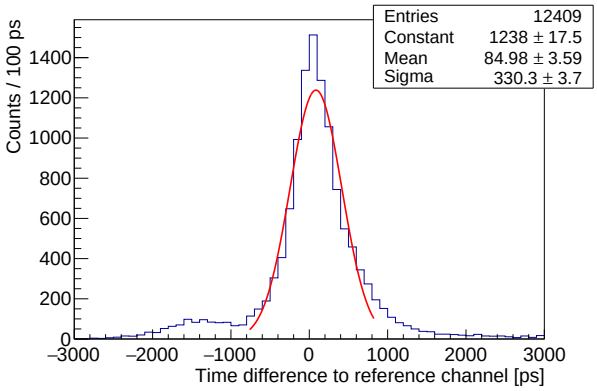

Figure 10.13.: CTR for the same channel for which the SPTR was calculated (figure 10.12). All coincident signals were taken into consideration resulting in at FWHM, which is about 63 % higher than the SPTR.

These results have also been compared to the CTRs of pairs of channels including all coincident signals, not only single photon signals. The corresponding histogram of the obtained time differences is shown in figure 10.13. It is the same channel, for which the best SPTR was found. The CTR was obtained in the same manner using a gauss fit in a ±800 ps interval around the peak. The CTR was (776 ± 9) ps. The systematic uncertainty inherent in the choice of the fit range was again estimated by fitting in a range of ±600 ps around the peak and in a range of ±1000 ps. For the first interval a CTR of (707 ± 9) ps was obtained while for the latter one the CTR was (844 ± 9) ps.
The final result on the best obtained CTR between a pair of channels under consideration of all coincident signals reads

$$\mathrm{CTR} = (786 \pm 9^{\mathrm{stat}} \pm 69^{\mathrm{syst}})\ \mathrm{ps}$$

Due to the small accumulation of unknown origin that appears next to the peak, the choice of the fit range had a larger impact on the result, explaining the excessive systematic uncertainty.

Summary and discussion on the coincidence time resolution:
This chapter demonstrated the implementation of a time difference correction based on the measured TOT values of coincident signals. A coincident measurement of Cherenkov photons on 64 channels resulted in a coincidence time resolution on the order of 1 ns. This result is significantly larger than the statement made by PETsys Electronics, who claim a CTR on the order of (201 ± 5) ps is possible. However, their result has been measured with a ^{22}Na gamma source and two single SiPMs coupled to LYSO scintillation crystals sitting on two separate Front End Modules [PET18e]. One reason for the discrepancy of the measured CTR to the manufacturer's statement could therefore be the difference in the measurement method. Another reason could be the use of a self-made connector to feed the channels from the four 16-channel SiPM arrays into the Front End Module of the read-out system. Temperature fluctuations during or in between measurements might contribute to the large CTR as well. However, considering only single photon events, a timing resolution of 481 ps was possible.

10.4. Contribution of Random Coincidences

Since every channel had a dark count rate on the order of 50 kcps, there is a non-negligible probability that an event that fulfills the required conditions is purely or partly based on random dark signals.
This section attempts an estimation of the contribution of additional random coincidences to a measurement based on the average DCR per channel, the CTW, the rnocc and the total measurement duration. The number of random coincidences was then obtained from a measurement in darkness, without the electron source.

10.4.1. Expectation

An expression for the number of random coincidences in darkness was derived [Fle19]. In the following t_m denotes the duration of a measurement in seconds and n_{Ch} is the variable describing the number of channels on the array, which was 64.
The number of signals from all channels on the array within the measurement duration can be written as

$$N = \mathrm{DCR} \cdot n_{\mathrm{Ch}} \cdot t_m \tag{10.4}$$

In order to obtain the number of coincident events that contain at least two channels, one has to multiply the above expression with the probability to have at least one additional channel within the CTW. Each channel has a probability of $p = \mathrm{DCR} \cdot \mathrm{CTW}$ to be involved in an event by chance [4], thus, the probability for the whole array to contribute with at least one additional channel is $p_{i\geq 1} = \mathrm{DCR} \cdot \mathrm{CTW} \cdot (n_{\mathrm{Ch}} - 1)$. Therefore, the number of events with at least 2 channels within the CTW reads

$$N_{i\geq 2} = N \cdot \mathrm{DCR} \cdot \mathrm{CTW} \cdot (n_{\mathrm{Ch}} - 1) \tag{10.5}$$

[4] Actually, the probability for a channel to fire within the CTW is Poisson distributed: $p(k, \lambda) = \lambda^k / k! \cdot \exp(-\lambda)$, where $k = 1$ and the expectation value is $\lambda = \mathrm{DCR} \cdot \mathrm{CTW}$. However, since $\lambda \ll 1$ (for realistic CTW and DCR values), the probability can be approximated as $p \approx \lambda$.

$N_{i\geq 2}$ also incorporates all events with more than 2 channels within the coincidence window. Consequently, the number of events with at least 3 channels per CTW is then

$$N_{i\geq 3} = N_{i\geq 2} \cdot \mathrm{DCR} \cdot \mathrm{CTW} \cdot (n_{\mathrm{Ch}} - 2) \tag{10.6}$$

For the general case of $n \leq n_{\mathrm{Ch}}$ channels per event, the expression becomes

$$N_{i\geq n} = N_{i\geq (n-1)} \cdot \mathrm{DCR} \cdot \mathrm{CTW} \cdot (n_{\mathrm{Ch}} - (n-1)) \tag{10.7}$$

which can be rewritten as follows:

$$N_{i\geq n} = (\mathrm{DCR})^n \cdot (\mathrm{CTW})^{n-1} \cdot \frac{n_{\mathrm{Ch}}!}{(n_{\mathrm{Ch}} - n)!} \cdot t_m \tag{10.8}$$

Expression 10.8 can be used to compute the expected number of random coincidences within a measurement period t_m. Figure 10.14 shows the expected number of random coincident events, which is abbreviated with NRCE due to limited space on the graph's y-axis. A measurement duration of 60 s was chosen for the calculations together with a coincidence time window of 5 ns. The graph displays results for various DCR values. A strong dependence of the number of random coincident events (NRCE) on the required number of coincident channels (rnocc) is observed. The larger the rnocc, the less likely the occurrence of an event with that number of entries becomes.

The contribution of NRCE to a measurement increases disproportionately with the DCR. Depending on the rnocc, doubling the dark count rate can increase the number of random coincidences by an order of magnitude or more.

Figure 10.15 shows the expected NRCE for various CTWs. A DCR of 75 kcps was chosen. A reduction of the CTW causes the likelihood of the occurrence of a coincident event to decrease. Therefore, significantly smaller numbers of random coincidences are expected for shorter CTW.

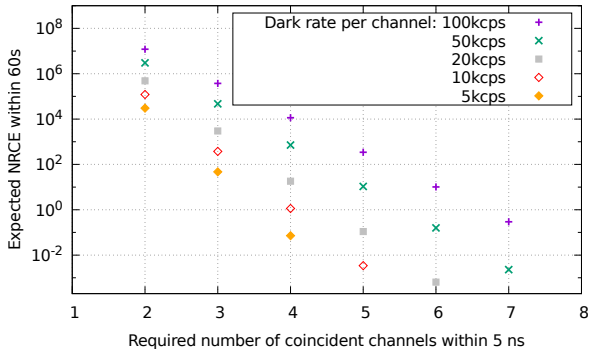

Figure 10.14.: DCR dependence of the expected number of random coincident events (NRCE) within 60 s. The CTW was 5 ns.

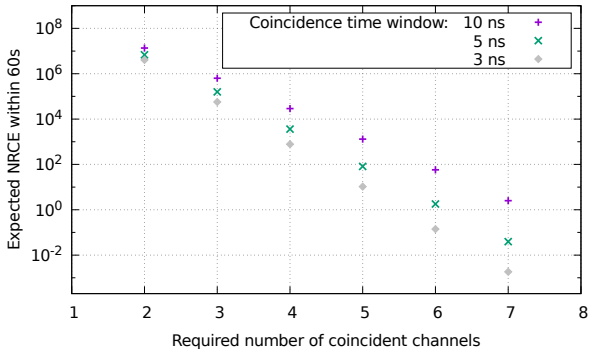

Figure 10.15.: Dependence of the expected number of random coincident events within 60 s on the CTW. A DCR of 75 kcps was chosen

It can be summarized that a reduction of the DCR is crucial for limiting the contribution of random coincidences to a measurement. If sufficient coincidence time resolution is achieved,

the CTW can be reduced to allow a further reduction of the NRCE. This would have another benefit: with optimized DCR and CTR, the required number of coincident channels can be decreased as well, which reduces the detection threshold for lower energetic electrons that emit fewer Cherenkov photons.

10.4.2. Measured Number of Random Coincidences

The contribution of random dark events has been measured. To that end the photon detector was thoroughly covered for maximum shielding from external light. Only the dark count rate inherent in the detector contributed to the measurement. Data was taken over a period of 60 s. The analysis was performed using a CTW of 10 ns. The calculation of the expected number of random coincidences was based on the measured average DCR of all SiPM channels, which was 59.2 kcps.
Figure 10.16 shows the results: for each number of channels on the horizontal axis the number of random events is plotted that contained at least that many channels. A very good agreement between data and expectation is observed. Small deviations can occur between the measurement and the calculation due to different DCR throughout the channel matrix. It could be observed that those channels with a higher DCR are involved in a random coincident event more frequently.

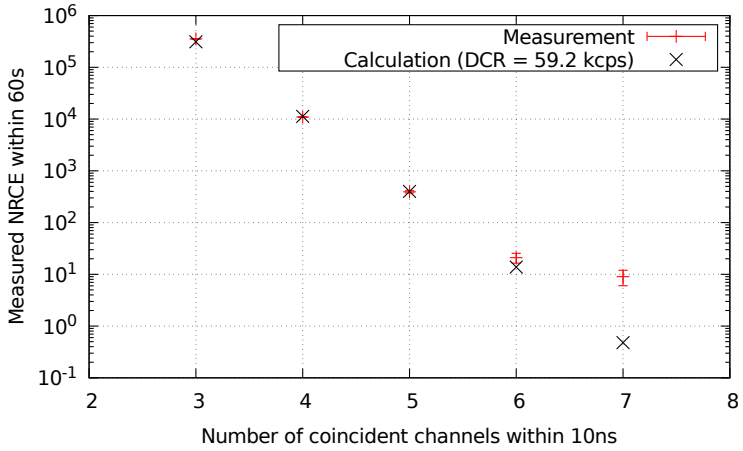

Figure 10.16.: Number of measured random coincident events in darkness over a period of 60 s. The values are compared to calculations based on equation 10.8 and using the average DCR per channel.

The data point for 7 coincident channels (which is 9 ± 3) shows significant deviation from the expected value, which was smaller than 1. Additional signals with higher numbers of coincident channels might originate from muons. These particles are created in the earth's atmosphere and have energies in the GeV range. Muons traversing the PMMA sample create Cherenkov light, which is distributed over several channels of the SiPM array. The predicted flux of muons on sea level is 1 per minute per square centimeter [Ram+12]. This value increases for higher altitudes. Given a PMMA area of $35 \times 35\,\mathrm{mm}^2 = 12.25\,\mathrm{cm}^2$, about 12 muons are expected within the measurement period. Thus, within the statistical uncertainty, the measured value of 9 ± 3 is in good agreement with this expectation value.

In fact, muons also contribute to coincidence measurements with the electron source. When the kinetic energy of a particle lies in the MeV range and above, the number of emitted Cherenkov photons per traveled distance is almost independent of the energy (see theory on Cherenkov effect section 2.1.4, figure 2.14). Thus, it is almost impossible to differentiate between a muon and an electron from the upper end of the ^{90}Sr spectrum.

Final remark on random coincicident events:
It can also be interesting to ask for the probability that an event of coincident Cherenkov photons is detected only with the help of an additional dark signal occurring within the CTW. For example, using an rnocc of 5, any event with 4 channels or less within the CTW would not be detected. For a DCR of 59.2 kcps, the probability that an event with 4 channels gets an additional fifth channel within 10 ns to be subsequently detected is

$$P(4+1) = 59.2\,\text{kcps} \cdot 60 \cdot 10 \cdot 10^{-9}\,\text{ns} = 3.6\,\%$$

The number 60 refers to the number of channels left on the array that could contribute with a dark event. Strictly speaking the above expression measures the probability for *at least one* more channel triggering within 10 ns. In general, given that in an event n channels have been triggered, the probability for at least one additional channel within the CTW can be written as

$$P(n+1) = \text{DCR} \cdot (n_{\text{Ch}} - n) \cdot \text{CTW} \tag{10.9}$$

It is worth mentioning that this probability decreases with increasing rnocc=$(n+1)$, however, only very slowly. For instance, the probability for $(6+1)$ channels is still 3.4 %.

11. Counting Coincident Cherenkov Photons

Contents

11.1 Relation between Time over Threshold and Number of Detected Photons **178**

11.2 Calibration Procedure **179**

11.2.1 Data Taking 179

11.2.2 Analysis Procedure 180

11.3 Application to Measurements **181**

11.3.1 Number of Detected Photons per Channel 182

11.3.2 Average Number of Detected Photons Per Event 184

11.3.3 Results with Various PMMA Thicknesses 186

11.3.4 Discussion 188

11.4 Applicability to Electron Energy Measurements **191**

One corner stone of the detection principle of Compton scattered photons that has been presented in chapter 5 is the deduction of information on the electron energy from the number of detected photons. Therefore, a photon counting modality needed to be found. In other words, one needs to define and measure a quantity that has a known relation to the number of detected photons. This quantity could be the deposited charge in an SiPM channel or the amplitude of a signal, or – like in the present work – the Time over Threshold (TOT).

This chapter presents the calibration of each individual detector channel so that a measured TOT value can be converted into a photon number and, thus, the number of detected Cherenkov photons can be counted. The calibration will be tested with UV transparent PMMA samples of different thicknesses and compared to results from simulation and calculation. The applicability of this photon counting method to an energy measurement of the electron will be discussed at the end of the chapter.

The first proof of the feasibility of this photon counting modality has been published in [Bay+20].

11.1. Relation between Time over Threshold and Number of Detected Photons

The general idea resides in the fact that the TOT value of a signal rises monotonously with increasing number of detected photons. The goal is therefore, to determine the relation between these two quantities to enable the calibration of each channel for photon counting. The principle is visualized in a sketch in figure 11.1.

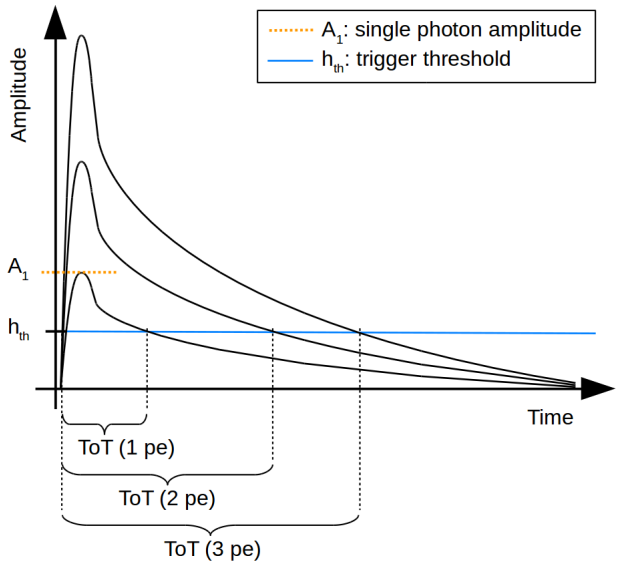

Figure 11.1.: Principle of photon counting using the Time over Threshold (TOT) of the SiPM signal. The measured ToT value increases non-linearly with the number of detected photons.

The following assumptions were made: Firstly, the rise-time τ_R of the SiPM signal is sufficiently small and especially tiny compared to the decay time τ_D of the signal: $\tau_R \ll \tau_D$. This means, the rise time of the signal plays a negligible role for the computation of the TOT and shall be ignored in the following. This assumption is justified since the SiPM used in this study has a rise time on the order of 1-2 ns. The decay time on the other hand was almost two orders of magnitude higher as will be demonstrated later in this chapter. The second assumption regarded the signal form: the falling edge behaves exponentially with the aforementioned constant τ_D. SiPMs actually have a fast and a slow time constant of the falling edge of the signal. However, given a sufficiently low trigger position (lower than the amplitude of a 1 p.e. signal), the TOT is predominantly determined by the slow time constant, which is why the fast constant is neglected in the following.
The falling edge of the signal form was therefore modeled using the following time dependent function:

$$V(t) = n \cdot A_1 \cdot \exp\left(-\frac{t}{\tau_D}\right) \tag{11.1}$$

Here, A_1 denotes the amplitude of a 1 p.e. signal while n is the number of photons creating that signal. Without loss of generality one can assume the signal to exceed the trigger

threshold h_{th} at time $t = 0$. Then, the total time $t = \mathrm{ToT}$, within which the signal stays above the trigger threshold level, can be computed using the following relation:

$$h_{\mathrm{th}} = n \cdot A_1 \cdot \exp\left(-\frac{\mathrm{ToT}}{\tau_{\mathrm{D}}}\right) \tag{11.2}$$

This can be solved for TOT and a relation between photon number n and TOT value is obtained:

$$\mathrm{ToT}(n) = \tau_{\mathrm{D}} \cdot \ln\left(n \cdot \frac{A_1}{h_{\mathrm{th}}}\right) = \tau_{\mathrm{D}} \cdot \left(\ln(n) - \ln\left(\frac{h_{\mathrm{th}}}{A_1}\right)\right) \tag{11.3}$$

There is a logarithmic dependency of the TOT on the number of detected photons n. Equation 11.3 can be solved for n as follows:

$$n = \frac{h_{\mathrm{th}}}{A_1} \cdot \exp\left(\frac{\mathrm{ToT}}{\tau_D}\right) \tag{11.4}$$

A calibration procedure must be performed to determine the two unknown parameters: the time constant τ_{D} of the signal and the trigger level h_{th} as a fraction of the 1 photon level A_1. In the following section, the procedure of data taking, analysis and calibration of every channel will be described. Afterwards, the results will be presented and limitations of this counting concept will be discussed.

11.2. Calibration Procedure

The calibration procedure consisted of the measurement of TOT values of low light signals beginning on single photon level. From these measurements, a TOT histogram for every SiPM channel individually was created, from which the photon number can be determined in the analysis algorithm.

11.2.1. Data Taking

Similar to the timing correction measurements (section 10.3), Cherenkov light was used to create coincident light signals on the array. A UV transparent PMMA sample with a thickness of 8 mm was coupled to the SiPM array and electrons from a ^{90}Sr source were used to create Cherenkov photons. The same overvoltage of 4 V as for the correction of time differences and for all further measurements was chosen. The temperature of the cooled detector was -6°C. A coincident measurement on single photon level was performed with a coincidence time window (CTW) of 5 ns and a required number of coincident channels (rnocc) of 5. Using this coincidence condition allowed for a rejection of most dark events. Dark signals mainly create single photon signals, which would not allow to record a conclusive TOT spectrum. Due to the limited size of the Cherenkov cone intersecting the array, the measurement was repeated with four different source locations to be able to cover all channels with Cherenkov light. The four source positions were the center of each of the four 16-channel sub-arrays of the detector matrix. Data was taken for a duration of 180 s at each position. Figure 11.2 shows the occupancy of the SiPM array for each of the measurements. When the source was moved to one position above one sub-array the trigger thresholds of the remaining

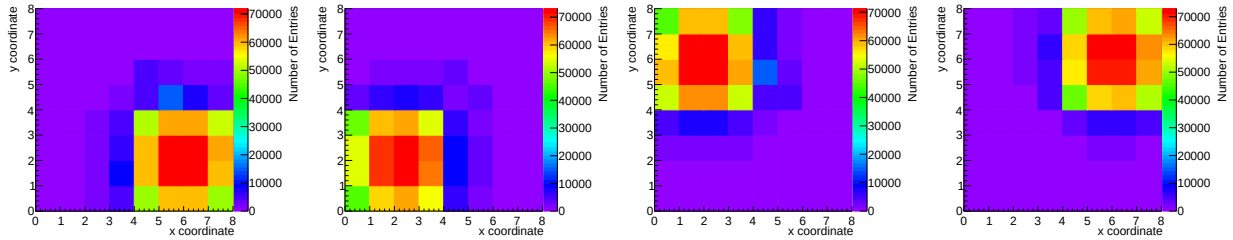

Figure 11.2.: Hit maps for the four calibration measurements with Cherenkov light. The electron source was moved to a different position above the array to sequentially cover all channels with Cherenkov light.

channels were set to a very high value to not contribute with dark events and slow down data taking and analysis procedure.
For every channel the TOT values of those signals that were involved in a coincident event were filled in a histogram with a bin width of 1.8 ns. These histograms were the basis for all further analyses and the calibration algorithm explained in the next section.

11.2.2. Analysis Procedure

A peak finding algorithm identified the peaks in the TOT histograms. A bin in the histogram was accepted as local maximum, if it had the most entries within an interval of ±3 bins. The algorithm assigned each peak an incrementing number of detected photons that contributed to that peak. The algorithm rejected any local maximum that was smaller than 10 % of the maximum peak hight in the spectrum. Figure 11.3 shows such a spectrum for one example channel, in which 7 peaks could be identified.

The ToT values of each of the peaks were then plotted against the number of detected photons. Equation 11.3 was used to perform the logarithmic calibration fit. Two parameters were used in the fit, one of which was the trigger threshold h_{Tr}/A_1 given as a fraction of the amplitude of a single photon signal. Its value should be between 0 and 1 for all channels, as the discriminator threshold was set to a trigger on 1 p.e. level. The second parameter is the slow time constant of the SiPM signal τ_{D}. The fit function for the example channel of figure 11.3 is shown right next to it in figure 11.4. For this example the obtained values were $h_{\mathrm{Tr}}/A_1 = 0.74 \pm 0.01$ and $\tau_{\mathrm{D}} = (74.5 \pm 0.3)\,\mathrm{ns}$.

Figure 11.5 demonstrates the conformity of all parameters with the expectations: all threshold values lie between 0 and 1 with a mean value of 0.63 ± 0.02, representing a trigger on single photon level. Most values lie within an interval of [0.4, 0.8] with a standard deviation of 0.13. This is shown in the top graph of figure 11.5. The threshold parameter h_{Tr}/A_1 is displayed in units of the amplitude of the 1 p.e. signal.

The time constants τ_{D} of all channels are shown in the bottom graph of figure 11.5. The mean value for the time constant is $(82.1 \pm 0.6)\,\mathrm{ns}$. All time constants lie in a narrow interval around the mean value with a standard deviation of 4.9 ns.

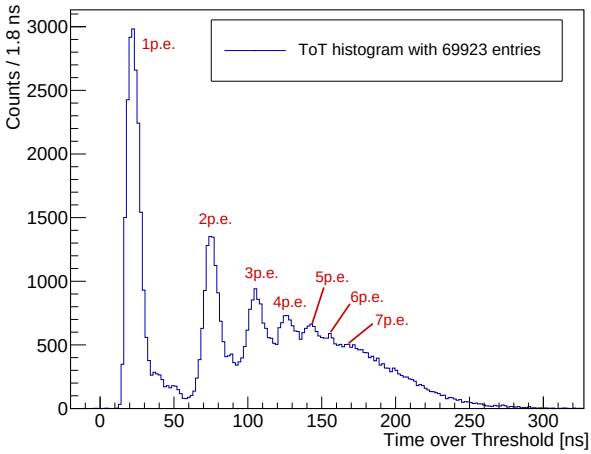

Figure 11.3.: Example of a TOT spectrum used for the calibration of one SiPM channel. Each peak corresponds to a number of detected photons.

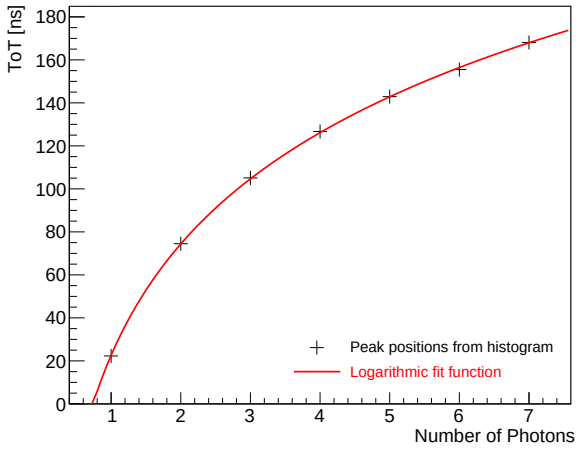

Figure 11.4.: Example of a logarithmic fit function for the calibration of a channel regarding the number of detected photons.

The relative uncertainties on both fit parameters are on the order of 1 %. The mean relative error for the time constant τ_D is 0.77 % and does not exceed 3.0 % and in case of the threshold h_Tr the mean relative error is at 1.1 % and the maximum is at 2.5 %.

The shape of the TOT spectrum can vary depending on the exact discriminator setting. This can change position and resolution of the peaks in the spectrum. Therefore, the above explained data taking and analysis procedure was performed 5 times while scanning the threshold on the 1 p.e. level. The DAC value for the threshold was varied in steps of 2 symmetrically around the center of the plateau as determined in section 9.3.1. Finally, that threshold setting that resulted in the lowest mean relative error on the parameters

$$\langle \sigma_\mathrm{rel} \rangle = \frac{1}{2} \left(\frac{\sigma_\mathrm{th}}{h_\mathrm{th}/A_1} + \frac{\sigma_\tau}{\tau_D} \right) \tag{11.5}$$

was taken for further measurement. This guaranteed the best threshold setting for the measurements and ensured the smallest uncertainties on the calculated photon number in later measurements.

11.3. Application to Measurements

The above described calibration was in the following applied to measurements with the electron source. The goal was to calculate the number of detected Cherenkov photons in every detector channel for every event. Afterwards, the average number of detected photons per event was calculated for various thicknesses of PMMA (see sections 11.3.2 and 11.3.3). Uncertainties on the obtained photon numbers are discussed in section 11.3.4. Eventually, in section 11.4, the applicability of counting Cherenkov photons to a measurement of the electron energy was investigated.

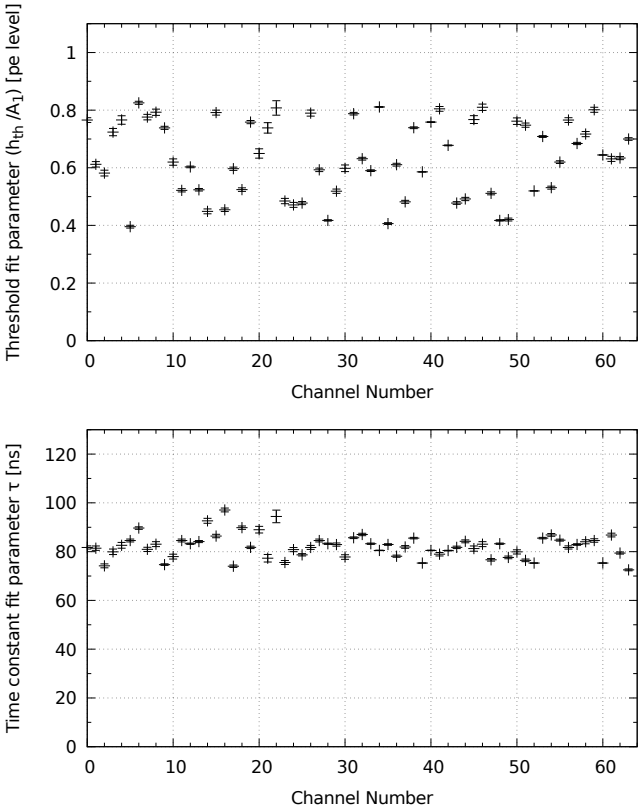

Figure 11.5.: Calibration fit parameters for all channels. The average threshold parameter given as fraction of the amplitude of the single photon signal (top graph) was $h_{\mathrm{Tr}}/A_1 = 0.74 \pm 0.01$. The average time constant of the falling edge of the signal in every channel (bottom graph) was $\tau_{\mathrm{D}} = (74.5 \pm 0.3)\,\mathrm{ns}$.

11.3.1. Number of Detected Photons per Channel

Cherenkov photons were created using electrons in UV transparent PMMA. The coincidence conditions were set according to table 10.1. As an example for this section, the photon counting will be demonstrated with a sample thickness of 8 mm. Figure 11.6 shows this measurement with a duration of 60 s. Here, figure 11.6 a) depicts the number of coincident hits per channel as it is already known from previous sections in this thesis. The color map in 11.6 b) contains the total number of detected photons in every channel accumulated over the whole measurement duration. In figure 11.6 c), the mean number of photons is shown for every channel. It was calculated using the total number of photons detected by a channel divided by the number of events that same channel was involved in. This implies that the mean value of every channel takes only those events into account, in which that channel was involved, and contributions with 0 photons do not appear in the mean value. All values are therefore greater than 1. Thus, figure 11.6 c) does *not* show the average number of detected photons for each channel *per event*, since not every channel is triggered in every coincident detection of Cherenkov photons. It rather shows how many photons were detected on average in case that corresponding channel was involved in an event.

These measurements reveal information that could not be obtained from investigating hit maps only: the channels in the center are not only involved in coincident events more

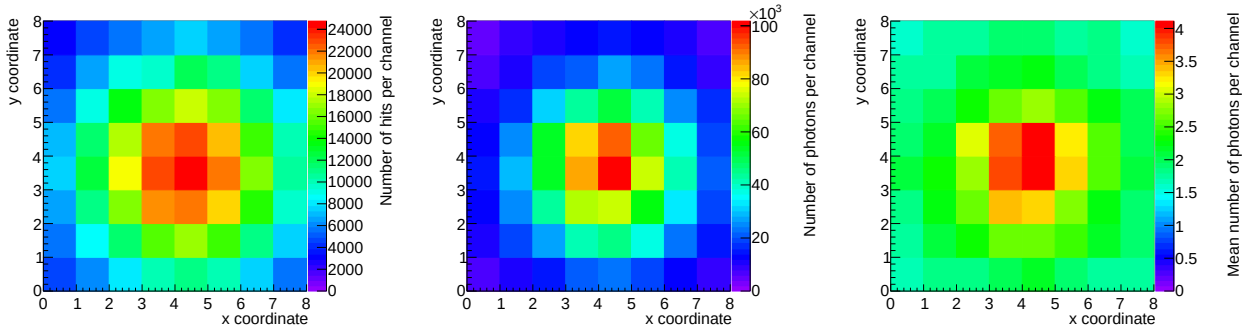

(a) Total number of coincident photon hits.

(b) Total number of photons in each channel.

(c) Mean number of photons per channel.

Figure 11.6.: Color plots for the number of hits, number of photons and mean number of photons per channel on the 64 channel SiPM array. The Cherenkov photons were created in a UV transparent PMMA sample with a thickness of 8 mm. The measurement duration was 60 s and at least 5 channels within 5 ns were required for a coincidence event.

frequently than channels at the edge of the array, but when they are, they also receive a higher number of photons at a time. The four channels in the center detected about 4 photons per event that they were involved in, whereas the ones in the corner detected only about 1.7 photons per event. In total, 38203 coincident events were registered within a measurement duration of 60 s.

A dark measurement with the same measurement parameters and coincidence conditions was performed as well. In 60 s 3333 events were measured in total. The corresponding color plots are shown in figure 11.7. Again, 11.7 a) shows the occupancy of the array with coincident hits, 11.7 b) contains the total number of photons in each channel, and 11.7 c) shows the mean value.

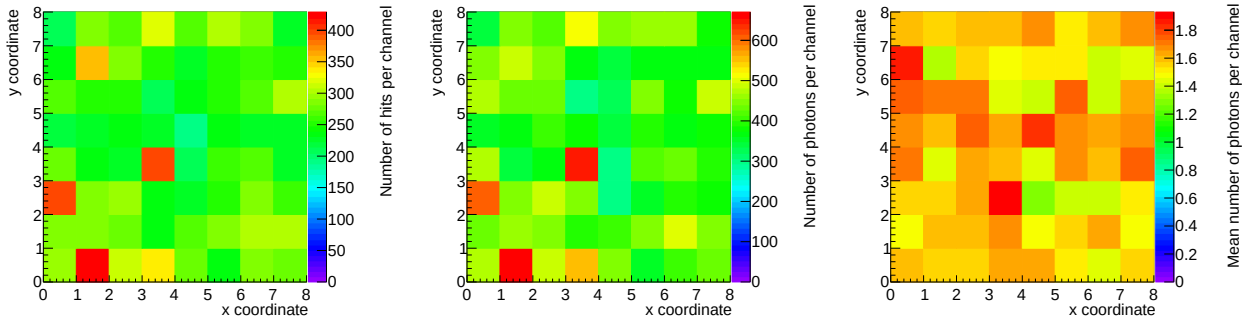

(a) Number of coincident hits in darkness.

(b) Total number of photons in darkness.

(c) Mean number of photons per channel in darkness.

Figure 11.7.: Dark measurement: color plots for the number of hits, number of photons and mean number of photons per channel on the 64 channel SiPM array. The measurement duration was 60 s and at least 5 channels within 5 ns were required for a coincidence event.

It can be deduced from figure 11.7 a) and b) that the number of events each channel is involved in is quite different, which represents the difference in DCR throughout the channel landscape. Despite the discrepancy of the total calculated number of photons in every channel, the mean values are roughly equally distributed. A mean value between 1.2 and 1.8 was found for all channels, which is reasonable considering a trigger threshold on 1 p.e. level and the fact that due to cross talk the average number of photons a channel detects is greater than 1.
Dark measurements were used to compensate for random coincident events in the measurements presented in the following.

11.3.2. Average Number of Detected Photons Per Event

In order to compare the measured photon numbers with simulations and theoretical predictions based on the algorithm from chapter 7, the mean number of detected Cherenkov photons per event had to be computed. This mean value can be seen as quantification of the Cherenkov light yield of a certain radiator sample. The measurements were conducted for all available thicknesses of 6 mm, 8 mm, 12 mm, 14 mm and 16 mm.
A dark measurement was performed afterwards with the same measurement parameters and coincidence conditions. This measurement enabled to estimate the contribution of random coincident events to the total number of detected photons.

A photon spectrum was created using the total number of photons in every single coincident event – meaning the sum of the photon numbers from those channels involved in that event. Such a spectrum is shown in figure 11.8 using an 8 mm thick sample of UV transparent PMMA. Here, the blue curve shows the raw measurement results, without a correction of the background contribution from random coincidences. The average number of detected photons per coincident event was 43.48 ± 0.22. In total 38203 coincident events were registered within 60 s.
The red curve shows the number of photons per event obtained in the background measurement. The event rate was significantly smaller than in the measurement where the electron source was applied. In 60 s 563 events were measured in total.[1] On average 11.01 ± 0.46 photons were registered per random coincident event. Due to a few extraordinarily high photon numbers – the origin of which will be discussed in section 11.3.4 – the mean value is distorted and appears to be higher than one might expect from a dark measurement. Based on the rnocc and the average light level a channel detects in darkness per random coincident event that it was involved in, a mean value of less than 10 can be expected. Using the median instead of the mean value, can give a more realistic result: The median of the photon number distribution in darkness is 7.5 for this measurement.
The green curve finally shows the corrected spectrum, where the dark contribution has been subtracted. The background subtraction only considers random coincident events where a certain number of channels $n \geq$ rnocc formed a valid coincident event. It does, however, not

[1] This is not the same dark measurement as the one shown as an example in figure 11.7. They were performed on two different days. A dark measurement needed to be performed on the same day as the measurement with the PMMA samples to ensure identical conditions – especially constant temperature. Otherwise the estimation of the contribution of random coincident events becomes inaccurate.

compensate for additional dark signals occurring within the CTW of a valid Cherenkov event. The probability to have an additional dark event within the coincidence time window depends on DCR and CTW and has been calculated in section 10.4. Even though this probability is only in the lower percent range, the contribution of dark events will eventually cause a slight overestimation of the average number of detected photons obtained from the spectrum.

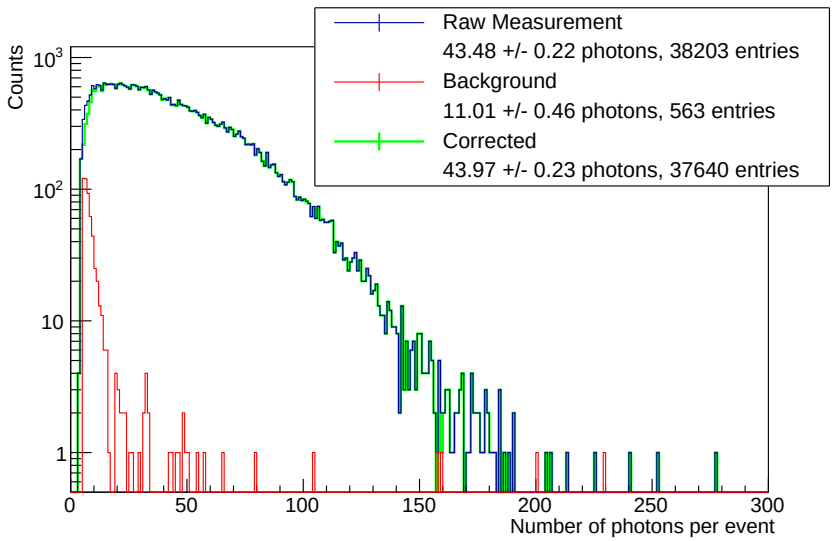

Figure 11.8.: Spectrum of the number of detected photons in an 8 mm thick sample of UV transparent PMMA. The raw measurement result is plotted in blue color and the background consisting of random coincidences is shown in red. The background corrected spectrum is drawn in green color. The influence of random coincidences is on the order of 1 %.

For the background corrected spectrum (green curve) the mean value was calculated and for this specific sample thickness a value of 43.97 ± 0.23 photons was obtained. 37640 events were measured in total. Photon spectra and calculated mean values for other sample thicknesses can be found in the addendum in figure A.2. The statistical uncertainty was calculated as the mean value divided by the square root of the number of events (see addendum A.2.1 for details on the calculation of uncertainties of photon numbers from photon spectra). The contribution of random coincidences to the photon number is on the order of 1 %.

Due to the non mono-energetic electron source, the spectrum has a broad distribution. Photon numbers larger than 200 per event were counted. For the peak energy in the spectrum of about 2.4 MeV the calculated number of created photons is 584 using the calculation algorithm described in chapter 7. A total number of 159 detected photons is predicted for that electron energy and that specific detector geometry and sample property, which is significantly smaller than the largest values obtained in the measurements. Although the number of generated and detected photons is subject to statistical fluctuations, a photon number of ≥ 200 seems exceptionally high and points towards the presence of additional effects and influences. These influences are discussed in section 11.3.4.

11.3.3. Results with Various PMMA Thicknesses

The above presented coincidence measurement was performed for different thicknesses of UV transparent samples of PMMA Since only a thickness of 6 mm and 8 mm was available as one piece, thicker radiators were created using optical grease. That way, also 12 mm, 14 mm and 16 mm thick samples could be built. In case of a thickness of 14 mm, the 6 mm sample was stacked on top of the 8 mm sample.

The results of these measurements are shown in figure 11.9 in black color. All measurement results are also listed in column 2 of table 11.1.
The mean number of detected photons per event decreases with growing PMMA thickness. Due to the increasing distance photons have to travel in thicker samples, the absorption reduces the number of photons reaching the read-out area. Furthermore, above a thickness of 11.8 mm, the Cherenkov cone exceeds the boundaries of the SiPM array and a certain fraction of photons is lost. Finally, multiple scattering influences the number of detected photons as well: due to the change of momentum direction of the electron along its trajectory the Cherenkov cone points in different directions as well. Thus, some photons would be emitted beyond the sensitive area and not be detected. The farther above the array the emission takes place, the larger the fraction of photons that are being lost due to this effect. This contributes to the increasing light loss of photons for greater PMMA thicknesses.

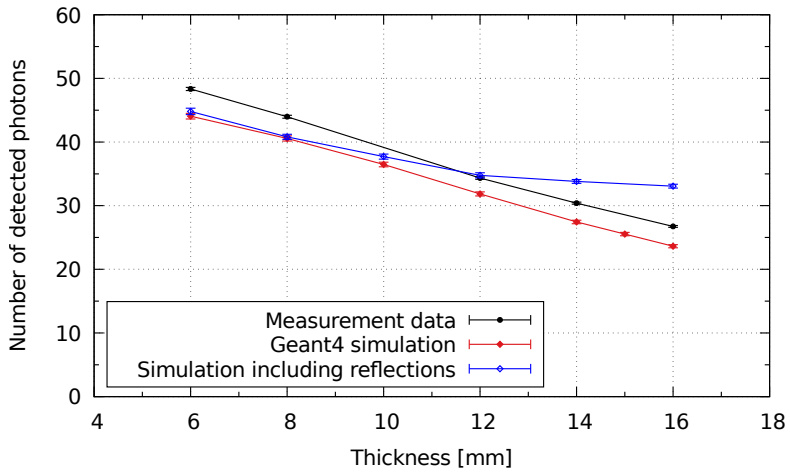

Figure 11.9.: Comparison of the number of detected photons for different thicknesses of UV transparent PMMA obtained from measurements (black) and simulations with (blue) and without (red) reflections off the side walls of the sample [Bä20a]. The data points were connected with lines to help visualize the development of every data set with varying thickness.

In the same graph, simulation results are presented as well for comparison. They can also be found in column 3 and 4 of table 11.1. For every thickness, 10000 electron events were simulated and only those events that involved at least 5 channels were considered in the analysis. Two data sets are shown, one of which includes reflections of photons from the side wall of the PMMA sample (blue points). The surfaces were defined as perfectly smooth and the refraction indices of air ($n = 1$) and PMMA ($n = 1.49$) were used to calculate the

reflectivity at the border between the two media [Bä20a]. For the other data set (red points) photons were absorbed once they reached the side wall.

The obtained values for both sets are very similar for a thickness of 6 mm and 8 mm, but show increasing deviation towards larger thicknesses. The Cherenkov cone increases for larger thicknesses and more photons reach the sidewalls and are potentially reflected back onto the sensitive detector volume. Therefore, the blue data points are significantly higher for a thickness of 12 mm and more.
A comparison to the measurement data suggests that the red data set, which does not consider reflections, represents the qualitative behavior of the measurements better than the blue data set. This can be deduced from the slope of the data points: while in the simulation with reflections the slope becomes smaller for larger thicknesses, no such change is observed in the measurement and in the simulation that did not incorporate reflections.
Absolute values deviate, however. On average, the measured mean values are by about 3.2 photons per event higher than the simulated ones. The reasons for these deviations can be sorted into two groups: there are on the one hand systematic uncertainties on the measurement parameters and the quality of the set-up and on the other hand there are uncertainties that arise from the photon counting method itself.
To the first group, one can count the uncertainty on the measured temperature, which has a large influence on the overvoltage, which in turn determines the PDE. Different PDEs in simulation an measurement give rise to discrepancies. Furthermore, the aforementioned occurrence of additional dark events within the CTW causes a slight increase of the obtained mean value of the photon number. Finally, all samples larger than 8 mm were made of two thinner samples glued together with optical grease. The amount of light that is lost at the boundary between the two layers is unknown. It might be considered small, since there is only a small difference in the refractive index of both samples ($n = 1.49$) and the layer of grease ($n = 1.47$, [Sai16]) in between.
The second group of uncertainties are inherent in the photon counting method and originate from several influences. Amongst these influences are the occurrence of after pulses on the falling edge of the signal and the timing jitter limiting the accuracy of the TOT measurement. These uncertainties are described and discussed in more detail in section 11.3.4.

Finally, the obtained measurement results were also compared to calculated expectation values based on the algorithm described in chapter 7. The calculated values are shown in figure 11.10 and in column 5 of table 11.1. The computation was performed for all thicknesses that were also available in the measurements. In the algorithm the difference in the material quality between 6 mm and 8 mm sample was taken into account – in contrast to the simulation. However, the deviation from the measurement is quite significant for some thicknesses and especially for 6 mm and 8 mm the general trend is not reproduced. The calculations predict a slight increase between 6 mm and 8 mm, whereas the measurement shows a decreasing number of photons throughout the whole range of thicknesses. The accuracy of the calculation is limited due to the negligence of multiple scattering and surface reflections. The calculation used the range tables provided by NIST to compute the total number of photons. The range describes the distance between the end point of the electron trajectory from the start point. However, due to multiple scattering, the total path length of the electron is larger and, thus,

more photons are created than predicted by the calculation based on the range. This might explain the higher mean value obtained from the measurement for 6 mm and 8 mm thickness in comparison to the calculated value.
The agreement between calculation and measurement improves for larger sample thicknesses: both data sets show decreasing values, which represents the loss of photons due to limited detector geometry and increasing photon absorption inside the sample.

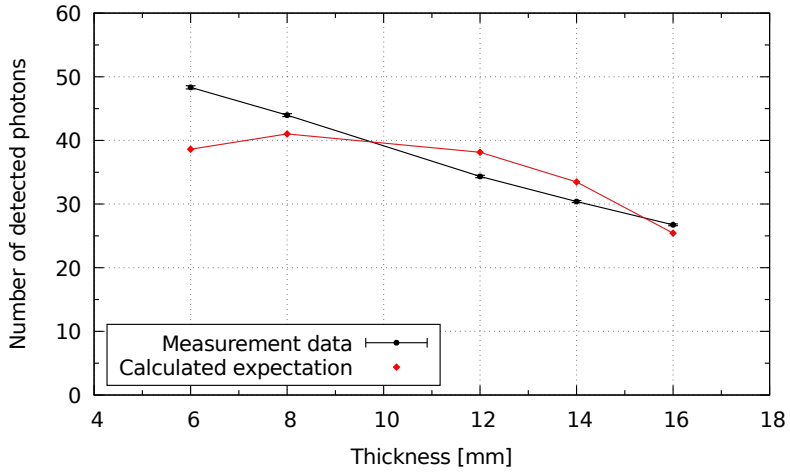

Figure 11.10.: Comparison of the number of detected photons for different thicknesses of UV transparent PMMA obtained from measurements (black) and calculations (red). The data points were connected with lines to help visualize the development of every data set with varying thickness.

	Average Number of Photons			
Thickness [mm]	**Measurement**	**Simulation [a] without reflections**	**Simulation [a] with reflections**	**Calculated estimation**
6	48.34 ± 0.25	44.06 ± 0.44	44.81 ± 0.5	38.62
8	43.97 ± 0.23	40.56 ± 0.41	40.81 ± 0.4	41.03
10	-	36.47 ± 0.36	37.71 ± 0.4	-
12	34.33 ± 0.18	31.85 ± 0.32	34.77 ± 0.4	38.14
14	30.39 ± 0.16	27.44 ± 0.27	33.81 ± 0.3	33.47
15	-	25.54 ± 0.26	-	-
16	26.74 ± 0.14	23.63 ± 0.24	33.07 ± 0.3	25.44

Table 11.1.: Comparison of the number of detected photons for different thicknesses of UV transparent PMMA obtained from measurements, simulations and calculations. [a] Simulation performed using Geant4 [Bä20a].

11.3.4. Discussion

The presented results demonstrate the countability of Cherenkov photons from electrons in PMMA using SiPM arrays. The influence of physical and geometrical properties of the

sample on the photon number has already been discussed. However, the results also exhibit some uncertainties originating from the photon counting method itself that shall be addressed in the following.

Starting from the calibration process, one uncertainty arises from the identification of the peaks in the histogram. As seen in figure 11.3, the peaks appear increasingly smeared out, reducing the accuracy on the peak positions and subsequently giving rise to the uncertainty on the fit parameters of that channel. However, the relative uncertainty on the fit parameters is only on the order of 1 %, so that the uncertainty on the obtained number of photons mainly depends on the accuracy of the TOT measurement of the signal, as discussed in the next paragraphs.

In the development of the photon calibration algorithm in section 11.1 the rise time of the signal has been ignored and only the falling edge has been considered for the derivation of formula 11.3. In an actual measurement, the rise time of the signal contributes to the TOT value of a signal. The measured TOT value consists of the rising and the falling part of the signal. The ratio of the contributions from rising and falling edge depends on the number of detected photons as could be shown in connection with the TOT dependent time difference corrections in section 10.3. For a given number of photons, this ratio is a constant, which is why the influence of the rise time on the photon counting process can be neglected not only for the development of the calibration function but also in the actual measurements.

The occurrence of after pulses on the falling edge of a signal constitutes a large source of uncertainty. The influence is explained schematically in figure 11.11.

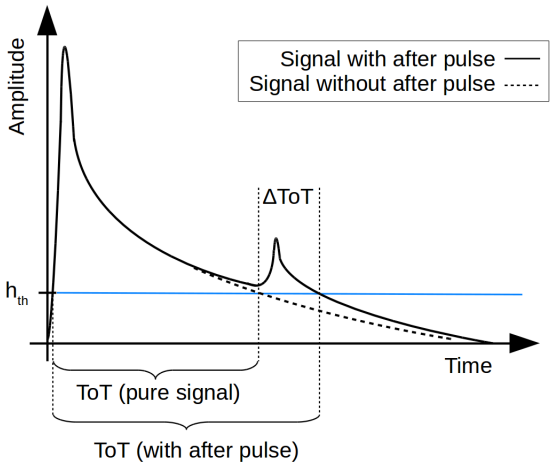

Figure 11.11.: Visualization of the influence of after pulsing on the measured Time over Threshold. The TOT value is increased significantly and the corresponding photon number is vastly overestimated.

The presence of an additional peak on the falling edge of an SiPM signal significantly increases the measured TOT value. Due to the logarithmic relation between the TOT value and the number of detected photons, an after pulse can severely distort the calculated photon number. Furthermore, the influence becomes more prominent for larger signals. As an example, an

SiPM signal with a time constant of $\tau_D = 80\,\text{ns}$ is considered, which is detected with a trigger threshold at $h_{\text{Tr}}/A_1 = 0.5$. For this configuration the 1 p.e. signal creates a TOT value of 55 ns. If an increase of this TOT value by 20 ns is assumed due to the presence of an after pulse, the calculated photon number would be 1.28 and would still be considered a 1 p.e. signal. For a 4-photon signal creating a TOT value of 166 ns, however, the same extension of 20 ns would result in a calculated photon number of 5.1. This photon number is off by more than 25 % compared to the real number of detected photons. Analogously, the same extension occurring on a 100-photon signal, would cause the obtained photon number to increase to 129. One can easily imagine that – depending on the position and amplitude of the after pulse and depending on the number of detected photons – the distortion can make the photon number grow to unrealistically high values.
This provides an explanation for the occurrence of high photon numbers as seen in the photon spectrum in figure 11.8. Unfortunately, with the read-out system used for this study, no filter method can be applied for the rejection of events that contain an after pulse in one of the signals. For that, some sort of wave form analysis would have to be implemented, which is not feasible for an implementation on a fast timing ASIC. For typical devices the after pulse probability is on the order of a few percent [Din13].
Due to the statistical nature of the amplitude and occurrence of after pulsing, a quantification of its influence on the measured photon numbers and the mean value was not possible in the scope of this investigation.

Finally, the measured TOT signal is subject to statistical fluctuations due to timing jitter. This effect has already been described in connection with the rise time of a signal, however, the influence is stronger on the falling edge, due to its dependence on the slope of the signal. The slope of the falling edge can be approximated assuming an exponential decay and the derivative of equation 11.1:

$$\frac{\mathrm{d}V(t)}{\mathrm{d}t} = -\frac{n \cdot A_1}{\tau_D} \cdot \exp\left(-\frac{t}{\tau_D}\right) \tag{11.6}$$

Using $t = \text{ToT}$ and employing equation 11.3 one obtains

$$\frac{\mathrm{d}V(t)}{\mathrm{d}t} = -\frac{h_{\text{Tr}}}{\tau_D} \tag{11.7}$$

which is independent of the amplitude of the signal and therefore constant for all measured TOT values. The size of the 1 p.e. peak has been determined in section 9.3.1 to be about 52.5 mV and the mean time constant for all channels was 82.1 ns. The value of the slope is therefore $\frac{\mathrm{d}V(t)}{\mathrm{d}t} = -639.5\,\text{kV/s}$. Thus, the timing jitter was estimated assuming a reasonable noise level of $\sigma_{\text{noise}} = 2\,\text{mV}$:

$$\sigma_{\text{time}} = \frac{\sigma_{\text{noise}}}{|\mathrm{d}V/\mathrm{d}t|} = \frac{2\,\text{mV}}{639.5\,\text{kV/s}} \approx 3\,\text{ns} \tag{11.8}$$

The influence of timing jitter on the obtained photon number is negligible for small signals in the 1 p.e. vicinity. However, the influence increases for larger TOT values, which originate from larger photon numbers:

The assumed noise level of 2 mV is not based on a measurement and, thus, an exact value for the timing jitter was not available. Therefore, a precise quantification of the uncertainty on the photon number due to timing jitter could not be performed.

Nevertheless, one can derive a general relation between the uncertainty on the photon number n and the uncertainty on the measured TOT value based on formula 11.4. Basically, a change of the TOT by a value of ΔToT causes a change of the measured photon number from n to $n + \Delta n$. Thus,

$$n + \Delta n = \frac{h_{\text{th}}}{A_1} \cdot \exp\left(\frac{\text{ToT} + \Delta\text{ToT}}{\tau_D}\right), \tag{11.9}$$

which allows to compute the relative uncertainty on the photon number:

$$\frac{\Delta n}{n} = \exp\left(\frac{\Delta\text{ToT}}{\tau}\right) - 1 \tag{11.10}$$

For a given uncertainty ΔTOT this implies a constant relative uncertainty on the measured photon number or – to put it in other word – proves that the uncertainty is proportional to the number of detected photons itself:

$$\Delta n \propto n \tag{11.11}$$

Using the example of $\Delta\text{ToT} = \sigma_{\text{time}} \approx 3\,\text{ns}$, a trigger threshold at 0.5 p.e. level and a time constant of 80 ns, the relative uncertainty on the photon number is about 4 %.

Because of the above derived relations it can be concluded that the measurement of the number of detected photons has the highest accuracy at small photon numbers, ideally on single photon level.

11.4. Applicability to Electron Energy Measurements

The detection concept for Compton electrons using Cherenkov light as described in chapter 5 includes the measurement of the electron energy by counting the number of detected photons. The energy transfer from the incoming higher energetic gamma onto the Compton electron is an essential part of the kinematic information contained in the whole scattering process and is required to reconstruct the origin of a gamma of unknown energy.

This section investigates the ability to measure the energy of electrons by the number of detected Cherenkov photons emitted by that electron in an optically transparent radiator material. To that end, a ^{207}Bi source was used to create Cherenkov light in a UV transparent PMMA sample. The spectrum of this source, which was measured with a Silicon-based semiconductor detector, is shown in figure 11.12. The vertical red line in the graph indicates the threshold for the Cherenkov effect, which according to formula 2.13 is at 177 keV for a refractive index of 1.49.
Several prominent lines can be seen in the spectrum originating from internal conversion. This is a radioactive decay process, in which an orbital electron couples to an excited state

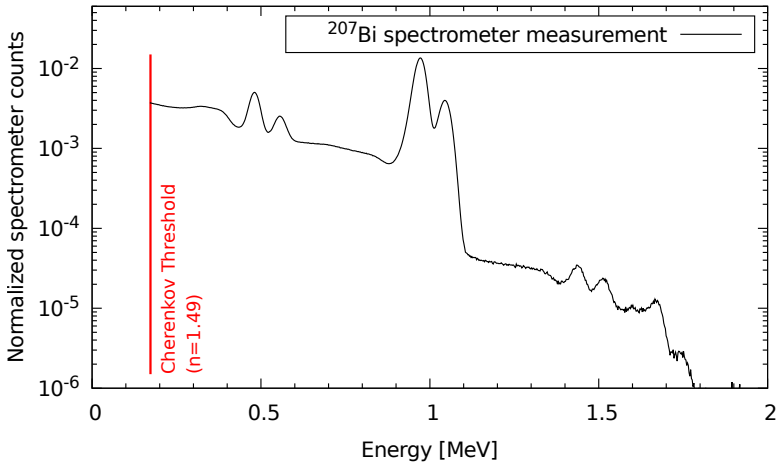

Figure 11.12.: Spectrum of a ^{207}Bi source. The neighboring peaks originate from internal conversion and can be used for energy calibration.

of the nucleus, which subsequently causes the electron to be emitted from the atom [Ros66]. In this case, the excited state is formed through the decay of ^{207}Bi to ^{207m}Pb via electron capture with a half life of 31.55 years [CEF99]. The energy released during the de-excitation of the Pb nucleus can either be transferred to a gamma or to the aforementioned internal conversion electron. The energy of that electron equals the energy of the excited state minus the binding energy of the electron in its shell. The individual lines in the ^{207}Bi spectrum represent conversions of electrons from different atomic shells. The two peaks at 482 keV and 553 keV represent conversion electrons from the K-shell and L-shell, respectively, and correspond to a de-excitation energy of ^{207m}Pb of 570 keV. Analogously, the two peaks at 975 keV and 1048 keV originate from K- and L-shell conversions based on a de-excitation energy of 1063 keV [LHP67]. The occurrence of the higher energetic peaks at about 1700 keV is considered too small to be used for this calibration.

Assuming that an electron of a certain energy produces a specific amount of photons, these distinct lines in the energy spectrum should also appear in a Cherenkov photon spectrum. Using the calculation program from chapter 7 a spectrum of the computed number of detected photons was created. It is shown in figure 11.13.
No threshold on the detected photon number per incident electron was set and all events were accepted. In the spectrum the peaks corresponding to 975 keV and 1048 keV can still be resolved and appear at photon numbers between 40 and 60. The two peaks at 482 keV and 553 keV are not resolved any more and appear as one peak between 10 and 25 photons. The energy values below these peaks create very little Cherenkov emission and cause the pile up at the lower end of the Cherenkov photon spectrum.

The calculation does not take reflections into account and does not include statistical fluctuations in the number of created Cherenkov photons per electron. Even though these idealized conditions are used the resolution is worse than in the energy spectrum.
This can mostly be explained by the fact that photon numbers are discrete integer values and

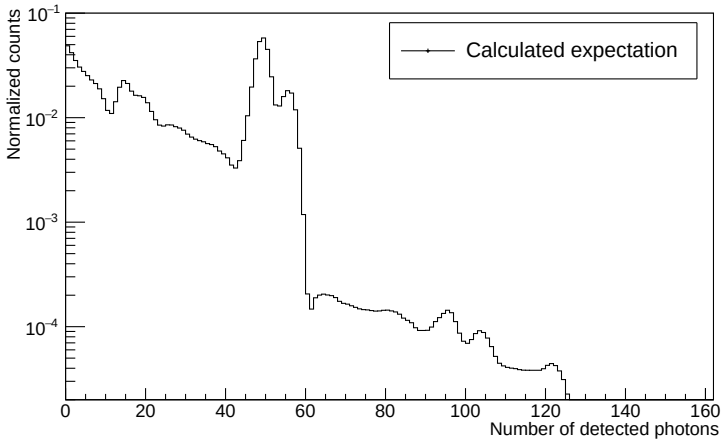

Figure 11.13.: Expected spectrum of detected Cherenkov photons created by electrons from a ^{207}Bi source. The peaks at 975 keV and 1048 keV can still be resolved.

furthermore by the scarcity of Cherenkov photons. Therefore, the spectrum only contains about 130 bins, whereas in the energy spectrum the depicted range contains almost 7000 bins. Furthermore, due to the Cherenkov threshold the photon spectrum appears to be shifted towards the lower end and features in the low energetic range of the spectrum appear squeezed together or cannot be displayed at all.

A long term measurement with a ^{207}Bi source was performed. Measurement data were collected over a total period of 120 min resulting in about 188000 coincident Cherenkov events consisting of 5 or more channels within a CTW of 5 ns. The obtained Cherenkov photon spectrum is shown in figure 11.14.

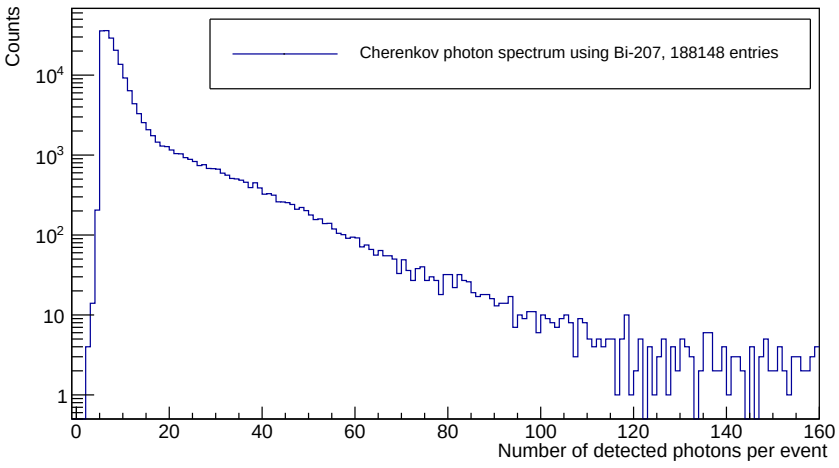

Figure 11.14.: Cherenkov photon spectrum measured with electrons from a ^{207}Bi source in a 8 mm thick sample of UV transparent PMMA. The distinct energy values cannot be reproduced in the measurement.

The measured spectrum could not reproduce the predicted peaks that appeared in the calculated spectrum at a position between 40 and 60 photons. One could argue that an accumulation is found at around 40 photons, but its width is too large to even attempt the calculation of an energy resolution with a gauss fit. Due to the large number of events it cannot be assumed that the peaks have been blurred out due to statistical uncertainties.

The possible reasons for the missing peak structure in the measured spectrum can be divided into two groups: physical and methodical reasons, both of which are of statistical nature. The first group comprises physical influences like multiple scattering of the electron, which on the one hand deflects the Cherenkov cone so that photons leave the sensitive area and which on the other hand causes statistical variations in the track length of the electron. The latter one has significant influence on the number of generated Cherenkov photons. Thus, it could be shown in simulations that the number of emitted photons for a fixed electron energy has a large standard deviation [Bä20a]. The distribution of the number of emitted Cherenkov photons has already been discussed in chapter 7 and has been shown in figure 7.2. The limited detector area causes light loss and the surface quality of the PMMA sample regarding reflections constitute further physical influences distorting the resolution in the spectrum.

Finally, the number of detected photons n_d strongly depends on the PDE and is binomially distributed around the expectation value of $n_d = n_i \cdot p$, with n_i the number of impinging photons and $p = 58.2\,\%$ the maximum probability for the detection of a photon at a wavelength of 450 nm and at an overvoltage of 4 V. Moreover, the PDE is wavelength dependent.

The methodical group of influences contains all uncertainties inherent in the photon counting method as they have been discussed in the previous section of this chapter. The most prominent uncertainty could be given by the influence of after pulses on the falling edge, which contributes to the spectrum with either distorted or very high photon numbers. This is also an explanation for photon numbers far above a value of 125, where the calculated prediction does not obtain any entries. The use of larger arrays with more, yet smaller, channels might be beneficial for the outcome of this measurement. Uncertainties on the measured photon number grow strongly for increasing photon number, as has been demonstrated in the previous section. Limiting the channel size could help distribute the photons over more read-out channels and, thus, detecting fewer photons in each individual channel. This might help reduce the uncertainty.

The first group of influences – the physical influences – are very hard to eliminate or even reduce as they are properties of physical effects taking place inside the detector and therefore inherent in the concept of detection itself. Increasing the size of the array and optimizing the detection efficiency is also only possible to a finite extend.

The largest part of the improvement must therefore be done through a methodical change of the photon counting modality: instead of using the TOT value, the charge deposited in each channel must be used to compute the photon number. Due to the linearity between charge and detected number of photons, a calibration with lower uncertainties is possible, which

is furthermore stable over a large range of photon numbers. However, a charge integrating ASIC capable of triggering on single photon level with sufficient charge sensitivity for photon counting was not commercially available at the time this thesis was written.

Summarizing, the electron energy could not be reconstructed by counting the number of detected Cherenkov photons emitted in PMMA. This might have severe impact on the applicability of this electron detection principle to Compton scattered electrons. Since the energy is required to be able to determine the opening angle of the Cherenkov cone – especially at lower electron energies – and to reconstruct the electron momentum and vertex position correctly, significant improvements need to be implemented. As pointed out, one promising improvement is the use of the charge signal instead of the TOT signal to count the detected photons.
A comparison to simulations in Geant4 substantiates this conjecture. In the simulation photon numbers are not impaired by uncertainties in the measurement method. A simulated spectrum with 10^6 electrons from a ^{207}Bi source is shown in figure 11.15. A peak can be seen with a maximum at 43 photons. This corresponds to electrons from the double peak with energies of 975 keV and 1048 keV, respectively. At low photon numbers, a pile up of low energetic electrons can be seen until a cut off occurs at the rnocc, which was 5. Even though the resolution is significantly worse compared to the energy spectrum in figure 11.12 or the calculated photon spectrum in figure 11.13, an improvement can be seen compared to the actual measurement where no peak occurred (figure 11.14). This is a strong indication that a change of the photon counting modality – using charge instead of TOT – is beneficial for future energy measurements based on the number of Cherenkov photons.

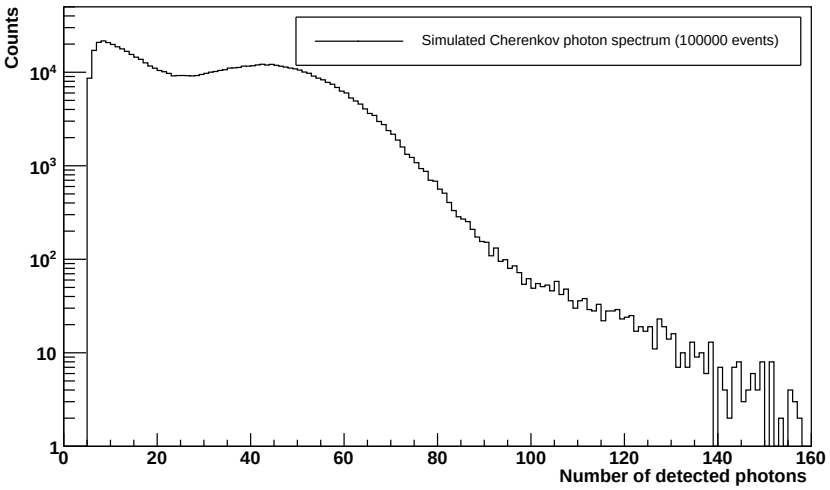

Figure 11.15.: Simulated Cherenkov photon spectrum with electrons from a ^{207}Bi source in an 8 mm thick sample of UV transparent PMMA. 10^6 events contribute to this plot. An improvement is observed compared to the measurements.

Part III.

Applicability to Photon Detection

12. Detection of 511 keV Photons

Contents

12.1 Dual-Face Coincidence Set-Up **200**
12.1.1 Details on the Instrumentation 200
12.1.2 Scintillation Materials and Photon Detectors 203
12.2 Data Processing and Analysis Method **205**
12.2.1 Preselected Events 205
12.2.2 List Mode Data 206
12.3 Detector Configuration and Parameter Setting **207**
12.3.1 Measurement Settings 208
12.3.2 Analysis Parameters 210
12.3.3 Correction of Inherent Time Differences 213
12.4 Characteristics of the Coincidence Measurement **214**
12.4.1 Quality of the Measurement Signal 214
12.4.2 Energy cut on 511 keV 217
12.4.3 Measured coincidence rate 218
12.4.4 Coincidence time resolution (CTR) 219
12.5 Efficiency Estimation for the Detection of 511 keV Photons **220**
12.5.1 Derivation of the Efficiency 220
12.5.2 Method Description 221
12.5.3 Background Estimation 223
12.5.4 Efficiency Estimation for NaI and $LaBr_3$(Ce) 227
12.5.5 Investigation of Systematic Uncertainties 227
12.5.6 Final Result and Discussion 230
12.6 Comparison to Simulation Results **231**
12.6.1 Implementation 231
12.6.2 Results and Discussion of Systematic Uncertainties 232
12.6.3 Efficiency at Higher Photon Energies 233
12.7 Further Measurements with the Cherenkov Detector **234**
12.7.1 Detected Pattern of Coincident Hits 234
12.7.2 Counting Cherenkov Photons from Compton- and Photoelectrons 236
12.7.3 Variable Gamma Source Positions 240

12.8 Summary of the Detection of 511 keV Photons **242**

The detection of Cherenkov photons from electrons is now applied to actual Compton scattered electrons created by 511 keV photons inside the radiator material. This chapter describes the set-up for this detection and its components as well as the developed analysis algorithm. All used settings and measurement parameters will be presented and discussed. The efficiency for the detection of 511 keV photons from a ^{22}Na source using Cherenkov light from Compton scattered electrons will be derived and calculated. The set-up will be characterized with respect to coincidence time resolution and its ability to count the number of detected photons. The response of the measured pattern from accumulated events to a shift in the gamma source position will be demonstrated.
The very first test results obtained in 2019 have also been presented and published in a conference record [Bay+19b].

12.1. Dual-Face Coincidence Set-Up

For the detection of photons via Cherenkov light from Compton scattered electrons, a set-up similar to a PET system was chosen:
In the center of the set-up was a ^{22}Na source, emitting positrons into a PMMA sample where annihilation with an electron takes place. In this process two 511 keV photons are sent out in opposite directions to be detected in coincidence. On one side of the arrangement, a detector containing a scintillation crystal was placed to identify an annihilation event with the emission of the two photons. The detector for Cherenkov light as it was described in chapter 9 was located opposite of it.
The reason for arranging the detectors in a dual-face set-up was twofold: Firstly, background reduction is possible through the use of a coincidence measurement between the two detectors. Secondly, the efficiency for the detection of Compton and photo electrons using Cherenkov light can be estimated (section 12.5).
The following section describes the set-up in more detail, afterwards the scintillation detector is presented and characterized.

12.1.1. Details on the Instrumentation

The radioactive source ^{22}Na:
The set-up is shown schematically in figure 12.1. A ^{22}Na source forms the heart of the system. This isotope undergoes beta-plus decay followed by the emission of two annihilation photons of 511 keV energy each corresponding to the rest mass of an electron or positron respectively. Subsequent to the de-excitation of the daughter nucleus ^{22}Ne a single gamma of 1.27 MeV is emitted [CEF99]. Thus, the energy spectrum contains two dominating peaks at 511 keV and 1.27 MeV.
The radioactive source of flat shape (shown in black in the sketch) emits its positrons into a circular plate of PMMA with a diameter of 15 mm. Source and PMMA sit in a small aluminum container with two windows on opposite sides so that the photons can exit (see

figure 12.3, number 3). Given these dimensions, the source is 2.5 cm away from each exit hole in the block. Photons are emitted isotropically in all directions, but only those photons can be detected, that are emitted into the solid angle between the holes in the block and the source location. The latter is assumed to be point-like, which is not entirely correct, as the ^{22}Na source is not a point-source itself and the emitted positrons have a certain range in PMMA. However, for further estimations of the solid angle, a point-like source is assumed. The aluminum source container is placed inside a lead block with 5 cm thickness, which also has two circular windows for the photons, with a diameter of 1 cm. Assuming a point-like source, the solid angle as a fraction of the full $4\,\pi$-angle is calculated as follows:

$$\Omega = \frac{2 \cdot A}{A_{\text{sphere}}} = \frac{2 \cdot 0.5^2 \cdot \pi}{4\,\pi\,r^2} = \frac{1.57\,\text{cm}^2}{78.54\,\text{cm}^2} = 0.02 = 2\,\%$$

The activity of the source when purchased was $A_0 = 40.7\,\text{MBq}$ (Mega-Becquerel). At the time of the measurement the age of the source was 21.5 years, which is about 8.3 half-lives. Given a half-life of 950.5 days or 2.604 years the activity at the time of the measurement can be estimated:

$$A_{\text{today}} = 40.7\,\text{MBq} \cdot \left(\frac{1}{2}\right)^{21.5/2.6} = 133.1\,\text{kBq}$$

Together with the aforementioned solid angle, one expects an effective activity of

$$A_{\text{eff}} = 133.1\,\text{kBq} \cdot 0.02 = 2.7\,\text{kBq}$$

that can be used for the detection. The number of photons emitted is reduced by Compton scattering or absorption within the PMMA. With the assumption of a point-source in the center of the PMMA slab, the average distance the photon has to travel through PMMA before exiting the block is 0.75 cm. The absorption coefficient $\mu = 9.410 \cdot 10^{-2\text{cm}^2/\text{g}}$ [Sel96] for 511 keV photons in PMMA yields a free mean path of 9.709 cm.
Employing formula 2.29, the probability for an interaction inside the PMMA is 7.43 %. Thus, the estimated effective activity is reduced to

$$A_{\text{eff}} = 2.662\,\text{kBq} \cdot (1 - 0.0743) = 2.464\,\text{kBq} \tag{12.1}$$

An exact value for the interaction probability had to be generated with the help of Geant4 simulations, due to the complex, non-point-like source geometry and the non-negligible positron range in the annihilator medium. In a simulation of 100000 events, a probability of $(7.79 \pm 0.09)\,\%$ for the photon to interact inside the PMMA was obtained [Den20]. This value is in good agreement with the theoretical prediction of 7.43 %.

Detector arrangement:
A photo of the set-up with corresponding explanations is shown in figure 12.2. Some parts of the set-up were movable to enable good alignment of the photon beam line with respect to the detectors and also to choose different gamma source locations. The scintillator is mounted on a platform movable via worm gears in direction perpendicular to the beam line of the photons. Also, the platform can be moved collinear to the beam to adjust the distance

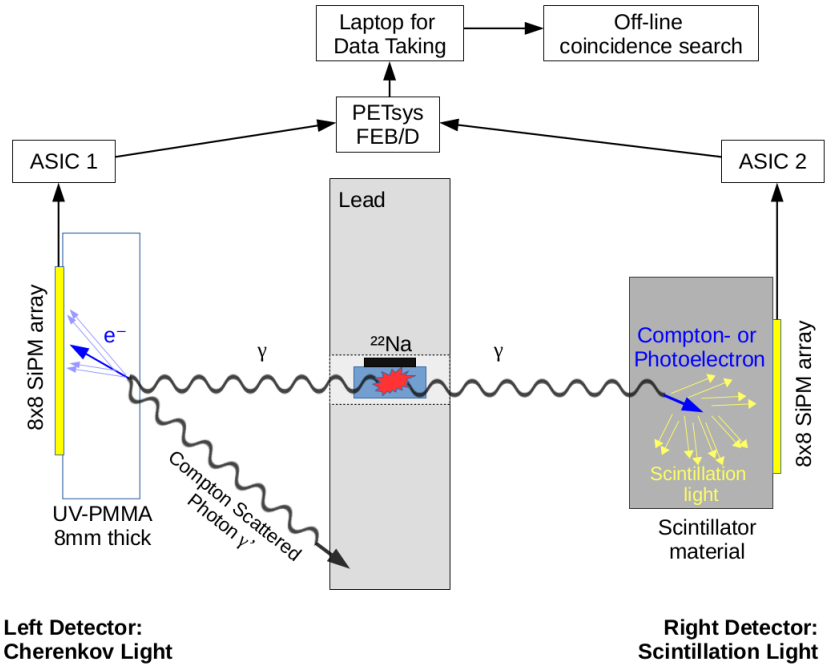

Figure 12.1.: Schematics of the dual-face coincidence set-up for the detection of 511 keV photons containing a ^{22}Na source in a lead block, two different detector types and the signal read-out system.

from the source. The lead block containing the radioactive source is mounted on rails so that the source can be moved with respect to the detectors. The detector for the Compton electrons using Cherenkov light is the only component fixed on the table due to the large amount of supply lines for dry air, cooling water, power for fans and SiPMs as well as for the data-transfer.

Photons that are not detected are shielded with lead blocks on both sides behind the set-up. Like before, the whole set-up is placed inside a dark box with a ventilation system for heat exchange. Also, an upgraded cooling system for the Peltier-elements was employed: The water was pre-cooled outside using two additional Peltier-elements. A significant reduction of the temperature at the SiPM could not be achieved, however, the temperature was more stable over a longer period of time.

The Cherenkov detector is the same as for the measurements with the electron source in the second part of this dissertation. However, to use it as one of two detectors in a dual-face set-up, the detector was turned by 90° so that it faces sideways. The UV-transparent PMMA sample had a thickness of 8 mm and an area of $35 \times 35\,\mathrm{mm}^2$.

The two detectors were placed in equal distances relative to the source location. They were both close enough to the lead block to collect all photons exiting the block through the circular holes on both sides, so that the solid angle into which photons are emitted is fully covered by the detectors. In PMMA as well as in the scintillator, photoelectrons and Compton scattered electrons are created, however, in case of PMMA the photo effect is far less likely to occur due to the low atomic number of its components.

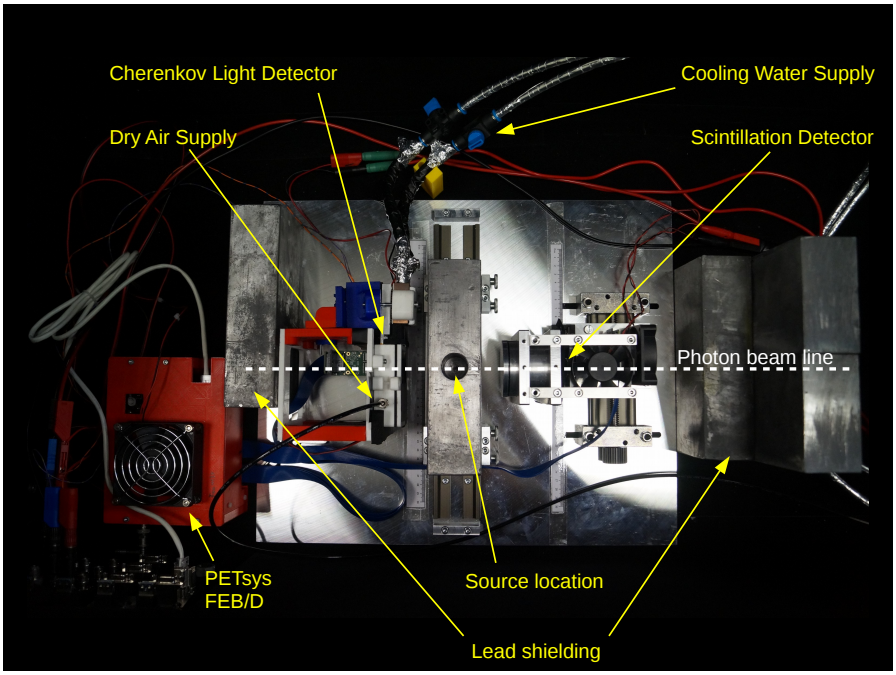

Figure 12.2.: Photo and explanations of the dual-face coincidence set-up.

12.1.2. Scintillation Materials and Photon Detectors

For the measurements three different scintillation materials were used. Their characteristics will be presented here together with the corresponding photon detectors.
A Sodium-Iodine (NaI) scintillator was used in the first test measurements coupled to a Ketek SiPM of type PM 3325-WB-0808 (detectors will be explained later in this section). Due to the very long time constant of the scintillation signal of about 250 ns, difficulties in the coincidence measurement occurred, as will be demonstrated later. Thus, a small plastic scintillator made of Polyvinyl Toluene (PVT) with a time constant of 1.2 ns was used. However, in later measurements only a thin sample of 9.8 mm thickness was available and the interaction probability for photons was too small and, thus, the event rate was too low for measurements with reasonable statistics. It will in the following only be used for a comparison of the coincidence time resolution. Finally, a large Cerium-doped Lanthan-Bromide ($LaBr_3$(Ce)) scintillation crystal with a time constant of 16 ns was coupled to a different Ketek SiPM of type PA 6650-WB-0808 and used for the measurements[1]. The properties of the three materials are listed and compared in table 12.1.
Sodium-iodine and PVT were each read out with the same detector type: A 8-by-8 SiPM array by Ketek of type PA 3325-WB-0808 with a channel size of $3 \times 3\,\mathrm{mm}^2$ and a pixel pitch of 25 μm (see figure 12.3, picture 2). The $LaBr_3$(Ce) crystal came already coupled to a SiPM of similar, yet not identical, type. The crystal is hygroscopic and therefore an exchange of the detectors was not easily possible. The SiPM array type was PA 3350-WB-0808 by Ketek with a pixel pitch of 50 μm. Four arrays were used to form a 16-by-16 matrix, but always 4 channels were connected together to a 2-by-2 sub-matrix and their signals were fed

[1]The device was borrowed from the group of Peter Thirolf at the LMU Munich

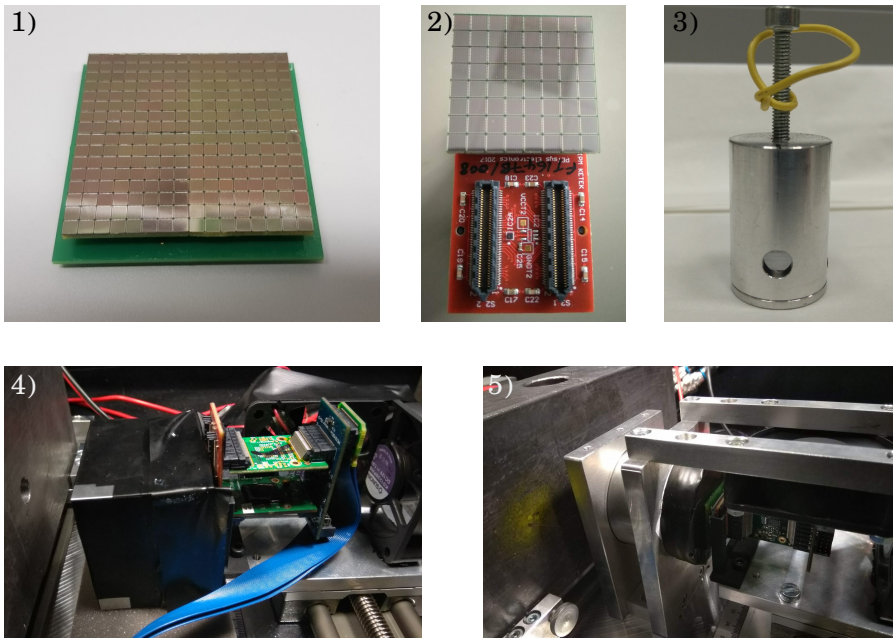

Figure 12.3.: Set-up components in more detail: **1)** Ketek array type PA 3350-WB-0808 with 16 times 16 channels in total, with 4 neighboring channels interconnected to one output line, making it an 8 times 8 array effectively. Picture taken by Tim Binder, LMU Munich, used with permission. **2)** Ketek array type PA 3325-WB-0808 on the front-end module by PETsys electronics for signal read-out. **3)** Source container made of aluminum with holes for the photons to exit. **4)** $LaBr_3(Ce)$ monolithic scintillation crystal connected to the SiPM and read out board in the set-up. **5)** NaI scintillator connected to the detectors and the read-out electronics in the set-up.

	Scintillator material		
Property	**NaI**	**PVT**	**$LaBr_3(Ce)$**
Emission maximum [nm]	$415^{(a)(b)}$	$425^{(d)}$	$380^{(b)}$
Refractive Index	$1.85^{(b)}$	$1.58^{(d)}$	$\approx 1.9^{(b)}$
Primary Decay Time [ns]	$220^{(a)}$ - $250^{(b)}$	$2.1^{(d)}$	$16^{(b)}$
Light yield [$^{\text{photons}}/_{\text{keV}}$]	$38^{(b)}$	$10^{(d)}$	$63^{(b)}$
Thickness for 50 % attenuation [cm]	2.0 at 511 keV$^{(c)}$	8.3 at 511 keV$^{(c)}$	1.8 at 662 keV$^{(b)}$
Density [$^{\text{g}}/_{\text{cm}^3}$]	$3.67^{(b)}$	$1.03^{(d)}$	$5.08^{(b)}$
Geometry and Dimensions	cylindric $d = 55$ mm $z = 60$ mm	cylindric $d = 30$ mm $z = 9.8$ mm	cuboid $50 \times 50 \times 30$ mm

Table 12.1.: Properties of the three scintillator materials used for the measurements. $^{(a)}$[Bir64], $^{(b)}$[Sai19], $^{(c)}$calculated using NIST data [Sel96], $^{(d)}$[Rex19].

Parameter	Value	Unit	Comment
Micro cell size	25	μm	-
Number of micro cells	13920		-
Breakdown voltage	24.7	V	-
Overvoltage	5	V	recommended; used in measurements
Peak PDE	45	%	at 430 nm and 5 V overvoltage
DCR	125	$^{\text{kcps}}/_{\text{mm}^2}$	at 5 V overvoltage
Gain	$1.74{\cdot}10^6$		at 5 V overvoltage
Cross talk probability	26	%	at 5 V overvoltage

Table 12.2.: Parameters and values for the SiPM type PA3325-WB-0808 by Ketek. Numbers taken from [KET19] and [KET18].

to one output channel. This detector matrix can be seen in figure 12.3, picture 1. Essentially, an 8-by-8 channel matrix was formed with a channel size of $6 \times 6\,\text{mm}^2$. The group from Munich, who built this modified 8-by-8 array, attempt to increase the energy resolution by increasing the channel size.
Unfortunately, the SiPM model with a 50 μm pixel pitch is an experimental prototype of the manufacturer Ketek and, thus, no data sheet exists. One can still characterize it by comparing it to the model with 25 μm, which is in principle identical except the size and number of micro cells per channel.
Table 12.2 shows the key quantities that characterize the detector of type PA 3350-WB-0808. In comparison, the model with larger pixel pitch has larger gain. The gain scales linearly with the pixel capacitance, which again scales linearly with the pixel area [KET20]. This implies that the signals produced by this device are larger than those of the other SiPM type, which is beneficial for the energy resolution of a scintillation measurement. Both devices have the same dynamic range, because of the same number of pixels per channel. The 3325-model has 13920 pixels per channel on a $3 \times 3\,\text{mm}^2$ area, while the 3350-model has only a fourth of that. But, since four channels are connected to one, the total number of pixels per channel is identical. The dark count rate (DCR) per detector area is the same for both devices and stated with $125\,^{\text{kcps}}/_{\text{mm}^2}$ at an overvoltage of 5 V.

12.2. Data Processing and Analysis Method

In the following, the word *signal* refers to a detection of light or dark count by one individual channel, while the word *event* denotes a coincidence under predefined conditions, that is, at least a certain number of coincident channels within a coincidence time window (CTW).

12.2.1. Preselected Events

Since the Cherenkov detector was operated at single photon level, most of the signals were dark count. The photons had far higher interaction probability in the scintillator than in the Cherenkov detector. Thus, a large fraction of signals only occurred on one of the detectors

without any coincident signal on the other one. A pre-selection of events was therefore used to reduce the amount of saved data:
for the conversion of raw measurement data to usable data written to a Root tree PETsys provides an application called `raw_to_coincidence`. This script parses through the raw signals and only writes them to the tree, if there was at least one signal from both detectors within a defined time window. The signals from all channels are then stored in frames together with the channel number, time stamp and TOT value and the total number of signals in the frame. Thus, the user receives a preselected event list where all those signals are thrown out that definitely cannot be involved in a coincidence. Different frame lengths were investigated and the results will be shown later in this chapter.
This preselected tree is then analyzed and searched for coincidences: At first the channels from each detector are treated separately, to see if each on its own fulfills the requirement for a coincident event. Then both detectors are checked for coincidence.
Signals from both detectors can be randomly distributed over the whole time frame, which is why sorting of the time stamps and subsequent coincidence search is necessary. There is a coincidence time window (CTW) for the Cherenkov detector and a reference-CTW for the scintillation detector for validation. These are used to check, if the individual detectors have measured light signals on the required number of coincident channels (rnocc). If both detectors fulfill the requirement, the first time stamp of the coincidence on both detectors is stored. If the time difference between these time stamps is smaller than the global CTW, the event is considered a validated event originating from the emission of two back-to-back photons from the sodium source detected with the two detectors. Usual CTWs for the Cherenkov detectors are in the range of 3 ns up to 10 ns, while for the scintillator it depends on the scintillator material. For NaI windows between 100 ns and 2000 ns have been tested, while for $LaBr_3$(Ce) shorter values down to 20 ns have been investigated. The global coincidence window is on the order of 50 ns up to 200 ns depending on the scintillation material. The required number of coincident channels (rnocc) for the scintillator is higher, (values between 8 and 30 have been tested), since the light yield is magnitudes higher than for Cherenkov light. On the other side rnocc values between 3 and 6 have been tested while a value of 4 was taken for most measurements. A smaller rnocc increases the detection efficiency for Cherenkov events, but increases the chance of random coincidences triggered by dark count. Due to the required global coincidence with the scintillation detector, this probability of random dark events is smaller than for the use of only one detector and the electron source.

12.2.2. List Mode Data

For the efficiency estimation performed in section 12.5 a different data taking and analysis modality is required. To estimate the efficiency, one needs to have access to the full amount of signals on both detectors, without any preselection of signals. It is especially important to collect all scintillation events within the duration of the measurement to compare the number of coincidences on the Cherenkov detector with those on the scintillator side. Therefore, all raw data are stored in list mode, using the so called `raw_to_singles` application by PETsys electronics.
This means the converted data are written to file in a string of signals, which is also called a list mode data set. Each signal contains information on the time stamp, the energy (TOT

information) and the channel ID. Data are written to a Root tree again where timing, TOT and channel ID are stored in a separate branch. A program has been created that reads in the data from the tree and searches for coincidences.

Since the signals are not by default sorted by their time of arrival, also in list mode, a sorting of the data is required. Thus, an artificial time frame is introduced similar to that in the preselected list.

The time frame can be set at the beginning. For first tests 1 μs has been chosen. Then, the CTW for the Cherenkov and scintillation detector are chosen, together with the rnocc. Signals are sorted into frames of above set length in the following way: The time stamp of the first event is saved and energy, time stamp and channel ID are saved in vectors. Then, all following events are saved as well until an event occurs that has a time stamp further away from the first one than the length of the time frame. Then this time frame is ready to be analyzed. One drawback of this method is that each frame basically has a random start time so that it could happen that the border of a frame cuts into a coincident event, which could be missed in the analysis. This effect and the influence of the choice of frame length on the results is investigated in section 12.3.2.

Only those frames are analyzed that contain at least as many signals as minimal required for a coincidence on both detectors. For example if on the Cherenkov detector array at least 4 channels are required and on the scintillation detectors at least 20 channels, then every frame with less than 4+20=24 signals is rejected and not further analyzed. Figure 12.4 demonstrates this principle.

A further improvement of the selection has been implemented as well: If in the current frame either the Cherenkov detector or the scintillation detector has received fewer counts than its corresponding requirement, the frame is rejected as well. If, for example, on the Cherenkov detector there were 5 coincident channels, and on the scintillator there were only 19, then the total number is not less than 24, but the frame gets rejected anyway since the scintillator did not meet the required minimum of channels.

Signals that lie within an accepted time frame and that fulfill the required number of channels are then sorted into vectors for energy, time stamp and channel ID. The signals from both detectors are written in separate lists for further treatment. After that, the lists are sorted by their time stamp using a bubble sort algorithm and coincidences are searched for.

After every analysis, the input parameters and some results on the coincidence search are printed into a log file. An example with explanations is shown in the appendix in figure A.3.

12.3. Detector Configuration and Parameter Setting

This section introduces the different parameters that configure the detector and the various settings required for the analysis. Their influence on the outcome of a measurement is discussed and the choice of the final parameters is stated and explained. At first measurement settings – which must be made before taking data – will be discussed in 12.3.1. Then, the analysis parameters are investigated in section 12.3.2.

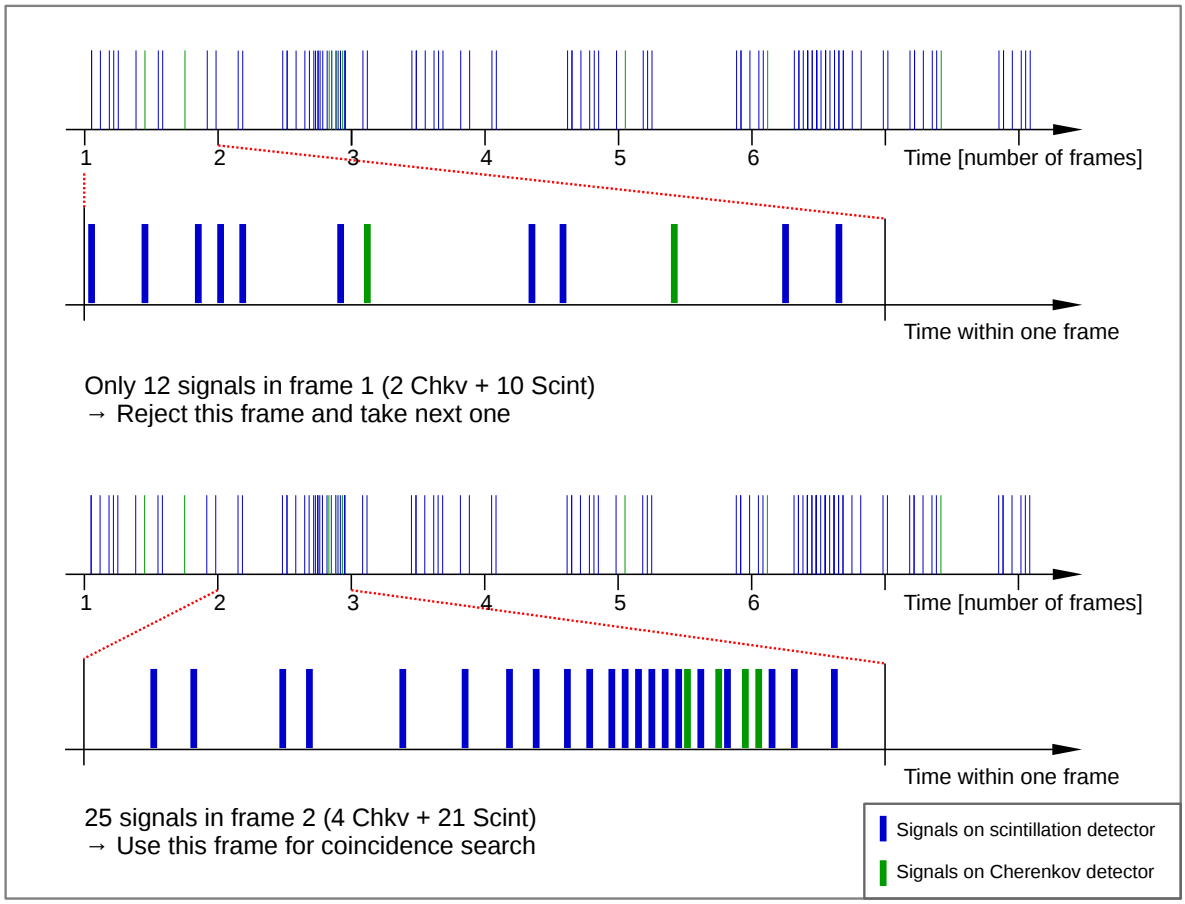

Figure 12.4.: Principle of sorting list mode data into frames of fixed length including the decision making on whether to keep or to reject a frame based on the number of entries.

12.3.1. Measurement Settings

Measurement settings include values like the applied overvoltage, the trigger thresholds and the measurement duration.

Overvoltage:
The overvoltage of the Hamamatsu array for the Cherenkov light detection was 4 V just like for the measurements with the electron source. In general, the settings for data taking have been left unchanged compared to the electron measurements from before. Only for the analysis, changes have been implemented. On the KETEK detector array for the scintillation light, a voltage of 5 V was applied, which corresponds to the upper end of the recommended voltage range according to the data sheet provided by Ketek. A high voltage creates higher signals, which is beneficial for the energy resolution of the scintillation detector. On the other hand, the dark count rate (DCR) increases with overvoltage as well. Thus, the trigger thresholds need to be adjusted to a level well above the one-photon level to not overwhelm the PETsys read-out electronics.

Trigger Treshold:
Unfortunately, the signals of the Ketek SiPM were too small to display and identify the individual steps between photon levels. Thus, the algorithm for finding the threshold value corresponding to a specific photon equivalent level as it has been done for the Cherenkov detector, could not be applied to the scintillation detector. The chosen solution was to take the DCR as reference: The threshold of every channel was not set to a certain photon level but to a certain DCR. Values between 100 cps and 2 kcps have been tested. The threshold would be scanned through its range in steps of one, until the measured DCR would be as close to the desired value as possible. All channels are set to the same level using the approach described.

In order to visualize the influence of the trigger level on the measurement, a spectrum of the scintillation signals detected with the Ketek array is created. The spectrum contains the sum of the Time over Threshold (TOT) values from all coincident channels and is therefore not linear in energy, since the measured TOT is not linear with the number of detected photons. This has already been shown and discussed in chapter 11. Figure 12.5 shows the obtained spectrum using the ^{22}Na source measured with the NaI scintillator at two different trigger levels, resulting in a DCR of 100 cps per channel and 2 kcps per channel, respectively. The required number of coincident channels was set to 20 with a coincidence time window of 200 ns. One can see the higher energetic peak corresponding to 1.27 MeV occurring at TOT values around $27 \cdot 10^6$ ps in case of the higher threshold (= lower DCR) and at $33 \cdot 10^6$ ps for the lower threshold. The difference is similarly distinct for the 511 keV peak appearing at around $7.5 \cdot 10^6$ ps for the 100 cps-threshold and at around $12 \cdot 10^6$ ps for the 2 kcps-threshold.

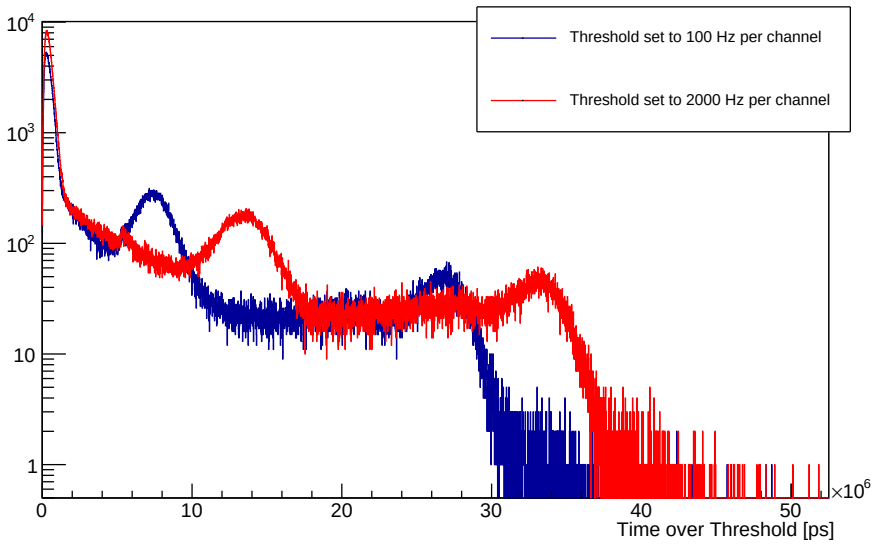

Figure 12.5.: ^{22}Na spectrum measured with NaI scintillator at two different detector thresholds, resulting each in a different dark count rate per channel. In order to not overwhelm the read-out electronics and to reduce data conversion time, a higher threshold value is preferred.

The larger DCR corresponds to a lower trigger level and consequently more channels contributing to the signal. Therefore, the signal with larger DCR is shifted towards larger TOT values.
The first impression is that the spectrum with lower level is stretched out and, therefore, has better resolution. However, the dark count contribution to the measurement is higher as well. Since every signal above the threshold is written to file in list mode and because the dark count rate increases exponentially with decreasing threshold, the time for data taking increases exponentially as well. The conversion of the raw hits into a usable `.root`-file format is the most time consuming part and can take up to 10 times the measurement duration, if the dark count contribution is too high. This influence is significantly smaller, if during the data conversion, preselection of signals takes place as described earlier in this chapter.
For an identification of the 511 keV peak, the higher threshold is sufficient allowing for an energy selective coincidence measurement as it is described later. Therefore, the thresholds were set to a level resulting in 100 Hz DCR per channel.

Measurement duration:
Clearly, longer measurements are preferred in order to collect sufficient data for statistically significant analysis. But the time consuming data conversion introduces some limits. Most measurements, therefore, consist of individual runs of 120 s each, added up during the analysis procedure. That way, file sizes are limited (still in the range of several Giga Byte per run) and more flexibility is gained.

12.3.2. Analysis Parameters

The analysis parameters that influence the results of a measurement are the time frame chosen for the coincidence search, the coincidence time window (CTW) on both detectors individually and the global CTW. *Global* means a coincidence on both Cherenkov and scintillation detector with a global CTW. Furthermore, the required number of coincident channels (rnocc) on each detector is important, as it has a major influence on the dark count contribution to a measurement.

Time frame settings:
Measurements with $LaBr_3$(Ce) are used to demonstrate the influence of the time frame on the results of the scintillator measurement. In general, an increased time frame reduces the chance of losing events that lie at the boundary between two frames and that would be split up consequently distributing their signals over two frames and being partly or entirely lost. In case of split-up signals, the TOT value would appear at a different position in the scintillator spectrum and, thus, change its shape. It can be shown that this influence is not strong until the time frame is shortened to values close to the time constant of the scintillator. Figure 12.6 compares time frames of 20 ns, 100 ns and 2000 ns. The TOT spectrum of the$LaBr_3$(Ce) scintillator is plotted and the two peaks corresponding to 511 keV and 1.27 MeV can be identified. The obtained difference between the analysis with a time frame of 100 ns and 2000 ns is not significant. Given a scintillator decay time of 16 ns one might expect 10-20 % of events being split up, but the effect only becomes clearly visible for a time frame of 20 ns.

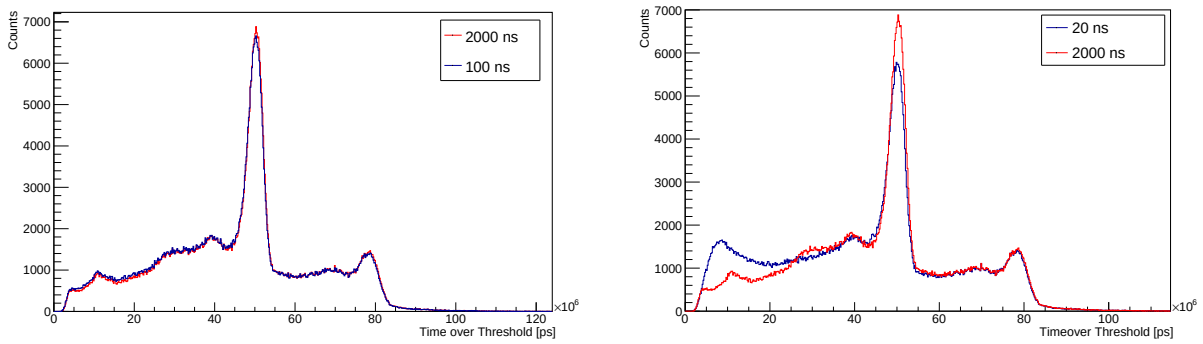

Figure 12.6.: Scintillation signal from the $LaBr_3(Ce)$ signal and ^{22}Na source for different time frame settings in the analysis procedure. A significant influence becomes only visible at frame lengths on the order of the scintillator time constant τ. In case of $LaBr_3(Ce)$ τ is 16 ns.

This can be explained by an investigation of the distribution of coincident events within a frame. See figure 12.7. In this scatter plot, the energy of each signal contained in a coincident event is plotted together with its time difference with respect to the first signal of the coincidence. At least 20 channels within 50 ns were required for a coincidence. One can see that the higher energetic events occur earlier and that even with a scintillator decay time of 16 ns, most signals are collected within 5 ns. The large red peak corresponds to the 511 keV signal and the smaller accumulation above denotes the 1.27 MeV signals. Small signals and dark count contribution occur at small TOT values and cover the whole time range.

To split as few events as possible, the frame time must be chosen significantly larger than the time constant of the scintillator. However, if the frame is chosen too long, events might be lost, since the program is built such that it can only detect one global coincidence per frame. Additionally, the dark count contribution increases with frame length as well, which is why the pre-selection of frames based on their number of entries would loose its effect, since frames filled with dark count signals would not be sorted out but passed on to the coincidence search. A trade-off had to be made and the time frame was chosen one order of magnitude larger than the decay time of the scintillator. For the $LaBr_3(Ce)$ measurements a time frame of 200 ns has been chosen and 2 μs in case of NaI. For the short test measurement with PVT, the same settings as for NaI were selected.

Coincidence time window:
For the Cherenkov detector the coincidence time window (CTW) has been investigated already in earlier chapters of this thesis, and a value of 5 ns has been chosen allowing to capture a signal completely while minimizing the contribution of random coincidences.

For the scintillator, the CTW again entails the danger of splitting a signal up, when chosen too short. However, another effect comes into consideration, which is dark count. Choosing a large window will necessarily increase the number of dark events, which will be integrated into the total signal, i.e. the TOT value. Furthermore, the chance of triggering on dark count in the absence of a real signal increases for larger coincidence time windows. But also for real

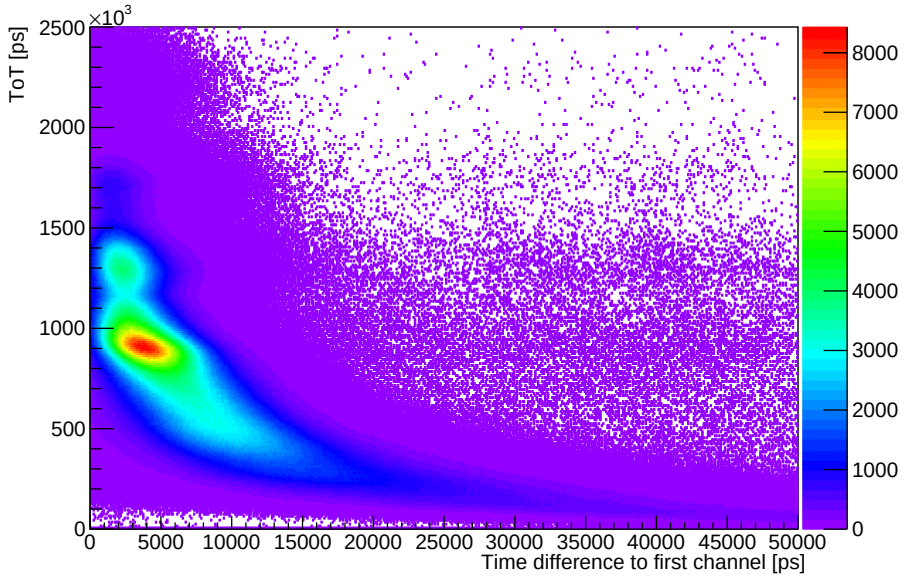

Figure 12.7.: Scatter plot of the TOT value and time after first trigger for every signal involved in a coincident scintillator signals using $LaBr_3(Ce)$ and the sodium source.

scintillation signals, large coincidence time windows implicate some problems: Since the dead time of a channel of the read-out electronics is on the order of 100 ns, the same channel could be triggered again within the CTW, if it is chosen too large. In case of $LaBr_3(Ce)$, where the whole scintillation signal can be captured within a few tens of nanoseconds, the CTW can be chosen short enough to prohibit double-triggering and double-counting of channels. In case of NaI with a time constant of 250 ns this is not possible. A trade-off must be made. Figure 12.8 shows the influence of the CTW on the example of a NaI measurement with the ^{22}Na source. The histogram has a bin width of $0.2 \cdot 10^6$ ps. At small bin numbers dark contributions can be seen, which occur more frequently at larger coincidence time windows. Splitting signals is represented by a shift in the peak position of the 511 keV signal for small CTWs. Figure 12.9 right next to it shows the dependency of the peak position of the chosen CTW. The peak position saturates at about $7.9 \cdot 10^6$ ps for windows of 400 ns width and higher.

Global coincidence time window:
This time window is used to check for global coincidences of the two detectors, after the algorithm has found a valid coincidence on each individual detector. The value of the global CTW is 50 ns for all measurements. It mainly serves the purpose to check if coincidences occurring on both detectors belong to the same event, i.e. the same photon-pair emitted subsequent to an electron-positron-annihilation in the PMMA block. Since the rate of impinging photons is on the order of kHz, there is only a negligible probability of having two events within 50 ns. One could lose some events, however, if the value is chosen too small. Large scintillation decay times of NaI or an inherent time difference between the two detectors could cause an event to lie outside the global CTW and therefore to be lost. In the

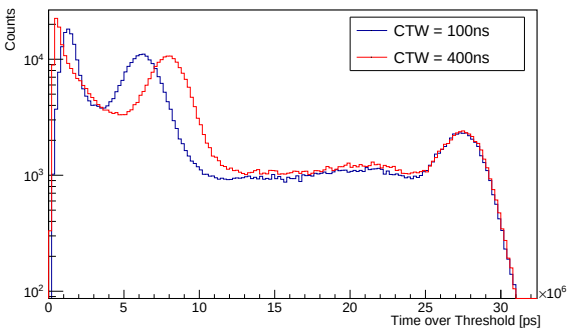

Figure 12.8.: Scintillator spectrum for two different CTWs. The peak shifts towards smaller values when the CTW is too short and events are split up.

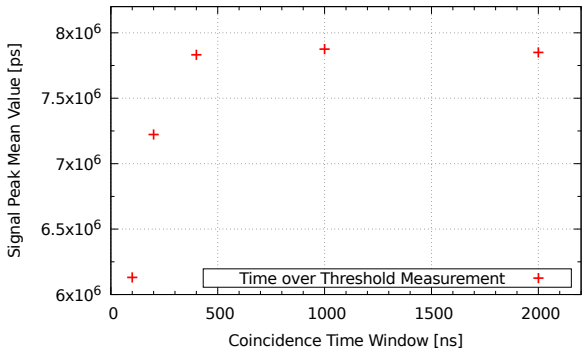

Figure 12.9.: Dependency of the 511 keV peak position on the CTW. A saturation occurs for CTWs of 400 ns and above.

investigation of the coincidence time resolution (CTR) later in this chapter it will be shown, that 50 ns is a sufficient choice for the measurements.

Required number of coincident channels (rnocc):
To choose the required amount of channels for a valid coincidence on the scintillator, the following quantities need to be taken into consideration: Firstly, the larger the CTW, the more channels randomly fire within that time. This increases the probability to trigger on dark events that happen to fulfill the coincidence requirement by chance. Since for the NaI scintillator a larger window needs to be chosen, the minimum number of coincident channels has to be higher. This can be seen in figure 12.10, where the number of coincident channels per event is depicted as histogram. For values below 30 the number of entries increases strongly due to dark counts. A rnocc of 30 is considered sufficient for the measurements with NaI, since any event must be coincident also with the Cherenkov detector and therefore, triggering on dark count is limited. With a rnocc of 30 the signal peak is uninfluenced by the rejection of events with less than that amount of channels. This is shown in the TOT histogram in figure 12.11.
For $LaBr_3(Ce)$, a rnocc of 20 was chosen, smaller than for NaI, since the CTW is shorter as well, therefore, the probability of triggering on random dark events is smaller. One can see in the histograms in figure 12.6 for the $LaBr_3(Ce)$ crystal that no contribution from dark count at small bin numbers exists at this rnocc.

12.3.3. Correction of Inherent Time Differences

For the Ketek array of type PA 3350-WB-0808, a correction of inherent time differences between individual channels was performed using short LED pulses creating coincident signals on the array. Pulses with a width of 10 ns and a frequency of 10 kHz were used to illuminate the bare detector array, without any materials coupled to it. A data base of TOT dependent time differences for every channel with respect to one fixed reference channel was created. The principle of time difference compensation using TOT values has been described in section 10.3. This Ketek device in combination with the application specific integrated circuit (ASIC) TOFPET2 by PETsys electronics shows some significant time differences

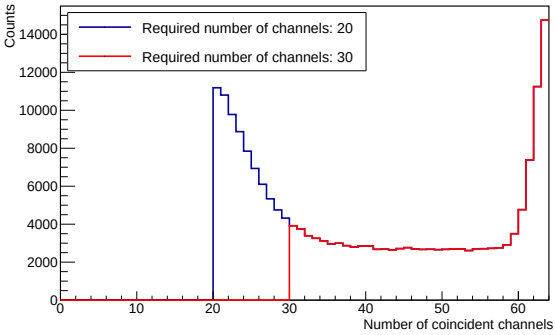

Figure 12.10.: Histogram for the number of coincident channels per event for two different minimum requirements. One can see the background contribution from dark counts decrease for higher rnocc.

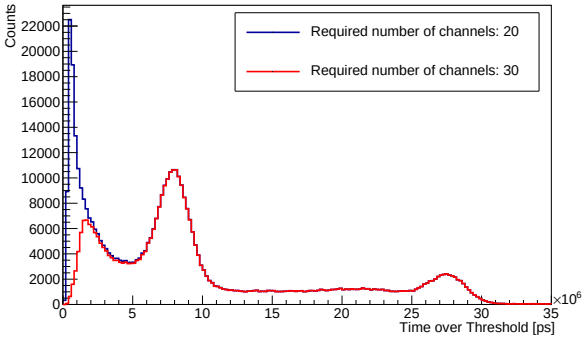

Figure 12.11.: TOT spectrum for the NaI scintillator shown for two different rnocc. The background contribution at smaller bin numbers decreases while the signal peak is largely uninfluenced.

as can be seen in figure 12.12. A histogram of the time difference with respect to the first channel of a coincidence is shown. Without correction of the time differences, no sharp peak arises in the histogram but rather a spectrum of peaks representing various inherent offsets between the channels. A measurement of only 10 s and fixed LED position and voltage was used to create this graph, which leads to the fact that the light distribution on the channels was different and, thus, the measured TOT values were significantly different throughout the matrix. Since the time difference between signals on different channels is TOT dependent as shown in section 10.3, large time differences between channels can occur explaining the wide distribution of peaks in the spectrum. A TOT dependent time difference correction enables to reproduce a sharp pulse representing the coincident arrival of LED light on the array. The coincidence time resolution for the LED measurement was determined using the distribution of the time differences of every channel with respect to a predefined reference channel from the center of the array (shown in figure 12.13). The full width at half maximum (FWHM) of the peak was used to define the CTR of the Ketek array of type PA 3325-WB-0808: FWHM = 639.2 ps [2].

12.4. Characteristics of the Coincidence Measurement

The measurements were carried out using the settings established in section 12.3 unless explicitly stated otherwise. They are summarized in table 12.3 for both scintillators $LaBr_3(Ce)$ and NaI. The measurement taken with PVT used the same settings as for NaI.

12.4.1. Quality of the Measurement Signal

The measured quantity on both detectors is the Time over Threshold (TOT). On the Cherenkov detector the TOT value from each channel is translated into a number of photons based on the calibration that was introduced in chapter 11. Scintillation signals are significantly larger than Cherenkov signals since up to several ten thousand photons per incident

[2] The statistical uncertainty on this result is smaller than the given number of decimals.

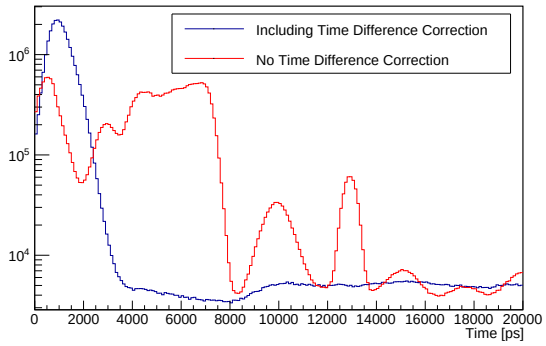

Figure 12.12.: Histogram of the time difference between every coincident signal on the KETEK SiPM array with respect to the first signal occurring in an event. A TOT dependent correction of the inherent time differences has a massive influence on the time distribution.

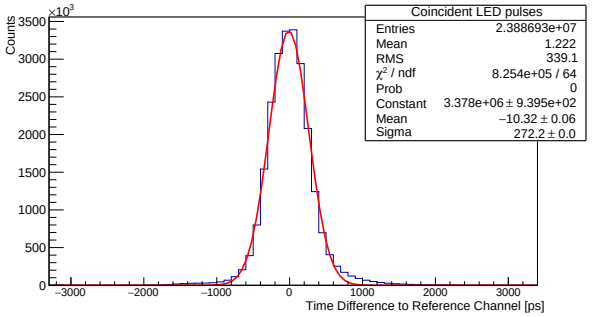

Figure 12.13.: Coincidence time resolution of the KETEK detector array for a measurement with pulsed LED. After correction of time differences, a CTR of FWHM = 639.2 ps could be achieved.

Parameter	**NaI**	**$LaBr_3$(Ce)**	**Unit**
	Cherenkov Detector		
Overvoltage	4	4	V
Threshold	1	1	pe-level
CTW	5	5	ns
rnocc	4	4	-
	Scintillation Detector		
Overvoltage	5	5	V
Threshold	100	100	cps/channel
CTW	400	50	ns
rnocc	30	20	-
	Regarding Both Detectors		
Time Frame	2	0.2	μs
Global CTW	50	50	ns

Table 12.3.: Parameters used for the measurements to characterize the detector. Parameters for the use of NaI (second column) and $LaBr_3$(Ce) (third column) are listed together with the corresponding unit. The threshold for the scintillation detectors was set to a level corresponding to a certain dark count rate per channel. Measurements with PVT used the same settings as the ones with NaI.

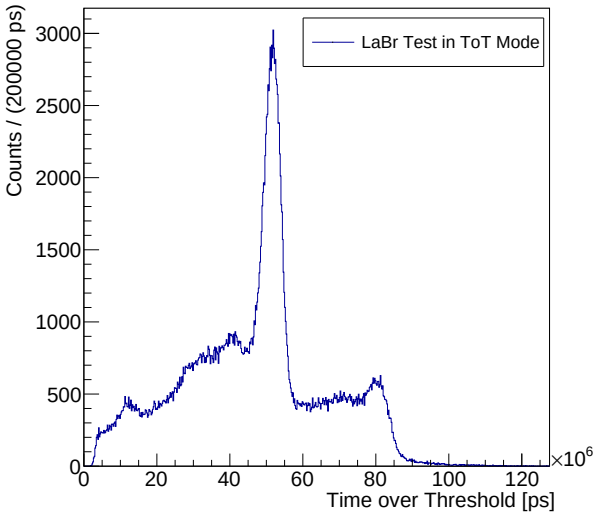

Figure 12.14.: TOT spectrum of the ^{22}Na source using the $LaBr_3$(Ce) monolithic scintillation crystal.

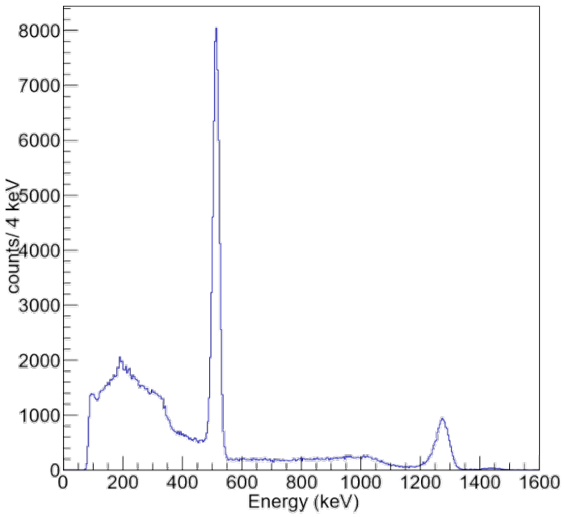

Figure 12.15.: ^{22}Na spectrum using the charge integrator of the TOFPET2-ASIC. The charge values have been calibrated and converted into energy. From Tim Binder, Munich. With permission.

particle can be created. Using the photon yield of the two detectors (table 12.1), the number of photons per incident 511 keV gamma in case of an interaction via photo effect can be estimated: In NaI about 19418 photons are created and in $LaBr_3$(Ce) the number increases to 32193 photons per incident gamma. The signals would therefore be high enough to trigger the charge integrator of the TOFPET2-ASIC. However, using the charge integrator on one ASIC and the TOT measurement on the other ASIC was not possible at that time. Since the Cherenkov detector can only work with the TOT values, also the scintillation signals were read out in that way.

Figure 12.14 shows a test measurement with the ^{22}Na source using the $LaBr_3$(Ce) scintillator and signal read-out in TOT mode. Figure 12.15 serves as direct comparison: the spectrum has been created using the ASIC's charge integrator and has been measured by Tim Binder, LMU, Munich. The x-axis has been converted to energy already. In both spectra, the large 511 keV peak can be seen as well as the peak at 1.27 MeV. The charge integrated spectrum has a linear dependence on energy, while the relation between TOT and energy is much more complicated as the value on the x-axis is the sum of all TOT values from the individual channels and those values scale logarithmically with the number of detected photons. This is why the spectrum seems to be compressed at higher energies – meaning higher TOT values – in comparison to the charge integrated version.

Both spectra show some features that could not be displayed using the NaI scintillator (as seen in figure 12.16 for example): the Compton edge for the photons with 511 keV can be seen at an energy of 340.7 keV. Also the Compton edge for the 1.27 MeV photons occurs at 1.057 MeV – but is smeared out due to limited resolution in both spectra. In general, the resolution is better in charge integration mode, as the sharper peaks indicate. This allows

	Coincidence Rate [cps]	
rnocc	**Energy cut on 511 keV**	**No energy cut**
3	0.92 ± 0.03	1.90 ± 0.04
4	0.50 ± 0.02	0.99 ± 0.03
5	0.33 ± 0.02	0.65 ± 0.02
6	0.23 ± 0.01	0.45 ± 0.02

Table 12.4.: Detected rate of global coincidences using NaI for different required number of coincident channels (rnocc) with and without energy cut around the signal peak in column 2 and 3 respectively. The obtained values are highly dependent on analysis and measurement parameters as well as on the chosen scintillator.

to reproduce also the so called *back-scatter peak* at small energy bins: if a photon travels through the detector without being detected and is then backscattered into the sensitive volume, it can still deposit its energy. The energy of the backscatter peak is equal to the incident photon energy minus the energy of the Compton edge.

12.4.2. Energy cut on 511 keV

The aim was to have a pure signal with low background and high signal rate. In order to characterize the patterns in the Cherenkov detector, a pure sample of 511 keV photons has to be selected. A signal range or region of interest (ROI) around the signal at 511 keV were defined for the measurements, such that a large fraction of background events and random coincidences between the two detectors are rejected. However, events from the Compton plateau of 511 keV photons in the scintillator would be rejected as well. This will be discussed in the scope of the efficiency estimation in section 12.5. The rejection of events that are actually created by 511 keV photons reduces the event rate, while on the other hand reducing the probability of counting false signals. Figure 12.16 shows the scintillator spectrum of NaI once more together with all events that were globally coincident with the Cherenkov detector. One can see that there are many global coincidences that created a signal in the Compton plateau in the scintillator and which are thrown away when using a symmetric ROI around the signal peak. Above the signal peak, there are almost no global coincidences as expected, since those events originate in the single high energy photon at 1.27 MeV, which cannot create a global coincidence.

The most obvious influence the energy cut has, is the reduction of the total number of coincidences and, thus, also the measured coincidence rate. This is subject of section 12.4.3. Further influences on various measurement results were investigated and will be explained in the corresponding sections in this chapter: The impact on the detected pattern of coincident hits is shown in the scope of section 12.7.1 and section 12.7.2 investigates the mean number of detected photons with analyses with and without energy cut.

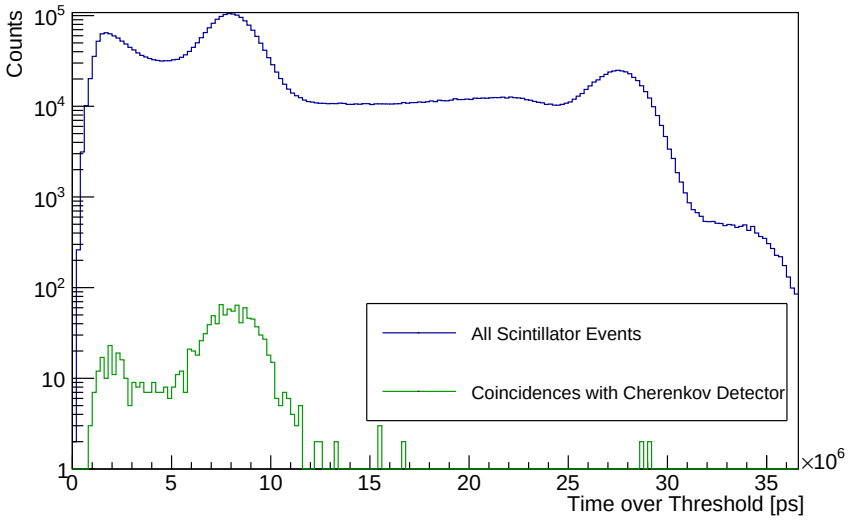

Figure 12.16.: Scintillator spectrum of NaI (blue) together with the spectrum of events that are globally coincident with the Cherenkov detector (green). Almost exclusively events from the signal peak at 511 keV and the Compton plateau before that contribute to global coincidences.

12.4.3. Measured coincidence rate

The coincidence rate is strongly dependent on the applied overvoltages, the thickness of the PMMA for the Cherenkov detector and the type and geometry of the scintillator for the reference detector. The measured global coincidence rates with NaI are shown in table 12.4 for different minimum required coincident channels. In case of an rnocc of 4, a rate of 0.50 ± 0.02 cps was recorded. This is a measurement result and does not contain any corrections for background and dark events and uses no interpolation at the boundaries of the ROI like for the efficiency estimation in section 12.5. The measured rate using the $LaBr_3(Ce)$ crystal was only 0.36 ± 0.01 cps. The ratio of the rates is therefore $0.50 : 0.36 = 1.39$. The difference could originate in the different thicknesses of both detectors. While the cylindric NaI scintillator has a length of 60 mm, the $LaBr_3(Ce)$ crystal only provides 30 mm of material for a photon interaction. The effective atomic number of both materials is comparable (38.5 for NaI and 47 for $LaBr_3(Ce)$ [Lip18]), thus, the photoelectric fraction is similar. The attenuation length for photons in these materials is roughly the same as well: A value of 2 cm is given for NaI for 511 keV photons and a value of 1.8 cm for $LaBr_3(Ce)$ at an energy of 662 keV (see table 12.1). The factor of two in scintillator thickness does however not translates into a factor of two in the detection rate, since the interaction probability of photons in a medium does not scale linearly with the thickness. Furthermore, the light collection efficiency for the NaI measurements was smaller due to a detector area being smaller by a factor of 4 compared to the $LaBr_3(Ce)$ measurements. This might cause some loss of events, indicated by the Compton plateau vanishing in the background at small bin numbers in the NaI spectrum. Summarizing, larger and thicker scintillators produce higher coincidence rates and allow for shorter measurement durations while still providing sufficient energy resolution.

12.4.4. Coincidence time resolution (CTR)

An important quantity for characterizing a coincidence measurement is the coincidence time resolution (CTR). Figure 12.17 shows the time difference between the Cherenkov signal and the scintillator signal defined as $\Delta T = T_{\text{Chkv}} - T_{\text{Scint}}$. The peak position is at negative times for all three materials, meaning that the Cherenkov signal occurred first. This is in agreement with the instantaneous nature of the Cherenkov photon emission compared to scintillation light, which is emitted over a certain period of time. Due to the decay time of the scintillator, the peak is non-gaussian and a determination of the FWHM as a measure of the CTR is not possible with a gauss fit. One could quantify the time resolution using the width of the peak at half peak height given in multiples of the bin width. Then, the CTR for measurements using $LaBr_3(Ce)$ is 4 ns. Measurements with NaI result in a CTR of 20 ns. Of course this result depends on the choice of the bin width, which is why the uncertainty on the obtained CTR is on the order of the bin width, which in this case is 1 ns.

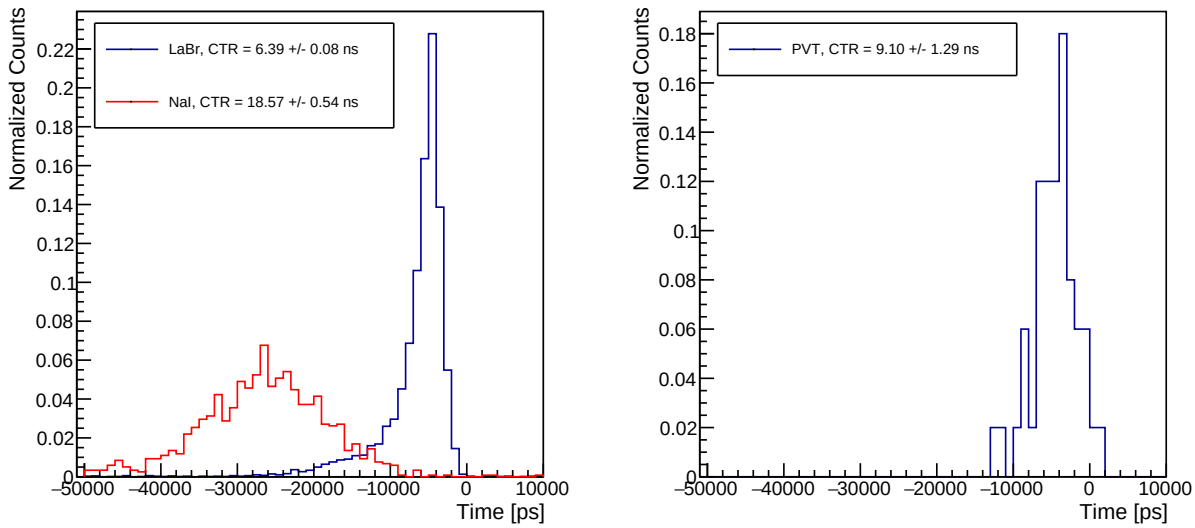

Figure 12.17.: Coincidence time resolution for the three different scintillators in the dual-face coincidence set-up. The PVT measurement has low statistical significance and is plotted separately.

Another more sophisticated way of determining the CTR is to use an interval around the peak value that contains 75.8 % of all entries. That percentage represents the fraction of entries in a gauss distribution that is enclosed by an interval of $[\mu - 1.17\sigma; \mu + 1.17\sigma]$, where $1.17 \cdot \sigma$ equals half the FWHM of the peak. The full width of that interval is then the desired CTR. The CTR for measurements with NaI is (18.57 ± 0.54) ns, while for $LaBr_3(Ce)$ a resolution of (6.39 ± 0.08) ns was obtained. The statistical uncertainties originate in the different measurement duration and the associated different numbers of coincident events. While with the NaI, only 1183 events were registered, the measurement with $LaBr_3(Ce)$ resulted in 6816 coincidences.

Due to its lack of thickness, PVT enabled only 50 events in total within a measurement of 1200 s. The result for the coincidence time resolution is therefore less statistically significant.

Nevertheless, a CTR of (9.10 ± 1.29) ns is promising and with a larger sample, one might be able to achieve a performance comparable to the $LaBr_3$(Ce) measurements.

The property of the scintillator is the limiting factor for the CTR of the measurements presented in this section. The emission of Cherenkov light happens on picosecond timescale and the CTR of the detection of Cherenkov photons is mainly limited by the read-out electronics. For scintillators, however, it depends on the decay time of the scintillating material.

12.5. Efficiency Estimation for the Detection of 511 keV Photons

12.5.1. Derivation of the Efficiency

A statistical approach has been chosen for the estimation of the efficiency for the detection of gamma rays at the energy of 511 keV using a coincident detection of Cherenkov light from Compton scattered electrons. To that end, the number of 511 kev gammas detected within the measurement period using the scintillator is compared to the number of detections in coincidence with the Cherenkov detector, which is about to be characterized with this method. In a first simplified approach, the efficiency of the Cherenkov detector can be expressed via the number of detected 511 keV photons in coincidence with the Cherenkov detector N_{Chkv} divided by the number of photons detected by the scintillator N_{Scint}:

$$\varepsilon_{\mathrm{simple}} = \frac{N_{\mathrm{Chkv}}}{N_{\mathrm{Scint}}} \tag{12.2}$$

This formula only represents the general logic behind the approach and needs to be completed by additional terms: the Cherenkov detector has a non-negligible probability to create a dark event, which is coincident together with the scintillator. Within the measurement period N_{Rand} of these random coincidences occur, which need to be subtracted from the total number of coincidences. Furthermore, not all events measured with the scintillator originate from a 511 keV photon. There is a background contribution based on dark count and in case of $LaBr_3$(Ce) there is a slight radioactivity of the scintillator itself, which needs to be taken into account. These two contributions shall be called N_{Dark} in the following since they create false signals in the absence of the radioactive ^{22}Na source, i.e. in darkness.

Another contribution to background in the scintillator in the presence of the source originates in signals from other photon energies, that is the 1.27 MeV photons. Even though their energy is far above the 511 keV signal, their Compton contribution constitutes the background lying in the region of interest (ROI). Their contributed number of events to the spectrum is in the following denoted with N_{BG}, where BG stands for background.

The ROI is an interval around the signal peak, which is used to define the validity of a detected photon. The choice of the signal region introduces a bias to the result and will be treated in the scope of systematic uncertainties in section 12.5.5. The total number of valid

photons with 511 keV – denoted with N_{511} – consists of contributions from the photo peak and the Compton plateau:

$$N_{511} = N_\gamma + N_\mathrm{C} \tag{12.3}$$

The total number of entries in the ROI N_tot consists of aforementioned background contributions and the signal:

$$\begin{aligned} N_\mathrm{tot} &= N_\gamma + N_\mathrm{C} + N_\mathrm{BG} + N_\mathrm{Dark} \\ \Leftrightarrow \qquad N_\gamma + N_\mathrm{C} &= N_\mathrm{tot} - N_\mathrm{BG} - N_\mathrm{Dark} \end{aligned} \tag{12.4}$$

Thus, the simplified expression 12.2 can be updated and now reads:

$$\varepsilon = \frac{N_\mathrm{Chkv} - N_\mathrm{Rand}}{N_{511}} = \frac{N_\mathrm{Chkv} - N_\mathrm{Rand}}{N_\mathrm{tot} - N_\mathrm{BG} - N_\mathrm{Dark}} \tag{12.5}$$

There is, yet, another influence to be considered: As mentioned in the set-up description, the photons are created inside a slab of PMMA with a diameter of 15 mm. Assuming a photon origin in the center of this slab, the average distance inside the PMMA is 7.5 mm. Calculations predict an interaction probability of $\delta = 0.0743$, which would remove the photon from the beam so that it would not reach the Cherenkov detector and would be lost for a detection. Simulations give a similar value of $\delta = (0.0779 \pm 0.0009)$. The number of detected coincidences minus random contributions should be equal to the number of impinging gammas N_{511} times the efficiency and multiplied by one minus the interaction probability within the PMMA slab:

$$N_\mathrm{Chkv} - N_\mathrm{Rand} = N_{511} \cdot \varepsilon \cdot (1 - \delta) \tag{12.6}$$

Finally, the expression for the efficiency is complete and reads as follows:

$$\varepsilon = \frac{N_\mathrm{Chkv} - N_\mathrm{Rand}}{(N_\mathrm{tot} - N_\mathrm{BG} - N_\mathrm{Dark}) \cdot (1 - \delta)} \tag{12.7}$$

The following part describes how the different terms in the expression above are determined through measurements and analysis.

12.5.2. Method Description

Long term coincidence measurements were performed once with NaI for 20 min and once with $LaBr_3$(Ce) for 78 min. PVT was not used for the efficiency estimation due to a lack of low statistical significance. Data were taken in List Mode and analyzed in two different ways: firstly, all coincidences matching the requirements of 20 (30) channels within 50 ns (400 ns) that were detected with the $LaBr_3$(Ce) crystal (NaI) scintillator were recorded independently of a global coincidence. That way, all valid scintillation signals were captured which are used to obtain the total number of counts N_tot in equation 12.7. Secondly, the coincidences with the Cherenkov detector N_Chkv were counted, if the event was captured within a global coincidence time window of 50 ns, which was used for both scintillator types.
The spectrum containing all scintillator counts was then used for further analysis and the dark contribution was subtracted. To obtain the number N_Dark of dark events, a measurement

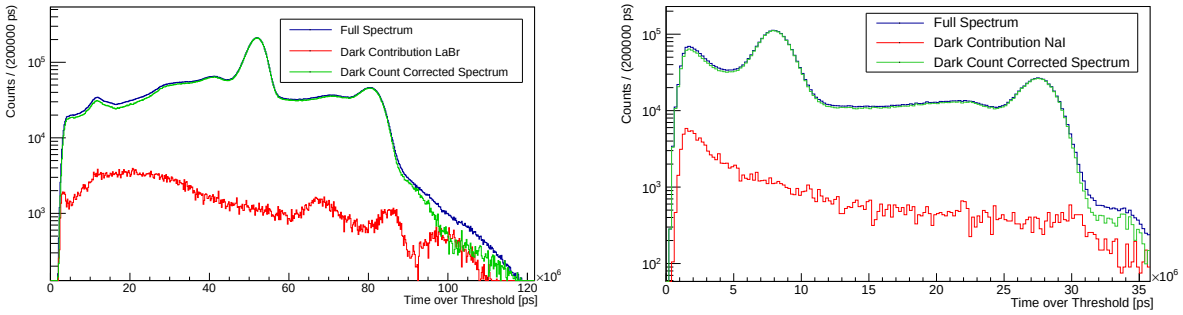

Figure 12.18.: Full spectrum of the ^{22}Na source taken with $LaBr_3(Ce)$ (left) and NaI (right) together with the dark count contribution in the absence of the source scaled up to match the measurement duration. The dark count corrected spectrum is shown in green.

without the radioactive source was performed for 300 s and coincident events on the scintillator were measured in the same way as for the measurement with the source. The spectrum was scaled up to match the measurement duration with source. In case of $LaBr_3(Ce)$ a factor of 15.6 was applied, whereas for NaI, only a multiplication by 4 was necessary. Figure 12.18 shows an example of the full spectrum taken with $LaBr_3(Ce)$ (left) and NaI (right) together with the background contribution in darkness. In case of $LaBr_3(Ce)$ one can see the intrinsic radioactivity in the peaks between $60 \cdot 10^6$ ps and $110 \cdot 10^6$ ps.

To obtain the background contribution, the dark count corrected spectrum is used for further analysis. It is shown in green color in figure 12.18. A fit is performed consisting of the functions for the signal and the background. The choice of the fit range constitutes another systematic uncertainty to be discussed in section 12.5.5. The function used for the fit and the results are presented individually for the two scintillator types. Based on the mean value and sigma of the signal peak a region of interest (ROI) can be defined and all numbers N_i from equation 12.7 refer to that range. The choice of ROI bares another systematic uncertainty.

The number of globally coincident events N_{Chkv} is then counted for events within the ROI and the random counts N_{Rand} are subtracted. These random counts were obtained with a dark measurement where the source was used, but the Cherenkov detector was misaligned from the beam and additionally placed behind a lead block. Thus, only random coincidences originating in the SiPM dark count are measured. Data was taken for 300 s and scaled up accordingly.
Finally, the probability for a gamma interaction within the PMMA was taken into consideration and the efficiency could be calculated using formula 12.7. The following list summarizes the whole procedure once more.

Summary of the calculation procedure for the efficiency estimation:

→ The full scintillator spectrum was obtained from the measurement

→ The dark contribution was subtracted from the spectrum

→ A fit range for the background estimation was defined

→ A fit to the spectrum was performed consisting of functions for signal and background. Here, the obtained mean value and sigma of the signal peak were saved

→ A region of interest (ROI) was defined based on the mean value and sigma of the signal peak

→ The exact number of dark events N_{Dark} that had been subtracted within the ROI before the fit was counted

→ The number of background counts N_{BG} within the ROI was obtained from the fit

→ The number of entries N_{tot} in the ROI was counted

→ The number N_{Chkv} of global coincidences with the Cherenkov detector was counted

→ Random coincidences N_{Rand} were subtracted

→ The correction was applied based on the interaction probability of a photon in the PMMA slab where it had been created

The fit functions for both detector types and the results for the background estimation are shown in the following section.

12.5.3. Background Estimation

The background estimation was performed using RooFit, a fitting toolkit based on C++ and the analysis framework Root [R B96]. A function is defined modeling the spectrum within a reasonable, predefined fit range. In a first attempt one could fit only the region around the signal peak, but since there is a significant Compton contribution from the high energetic photon, the range is extended. Thus, for both scintillator types, the signal peak at 511 keV and the 1.27 MeV peak are included. A modification of the fit range and the ROI is investigated later in this chapter in the scope of systematic uncertainties. The full model $F(x)$ can be expressed as a sum of the signal $S(x)$ and the background $BG(x)$.

$$F(x) = S(x) + BG(x) \tag{12.8}$$

The variable x represents the Time over Threshold.
In RooFit, the fit functions are defined as probability density function (p.d.f.) normalized over the fit range. In order to get the correct ratio between the individual functions the number of counts contributing to each function is a fit parameter as well. For example, a gauss function would have three parameters, one of which is the mean value, the other one the sigma and the third parameter is the number of entries under the gauss curve. If the fit is good, the sum of the counts obtained from the fit of all p.d.f.s should be close to the number of counts in the spectrum within the fit range.

Due to different resolution of the spectra of $LaBr_3$(Ce) and NaI, and because of the fact that the background peak at low TOT values for NaI cannot be suppressed entirely, the two

spectra need to be treated differently. This implies that an individual fit function needs to be defined for each scintillator material. This section on the background estimation is therefore divided into two parts.

Background estimation with Cerium-doped Lanthan-Bromide ($LaBr_3(Ce)$):

The range for the fit was chosen from $38 \cdot 10^6$ ps to $83 \cdot 10^6$ ps, which comprises the two photon peaks, the plateau in between and the Compton edges. The signals are each modeled using a gauss fit. Since the limited resolution causes the Compton edges to be smeared out, a gauss fit was applied there as well. Finally, a constant background was added. The full fit function for the $LaBr_3(Ce)$ spectrum reads

$$F_{\mathrm{LaBr}}(x) = G_{511,C}(x) + G_{511,\gamma}(x) + G_{1.27,C}(x) + G_{1.27,\gamma}(x) + const, \tag{12.9}$$

where

$$G(x) = \frac{1}{\sqrt{2\pi\sigma^2}} \cdot \exp\left(-\frac{(x-\mu)^2}{2\sigma^2}\right)$$

is the normalized p.d.f. of a gauss distribution, which has three fit parameters (μ, σ and the number of entries contributing to it). The index C designates the contribution from the Compton edge, while γ stands for the photo peak. The constant (*const*) represents only one fit parameter, which is the number of evenly distributed entries within the fit range forming a constant offset over the whole range. The two gauss functions of the 511 keV peak were considered signal $S(x) = G_{511,C}(x) + G_{511,\gamma}(x)$, while the rest was counted as background $BG(x) = G_{1.27,C}(x) + G_{1.27,\gamma}(x) + const$. The number of fit parameters was 13. There were 225 bins within the fit range with a bin width of 200000 ps. Thus, the total number of degrees of freedom is $ndf = 225 - 13 = 212$.
Figure 12.19 shows the spectrum with the full fit model (blue dashed lines) and the background fit (red). The signal is printed as green line. One can see an overlap between the Compton edge of the 511 keV photons with the photo peak. Both functions contribute to the signal in the ROI defined in the next paragraph.
The chi-squared over the number of degrees of freedom (χ^2/ndf) has a value of 72.753, which indicates that the fit is not perfect. One reason is that the peaks in the spectrum are in fact not gaussian shaped, since the measured quantity is the Time over Threshold, which is non-linear in energy. The deviation of the fit curve from the data points can be seen especially right before and right after the signal peak. Since the χ^2 sums up the squares of the deviations of the fit curve from each data point for all bins, these discrepancies give strong rise to the obtained χ^2/ndf.

The obtained mean value of the gauss fit for the signal is $\mu = (51.806 \pm 0.002) \cdot 10^6$ ps with a sigma of $\sigma = (2.148 \pm 0.003) \cdot 10^6$ ps. The parameter σ is now used to define the range of interest: Events within the interval from $\mu - \sigma$ until $\mu + \sigma$ are now considered to lie in the ROI, which corresponds to a TOT interval from $49.658 \cdot 10^6$ ps to $53.954 \cdot 10^6$ ps. A total amount of $(4.121 \pm 0.002) \cdot 10^6$ entries have been counted within the signal range, amongst which $(0.422 \pm 0.003) \cdot 10^6$ entries belong to background obtained from the fit. In addition,

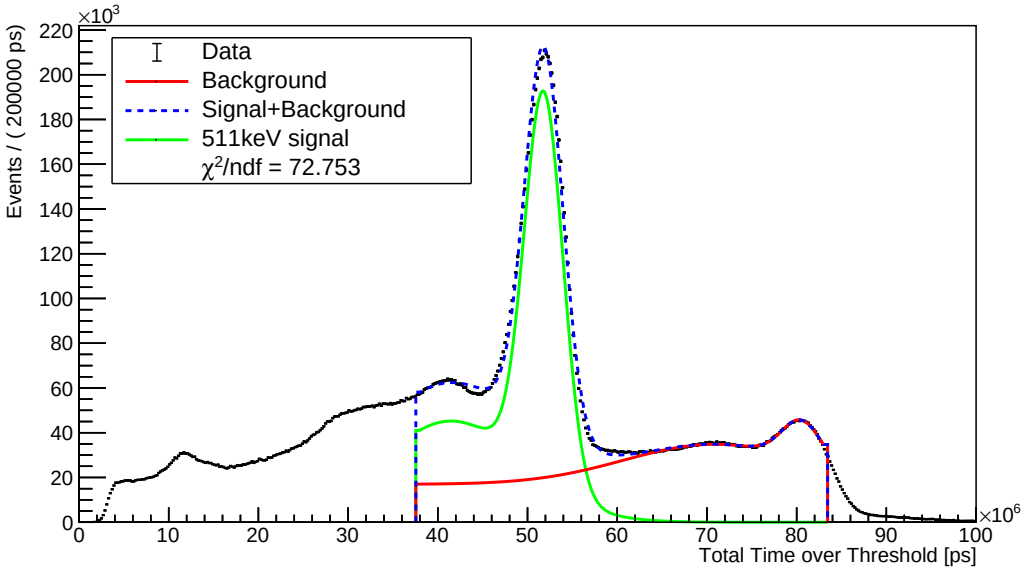

Figure 12.19.: Background estimation with $LaBr_3(Ce)$ using a fit function with four gauss functions and a constant offset. The signal is printed in green color and consists of the photo peak and the smeared-out Compton edge, the background is shown in red color and the full model is printed in dashed blue lines.

25242 ± 2383 entries are dark events counted within the signal range. The stated uncertainties are statistical. Systematic uncertainties are discussed later in section 12.5.5.
For all of these events 2012 ± 45 global coincidences and 90 ± 37 random coincidences were counted. The large uncertainty of the random coincidences originates from the low statistics. During the 300 s dark measurement for the estimation of random coincidences on the Cherenkov detector, only 16 globally coincident dark counts were obtained in total, 5.8 of which were found in the ROI [3]. The scaling factor of 15.6 for this dark measurement is propagated in the uncertainty as well. Results can be found in table 12.5

Background estimation with Sodium-Iodine (NaI):

The range for the fit was chosen from $1.6 \cdot 10^6$ ps to $29 \cdot 10^6$ ps, which again comprises the two peaks, the plateau in between and the Compton edge of the higher energetic peak. The lower Compton edge is not clearly visible due to the limited resolution and the in general lower signals compared to the $LaBr_3(Ce)$ measurements. The cautious reader may notice that the signals of the 511 keV peak in the spectrum of $LaBr_3(Ce)$ appears at a TOT value, which is about 6-7 times higher than in the spectrum taken with NaI. The 511 keV Compton edge therefore, disappears in the background peak at small bin numbers. This is the reason, why the fit function had to be modified and an exponential decay was introduced. The full fit function for the NaI spectrum becomes:

$$F_{\mathrm{NaI}}(x) = E(x) + G_{511,\gamma}(x) + G_{1.27,C}(x) + G_{1.27,\gamma}(x) + const, \tag{12.10}$$

[3] Non-integer numbers of entries originate in an interpolation at the lower and upper boundary of the ROI.

	Scintillator material	
Parameter	**$LaBr_3$(Ce)**	**NaI**
Signal mean μ [ps]	$(51.806 \pm 0.002) \cdot 10^6$	$(7.978 \pm 0.001) \cdot 10^6$
Signal sigma σ [ps]	$(2.148 \pm 0.003) \cdot 10^6$	$(1.153 \pm 0.002) \cdot 10^6$
Fit range [ps]	from $38 \cdot 10^6$ to $83 \cdot 10^6$	from $1.6 \cdot 10^6$ to $29 \cdot 10^6$
ROI ($\mu \pm 1\,\sigma$) [ps]	from $49.658 \cdot 10^6$ to $53.954 \cdot 10^6$	from $6.825 \cdot 10^6$ to $9.131 \cdot 10^6$
N_{tot}	$(4.121 \pm 0.002) \cdot 10^6$	$(1.140 \pm 0.001) \cdot 10^6$
N_{BG}	$(0.422 \pm 0.003) \cdot 10^6$	$(0.197 \pm 0.001) \cdot 10^6$
N_{Dark}	25242 ± 2383	3751 ± 245
N_{Rand}	90 ± 37	0 ± 0
N_{Chkv}	2012 ± 45	555 ± 24
Efficiency	$\mathbf{(0.567 \pm 0.016) \cdot 10^{-3}}$	$\mathbf{(0.641 \pm 0.027) \cdot 10^{-3}}$

Table 12.5.: Fit parameters, obtained values and result of the efficiency estimation for the detection of 511 keV photons using Cherenkov photons from Compton scattered electrons. Results for the measurement with $LaBr_3$(Ce) and NaI are listed. This table does not consider systematic uncertainties.

where

$$E(x) = c \cdot \exp(-c \cdot x)$$

is the normalized p.d.f. of an exponential distribution, which in this case describes the slope at the beginning of the range (See figure 12.20). The only signal function is the gauss peak at 511 keV: $S(x) = G_{511,\gamma}(x)$. The other terms in equation 12.10 are considered background: $BG(x) = E(x) + G_{1.27,C}(x) + G_{1.27,\gamma}(x) + const$

The obtained mean value of the gauss fit for the signal is $(7.978 \pm 0.001) \cdot 10^6$ ps with a sigma of $(1.153 \pm 0.002) \cdot 10^6$ ps. The ROI lies in the interval between $6.825 \cdot 10^6$ and $9.131 \cdot 10^6$. The chi-squared over the number of degrees of freedom (χ^2/ndf) has a value of 18.745 and is therefore significantly better than for the analysis using $LaBr_3$(Ce).

A total amount of $(1.140 \pm 0.001) \cdot 10^6$ entries has been counted within the signal range, amongst which $(0.197 \pm 0.001) \cdot 10^6$ entries belong to background obtained from the fit. In addition, 3751 ± 245 entries are dark events counted within the signal range.
555 ± 24 global coincidences were counted. No random coincidence counts were obtained in the 300 s measurement with the sodium source and the Cherenkov detector being covered. There were 10 events on the Cherenkov detector, but they were not globally coincident with a scintillator signal within the global coincidence time window. In comparison, the measurement using $LaBr_3$(Ce) resulted in 5.8 globally coincident random counts within the signal range.
Results can also be found in table 12.5.

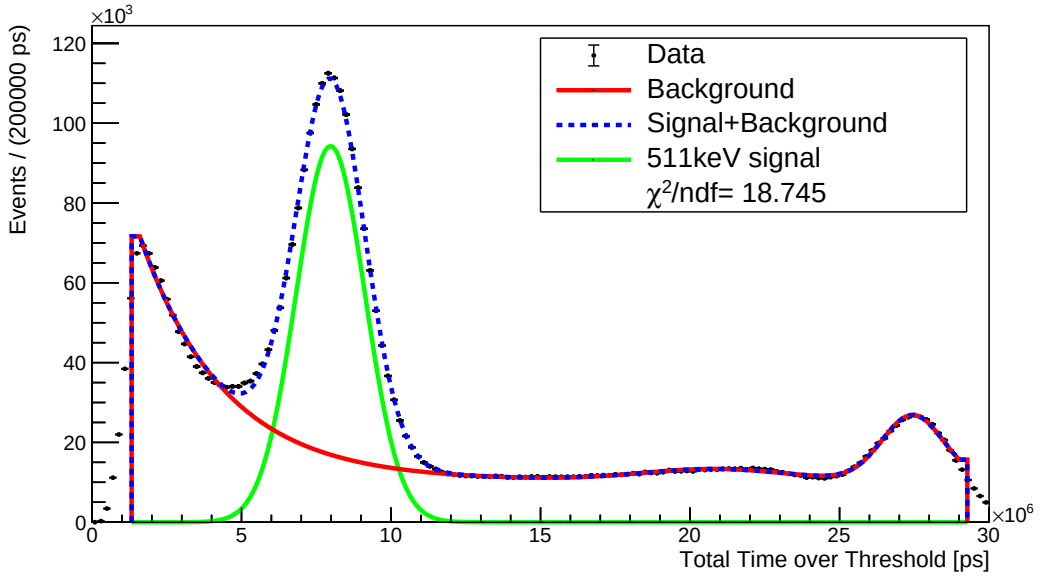

Figure 12.20.: Background estimation with NaI using a fit function with an exponential decay, three gauss functions and a constant offset. The signal gauss function is plotted in green. The high energy peak and the corresponding smeared out Compton edge are modeled as gauss functions as well (red curve). The full model is printed in dashed blue lines.

12.5.4. Efficiency Estimation for NaI and $LaBr_3$(Ce)

The resulting efficiency is calculated using equation 12.7 and uncertainties of the individual components in the formula are propagated using Gaussian error propagation. (See addendum, A.2.2 for details)
The uncertainty on the number of background counts was obtained from the errors of the fit. The uncertainties on all other contributions (N_{Dark}, N_{Chkv}, N_{tot} and N_{Rand}) are estimated using the square root of that number.

Finally, an efficiency of $\varepsilon = (0.567 \pm 0.016) \cdot 10^{-3}$ is obtained from measurements using the monolithic $LaBr_3$(Ce) crystal.
With the NaI scintillator an efficiency of $\varepsilon = (0.641 \pm 0.027) \cdot 10^{-3}$ is found. Systematic uncertainties are not included in the result yet. All results are listed in table 12.5.

12.5.5. Investigation of Systematic Uncertainties

Three sources of systematic uncertainties were considered:

Fit Range
The choice of the fit range introduces a bias to the analysis and therefore constitutes a systematic uncertainty. To estimate this uncertainty, the fit range was varied for both detectors. Both ends of the range were modified, but not at the same time. For $LaBr_3$(Ce), the upper end was moved to $75 \cdot 10^6$ ps and $64 \cdot 10^6$ ps, respectively and the efficiency was

calculated. Then the lower end was modified to $35 \cdot 10^6$ ps and $41 \cdot 10^6$ ps, while the upper end was held at the nominal value. The largest deviation from the nominal efficiency was observed for a range from $38 \cdot 10^6$ ps to $64 \cdot 10^6$ ps, with an absolute deviation of $0.035 \cdot 10^{-3}$. All results from the range variation are shown in table 12.6.

In case of NaI the range has been changed threefold: the upper end has been set to $17 \cdot 10^6$ ps and $23 \cdot 10^6$ ps respectively, while keeping the lower edge unchanged. Then the lower end of the range has been modified to $3 \cdot 10^6$ ps using the upper end of the nominal efficiency calculation. The only significant deviation with a value of $0.012 \cdot 10^{-3}$ was observed for a range from $3 \cdot 10^6$ ps to $29 \cdot 10^6$ ps.

Region of interest (ROI):
To estimate the influence of the choice of the ROI on the result, different ranges were tested. In this paragraph, symmetric ranges of interest are considered. The asymmetric range is discussed in the next paragraph. ROIs of $\mu \pm 0.5\,\sigma$, $\mu \pm 2\,\sigma$ and $\mu \pm 3\,\sigma$ were tested. The result is presented in figure 12.21, where the interval half width of the ROI is plotted on the x-axis and the resulting efficiency is plotted against the y-axis. The results using the $LaBr_3(Ce)$ crystal change far less than the results with NaI. Since in the signal range of the NaI spectrum, no Compton contribution is considered, the estimated background increases, when the range becomes larger. This circumstance leads to an overestimation of the efficiency. Due to this overestimation for larger ROI, the values for 2σ and 3σ are not taken into consideration for the estimation of the systematic uncertainties.

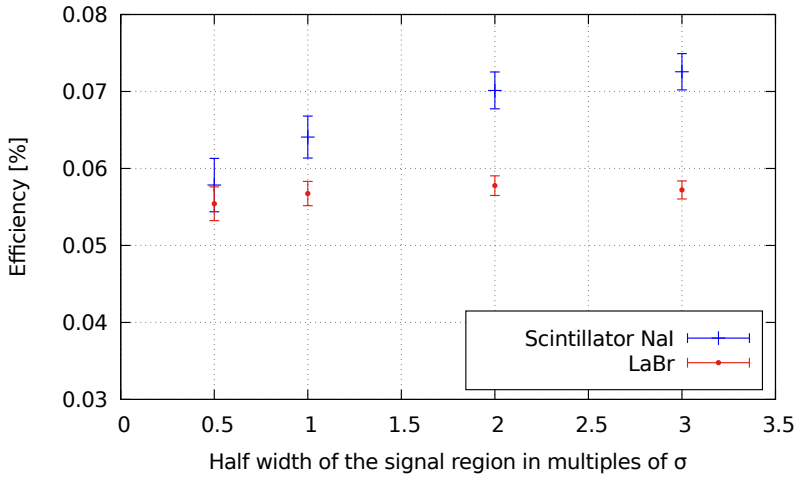

Figure 12.21.: Efficiency for various ranges of interests (ROI). The increase of the efficiency in case of NaI originates from an increasing overestimation of the background contribution to the ROI. Due to the overestimation of the background for larger ROI in case of NaI, the values for 2σ and 3σ are not taken into consideration for the estimation of the systematic uncertainties.

Asymmetric ROI:
In the $LaBr_3(Ce)$ spectrum the Compton contribution is visible and has been taken into consideration in the signal and background model. Compton scattered photons in the scintil-

Systematic uncertainties when using $LaBr_3(Ce)$			
Quantity	**Values**	**Efficiency ε**	**Deviation $\lvert\Delta\varepsilon\rvert$**
Fit range [10^6 ps]	from 35 to 83	$(0.564 \pm 0.016) \cdot 10^{-3}$	$0.004 \cdot 10^{-3}$
	from 41 to 83	$(0.549 \pm 0.015) \cdot 10^{-3}$	$0.018 \cdot 10^{-3}$
	from 38 to 64	$(0.603 \pm 0.017) \cdot 10^{-3}$	$0.035 \cdot 10^{-3}$
	from 38 to 75	$(0.580 \pm 0.016) \cdot 10^{-3}$	$0.012 \cdot 10^{-3}$
ROI	$\mu \pm 0.5\sigma$	$(0.555 \pm 0.022) \cdot 10^{-3}$	$0.013 \cdot 10^{-3}$
	$\mu \pm 2\sigma$	$(0.578 \pm 0.013) \cdot 10^{-3}$	$0.010 \cdot 10^{-3}$
	$\mu \pm 3\sigma$	$(0.572 \pm 0.012) \cdot 10^{-3}$	$0.005 \cdot 10^{-3}$
Asymmetric ROI	from $\mu - 3\sigma$ to $\mu + \sigma$	$(0.562 \pm 0.013) \cdot 10^{-3}$	$0.006 \cdot 10^{-3}$
	from $\mu - 4\sigma$ to $\mu + 2\sigma$	$(0.567 \pm 0.012) \cdot 10^{-3}$	$0.000 \cdot 10^{-3}$
	from $\mu - 5\sigma$ to $\mu + 1\sigma$	$(0.550 \pm 0.013) \cdot 10^{-3}$	$0.017 \cdot 10^{-3}$
Systematic uncertainties when using NaI			
Quantity	**Values**	**Efficiency ε**	**Deviation $\lvert\Delta\varepsilon\rvert$**
Fit range [10^6 ps]	from 1.6 to 17	$(0.641 \pm 0.027) \cdot 10^{-3}$	$0.000 \cdot 10^{-3}$
	from 1.6 to 23	$(0.640 \pm 0.027) \cdot 10^{-3}$	$0.000 \cdot 10^{-3}$
	from 3 to 29	$(0.652 \pm 0.028) \cdot 10^{-3}$	$0.012 \cdot 10^{-3}$
ROI	$\mu \pm 0.5\sigma$	$(0.578 \pm 0.035) \cdot 10^{-3}$	$0.062 \cdot 10^{-3}$
	$\mu \pm 2\sigma$	$(0.701 \pm 0.024) \cdot 10^{-3}$	$0.061 \cdot 10^{-3}$
	$\mu \pm 3\sigma$	$(0.726 \pm 0.024) \cdot 10^{-3}$	$0.085 \cdot 10^{-3}$

Table 12.6.: Estimated systematic uncertainties arising from the choice of fit range ROI and an asymmetric fit range. The two scintillator materials are treated separately. The reader may notice that the values in this table have been rounded to three decimals.

lator are also considered valid, as they can occur in coincidence with the Cherenkov detector. Thus, the ROI is modified to be asymmetric with an overlap to lower TOT values. This is not applicable for NaI, since only the gauss peak at 511 keV is considered as signal and an asymmetric ROI again leads to an overestimation of the background within the range and subsequently to an overestimation of the efficiency. The tested ROIs are $[\mu - 3\,\sigma; \mu + 1\,\sigma]$, $[\mu - 4\,\sigma; \mu + 2\,\sigma]$ and $[\mu - 5\,\sigma; \mu + 1\,\sigma]$, the latter of which shows the largest deviation of $0.017 \cdot 10^{-3}$. All values are listed in table 12.6.

The efficiency calculated in the previous section 12.5.4 is the nominal value $\varepsilon_{\text{nominal}}$. Deviations of the efficiency based on systematic uncertainties are given with respect to this nominal value. All stated systematic uncertainties add up to the total systematic uncertainty

$$\Delta\varepsilon^{\text{syst}} = \sqrt{(\Delta\varepsilon_{\text{ROI}})^2 + (\Delta\varepsilon_{\text{fitrange}})^2 + (\Delta\varepsilon_{\text{asym.range}})^2}, \tag{12.11}$$

where each $\Delta\varepsilon_i = \varepsilon_{\text{nominal}} - \varepsilon_i$ is defined as the deviation of the efficiency from the nominal value. Only the largest deviation from the nominal efficiency is considered. The only exception was the variation of the ROI in case of NaI, where the 2σ and 3σ ranges were excluded due to an overestimation of the background contribution.
The total systematic uncertainty for the measurements with $LaBr_3$(Ce) was $(\Delta\varepsilon)^{\text{syst}} = 0.042 \cdot 10^{-3}$. In case of NaI, a value of $(\Delta\varepsilon)^{\text{syst}} = 0.063 \cdot 10^{-3}$ was found.

12.5.6. Final Result and Discussion

Under consideration of the aforementioned systematic uncertainties (section 12.5.5) and together with the efficiency values obtained after the background estimation (section 12.5.3), the final result can be computed:

Using the $LaBr_3$(Ce) scintillator as reference detector, the calculated efficiency for the detection of 511 keV photons using Cherenkov light from Compton scattered electrons is

$$\boldsymbol{\varepsilon = 0.567 \cdot 10^{-3} \pm (0.016 \cdot 10^{-3})^{\text{stat}} \pm (0.042 \cdot 10^{-3})^{\text{syst}}} \tag{12.12}$$

And for the measurement using NaI, the following final result can be given:

$$\boldsymbol{\varepsilon = 0.641 \cdot 10^{-3} \pm (0.027 \cdot 10^{-3})^{\text{stat}} \pm (0.063 \cdot 10^{-3})^{\text{syst}}} \tag{12.13}$$

Even though NaI shows a slightly higher value, both scintillators agree well within the calculated uncertainties. One reason for a slightly higher efficiency measured with NaI might be that the signal was only modeled using a single gauss function, and the Compton contribution was neglected. The background in the ROI could have been overestimated resulting in an overestimated efficiency. Furthermore, the number of random coincidences with the Cherenkov detector are zero and nothing needs to be subtracted in the nominator of formula 12.7. The reason for this lack of random counts might be the higher threshold of 30 channels per coincidence on the scintillator (instead of 20 as with the $LaBr_3$(Ce) scintillator) making a trigger on dark count less likely.

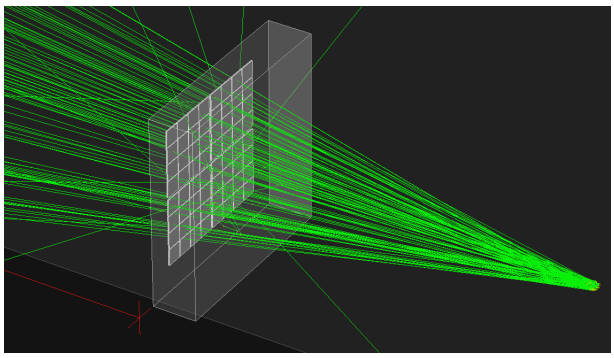

Figure 12.22.: Simulated set-up including PMMA, SiPM array and 100 simulated gamma tracks shown as green lines. A certain fraction of gammas scatters inside the PMMA or is absorbed. An event is defined as the detection of Cherenkov photons on at least four different channels.

An improvement could be achieved by reducing the number of required channels on the Cherenkov detector. The efficiency depends strongly on the applied rnocc. However, this could also give rise to false coincidences originating in the increased dark count contribution and might be subject to further investigations.

12.6. Comparison to Simulation Results

12.6.1. Implementation

A simulation using Geant4 was used to compute the efficiency of the detection of 511 keV photons with the described detector. Only the Cherenkov detector was implemented and bombarded with gammas. The geometry of the source was implemented to be not point-like, in order to mimic the origin of the photons to lie at the end point of the positron trajectory inside the source container. The source container was not implemented in this simulation to not loose gammas due to scattering or absorption in the container medium. Photon losses in air were negligible. In the scope of the development of this Geant4 application, it could be shown that less than 0.1 % of gammas were lost in air between source and Cherenkov detector [Den20]. The choice of the initial momentum direction of the gamma was based on random numbers and under consideration of the geometric constraint given by the aperture in the lead block. The rest of the set-up is basically identical to the described implementation in 9. Figure 12.22 shows a picture of the simulated set-up including the tracks of 100 gammas. An overvoltage of 4 V was chosen and the source position was centered with respect to the SiPM array. For the efficiency estimation, $N = 10^6$ gammas were simulated that way. An interaction of the gamma inside the PMMA would create a photo or Compton electron, which in turn would undergo Cherenkov effect, if the energy was sufficient. A valid event was defined as the detection of Cherenkov photons in at least 4 different channels. Finally, the efficiency was defined as the total number of these valid events N_{valid} divided by the number of initial gammas.

$$\varepsilon = \frac{N_{\text{valid}}}{N} \tag{12.14}$$

12.6.2. Results and Discussion of Systematic Uncertainties

The efficiency for the detection of 511 keV photons from simulated events was found to be

$$\varepsilon = 1.527 \cdot 10^{-3} \pm (0.012 \cdot 10^{-3}) \tag{12.15}$$

The value from the simulation was by a factor of three larger than the value obtained from measurements. Possible explanations are discussed later in this section. The statistical uncertainty is based on the assumption that for fixed N, the number of valid events is binomially distributed with an expectation value of $\varepsilon \cdot N$. For details on the uncertainty estimation see addendum A.2.2.

Estimation of systematic uncertainties:
The overvoltage constitutes one source of systematic uncertainty. It determines the photon detection efficiency (PDE) and depends on the break-down voltage, which again changes with temperature. In the set-up the temperature could only be measured at the aluminum cooling finger in about 2 cm distance from the SiPM array. Furthermore, a special gap filler between SiPM and cooling finger was used for increased thermal conductivity, making a precise temperature measurement at the SiPM even more difficult. Thus, an uncertainty on the temperature measurement on the order of 10°C had to be assumed. This translated to a maximum uncertainty on the break-down point and the overvoltage of 0.5 V. Thus, the simulation was repeated with 3.5 V and 4.5 V to estimate the systematic uncertainty on the result. Efficiencies of $(1.326 \pm 0.030) \cdot 10^{-3}$ and $(1.733 \pm 0.040) \cdot 10^{-3}$ were found, respectively.

Another systematic uncertainty lies in the positioning of the source location with respect to the array. Due to the extended source location a precise alignment of the beam with the center of the array was not possible. To estimate the influence of such a misalignment, the simulation was repeated using a shift of the source location by 3 mm in one direction, which corresponds to a shift by one SiPM channel. The efficiency sank slightly with respect to the nominal value to $(1.472 \pm 0.040) \cdot 10^{-3}$.

In total the systematic uncertainty was $\Delta\varepsilon^{\text{syst}} = 0.213 \cdot 10^{-3}$.
The simulated efficiencies for the individual parameter changes are listed in table 12.7. The final result on the simulated efficiency was

$$\boldsymbol{\varepsilon = 1.527 \cdot 10^{-3} \pm (0.012 \cdot 10^{-3})^{\text{stat}} \pm (0.213 \cdot 10^{-3})^{\text{syst}}} \tag{12.16}$$

Discussion of the result:
It has already been pointed out that the above value is significantly larger than the result from the measurement. One possible explanation is an overestimated photon detection efficiency (PDE) of the photon detector. First of all, the exact overvoltage was unknown as explained above. Besides that, the detection efficiency depends strongly on the surface quality of the SiPM windows. Due to several rebuilds and improvements of the set-up and countless changes of samples during the measurements with the electron source, scratches on the surface might have impaired the transmission through the silicone window.
Thus, one can assume that the efficiency of the SiPMs was lower than the value of 58.2 % given in the data sheet for an overvoltage of 4 V [Ham16]. Simulations show that an efficiency

Quantity	Values	Efficiency ε	Deviation $\lvert\Delta\varepsilon\rvert$
Overvoltage [V]	3.5	$(1.326 \pm 0.030) \cdot 10^{-3}$	$0.201 \cdot 10^{-3}$
	4.5	$(1.733 \pm 0.040) \cdot 10^{-3}$	$0.206 \cdot 10^{-3}$
Position shift [mm]	3	$(1.472 \pm 0.040) \cdot 10^{-3}$	$0.055 \cdot 10^{-3}$

Table 12.7.: Estimated systematic uncertainties on the simulation results arising from the choice of the overvoltage and the exact source position. The reader may notice that the values in this table have been rounded to three decimals.

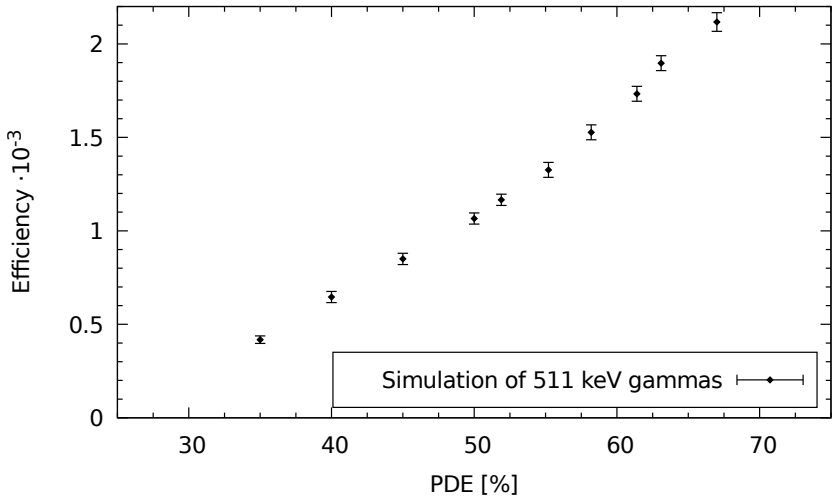

Figure 12.23.: Efficiency for the detection of 511 keV gammas versus photon detection efficiency of the SiPMs.

close to the value from the measurement can be obtained when using a PDE of about 40 %. Figure 12.23 shows the efficiencies from simulations using different PDEs. The efficiency increases strongly with the PDE.

Another explanation for the discrepancy between simulation and measurement is the reflection behavior of Cherenkov photons at the sidewalls of the PMMA sample. In the simulation, the surface was defined as *back-painted*, which means that photons would be absorbed at the side wall. Also in the measurement set-up the side walls of the PMMA sample were wrapped in black tape and the top surface was covered with thin black plastic foil. However, it cannot be clarified if the simulation resembles the real set-up precisely.

12.6.3. Efficiency at Higher Photon Energies

Unlike in the real measurement, the energy of the initial photon can be chosen in the simulation. The efficiency on the detection of photons was investigated for different energies. Furthermore the rnocc could be easily and quickly changed. Figure 12.24 shows the results of

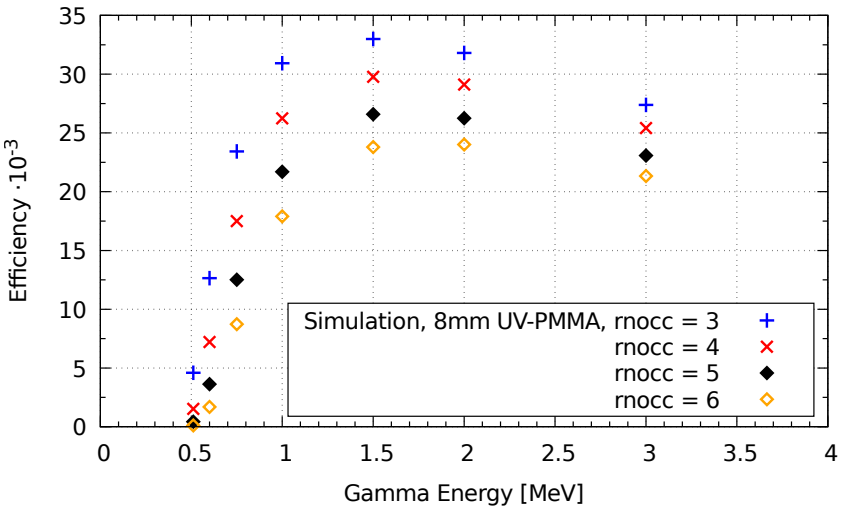

Figure 12.24.: Efficiency for the detection of 511 keV gammas versus gamma energy from simulated events. Results for different rnocc are shown.

these simulations. The efficiency is plotted versus energy for different rnocc. The smaller the requirement on the channel number, the larger the efficiency, since the acceptance threshold for Cherenkov events is lower and more events are registered. In the lower range of the graph, the efficiencies increase very rapidly with increasing gamma energy. This is due to the fact that on average the energy of a Compton electron increases for higher gamma energies and therefore produces more Cherenkov photons. This increases the detection probability for that electron. The curve flattens and starts dropping above a value of 1.5 MeV, due to the decreasing cross section for Compton scattering for higher gamma energies. Independent of the chosen rnocc, the set-up in its current configuration has the highest efficiency for the detection of gammas that have an energy of about 1.5 MeV. For a rnocc of 4, a simulated efficiency of up to 3 % is possible.

12.7. Further Measurements with the Cherenkov Detector

In this chapter the measurements that characterize the Cherenkov detector will be shown. This characterization is independent of the choice of the scintillator type. The patterns of coincident Cherenkov photon hits from Compton and photo electrons will be shown. The average number of detected Cherenkov photons for different rnocc was computed and will be discussed. Finally, the response to a shift of the gamma source location from accumulated events is presented. All results will be compared to simulations, where an investigation of the influence of the gamma energy on the results was performed.

12.7.1. Detected Pattern of Coincident Hits

The detected coincident hits of Cherenkov photons from accumulated events were investigated. The stated measurement and analysis parameters from table 12.3 were employed. The results were afterwards compared to simulations.

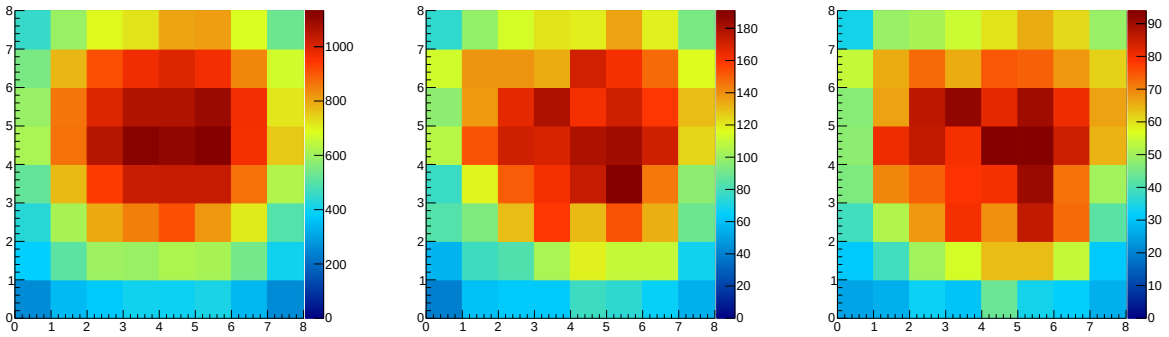

Figure 12.25.: Coincident hits of Cherenkov photons from (mostly) Compton scattered electrons in PMMA for different materials used for the reference detector. Long term measurement with $LaBr_3(Ce)$ (left) and NaI (middle) both without a cut on the photon energy of 511 keV. The cut is applied for the NaI measurement in the right picture.

Figure 12.25 shows the distribution of hits from accumulated events over the total measurement duration of 20 min (using NaI) and 78 min (using $LaBr_3(Ce)$) respectively. The obtained patterns on the Cherenkov detector when applying an energy cut on the 511 keV peak energy in the scintillator spectrum are shown as well for comparison. The plot then contains only events that were in coincidence with a photon from a $\pm 1\sigma$-interval around the 511 keV peak in the scintillator spectrum.
The measured pattern is an accumulation of Cherenkov cones intersecting the array, which were created by energetic electrons in the PMMA sample. Compton electrons are created all along the beam line of the gamma source (compare figure 12.2) under various Compton scattering angles. The electrons are created with a momentum in forward direction with respect to the initial gamma momentum direction. Consequently, also the Cherenkov cones are pointed in forward direction forming an accumulation on the read-out plane with a center of gravity in the center of the array. Therefore, the pattern indicates where the beam of 511 keV photons hit the PMMA sample.
Both Compton scattered electrons and photo electrons contribute to the signal in the Cherenkov detector, however, to very different extends: simulations predict that in PMMA only $(0.37 \pm 0.06)\,\%$ of photons with 511 keV interact via photo effect [Bä20b].

The measured patterns are expected to be independent of the scintillator used for the reference detector. This was investigated by measuring the width of the distribution of hits using the σ-parameter of a two-dimensional gauss fit. A symmetric distribution in x- and y-direction was expected, which is why a symmetric gauss function with only one σ-parameter for both directions was chosen. The results are shown in table 12.8.
Within the statistical uncertainties, the widths of the measurements for both scintillator types are in good agreement with one another, as expected: for $LaBr_3(Ce)$, the width was $\sigma = 3.26 \pm 0.03$ and for NaI $\sigma = 3.41 \pm 0.07$. Furthermore, applying an energy cut has no significant influence on the obtained mean value or width of the pattern but only reduces the number of entries for the same measurement duration.

	Mean x	**Mean y**	**Width σ**
$LaBr_3$(Ce)	4.24 ± 0.02	4.95 ± 0.03	3.26 ± 0.03
NaI	4.38 ± 0.06	4.93 ± 0.07	3.41 ± 0.07
NaI (with energy cut)	4.37 ± 0.09	4.78 ± 0.10	3.38 ± 0.10
Simulation	3.91 ± 0.01	5.70 ± 0.01	2.82 ± 0.02

Table 12.8.: Coordinates of the the center of gravity and the width of the distribution of accumulated coincident Cherenkov hits. The measurements with the two different scintillator types are shown together with an analysis using an energy cut and results from simulations in Geant4.

	Average Number of Detected Photons		
rnocc	**Energy cut on 511 keV**	**No energy cut**	**Simulation**
3	12.18 ± 0.37	12.04 ± 0.25	5.28 ± 0.08
4	16.89 ± 0.69	17.15 ± 0.50	6.55 ± 0.17
5	20.96 ± 1.05	21.06 ± 0.76	7.75 ± 0.37
6	24.50 ± 1.49	24.76 ± 1.07	9.13 ± 0.86

Table 12.9.: Average number of detected Cherenkov photons per event for different required number of coincident channels (rnocc) with and without energy cut around the signal peak in column 2 and 3 respectively. A comparison to simulation results is shown in column 4.

The mean values of the distribution in x- and y-direction were free parameters. The center of the array had the coordinates $(\mu_x, \mu_y) = (4, 4)$. The obtained values demonstrate that the gamma source was not perfectly centered with respect to the Cherenkov array. In case of $LaBr_3$(Ce) for example, $\mu_x = 4.24 \pm 0.02$ and $\mu_y = 4.95 \pm 0.03$ was found. The shift in x-direction corresponds to about one third of a channel. The side length of one channel was 3 mm. In y-direction, a misalignment by about the size of one channel was found in all measurements.

In the simulation the source was shifted by 1 mm in x-direction and 3 mm in y-direction on purpose to allow for a better comparison. 10^6 gammas were simulated, about 8 percent of which interacted in PMMA. In total, about 1527 coincident events with at least 4 channels were registered. $\mu_x = 3.91 \pm 0.02$ and $\mu_y = 5.70 \pm 0.03$ was found for the mean value of the gauss fit, and a width of $\sigma = 2.82 \pm 0.02$ was calculated. Thus, there is a deviation from the position setting, most likely due to the geometry of the source, which is not point-like. The response to a shift in source position is further investigated in section 12.7.3.

12.7.2. Counting Cherenkov Photons from Compton- and Photoelectrons

One main goal of the detection of electrons using Cherenkov light in an application in a Compton camera is to count the number of photons created in the radiator material. The photon number yields information on the electron energy. However, the energy resolution has

already been proven to be unsatisfactory and the expected number of photons per 511 keV photo electron is low. A calculated value using the algorithm described in section 7 yields 14.7 detected photons per electron with an energy of 511 keV. In this set-up using PMMA as radiator material, most electrons are Compton electrons with a maximum energy of only 341 keV, thus, producing a fewer amount of photons. In this case, the calculation predicts 20.4 created photons and an expected number of 4.8 detected photons – not including cross talk or after pulsing in the calculation.

Nevertheless, the number of photons can be counted using the TOT value of each signal. For the measurements the NaI scintillator was used. Results are listed in table 12.9. The resulting mean value of the measured number of photons depends strongly on the required number of coincident channels. For the default rnocc for these measurements, which is 4, 16.89 ± 0.69 photons were detected on average. When choosing a rnocc of 3, the mean value drops significantly to 12.04 ± 0.25 photons per event.

One reason is that a smaller requirement on the channel number allows dark events to contribute more strongly to the result. The influence is, however, relatively small: assuming an average dark count rate per channel of 50 kcps the probability of having a thermally triggered dark event on one channel within the CTW of 5 ns is about 1.6 %. The probability that 2 detected Cherenkov photons are registered as a coincidence event by the algorithm (with rnocc=3) due to an additional dark event is 1.5 %. These probabilities were calculated using a Poisson probability distribution for the occurrence of a dark event in one channel within the CTW and then taking a binomial probability distribution for having a certain number of channels of the array fire within that CTW.

The second reason for the strong dependence of the mean value on the rnocc is as follows: it is reasonable to assume that there is a large number of Cherenkov events with only a very small amount of photons being created and even fewer being detected. This is due to the fact that electrons with an energy of 511 keV and below produce only a few dozen photons in PMMA. Multiple scattering causes electrons to be deflected from their original momentum direction. Then, the Cherenkov cone will intersect the photon detection plane at a different position as well, or photons could even leave the photon sensitive area and would be lost for detection. These events also give rise to smaller numbers of detected photons per event. The threshold on the channel number imposes a strong cut on the number of accepted events. The rnocc can therefore be seen as some sort of energy trigger for the electrons. The higher the requirement for the number of channels, the higher the required average electron energy to be detected via Cherenkov emission. And, therefore, with larger rnocc the average number of detected Cherenkov photons increases.

Influence of the energy cut on 511 keV:
Figure 12.26 shows a histogram for the number of photons per event with and without an energy selection. While the blue histogram contains all coincident events, the green one only shows those, that were in coincidence with a photon from the ROI around the 511 keV peak in the scintillator spectrum of NaI. For this measurement an rnocc of 4 was chosen. The general shape is the same in both cases. Also, the mean value on the number

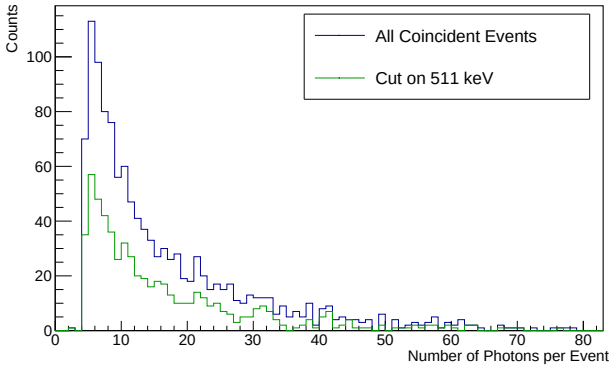

Figure 12.26.: Histogram of the number of photons per event with and without energy cut.

of detected photons is unchanged by the energy cut. A value of 16.89 ± 0.69 photons per event was obtained when applying the energy cut on 511 keV. This value is only by 0.26 photons higher than the mean value obtained without the cut. This constitutes an insignificant change considering the statistical uncertainties of the result. The same behavior is observed for all other analyses using other rnocc. The results are also listed in table 12.9.

Comparison to simulations:
In figure 12.27 the photon number distribution is plotted for different rnocc. Absolute numbers shrink with increasing rnocc and the distribution shifts to higher bin numbers. This happens because the minimum possible number of photons per event is equal to the number of channels required for a coincidence, since the lowest number of photons per channel is one.

Figure 12.28 shows the photon number distribution from simulated events for various rnocc. Similar to the measurements, the distribution also shifts towards higher photon numbers with growing rnocc. Furthermore, the long tail towards higher photon numbers does not occur in the simulated data. In fact the largest obtained photon number per event was 17. This has also an influence on the mean value of the number of detected photons: for an rnocc of 4 for instance, the mean value is 6.55 ± 0.17, which is less than half of what was obtained in the measurement. These simulation results are listed together with measurement results in table 12.9. One reason for this large discrepancy lies inherent in the method for photon counting using TOT values: the TOT scales logarithmically with the detected number of photons. A small change in TOT can lead to a large change in the calculated photon number. Furthermore, noise on the falling edge of the signal can have a large influence on the measured TOT value. After pulses occurring on the falling edge can cause an even larger distortion of the TOT value giving rise to vastly overestimated photon numbers. This explains why very high photon numbers can occur in the measurement even though the theoretically expected number of created Cherenkov photons is smaller.

Another reason for the differences between measurement and simulation is the fact that dark count was not implemented in Geant4. The influence of dark count on the mean value is only on the order of a few percent, however.

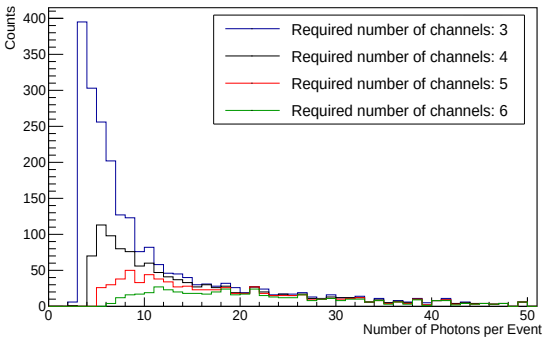

Figure 12.27.: Histogram of the number of photons per event for various required numbers of channels.

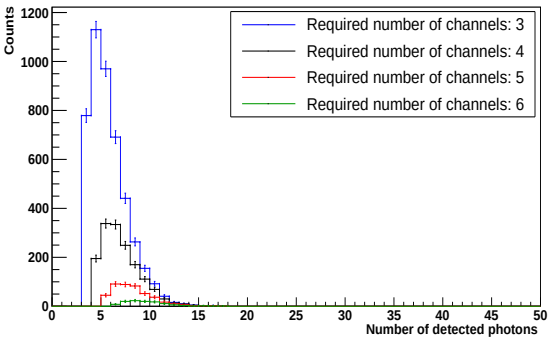

Figure 12.28.: Histogram of the number of photons per event for difference rnocc from simulated gamma events.

Number of detected Cherenkov photons for higher gamma energies:
The simulation allowed to test fictitious gamma sources with higher energy, which were not available in the laboratory. The mean value of the number of detected Cherenkov photons was calculated from simulated gamma events of different energies. The results are shown in figure 12.28 for different rnocc. As expected the mean value increases when the rnocc is incremented. Furthermore, larger gamma energies cause the mean value on the detected Cherenkov photon number to increase. This represents the increasing energy of the Compton electron for higher gamma energies, which subsequently causes more Cherenkov photons to be created and detected. A larger photon number is beneficial for the reconstruction of momentum information on the electron and the scattering vertex for a potential application in a Compton camera.

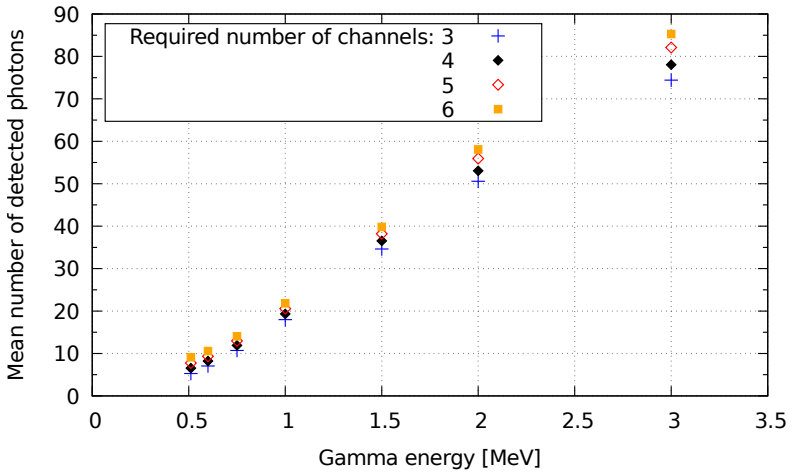

Figure 12.29.: Mean number of detected photons from simulated events for different gamma energies and rnocc. The mean value increases both with energy and rnocc.

12.7.3. Variable Gamma Source Positions

The response of the detector to a shift of the gamma source position was investigated. To that end the lead block containing the ^{22}Na source was moved in steps of 1 cm perpendicular to the beam axis in both directions. This movement caused the photon beam to hit the PMMA on different positions. Compton and photo electrons therefore emerged at different positions as well, creating Cherenkov cones covering different areas of the array. Thus, the pattern from accumulated events was expected to shift together with the source.
Figure 12.30 shows the results from measurements with 300 s exposure on every position. One can see the pattern from accumulated events shifts with the source location. The channel side length is 3 mm. Considering the space in between the channels and in the center of the array, a movement by 1 cm should shift the center of gravity of the pattern by about 3 channels.
To quantify the obtained shift in the pattern, the entries of each column were projected onto the x-axis and a gauss fit was performed. The mean values were used to compare the measured pattern at different position settings. The corresponding histograms and fits are also shown in figure 12.30.

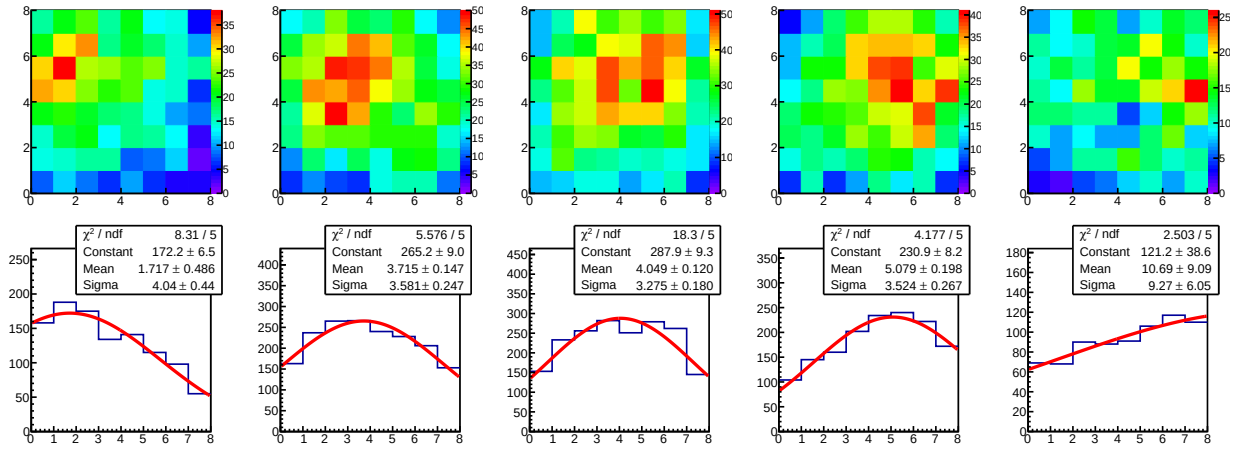

Figure 12.30.: Occupancy plot of coincident Cherenkov photons from accumulated Compton and photo electrons for five different gamma source positions. The individual source positions were separated by 1 cm. The histograms below show the projection of entries in each column onto the x-axis. The shift of the pattern was investigated using gauss fits.

Even though a clear shift of the pattern is obtained for each source position, the absolute values differ from the expectations. The reconstructed shift is defined as the difference of the mean value with respect to the center position. For example, for the position setting 1 cm to the right, the obtained difference was

$$(\mu_{1\,\mathrm{cm}} - \mu_0) \cdot 3\,\mathrm{mm} = ((4.049 \pm 0.120) - (5.079 \pm 0.198)) \cdot 3\,\mathrm{mm} = (3.09 \pm 0.696)\,\mathrm{mm}$$

Reconstructed and true source positions can be seen in the plot in figure 12.32. Results from measurement and simulation are compared with the actual position setting: this visualizes the discrepancy.

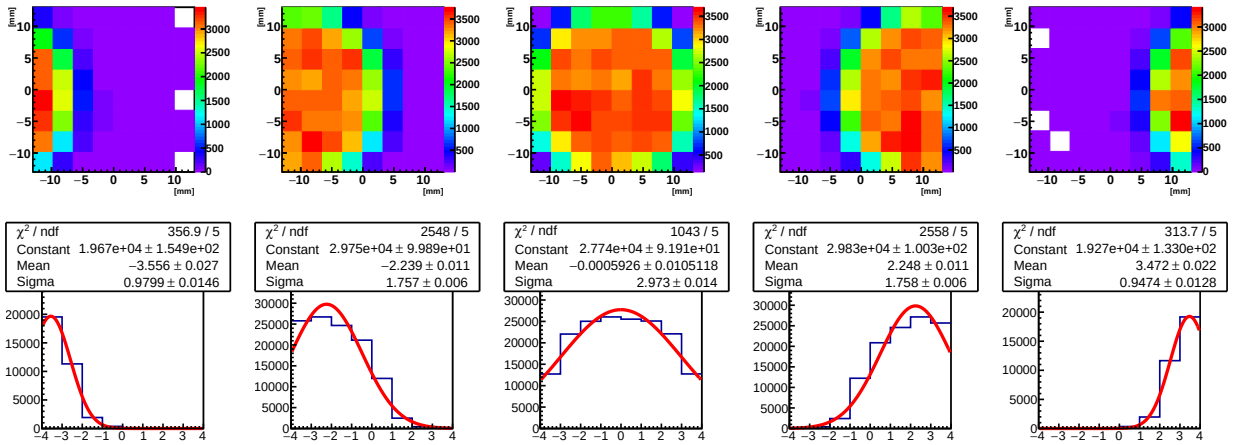

Figure 12.31.: Simulated distributions of coincident Cherenkov photons from Compton and photo electrons. A white field in the hit map indicates that there was no photon detected in that channel. The five individual positions were separated by 1 cm. A gauss fit was used to quantify the response to the shifted source location.

The simulation results are shown in figure 12.31. Again 10^6 gammas were simulated and the detected Cherenkov photons were plotted in the same fashion as the measurement data. The simulated patterns show sharper contours. The position of the pattern on the array was quantified in the same way using a gauss fit to the projection of the column entries onto the x-axis. However, also the simulation does not enable to draw precise conclusions on the source locations: using again the example of a shifted position to the right by 1 cm, the reconstructed position is off by about one channel size.

There are several potential explanations for this discrepancy from the position setting: Firstly, the area of the beam intersecting the PMMA surface has a diameter of > 2 cm. Thus, at certain positions, a significant fraction of photons is lost when the beam is misaligned and not all photons hit the PMMA. This causes the pattern to be cut off and a correct reconstruction is not possible. This is especially obtained from the simulation data, where the fit to the projected distribution has much smaller width due to the missed photons outside the boundaries of the array. A larger array side length would help overcome this limitation.

Furthermore, the array has high granularity, since only 64 channels are available for the detection of Cherenkov light. The reconstruction of the shift could be significantly improved by the use of smaller channels.

Also, reflections from the side wall of the PMMA sample could smear out the patterns from individual events. This influence is less prominent in the simulation, since the surfaces of the PMMA had been defined as *back-painted*, thus, photons should be absorbed when hitting the side walls. The patterns appear sharper than the ones from the real measurement.

Finally, taking longer measurements at each position and therefore increasing the statistics, could also improve the accuracy of the source reconstruction.

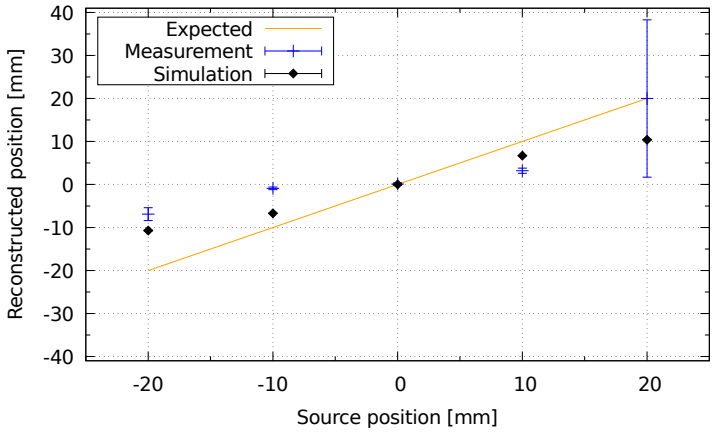

Figure 12.32.: True and reconstructed source position from experimental and simulation data using accumulated events. Only low accuracy on the reconstructed source location was achieved.

12.8. Summary of the Detection of 511 keV Photons

This chapter has demonstrated the feasibility of the detection of Cherenkov photons from Compton scattered electrons and photo electrons created by 511 keV gammas in UV transparent PMMA using an array of SiPMs. A dual-face detector set-up has been used as reference detector. Two different scintillator types were tested. A characterization of the measurement set-up yielded a coincidence time resolution (CTR) for the detection of two 511 keV photons on the order of 6-19 ns depending on the scintillator type used.
The efficiency for the detection of gammas was calculated and a value of

$$\varepsilon = 0.567 \cdot \ 10^{-3} \pm (0.016 \cdot 10^{-3})^{\text{stat}} \pm (0.042 \cdot 10^{-3})^{\text{syst}}$$

was found using the $LaBr_3(Ce)$ scintillator and

$$\varepsilon = 0.641 \cdot 10^{-3} \pm (0.027 \cdot 10^{-3})^{\text{stat}} \pm (0.063 \cdot 10^{-3})^{\text{syst}}$$

using NaI, respectively. Comparisons with simulations showed that the efficiency increased for larger gamma energies with a maximum in the lower percent range at about 1.5 MeV. Surely, the scratches on the SiPM entrance windows impaired the PDE of the detectors and subsequently reduced the efficiency for the detection of 511 keV gammas with this detection concept. Simulations indicated that employing new and undamaged photon detection devices could increase the efficiency by a factor of 3.

The patterns of coincident hits were investigated using accumulated events and a response to a shift of the gamma source location was obtained. The number of detected photons on the array was counted using the signal's TOT values. Large discrepancies between measurement and simulation were found originating from the inherent uncertainty in the calculation method of the photon number using TOT values. Due to the scarcity of the created Cherenkov photons, the mean value on the number of detected photons per event was low. Only about 17 photons were obtained in the measurement on average, while the simulation gave a value

of about 7 (both for an rnocc of 4). The computed mean values also show strong energy dependency and depend furthermore on the number of required coincident channels on the array.

The results might benefit from a measurement of the inherent time difference between the channels of the two detectors. The time difference could be measured using a light source in the center between the two detectors sending coincident pulsed light signals onto both detector arrays. Knowledge of the inherent time difference would allow for a reduction of the global coincidence time window in the algorithm. This might improve the rejection of background events and random coincidences.

Summarizing, the detection of Compton electrons via coincident measurement of Cherenkov photons could be successfully demonstrated.

13. Summary and Outlook

Contents

13.1 Summary of the Contents **245**
13.2 Prospect and Future Potential **247**
13.3 Conclusion **249**

13.1. Summary of the Contents

A novel detection concept for electrons that uses a coincidence measurement of Cherenkov photons in optically transparent radiator materials has been investigated. This detection modality was proposed as part of a Compton camera for higher energetic gammas ($\geq 1\,\mathrm{MeV}$) in medical applications. This work was able to provide a first proof of the principle, starting with a test of the very fundamental concept in a simplified test set-up, culminating in a measurement of 511 keV photons. 64 SiPM channels were used to detection coincident Cherenkov light from Compton scattered electrons.

The first tests were performed using a 16 channel SiPM array to detect Cherenkov photons created by electrons from a ^{90}Sr source in transparent samples like PMMA. While the ASIC based read-out with the STiC evaluation board enabled a coincidence measurement on all channels with a very good timing resolution of 242 ps, no trigger on single photon level was possible and the number of detected photons was not counted. The set-up that uses a 4 GHz oscilloscope enabled counting the Cherenkov photons in each channel with a calibration method based on peak integral spectra. However, only 4 channels at a time could be read out with that technique. Nevertheless, the proof of the concept could be provided with these two measurement methods. The patterns of coincident Cherenkov photons showed good response to the thickness of the PMMA samples and the location of the electron source. Using 2-dimensional fits of Gaussian distributions, the position of the source could be reconstructed from accumulated coincident events with an accuracy on the order of 1 mm.

These results proved to be in good agreement with theoretical calculations of the expected number of Cherenkov photons performed with a C++ program. To provide realistic estimations, this program took key parameters of the measurement, physical properties and geometric dimensions of the set-up into account. The emission and the propagation of Cherenkov light were based on electron energy, track length, sample thickness and wavelength dependent absorption coefficient. A wavelength and bias dependent photon detection efficiency (PDE) was implemented in the algorithm and geometric boundaries of the detector array were taken into consideration. This program provides deeper understanding of the

physical properties of the set-up and supports the interpretation of the outcome of the measurements.

As part of the development process of the different set-ups used in this work, the detector components were investigated. Some key properties of the photon detector were further examined like the dark count rate (DCR), the optical cross talk (OCT) and the breakdown voltage. All these quantities were investigated at different temperatures. An enhanced detector performance at low temperatures was obtained.
Furthermore, the transmission properties of different radiator materials were measured. The goal was to find the most suitable material with maximum transparency in the near UV. Additional constraining properties are physical qualities like high refractive index and low density. In the scope of these measurements, UV transparent PMMA turned out to be the best suited radiator material available and was used for all further measurements.

An extended and improved set-up using 64 SiPM channels, UV transparent PMMA and a read-out system based on the TOFPET2 ASIC by PETsys Electronics was implemented. It incorporated vast improvements like a cooling system that was capable of reducing the temperature of the SiPM array to values below 0°C. This reduced the dark rate and, thus, enabled triggering on single photon level on all 64 channels at a time. The pattern of accumulated Cherenkov events enabled a reconstruction of the source location with sub-mm accuracy. The width of the patterns was quantified for various sample thicknesses and the results were in good agreement with simulations obtained with Geant4. Simulations also demonstrated the energy dependence of the opening angle of the cone and consequently the width of the distribution of coincident hits. This proved the necessity of measuring the electron energy for the feasibility of the detection concept.
Time differences inherent in the ASIC as well as time walk effects were compensated. With this read-out board, the coincidence time resolution (CTR) for the detection of Cherenkov light was about 1.1 ns. The single photon timing resolution (SPTR) achieved for a pair of channels of about 480 ps.

An important achievement was the implementation of photon counting: the number of detected Cherenkov photons could be counted for each event and each channel individually based on the TOT value of the SiPM signal. To that end, an analytic relation between TOT and the number of detected photons was derived to calibrate each channel. The average number of photons per event was calculated for various sample thicknesses. Again, good agreement with simulations was obtained, despite unknown contributions like reflections inside the sample or the uncertainty on the PDE. However, significant deviations have been observed between calculation and measurement for thin radiator samples. This can mostly be pinned down to the negligence of reflections and especially multiple scattering in the calculation.
An application of the photon number counting to a measurement of the electron energy was not successful due to several statistical influences like fluctuating particle range, multiple scattering, the SiPM's PDE and the transmission of the samples. Furthermore, uncertainties were also inherent in the photon counting method itself, especially due to after pulsing and timing jitter.

Nevertheless, potential improvements could be pointed out, one of which is an improved method of photon counting: due to its linearity, the deposited charge per detected photon promises photon counting with lower uncertainty and significantly reduced vulnerability to after pulses or timing jitter.

Finally, the developed detector for Cherenkov light was applied to the detection of Compton and photo electrons created by 511 keV photons in UV transparent PMMA. A dual-face PET-like set-up was developed with a scintillator as reference detector. The coincident detection of Cherenkov photons from (almost exclusively) Compton electrons was possible. The number of detected photons could be counted. The average number of detected photons per event depended strongly on the required number of coincident channels on the SiPM array. An estimation of the efficiency for the detection of 511 keV photons with this detector resulted in a value of less than 10^{-3}. The corresponding results from the simulations deviate by more than a factor of 2. This may be explained by by a potentially reduced PDE in the actual measurement and the uncertainty on the temperature, which impacts the overvoltage. Independent of that, simulations point to a significant improvement of the efficiency on the order of 3 % for higher photon energies in the MeV range, which would be the interesting energy range in case of an application to prompt gamma detection.
The coincidence time resolution (CTR) for the detection of gammas in this dual-face set-up depended on the scintillator type. With NaI, 19 ns were achieved, $LaBr_3$(Ce) resulted in 6 ns and PVT gave a value of 9 ns. While the CTR for Cherenkov light is limited by the read-out electronics, for scintillators the limiting factor is their time constant.
The measured coincidence patterns from accumulated events showed response to a shift of the gamma source position. The sensitivity was limited by the divergence of the photon beam, the geometric boundaries of the SiPM array and the coarseness of the detector matrix. Thus, there is great potential for improvement, which is subject to future research.

13.2. Prospect and Future Potential

In the long term, the reconstruction of individual Compton scattering events is envisaged. The measured number and distribution of detected Cherenkov photons can be used to reconstruct the scattering vertex, the energy transfer from the photon to the Compton electron and the electron's momentum direction. Up to this point, the number of detected Cherenkov photons does not allow for a reconstruction of the electron energy, since the resolution is reduced by several quantities of statistical nature described above. Potential improvements have been presented and need thorough testing in the future.
The impact of multiple electron scattering inside the radiator imposes a complication on the reconstruction process and will eventually reduce the efficiency of the detector as a certain fraction of events might be rendered unusable. However, Geant4 simulations indicate that photons emitted at the beginning of the electron track show a very well confined ring structure on the detector plane. Only after a certain traveled distance, this structure is blurred due to multiple scattering and shrinking Cherenkov cone subsequent to the energy loss of the electron [Bä20a]. This is indicated by accumulated events from 1.5 MeV electrons in PMMA as shown in figure 13.1. 10^5 events were simulated and the photon hits from three different

parts of the electron trajectory were plotted. The graph shows the hit points of the photons on the read-out plane and does not contain a binning representing 64 SiPM channels.

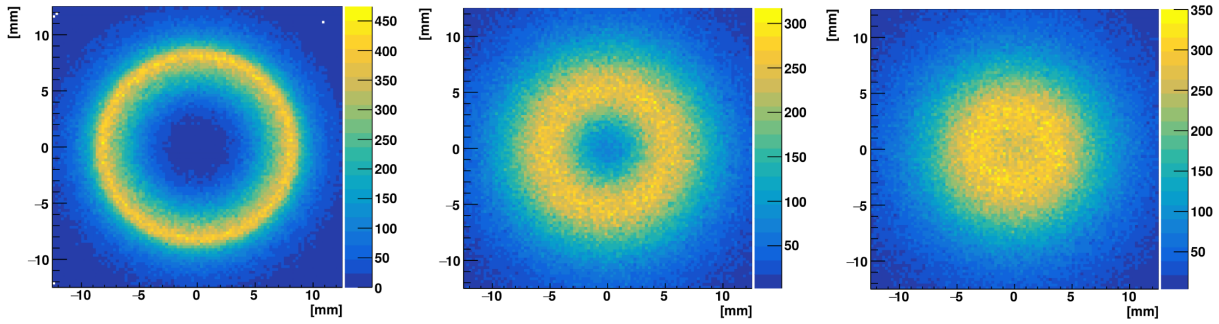

Figure 13.1.: Accumulated photon hits from different parts of the electron track. A well confined ring is seen for the first (left picture) and second (center picture) half millimeter of the electron trajectory until multiple scattering blurs out the structure (right picture). This indicates that information on the electron momentum and scattering vertex might be contained on the measured pattern and could be extracted with appropriate algorithms. [Bä20a]

A better understanding of the distribution of photons from single electrons must be gained through simulations and the analysis of measured events. This could allow for an identification of the ring created by photons from the first part of the track and separating it from the rest of the distribution. Pattern recognition algorithms based on deep learning and especially neural networks might be beneficial for achieving this goal.

First circle reconstructions have been performed already in 2018 using Hough transforms applied to simulation data [Kha18]. The reconstruction of the pattern on 64 channels that were formed by Cherenkov photons created by electrons of various incident angles was performed in 2019 [Ben20]. A fit of an elliptical function was used and the corresponding Cherenkov cone was reconstructed. Due to the coarseness of the detector matrix, an accurate reconstruction of the electron source position or the incidence angle was not possible yet.

To increase the resolution of the pattern, more and smaller detector channels are required. This has been tested and investigated in simulations using accumulated events [Bä20a].
In the prospect of building an extended set-up, parameters like the channel number and size, the arrangement of the SiPM array and the thickness and shape of the radiator sample must be optimized using simulations.

An ongoing simulation study using Geant4 investigates the implementation of SiPM arrays on the side walls of the PMMA sample to increase the Cherenkov light collection efficiency. This realizes a suggestion that was made already when this detection concept was proposed [PBW12]. A similar detector arrangement has also been presented by [SSI15] for the detection of 511 keV photons in PET applications using Cherenkov light from Compton electrons. A picture of such a detector arrangement is shown in figure 13.2. First results indicate a significant increase of the efficiency for the detection of 1.5 MeV gammas to values on the order of 10 % [Den20]. This value does, however, not contain information on the

reconstruction efficiency which quantifies the ability to obtain information on the Compton electron from the measured coincidence pattern. Parameters like the required number of coincident channels will surely have a large impact on this quantity.

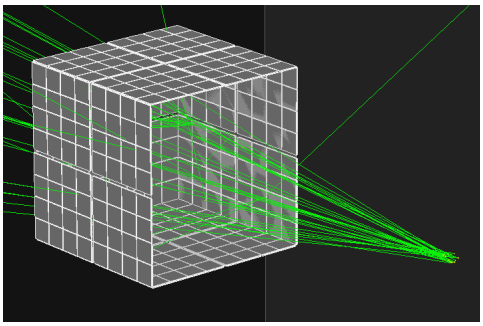

Figure 13.2.: Extended set-up with SiPM arrays at the side walls of the radiator, which in this case is a PMMA block with a depth of 24.7 mm. The picture shows its implementation in Geant4 together with 30 incident gammas with a source geometry similar to the one used in chapter 12.

An improvement of the timing resolution with the PETsys read-out system could be achieved by cooling the ASIC. As demonstrated in [Wac+16], cooling the chip by 13°C improves the coincidence time resolution by about 30 %. This indicates that the detection of Cherenkov photons on 64 – or even more – channels could be possible with a coincidence time resolution of better than 800 ps.

13.3. Conclusion

Despite the above listed achievements and the vast potential for improvements, there are many unknowns and unresolved issues before this electron detection modality can be applied to a Compton camera.

One issue relates to the measurement of the electron energy. Since the opening angle of the Cherenkov cone and, thus, the size of the ellipse on the read-out plane are strongly energy dependent, a measurement of that energy seems indispensable to obtain full information on the vertex and momentum direction of the electron. Due to statistical fluctuations of the number of created Cherenkov photons and because of uncertainties on the measured photon number, sufficient accuracy of this energy measurement might not be guaranteed. Without an energy measurement, a reconstruction of gammas in a Compton camera is only possible, if the energy of the incoming photon is known [PBW12].

Multiple scattering of the electron constitutes a great challenge for any reconstruction algorithm that attempts to retrieve information on the Compton electron. To this day, no successful reconstruction of single events was possible.

If an application to the detection of prompt gammas in particle therapy is envisaged the question of high event rates needs to be addressed. Even with sub-nanosecond time resolution,

a detection of prompt gammas emitted along the trajectory of bunched proton beams with up to 10^{10} protons per bunch is highly challenging. Furthermore, multi-scattering events with more than one Compton scattering site or events with more than one incoming gamma at the same time impose a significant complication to the reconstruction of individual events.

Until these questions have been addressed through further investigations, measurements and simulations, a final conclusion on the feasibility of this electron detection concept for the application in a Compton camera cannot be made.

A. Addendum

A.1. Tables and Values

Dark count rate scans for different temperatures for SiPM array S13361-3075AS by Hamamatsu:

The discriminator threshold was scanned from the noise level to a level of several photon equivalent. The dark rate was counted at each step. Measurements were performed for temperatures between 5°C and 35°C. The results for all temperatures are shown in figure A.1. The measurement details are presented in section 6.4.3.

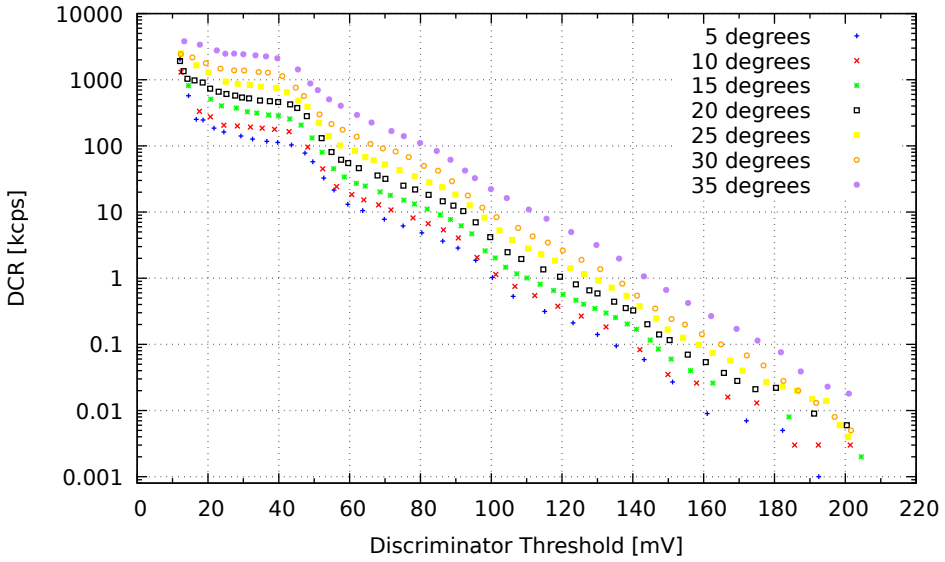

Figure A.1.: Dark count rate versus discriminator threshold measured at different temperatures.

Dark count rate and cross talk for SiPM array S13361-3075AS by Hamamatsu:

Table A.1 shows the measured dark date at 1 p.e. level for two different set-ups in columns 2 and 3, respectively, and lists the obtained optical cross talk (OCT) values in column 4. The measurement procedure is discussed in section 6.4.3.

	STiC	Discriminator and Counter	
Temperature	**DCR** [10^3 kcps]	**DCR** [10^3 kcps]	**Cross talk probability** [%]
5	156.37 ± 0.42	112.85 ± 5.73	2.5 ± 0.77
10	228.03 ± 0.58	199.37 ± 5.10	2.7 ± 0.49
15	337.74 ± 3.92	285.33 ± 16.30	2.7 ± 0.95
20	536.32 ± 1.71	473.91 ± 10.03	2.6 ± 0.83
25	871.33 ± 3.54	752.54 ± 59.54	3.3 ± 0.79
30	1505.9 ± 2.34	1375.49 ± 33.25	5.2 ± 0.75
35	2447.93 ± 4.88	2478.90 ± 25.50	-

Table A.1.: Temperature dependent dark count rate and cross talk probability for S13361-3075AS by HAMAMATSU. The dark measurements were performed with two different set-ups, an ASIC-based digital read-out system and an analog set-up using a discriminator and a counter, which was also used for cross talk estimations. Values taken from [Ali18].

A.2. Calculation of Statistical Uncertainties

A.2.1. Mean Number of Detected Photons

The mean value on the number of detected photons was calculated from photon spectra. The statistical uncertainty on that mean value was calculated by dividing that mean value by the number of entries in the photon spectrum. This section explains the uncertainty estimation based on the Central Limit Theorem (CLT) and the calculation of weighted means. [Bar93; Li18]

A.2.1.1. Central Limit Theorem (CLT)

May X be the sum of N independent variables with $X = \sum_{i=1}^{N} x_i$ where the x_i come from distributions with mean value μ_i and variance $V_i = \sigma_i^2$, then

a)

$$\langle X \rangle = \sum \langle x_i \rangle = \left\langle \sum x_i \right\rangle = \sum \mu_i \tag{A.1}$$

The expectation value $\langle X \rangle$ of the quantity X is the sum of the mean values of all N distributions.

b)

$$V(X) = \sum V_i = \sum \sigma_i^2 \tag{A.2}$$

The variance of the quantity X is the sum of the variances of all N distributions.

c)

$$\text{The distribution of } X \text{ becomes Gaussian for } N \to \infty \tag{A.3}$$

Special (and most useful) case:
If the *same* quantity x_i from the *same* distribution is measured N times, the CLT can be applied as follows:

- All μ_i are identical and $\mu_i = \mu$
- All σ_i are identical and $\sigma_i = \sigma$
- From equation (A.1) follows for the expectation value of X:

$$\langle X \rangle = \sum \mu_i = N \cdot \mu \tag{A.4}$$

- The average value of all x_i is

$$\overline{x} = \frac{\sum x_i}{N} = \frac{X}{N} \tag{A.5}$$

- The average average x is [1]

$$\langle \overline{x} \rangle = \left\langle \frac{X}{N} \right\rangle = \frac{N \cdot \mu}{N} = \mu \tag{A.6}$$

- The variance of the average of all x_i is

$$V(\overline{x}) = \frac{\sum V_i}{N^2} = \frac{\sum \sigma_i^2}{N^2} = \frac{N \cdot \sigma^2}{N^2} = \frac{\sigma^2}{N} \tag{A.7}$$

$$\Rightarrow \ \sigma(\overline{x}) = \frac{\sigma}{\sqrt{N}} \tag{A.8}$$

  This describes the standard error on the mean value of all x_i. It is the statistical uncertainty of the mean value of all x_i.

  This quantity $\frac{\sigma}{\sqrt{N}}$ gives a resolution with which the real mean value μ of the distribution can be calculated from the N independent measurements of x. It states that the probability of the mean value $\overline{x'}$ of a repeated measurement to lie within the interval of $\pm\frac{\sigma}{\sqrt{N}}$ is 68.3%.

Most important remark:
The above $1/\sqrt{N}$-relation holds for *any kind of distribution*, not only Gaussian.

A.2.1.2. Averaging Weighted Errors

General Remarks

If the mean value of a quantity x is to be determined where the error σ_i is not the same for all x_i, then the individual x_i get different weighting based on their error/resolution σ_i. A

[1] The term *average average* might seem odd at first, but it simply descibes the average value of several independent data sets consisting of variables x_i, each of which has its own average value $\overline{x}$.

measurement with better resolution (i.e. smaller σ_i) should get more weight than one with a larger σ_i.
If x_1 has an error of σ_1, which is better (i.e. smaller) than some other σ_2, then one can calculate a factor N to quantify the weight of each measurement as follows:

$$\frac{\sigma_2}{\sqrt{N}} = \sigma_1 \qquad \Leftrightarrow \qquad N = \frac{\sigma_2^2}{\sigma_1^2} \tag{A.9}$$

Measurement 1 is N times as good as measurement 2 and x_1 should get N times more weight than x_2. In other words, one needs N measurements with resolution σ_2 to have a measurement that as is good as one measurement with σ_1.
A generalization is as follows: The weight ω_i of a quantity x_i should be proportional to the inverse square of its error σ_i:

$$\omega_i \propto \frac{1}{\sigma_i^2} \tag{A.10}$$

with a constant proportionality factor (which we shall simply call σ_0^2 here), one gets

$$\omega_i = \frac{\sigma_0^2}{\sigma_i^2} \tag{A.11}$$

For the mean value of all x_i one obtains:

$$\overline{x} = \frac{\sum_i^N x_i \cdot \omega_i}{\sum_i^N \omega_i} = \frac{\sum_i^N x_i \cdot \frac{\sigma_0^2}{\sigma_i^2}}{\sum_i^N \frac{\sigma_0^2}{\sigma_i^2}} = \frac{\sum_i^N x_i \cdot \frac{1}{\sigma_i^2}}{\sum_i^N \frac{1}{\sigma_i^2}} \tag{A.12}$$

And for the variance $V(\overline{x})$ of this mean value, the following equation holds:

$$V(\overline{x}) = \frac{1}{\sum_i^N \frac{1}{\sigma_i^2}} \equiv \sigma^2 \tag{A.13}$$

Application to Photon Counting Using Photon Spectra

Let n_i be the possible outcomes ($n_i \in [0; \infty]$) of a photon counting measurement of *one* event. Specifically: $n_0 = 0,\ n_1 = 1,$ ... meaning that n_i denotes the bin number in the histogram. The content N_i then states how many times a number of i photons were counted. The total number of triggered events is equal to the sum: $N = \sum_{i=0}^{i=\infty} N_i$. In practical applications, the summation can be terminated once the last bin with content larger than 0 has been taken into account.
The weighted mean value of the number of photons from all events is then given as:

$$\overline{n}_{\text{weighted}} = \frac{\sum_{i=0}^{i=\infty} n_i \cdot \omega_i}{\sum_{i=0}^{i=\infty} \omega_i} \tag{A.14}$$

The weight of each photon count is proportional to the number of entries in the corresponding bin with relative deviation $\sigma_{rel,i}$:

$$\sigma_{rel,i} = \frac{\sqrt{N_i}}{N_i} \qquad \Rightarrow \qquad \omega_i = \frac{1}{\sigma_{rel,i}^2} = N_i \tag{A.15}$$

meaning that bins with no entries do not appear in the mean value under equation (A.14), while the largest bin gets the largest weight. It was assumed that the deviation of each bin is equal to the square-root of the number of entries in the bin, which holds for Poisson distributions. This implies for the photon mean value in equation (A.14):

$$\overline{n}_{\text{weighted}} = \frac{\sum_{i=0}^{i=\infty} \frac{1}{\sigma_{rel,i}^2} \cdot n_i}{\sum_{i=0}^{i=\infty} \frac{1}{\sigma_{rel,i}^2}} = \frac{\sum_{i=0}^{i=\infty} N_i \cdot n_i}{\sum_{i=0}^{i=\infty} N_i} = \overline{n} \tag{A.16}$$

This is the definition of the mean value as known from the unweighted mean. Using equation (A.13) for the *relative* variance one obtains:

$$\sqrt{V(\overline{n}_{\text{weighted}})} = \sigma_{rel} = \sqrt{\frac{1}{\sum_{i=0}^{i=\infty} \frac{1}{\sigma_{rel,i}^2}}} = \sqrt{\frac{1}{\sum_{i=0}^{i=\infty} N_i}} = \sqrt{\frac{1}{N}} \tag{A.17}$$

$$\Rightarrow \sigma_{rel} = \frac{1}{\sqrt{N}} \tag{A.18}$$

Therefore, the *absolute* uncertainty on the mean value is:

$$\sigma_{\text{abs}} = \overline{n} \cdot \sigma_{rel} = \frac{\overline{n}}{\sqrt{N}} \tag{A.19}$$

A.2.1.3. Conclusions

Using the laws of CLT and weighted average, it could be shown that the mean value of the photon number in case of weighted mean is the same as for the unweighted case. The relative statistical uncertainty on the calculated mean value is equal to the inverse sqareroot of the number of entries that contributed to the histogram of the photon numbers. This makes an error-calculation relatively easy and practicable.

A.2.2. Efficiency estimation:

In general, for a quantity S depending on one or several variables x_i, each of which is assumed to be gaussian distributed with an uncertainty of Δx_i, the errors can be estimated using gaussian error propagation:

$$\Delta S = \sqrt{\sum_i \left(\frac{\mathrm{d}S}{\mathrm{d}x_i} \cdot \Delta x_i \right)^2} \tag{A.20}$$

Simulation results:
For the estimation of the efficiency using simulations, it was assumed that the number of valid events N_{valid} is binomially distributed with a fixed total number of events N. The expectation value for the number of valid events is therefore

$$N_{\text{valid}} = \varepsilon \cdot N \tag{A.21}$$

with ϵ being the efficiency, which is defined by the above equation. The variance is then given as

$$\mathrm{Var}(N_{\mathrm{valid}}) = \varepsilon \cdot (1-\varepsilon) \cdot N = (\Delta N_{\mathrm{valid}})^2 \tag{A.22}$$

For *fixed* N the statistical uncertainty on the efficiency can be expressed as

$$\Delta\varepsilon = \frac{\Delta N_{\mathrm{valid}}}{N} = \frac{\sqrt{\mathrm{Var}(N_{\mathrm{valid}})}}{N} = \sqrt{\frac{\varepsilon \cdot (1-\varepsilon)}{N}} \tag{A.23}$$

This formula has been used to compute the statistical uncertainty on the efficiency from simulation data.
The validity of this formula can also be shown using formula A.20 for the error propagation:

$$\begin{aligned} \Delta\varepsilon &= \sqrt{\left(\frac{\mathrm{d}\varepsilon}{\mathrm{d}N_{\mathrm{valid}}} \cdot \Delta N_{\mathrm{valid}}\right)^2 + \left(\frac{\mathrm{d}\varepsilon}{\mathrm{d}N} \cdot \Delta N\right)^2} \\ &= \sqrt{\frac{\varepsilon \cdot (1-\varepsilon) \cdot N}{N^2}} = \sqrt{\frac{\varepsilon \cdot (1-\varepsilon)}{N}} \end{aligned} \tag{A.24}$$

in the first line, $\Delta N = 0$ was used, because N is fixed in simulations. In cases, where N is not fixed, the uncertainty calculation needs to be extended to take the second part under the root into account, which is demonstrated in the next paragraph.

Results from measurements:
Using measurement data the efficiency was calculated using the following formula (equation 12.7 in the thesis):

$$\varepsilon = \frac{N_{\mathrm{Chkv}} - N_{\mathrm{Rand}}}{(N_{\mathrm{tot}} - N_{\mathrm{BG}} - N_{\mathrm{Dark}}) \cdot (1-\delta)} \tag{A.25}$$

explanations on the individual terms are given in section 12.5. Again, using error propagation, the statistical uncertainty on the efficiency can be estimated as follows:

$$\begin{aligned} \Delta\varepsilon = \Bigg[&\left(\frac{1}{N_{\mathrm{tot}} - N_{\mathrm{BG}} - N_{\mathrm{Dark}}}\right)^2 \cdot \left(\Delta N_{\mathrm{Chkv}}^2 + \Delta N_{\mathrm{Rand}}^2\right) \\ &+ \left(\frac{1}{(N_{\mathrm{tot}} - N_{\mathrm{BG}} - N_{\mathrm{Dark}})^2}\right)^2 \cdot \left(\Delta N_{\mathrm{tot}}^2 + \Delta N_{\mathrm{Dark}}^2 + \Delta N_{\mathrm{BG}}^2\right) \\ &+ \left(\frac{1}{N_{\mathrm{tot}} - N_{\mathrm{BG}} - N_{\mathrm{Dark}}} \cdot \frac{1}{1-\delta}\right)^2 \cdot \Delta\delta^2 \Bigg]^{\frac{1}{2}} \cdot \frac{1}{1-\delta} \end{aligned} \tag{A.26}$$

Calculating the uncertainty with the simpler formula A.23, the uncertainty on the total number of events in the denominator would be neglected and also the scaling of N_{Rand}, which increases the uncertainty, would not be taken into consideration. On average the relative difference between the two ways of calculating the uncertainty is on the order of 3 %.

A.3. Number of Detected Photons per Sample Thickness

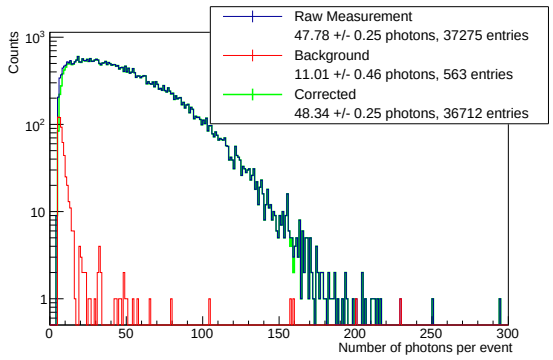

(a) Thickness: 6 mm.

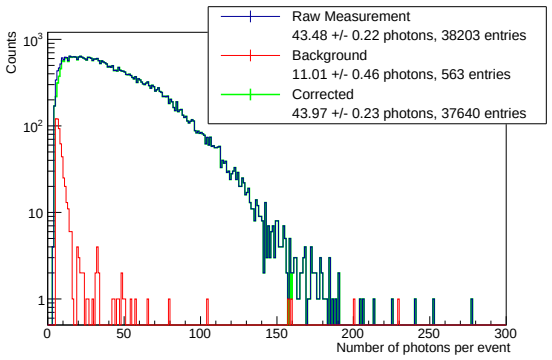

(b) Thickness: 8 mm.

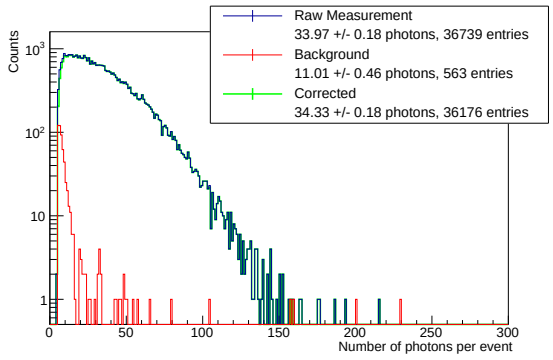

(c) Thickness: 12 mm.

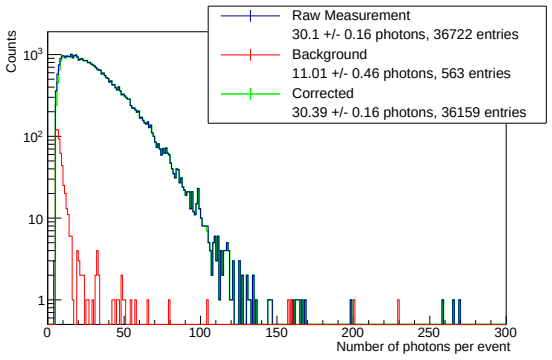

(d) Thickness: 14 mm.

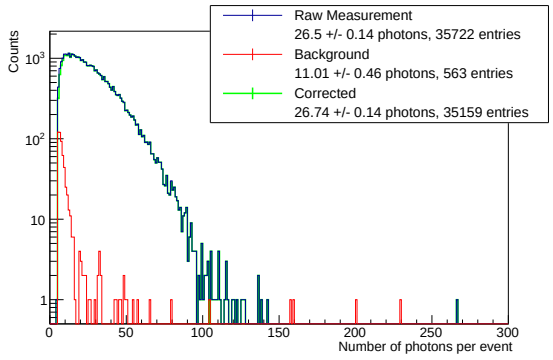

(e) Thickness: 16 mm.

Figure A.2.: Cherenkov photon spectrum for a 60 s measurement in different thicknesses of UV transparent PMMA.

A.4. Log File in Dual-Face Detector Analysis

After every analysis of data taken with the dual-face detector set-up, the input parameters and some results on the coincidence search are printed into a log file. An example is shown in figure A.3. At first, output file names are listed, then the input parameters for the analysis

```
Log file for measurement        /media/reimund/Elements/20200206_Different_Positions_Gamma_Source/
Measurements/24_0cm_300sec.root
ROOT file with results          /media/reimund/Elements/20200206_Different_Positions_Gamma_Source/
Measurements/24_0cm_300sec_Coin_DF.root
------------------------------
Input Parameters for this run:
use_TD_DataBase (0=no, 1=yes):  0
Cut on 511 keV (0=no, 1=yes):   0
FullReadOutMode (0=no, 1=yes):  0
CTW[ps] chkv:   5000
        scint:  200000
        global: 200000
rnocc   chkv:   4
        scint:  20
------------------------------
Number of coincidences on
        chk:    272
        scint:  19952
        both:   272
------------------------------
Number of events with certain number of coincident channels on the Chkv detector:
num_coin_ch     num_evts
4               95
5               48
6               32
7               30
8               12
9               15
10              9
11              8
12              6
13              5
14              4
15              3
16              2
17              0
(ends when first bin is zero)
------------------------------
```

Figure A.3.: Log file example for the analysis of list mode data. It contains input parameters for the analysis and a brief summary of the coincidence results.

including CTWs, rnocc and some boolean flags stating the use of the time difference data base (`Use_TD_DataBase`), a cut on an energy of 511 keV (`Cut on 511 keV`) and if list mode data or preselected data are analyzed (`FullReadOutMode`). After that the number of coincidences on the Cherenkov and on the scintillation detector are shown and the number of globally coincident events. The short list at the end of the log file states how often a certain number of coincident channels has occurred and it ends when the first entry is zero.

B. List of Abbreviations

ADC analog-to-digital converter 151
APD Avalanche Photodiode 70
ASIC application specific integrated circuit 8
CC Compton camera 47
CLT Central Limit Theorem 252
CT Computed tomography 54
CTR coincidence time resolution 87
CTW coincidence time window 76
DAC digital-to-analog converter 93
DAQ data acquisition 94
DCR dark count rate 76
DOI depth of interaction 83
e-*h* electron-hole 65
FEB/D Front End Board type D 146
FEM Front End Module 146
FPGA field programmable gate array 85
FWHM full width at half maximum 51
ILD inverse logarithmic derivative 102
$LaBr_3$(Ce) Cerium-doped Lanthan-Bromide 203
LOR line of response 46
LSB least significant bit 152
LUT look-up table 169
MC Monte Carlo 47
MCS Multiple Coulomb Scattering 51
MRI Magnetic resonance imaging 56
NaI Sodium-Iodine 203
NIST National Institute of Standards and Technology 15
NRCE number of random coincident events 174
OAR organs at risk 53
OCT optical cross talk 74
PCB printed circuit board 96
PDE photon detection efficiency 74
p.d.f. probability density function 223
p.e. photon equivalent 72
PET Positron Emission Tomography 45
PG prompt gamma 47
PLL Phase Locked Loop 94
PMT Photomultiplier Tube 62
PMMA Polymethyl Metacrylate 15
PVT Polyvinyl Toluene 131
rnocc required number of coincident channels 123
ROI region of interest 217

SiPM Silicon Photomultiplier . . . 2
SOBP spread-out Bragg peak . . . 49
SPAD Single Photon Avalanche Diode . . . 70
SPCI single plane Compton imaging . . . 63
SPECT Single Photon Emission Computed Tomography . . . 6
SPTR single photon timing resolution . . . 171
STiC Silicon Photomultiplier Timing Chip . . . 91
TDC time to digital converter . . . 91
TOF time of flight . . . 46
TOT Time over Threshold . . . 85
UV ultraviolet . . . 26
VCO Voltage Controlled Oscillator . . . 94

C. List of Figures

1.1 Number of patients treated in particle therapy facilities 6

2.1 Proton stopping power in PMMA, Al and Pb 15
2.2 Electron stopping power 17
2.3 Collision and radiation loss of electrons in lead 17
2.4 Proton ranges in different materials 19
2.5 Stopping power and Bragg peak of protons with 10 MeV 19
2.6 Electron range for different materials 20
2.7 Schematic visualization of the scattering angle 21
2.8 Scattering angle of electrons in PMMA 22
2.9 Polarization of a medium by a charged particle 23
2.10 Huygens principle of the interference of electro-magnetic waves 24
2.11 Differential Cherenkov photon spectrum 26
2.12 Dispersion curve for a transparent medium 27
2.13 Number of Cherenkov photons per distance versus particle speed for electrons in PMMA 27
2.14 Number of Cherenkov photons per distance versus particle energy 28
2.15 Mass attenuation coefficient of photons in Pb, NaI and PMMA 31
2.16 Mean free path of photons in Pb, NaI and PMMA 31
2.17 Importance of the three photon interaction types 32
2.18 Gamma ray interaction probability in PMMA for different energies 34
2.19 Gamma ray interaction probability for fixed energy in various materials . 34
2.20 Compton Effect 37
2.21 Compton energy versus photon scattering angle 39
2.22 Energy transfer from photon to Compton electron for different scattering angles of the photon 39
2.23 Angular relation between Compton electron and scattered photon 39
2.24 Angular distribution of Compton scattered photons 41
2.25 Polar representation of the differential Compton photon cross section . . . 42
2.26 Polar representation of the differential Compton electron cross section . . 42

3.1 Principle of Positron Emission Tomography (PET) 46
3.2 Dose distributions of protons in water forming a spread-out Bragg peak (SOBP) 50
3.3 Influence of multiple Coulomb scattering (MCS) on a proton beam with an energy of 177 MeV 52
3.4 Dose delivery distribution and range uncertainty for photon and proton beams 53

3.5 Principle of the Slit Camera for range verification . . . 58
3.6 Principle of Prompt Gamma Timing for range verification . . . 59
3.7 Compton Camera working principle . . . 60
3.8 Reconstructed Compton Cones from Simulated Events . . . 62
3.9 Single plane Compton imaging pixel matrix . . . 63
3.10 Gamma source reconstruction using single plane Compton imaging . . . 63
3.11 Compton Camera mounted to a treatment couch . . . 64

4.1 Band structure and electron-hole creation in a semiconductor . . . 66
4.2 Visualization of the processes at a pn-junction . . . 68
4.3 PIN diode structure . . . 69
4.4 The three operational regimes of a photodiode . . . 71
4.5 Equivalent circuit of a Geiger-mode APD . . . 72
4.6 Geiger-mode APDs connected in parallel . . . 73
4.7 Sketch of the general SiPM design . . . 73
4.8 Oscilloscope graph for a signal waveform of an SiPM of type S13360-3050 by HAMAMATSU . . . 73
4.9 SiPM charge spectrum . . . 73
4.10 Response of SiPMs with different number of micro cells . . . 75
4.11 Waveform sketches explaining correlated noise signals . . . 76
4.12 Illustration of optical cross talk . . . 77

5.1 Concept of Compton electron detection using the reconstruction of Cherenkov cones . . . 83
5.2 Cherenkov cone opening angle versus electron energy in PMMA . . . 84
5.3 Simulated coincident hits with and without multiple scattering . . . 86
5.4 Test set-up for a proof of principle . . . 88

6.1 ^{90}Sr spectrum . . . 90
6.2 Schematics of the two set-ups for the first proof of principle . . . 92
6.3 STiC and its evaluation board . . . 93
6.4 Data flow of the signal read-out using STiC . . . 95
6.5 Trigger merging in the hit logic of STiC . . . 95
6.6 Small box with 16 channel SiPM array to be read out with an oscilloscope 97
6.7 Technical drawing with dimensions for the SiPM S13361-3075AS . . . 98
6.8 TSV and pixel structure of SiPM . . . 99
6.9 PDE, CT and gain for SiPM S13360-3075 . . . 99
6.10 Relative PDE for SiPM S13360-3075 . . . 99
6.11 Measured gain versus overvoltage . . . 100
6.12 Current-voltage characteristics for different temperatures . . . 102
6.13 Inverse logarithmic derivative and breakdown point . . . 103
6.14 Measured breakdown voltage versus temperature . . . 104
6.15 DCR versus discriminator threshold for two different temperatures . . . 105
6.16 DCR versus temperature for measurement methods . . . 106
6.17 Transmission of various radiator materials of different thicknesses . . . 108
6.18 Examples of transmission curves for four different sample types . . . 111

6.19 Comparison of TPX transmission with the data sheet . . . 111
6.20 Absorption coefficients for TPX R18, NAS 30 and TOPAS 8007 . . . 113
6.21 Absorption coefficients of various potential radiator materials of different thicknesses . . . 114

7.1 Calculated number of generated Cherenkov photons versus electron energy in PMMA displayed for different sample thicknesses . . . 117
7.2 Simulated number of Cherenkov photons for a 1.5 MeV electron in PMMA 117
7.3 Flow chart of the algorithm for the computation of the number of generated and detected Cherenkov photons . . . 119
7.4 Generated and detected photons for a 1.5 MeV electron in PMMA together with transmission and PDE . . . 120
7.5 Sketch for the consideration of boundaries of the SiPM array in the calculation algorithm . . . 121
7.6 Calculated number of detected photons with and without consideration of the detector geometry . . . 122
7.7 Calculated number of detected photons versus energy for different sample thicknesses . . . 124
7.8 Mean number of detected photons for various thicknesses . . . 125
7.9 Calculated Cherenkov photon spectrum for three different thicknesses . . 125

8.1 Motorized source holder for different source positions with STiC and oscilloscope . . . 128
8.2 Coincidence search algorithm in STiC . . . 129
8.3 Time difference between two channels in STiC . . . 131
8.4 Time difference for all channels in STiC . . . 131
8.5 CTR with and without time difference correction in STiC . . . 132
8.6 CTR for the detection of Cherenkov light and scintillation light . . . 133
8.7 Distribution of coincident hits on 16 channels for centered electron source position . . . 134
8.8 Distribution of coincident hits on 16 channels for shifted electron source position . . . 134
8.9 Distribution of scintillation light on 16 channels measured with STiC . . . 134
8.10 Integration over a waveform with the oscilloscope read-out . . . 136
8.11 Peak integral spectrum . . . 137
8.12 Calibration curve from a peak integral spectrum . . . 137
8.13 Slope of the calibration curve from all 16 channels of the SiPM array . . . 137
8.14 Number of detected photons per calibrated channel . . . 138
8.15 Number of detected photons per calibrated channel in darkness . . . 138
8.16 Measured light intensity with STiC and oscilloscope set-up . . . 139
8.17 Width of Cherenkov Photons versus Sample Thickness . . . 143
8.18 Reconstructed electron source positions from accumulated events . . . 143

9.1 General design of the PETsys based read-out system including detector cooling . . . 146

9.2 Generated and detected photons for a 1.5 MeV electron in UV-transperent PMMA together with transmission and PDE . . . 147
9.3 Assembling of the improved set-up and overall view . . . 149
9.4 Front End Module of the PETsys read-out system . . . 150
9.5 Front End Board type D of the PETsys read-out system . . . 150
9.6 Staircase function measured with TOFPET2 ASIC for two different discriminator step sizes . . . 153
9.7 SiPM dark count rate at −6°C measured with TOFPET2 ASIC . . . 154
9.8 Cross talk probability versus overvoltage measured with TOFPET2 ASIC 154

10.1 Coincident hits of Cherenkov photons from electrons in PMMA of different thicknesses . . . 160
10.2 Simulated coincident hits of Cherenkov photons from electrons in PMMA 161
10.3 Sensitivity of the occupancy to different electron source locations . . . 162
10.4 Quantification of the width of the distribution of coincident Cherenkov photons . . . 163
10.5 Simulated distributions of coincident Cherenkov hits from electrons with fixed energy . . . 165
10.6 Quantification of the width of the distributions of coincident Cherenkov photons from simulated mono-energetic electron events . . . 166
10.7 Reconstruction of the electron source position from accumulated coincident events on 64 channels . . . 167
10.8 Schematic description of the time walk effect . . . 168
10.9 Color plot of ToT dependent time differences for a pair of channels . . . 169
10.10 Color map of the statistical uncertainty of the obtained time differences . 169
10.11 Coincidence time resolution of the detection of Cherenkov light in UV-transparent PMMA . . . 171
10.12 Best single photon timing resolution . . . 172
10.13 CTR for one example channel . . . 172
10.14 DCR dependence of the expected number of random coincident events . . 174
10.15 Dependence of the expected number of random coincident events on the coincidence time window . . . 174
10.16 Number of measured random coincident events in darkness . . . 175

11.1 Principle of photon counting using Time over Threshold . . . 178
11.2 Hit map of the calibration measurements at four different source positions 180
11.3 Example of a ToT spectrum for the calibration of one SiPM channel . . . 181
11.4 Example of a logarithmic calibration fit function . . . 181
11.5 Calibration fit parameters for all channels . . . 182
11.6 Color plots for number of hits, number of photons and mean number of photons on 64 channels . . . 183
11.7 Color plots for number of hits, number of photons and mean number of photons in darkness . . . 183
11.8 Spectrum of the number of detected photons in 8 mm UV PMMA . . . 185
11.9 Number of detected photons for different thicknesses from measurements and simulations . . . 186

11.10 Number of detected photons for different thicknesses from measurements and calculations . . . 188
11.11 Visualization of the influence of after pulsing on the ToT . . . 189
11.12 Spectrum of a ^{207}Bi source . . . 192
11.13 Calculated expectation for the spectrum of photon numbers using a Bismuth source . . . 193
11.14 Cherenkov photon spectrum using ^{207}Bi as electron source . . . 193
11.15 Simulated Cherenkov photon spectrum using ^{207}Bi as electron source . . . 195

12.1 Dual-face coincidence set-up for photon detection . . . 202
12.2 Foto showing the Dual-face coincidence set-up from above . . . 203
12.3 Dual-face set-up components in detail . . . 204
12.4 Sorting of list mode data into frames . . . 208
12.5 ^{22}Na spectrum measured with NaI scintillator at two different detector thresholds . . . 209
12.6 Influence of different time frames on the scintillator signal . . . 211
12.7 Energy versus time difference to first signal . . . 212
12.8 Scintillator spectrum for two different coincidence time windows . . . 213
12.9 Dependency of the 511 keV peak position on the coincidence time window 213
12.10 Comparison of different rnocc for the reference detector . . . 214
12.11 NaI scintillator spectrum for different rnocc . . . 214
12.12 Comparison of the time distribution of SiPM signals with and without correction of inherent time differences . . . 215
12.13 Coincidence time resolution of the Ketek detector array for a measurement with pulsed LED . . . 215
12.14 LaBr spectrum from a test measurement in ToT mode . . . 216
12.15 LaBr spectrum using charge integration . . . 216
12.16 NaI scintillator spectrum together with global coincidences . . . 218
12.17 Coincidence time resolution for three different scintillators in the dual-face coincidence set-up . . . 219
12.18 Full and dark count corrected spectra of $LaBr_3$(Ce) and NaI . . . 222
12.19 Background estimation fit with $LaBr_3$(Ce) . . . 225
12.20 Background estimation fit with NaI . . . 227
12.21 Efficiency for various ranges of interests . . . 228
12.22 Dual-face set-up for gamma ray detection implemented in Geant4 . . . 231
12.23 Efficiency for gamma detection versus photon detection efficiency of the SiPM 233
12.24 Efficiency for gamma detection versus gamma energy from simulated events 234
12.25 Coincident hits of Cherenkov photons for different scintillator materials for the reference detector with and without an energy cut . . . 235
12.26 Histogram of the number of detected photons per event with and without energy cut . . . 238
12.27 Histogram of the number of photons per event for various required numbers of channels . . . 239
12.28 Histogram of the number of photons per event from simulated events . . . 239
12.29 Mean number of detected photons from simulated events for different gamma energies and rnocc . . . 239

12.30 Coincident hits for five different gamma source locations 240
12.31 Simulated coincident hits for five different gamma source locations 241
12.32 True and reconstructed source position from measurement and simulation data 242

13.1 Accumulated photon hits from different parts of the electron track 248
13.2 Extended set-up with SiPM arrays at the side walls of the radiator. 249

A.1 Dark count rate versus threshold at different temperatures 251
A.2 Photon spectra for different PMMA thicknesses 257
A.3 Log file example for the analysis of list mode data 258

D. List of Tables

4.1 Band gap energies of some semiconductor types 67
4.2 Characteristics of PIN diode, APD and Geiger-mode APD 71

6.1 Parameters and values for the SiPM type S13360-3075 by HAMAMATSU . . . 100
6.2 Radiator material properties and mean transmission 109

8.1 Results for the number of detected photons and Time over Threshold 141

9.1 Dark count rate and cross talk probability $-6°C$ 155

10.1 Data taking and analysis parameters with PETsys 160

11.1 Number of detected photons from measurement, simulation and calculation . 188

12.1 Comparison of scintillator materials 204
12.2 Parameters and values for the SiPM type PA3325-WB-0808 by KETEK . . . 205
12.3 Parameters for the measurements with the dual-face gamma detection set-up 215
12.4 Coincidence rate for gamma detection using NaI 217
12.5 Fit parameters and result from the efficiency calculation 226
12.6 Systematic uncertainties on the efficiency 229
12.7 Systematic uncertainties on the efficiency obtained with simulations 233
12.8 Center and width of distribution of accumulated hits 236
12.9 Number of detected Cherenkov photons per detected gamma event 236

A.1 Temperature dependent dark count rate and cross talk probability for S13361-3075AS by HAMAMATSU 252

References

[Agi20] Agilent Technologies. *Specification Sheet, Varian Cary® 50 UV-Vis spectrophotometer*. visited online: March 3, 2020. 2020. URL: https://www.agilent.com/cs/library/specifications/public/si-0270.pdf.

[Ago+03] S Agostinelli et al. "GEANT4 – a simulation toolkit". In: *Nuclear Instruments and Methods in Physics Research Section A: Accelerators, Spectrometers, Detectors and Associated Equipment* **506** (3 July 2003), pp. 250–303. DOI: 10.1016/S0168-9002(03)01368-8.

[Ahm09] R M Ahmed. "Optical study on poly (methyl methacrylate)/poly (vinyl acetate) blends". In: *International Journal of photoenergy* **2009** (2009). DOI: 10.1155/2009/150389.

[Ali18] Ayesha Ali. "Characterization of Silicon Photomultipliers". MA thesis. University of Siegen, 2018.

[BYB13] Kwamena E Baidoo, Kwon Yong, and Martin W Brechbiel. "Molecular pathways: targeted α-particle radiation therapy". In: *Clinical cancer research* **19**.3 (2013), pp. 530–537. DOI: 10.1158/1078-0432.CCR-12-0298.

[Bar93] Roger J Barlow. *Statistics: a guide to the use of statistical methods in the physical sciences*. Vol. **29**. John Wiley & Sons, 1993.

[Bay+19a] Reimund Bayerlein et al. "Coincident detection of Cherenkov light from higher energetic electrons using silicon photomultipliers". In: *Nuclear Instruments and Methods in Physics Research Section A: Accelerators, Spectrometers, Detectors and Associated Equipment* **930** (2019), pp. 74–81. DOI: 10.1016/j.nima.2019.03.049.

[Bay+19b] Reimund Bayerlein et al. "Gamma-Ray Imaging Using Cherenkov Cone Detection from Energetic Compton Electrons". In: *2019 IEEE Nuclear Science Symposium and Medical Imaging Conference (NSS/MIC)*. 2019, pp. 1–3. DOI: 10.1109/NSS/MIC42101.2019.9059810.

[Bay+20] Reimund Bayerlein et al. "Coincident detection of Cherenkov photons from Compton scattered electrons for medical applications". In: *Nuclear Instruments and Methods in Physics Research Section A: Accelerators, Spectrometers, Detectors and Associated Equipment* **958** (2020). Proceedings of the Vienna Conference on Instrumentation 2019, p. 162797. ISSN: 0168-9002. DOI: https://doi.org/10.1016/j.nima.2019.162797.

[Bea+15] Guy Beadie et al. "Refractive index measurements of poly (methyl methacrylate)(PMMA) from 0.4–1.6 μm". In: *Applied optics* **54**.31 (2015), F139–F143. DOI: 10.1364/AO.54.00F139.

[Ben20] Jona Bensberg. "Rekonstruktion von Elektronen durch koinzident detektierte Cherenkov-Photonen". BA thesis. University of Siegen, Feb. 2020.

[Ber+99] Martin J Berger et al. "Stopping-Power & Range Tables for Electrons, Protons, and Helium Ions". In: *NIST Standard Reference Database 124* (1999). DOI: 10.18434/T4NC7P.

[Bir64] J B Birks. *The Theory and Practice of Scintillation Counting*. Pergamom, 1964.

[Bon93] D E Bonnett. "Current developments in proton therapy: a review". In: *Physics in Medicine and Biology* **38**.10 (1993), pp. 1371–1392. DOI: 10.1088/0031-9155/38/10/001.

[Bow03] David I Bower. *An introduction to polymer physics*. American Association of Physics Teachers, 2003.

[Bä20a] Hedia Bäcker. "Geant4 Simulation of a Cherenkov-Based SiPM Compton Camera Prototype Setup". MA thesis. University of Siegen, Feb. 2020.

[Bä20b] Hedia Bäcker. *Simulation in Geant4*. private communication, University of Siegen. Mar. 2020.

[Chm+17] V Chmill et al. "Study of the breakdown voltage of SiPMs". In: *Nuclear Instruments and Methods in Physics Research Section A: Accelerators, Spectrometers, Detectors and Associated Equipment* **845** (2017), pp. 56–59. DOI: 10.1016/j.nima.2016.04.047.

[CEF99] S Chu, L Ekström, and R Firestone. *WWW Table of Radioactive Isotopes - The Lund / LBNL Nuclear Data Search*. visited online: January 22, 2020. 1999. URL: http://nucleardata.nuclear.lu.se/toi/.

[Dav19] Charles Patrick Davis. *MedicineNet – Cancer*. visited online: April 19, 2020. 2019. URL: https://www.medicinenet.com/cancer/article.htm.

[Dav68] C M Davisson. "Interaction of γ-radiation with matter". In: *Alpha-, beta-and gamma-ray spectroscopy*. Elsevier, 1968, pp. 37–78. DOI: 10.1016/B978-0-7204-0083-0.50007-9.

[Den20] Sophia Denker. *Simulation in Geant4*. private communication, University of Siegen. Mar. 2020.

[Din13] Nicoletta Dinu. "Instrumentation on Silicon Detectors: from properties characterization to applications". Habilitation thesis. Université Paris Sud - Paris XI, 2013.

[Dra+18] E Draeger et al. "3D prompt gamma imaging for proton beam range verification". In: *Physics in Medicine & Biology* **63**.3 (2018), p. 035019. DOI: 10.1088/1361-6560/aaa203.

[Dys93] Norman Allen Dyson. *Radiation physics with applications in medicine and biology*. New York, NY (United States); Ellis Horwood, 1993.

[Eck+10] Patrick Eckert et al. "Characterisation studies of silicon photomultipliers". In: *Nuclear Instruments and Methods in Physics Research Section A: Accelerators, Spectrometers, Detectors and Associated Equipment* **620**.2-3 (2010), pp. 217–226. DOI: 10.1016/j.nima.2010.03.169.

[Eid+04] S Eidelman et al. "Review of Particle Physics". In: *Physics Letters B* **592**.1 (2004). Review of Particle Physics, pp. 1 –5. DOI: 10.1016/j.physletb.2004.06.001.

[Eva55] Robley Dunglison Evans. *The atomic nucleus*. McGraw-Hill New York, 1955.

[Fis+18] M Fischetti et al. "Characterisation of the secondary-neutron production in particle therapy treatments with the MONDO tracking detector". In: *IL NUOVO CIMENTO* **100**.206 (2018), p. 41. DOI: 10.1393/ncc/i2018-18206-5.

[Fle19] Ivor Fleck. *Number of random coincidences in darkness*. private communication, University of Siegen. May 2019.

[Gar11] Erika Garutti. "Silicon photomultipliers for high energy physics detectors". In: *Journal of Instrumentation* **6**.10 (2011), p. C10003. DOI: 10.1088/1748-0221/6/10/C10003.

[Glo19] Global Cancer Obervsatory, International Agency for Research on Cancer, World Health Organization. *Cancer fact sheets*. visited online: April 19, 2020. 2019. URL: http://gco.iarc.fr/today/data/factsheets/cancers/39-All-cancers-fact-sheet.pdf.

[Gol+14] Christian Golnik et al. "Range assessment in particle therapy based on prompt gamma ray timing measurements". In: *Physics in Medicine and Biology* **59**.18 (2014), pp. 5399–5422. DOI: 10.1088/0031-9155/59/18/5399.

[Gro19] Particle Therapy Co-Operative Group. *PTCOG Patient Statistics*. visited online: March 16, 2020. 2019. URL: https://www.ptcog.ch/index.php/ptcog-patient-statistics.

[GS08] Claus Grupen and Boris Shwartz. *Particle detectors*. Vol. **26**. Cambridge university press, 2008.

[GH20] Stefan Gundacker and Arjan Heering. "The silicon-photomultiplier: fundamentals and applications of a modern solid-state photon detector". In: *Physics in Medicine & Biology* (2020). DOI: 10.1088/1361-6560/ab7b2d.

[Hai+63] Roland H Haitz et al. "Avalanche effects in silicon p—n junctions. I. Localized photomultiplication studies on microplasmas". In: *Journal of applied physics* **34**.6 (1963), pp. 1581–1590. DOI: 10.1063/1.1702639.

[Ham16] Hamamatsu Photonics K.K. *MPPC (Multi-Pixel Photon Counter) arrays, S13360 series*. visited online: February 29, 2020. 2016. URL: https://www.hamamatsu.com/resources/pdf/ssd/s13360_series_kapd1052e.pdf.

[Ham18] Hamamatsu Photonics K.K. *MPPC (Multi-Pixel Photon Counter) arrays, S13361-3050 series*. visited online: February 29, 2020. 2018. URL: https://www.hamamatsu.com/resources/pdf/ssd/s13361-3050_series_kapd1054e.pdf.

[Har+14] T Harion et al. "STiC—a mixed mode silicon photomultiplier readout ASIC for time-of-flight applications". In: *Journal of Instrumentation* **9**.02 (2014), p. C02003. DOI: 10.1088/1748-0221/9/02/C02003.

[Har15] Tobias Harion. "The STiC ASIC High Precision Timing with Silicon Photomultipliers". PhD thesis. Ruprecht-Karls-Universität Heidelberg, 2015. DOI: 10.11588/heidok.00019194.

[HB19] Christiana Honsberg and Stuart Bowden. *PV Education – Optical Properties of Silicon*. 2019. URL: https://www.pveducation.org/pvcdrom/materials/optical-properties-of-silicon.

[HH89] Paul Horowitz and Winfield Hill. *The art of electronics*. Cambridge Univ. Press, 1989.

[HG+16] Fernando Hueso-González et al. "Compton camera and prompt gamma ray timing: two methods for in vivo range assessment in proton therapy". In: *Frontiers in oncology* **6** (2016), p. 80. DOI: 10.3389/fonc.2016.00080.

[HG+18] Fernando Hueso-González et al. "A full-scale clinical prototype for proton range verification using prompt gamma-ray spectroscopy". In: *Physics in Medicine & Biology* **63**.18 (2018), p. 185019. DOI: 10.1088/1361-6560/aad513.

[Ind07] Inductiveload via wikibooks.org. *Pn Junction Diffusion and Drift*. visited online: March 19, 2020. 2007. URL: https://en.wikibooks.org/wiki/File:Pn_Junction_Diffusion_and_Drift.svg.

[Ine16] Ineos Styrolution. *NAS® 30 – Styrene Methylmethacrylate Copolymer (SMMA), Technical Datasheed*. 2016. URL: www.ineos-styrolution.com.

[Jel58] John Vernon Jelley. *Cherenkov radiation and its applications*. Pergamon, 1958.

[Joh17] Robert P Johnson. "Review of medical radiography and tomography with proton beams". In: *Reports on Progress in Physics* **81**.1 (2017), p. 016701. DOI: 10.1088/1361-6633/aa8b1d. URL: https://doi.org/10.1088%2F1361-6633%2Faa8b1d.

[KET18] KETEK, GmbH. *Product Data Sheet SiPM – Silicon Photomultiplier PA3325-WB-0808*. visited online: March 4, 2020. 2018. URL: https://www.ketek.net/wp-content/uploads/2016/12/KETEK-PA3325-WB-0808-Datasheet.pdf.

[KET19] KETEK GmbH. *Product Data SheetSiPM – Silicon Photomultiplier PM3325-WB-D0*. visited online: March 4, 2020. 2019. URL: https://www.ketek.net/wp-content/uploads/2018/12/KETEK-PM3325-WB-D0-Datasheet.pdf.

[KET20] KETEK GmbH. *Device Parameters*. visited online: March 4, 2020. 2020. URL: https://www.ketek.net/sipm/technology/device-parameters/.

[Kha18] Waleed Khalid. "Detection of Cherenkov Photons Using Silicon Photomultipliers". Master's thesis. University of Siegen, Feb. 2018.

[Kno10] Glenn F Knoll. *Radiation detection and measurement*. John Wiley & Sons, 2010.

[KL13] Antje-Christin Knopf and Antony Lomax. "In vivo proton range verification: a review". In: *Physics in Medicine and Biology* (2013). DOI: 10.1088/0031-9155/58/15/R131.

[KW16] H Kolanoski and N Wermes. *Particle Detectors*. Springer Spektrum, 2016.

[Kor+13] S Korpar et al. "Study of a Cherenkov TOF-PET module". In: *Nuclear Instruments and Methods in Physics Research Section A: Accelerators, Spectrometers, Detectors and Associated Equipment* **732** (2013), pp. 595–598. DOI: 10.1016/j.nima.2013.05.137.

[Lan15] Christian Lang. "Design of a Compton camera for medical imaging and characterization of its components". PhD thesis. Ludwig-Maximilians-Universität München, 2015.

[LHP67] C Michael Lederer, Jack M Hollander, and Isadore Perlman. *Table of Isotopes*. 6th ed. John Wiley and Sons, Inc., New Yoek, 1967.

[Leh+17] Sebastian Lehrack et al. "Submillimeter ionoacoustic range determination for protons in water at a clinical synchrocyclotron". In: *Physics in Medicine & Biology* **62**.17 (2017), pp. L20–L30. DOI: 10.1088/1361-6560/aa81f8.

[Leo87] William R Leo. *Techniques for Nuclear and Particle Physics Experiments – A How-to Approach*. 1st edition. Springer Verlag, 1987.

[LR09] Claude Leroy and Pier-Giorgio Rancoita. *Principles of Radiation Interaction in Matter and Detection*. 2nd. World Scientific Publishing Co. Pte. Ltd., 2009.

[Li18] Yichen Li. *Poissonian statistics and error estimation*. private communication, University of Siegen. Mar. 2018.

[Lip18] Silvia Liprandi. "Development and performance evaluation of detectors in a Compton camera arrangement for ion beam range monitoring in particle therapy". PhD thesis. Ludwig-Maximilians-Universität München, 2018.

[Lom09] Antony Lomax. "Charged Particle Therapy: The Physics of Interaction". In: *The Cancer Journal* (2009). DOI: 10.1097/PPO.0b013e3181af5cc7.

[Lui19] Luis Ferramacho, PETsys Electronics. *TOFPET2 ASIC – capabilities and limitations*. private communication, IEEE/MIC/NSS Manchester. Nov. 2019.

[Lui20] Luis Ferramacho, PETsys Electronics. *TOFPET2 ASIC – Meaning of LSB values*. private email exchange. Apr. 2020.

[Lyu+19] Yang Lyu et al. "Mini EXPLORER II: a prototype high-sensitivity PET/CT scanner for companion animal whole body and human brain scanning". In: *Physics in medicine and biology* (2019). DOI: 10.1088/1361-6560/aafc6c.

[MS69] Pierre Marmier and Eric Sheldon. *Physics of nuclei and particles*. Vol. **1**. Academic Press, 1969.

[Mat20] MatWeb Material Property Data. *Searchable database for material properties*. visited online: March 4, 2020. 2020. URL: http://www.matweb.com.

[McI85] R J McIntyre. "Recent developments in silicon avalanche photodiodes". In: *Measurement* **3**.4 (1985), pp. 146–152. DOI: 10.1016/0263-2241(85)90024-7.

[Min+06] Chul-Hee Min et al. "Prompt gamma measurements for locating the dose falloff region in the proton therapy". In: *Applied physics letters* **89**.18 (2006), p. 183517. DOI: 10.1063/1.2378561.

[Mit18] Mitsui Chemicals. *TPX – Transparent Polymer X*. visited online: March 3, 2020. 2018. URL: https://www.mitsuichemicals.com/tpx.htm.

[Moy+01] Michael F Moyers et al. "Methodologies and tools for proton beam design for lung tumors". In: *International Journal of Radiation Oncology*Biology*Physics* **49**.5 (2001), pp. 1429 –1438. ISSN: 0360-3016. DOI: https://doi.org/10.1016/S0360-3016(00)01555-8.

[Nah12] J H Nahida. "Spectrophotometric analysis for the UV-irradiated (PMMA)". In: *Int. J. Basic Appl. Sci* **12**.2 (2012), pp. 58–67.

[Nat18] National Cancer Institute at the National Institutes of Health, US. *Cancer Statistics*. visited online: April 19, 2020. 2018. URL: https://www.cancer.gov/about-cancer/understanding/statistics.

[NR91] G Nelson and D Reilly. "Gamma-ray interactions with matter". In: *Passive nondestructive analysis of nuclear materials* (1991), pp. 27–42.

[NT19] David B Newell and Eite Tiesinga. *The International System of Units (SI)*. Tech. rep. 2019. DOI: 10.6028/NIST.SP.330-2019.

[NZ15] Wayne D Newhauser and Rui Zhang. "The physics of proton therapy". In: *Physics in Medicine & Biology* **60**.8 (2015), R155. DOI: 10.1088/0031-9155/60/8/R155.

[Nob20a] Nobel Media AB 2020. *The Nobel Prize in Physics 1927*. visited online: May 01, 2020. 2020. URL: https://www.nobelprize.org/prizes/physics/1927/summary/.

[Nob20b] Nobel Media AB 2020. *The Nobel Prize in Physics 1958*. visited online: May 01, 2020. 2020. URL: https://www.nobelprize.org/prizes/physics/1958/summary/.

[Nur+15] T Conka Nurdan et al. "Design criteria for a high energy Compton camera and possible application to targeted cancer therapy". In: *Journal of Instrumentation* **10**.07 (2015), p. C07018. DOI: 10.1088/1748-0221/10/07/C07018.

[Oto+08] H Otono et al. "Study of the internal mechanisms of Pixelized Photon Detectors operated in Geiger-mode". In: *arXiv preprint arXiv:0808.2541* (2008).

[PP18] Katia Parodi and Jerimy C Polf. "In vivo range verification in particle therapy". In: *Medical Physics* **45**.11 (2018), e1036–e1050. DOI: 10.1002/mp.12960.

[Pau+16] Guntram Pausch et al. "A novel scheme of compton imaging for nuclear medicine". In: *2016 IEEE Nuclear Science Symposium, Medical Imaging Conference and Room-Temperature Semiconductor Detector Workshop (NSS/MIC/RTSD)*. IEEE. 2016, pp. 1–5. DOI: 10.1109/NSSMIC.2016.8069921.

[Pau+18] Guntram Pausch et al. "Detection systems for range monitoring in proton therapy: Needs and challenges". In: *Nuclear Instruments and Methods in Physics Research Section A: Accelerators, Spectrometers, Detectors and Associated Equipment* (2018). DOI: 10.1016/j.nima.2018.09.062.

[Pes+13] Eric Pessis et al. "Virtual Monochromatic Spectral Imaging with Fast Kilovoltage Switching: Reduction of Metal Artifacts at CT". In: *Radiographics* **33**.2 (2013). DOI: 10.1148/rg.332125124.

[PBW12] T E Peterson, A B Brill, and A H Walenta. "High energy gamma-ray imaging using Cherenkov cone detection-A Monte Carlo study with application to a Compton camera system". In: *2012 IEEE Nuclear Science Symposium and Medical Imaging Conference Record (NSS/MIC)*. IEEE. 2012, pp. 3246–3253. DOI: 10.1109/NSSMIC.2012.6551741.

[PET18a] PETsys Electronics. *Time-of-Flight Front End Board D (TOF FEB/D_v2) – Hardware User Guide (v1.3)*. July 2018.

[PET18b] PETsys Electronics. *TOFPET 2 SiPM readout ASIC*. 2018.

[PET18c] PETsys Electronics. *TOFPET2 ASIC Evaluation Kit – Hardware User Guide (v1.2)*. May 2018.

[PET18d] PETsys Electronics. *TOFPET2 ASIC SiPM Readout System – Hardware User Guide (v1.5)*. Dec. 2018.

[PET18e] PETsys Electronics. *TOFPET2 ASIC SiPM Readout System – Software User Guide v2018.09*. Sept. 2018.

[PAE15] Gavin Poludniowski, NM Allinson, and PM Evans. "Proton radiography and tomography with application to proton therapy". In: *The British journal of radiology* **88**.1053 (2015), p. 20150134. DOI: 10.1259/bjr.20150134.

[R B96] R Brun and F Rademakers. *ROOT - An Object Oriented Data Analysis Framework*. Proceedings AIHENP'96 Workshop, Lausanne. Nucl. Inst. & Meth. in Phys. Res. A 389. 1996. URL: http://root.cern.ch/.

[Ram+12] Nepal Ramesh et al. "Flux variation of cosmic muons". In: *arXiv preprint arXiv:1203.0101* (2012).

[Ram08] Marco Ramilli. "Characterization of SiPM: temperature dependencies". In: *2008 IEEE Nuclear Science Symposium Conference Record*. IEEE. 2008, pp. 2467–2470. DOI: 10.1109/NSSMIC.2008.4774854.

[RL09] D Renker and E Lorenz. "Advances in solid state photon detectors". In: *Journal of Instrumentation* **4**.04 (2009), P04004. DOI: 10.1088/1748-0221/4/04/P04004.

[Rex19] Components Inc. Rexon. *RP-408*. visited online: February 3, 2020. 2019. URL: https://www.rexon.com/RP408.htm.

[Roe+11] F Roellinghoff et al. "Design of a Compton camera for 3D prompt-γ imaging during ion beam therapy". In: *Nuclear Instruments and Methods in Physics Research Section A: Accelerators, Spectrometers, Detectors and Associated Equipment* **648** (2011), S20–S23. DOI: 10.1016/j.nima.2011.01.069.

[Rom+18] Giuseppe Romeo et al. "Novel silicon photomultipliers suitable for dual-mirror small-sized telescopes of the Cherenkov telescope array". In: *Nuclear Instruments and Methods in Physics Research Section A: Accelerators, Spectrometers, Detectors and Associated Equipment* **908** (2018), pp. 117–127. DOI: 10.1016/j.nima.2018.08.035.

[Ros66] M E Rose. "Internal Conversion Theory". In: *Internal Conversion Processes*. Elsevier, 1966, pp. 15–33. DOI: 10.1016/B978-0-12-395610-1.50006-7.

[SNS57] C Sah, R N Noyce, and W Shockley. "Carrier Generation and Recombination in P-N Junctions and P-N Junction Characteristics". In: *Proceedings of the IRE* **45**.9 (1957), pp. 1228–1243. ISSN: 2162-6634. DOI: 10.1109/JRPROC.1957.278528.

[Sai16] Saint-Gobain Ceramics and Plastics, Inc. *Detector Assembly Materials*. 2016.

[Sai19] Saint-Gobain Ceramics and Plastics, Inc. *Scintillation Products Technical Note*. visited online: February 3, 2020. 2019. URL: www.crystals.saint-gobain.com/sites/imdf.crystals.com/files/documents/labr-performance-summary-2019.pdf.

[Sch+03] Reinhard Schulte et al. "Design of a proton computed tomography system for applications in proton radiation therapy". In: *2003 IEEE Nuclear Science Symposium. Conference Record (IEEE Cat. No. 03CH37515)*. Vol. **3**. IEEE. 2003, pp. 1579–1583. DOI: 10.1109/NSSMIC.2003.1352179.

[Sel96] S Seltzer. "Tables of X-ray mass attenuation coefficients and mass energy-absorption coefficients". In: *NISTIR-5632* (1996). URL: https://www.nist.gov/pml/x-ray-mass-attenuation-coefficients.

[Sem18] Semiconductor Components Industries. *Introduction to the Silicon Photomultiplier (SiPM)*. 2018. URL: https://www.onsemi.com/pub/Collateral/AND9770-D.PDF.

[She+12] Wei Shen et al. "STiC-A mixed mode chip for SiPM ToF applications". In: *2012 IEEE Nuclear Science Symposium and Medical Imaging Conference Record (NSS/MIC)*. IEEE. 2012, pp. 877–881. DOI: 10.1109/NSSMIC.2012.6551231.

[SJ16] William C Shiel Jr. *MedicineNet – Radiation Therapy*. visited online: April 20, 2020. 2016. URL: https://www.medicinenet.com/radiation_therapy/article.htm#what_are_the_types_of_radiation_therapy.

[SK06] A K Shukla and Utham Kumar. "Positron emission tomography: An overview". In: *Journal of medical physics/Association of Medical Physicists of India* **31**.1 (2006), p. 13. DOI: 10.4103/0971-6203.25665.

[Sme+12] J Smeets et al. "Prompt gamma imaging with a slit camera for real-time range control in proton therapy". In: *Physics in Medicine and Biology* **57**.11 (2012), pp. 3371–3405. DOI: 10.1088/0031-9155/57/11/3371.

[Smi06] Alfred R Smith. "Proton therapy". In: *Physics in Medicine & Biology* **51**.13 (2006), R491. DOI: 10.1088/0031-9155/51/13/R26.

[Sol+16] Paola Solevi et al. "Performance of MACACO Compton telescope for ion-beam therapy monitoring: first test with proton beams". In: *Physics in Medicine & Biology* **61**.14 (2016), p. 5149. DOI: 10.1088/0031-9155/61/14/5149.

[SSI15] I Somlai-Schweiger and Ziegler S I. "CHERENCUBE: Concept definition and implementation challenges of a Cherenkov-based detector block for PET". In: *Medical hysics* **42** (4 Mar. 2015), pp. 1825–1835. DOI: 10.1118/1.4914857.

[Sot+13] Orlando Soto et al. "Characterization of novel hamamatsu multi pixel photon counter (MPPC) arrays for the GlueX experiment". In: *Nuclear Instruments and Methods in Physics Research Section A: Accelerators, Spectrometers, Detectors and Associated Equipment* **732** (2013), pp. 431–436. DOI: 10.1016/j.nima.2013.06.071.

[Spi05] Helmuth Spieler. *Semiconductor detector systems*. Vol. **12**. Oxford university press, 2005.

[SN14] National Institute of Standards and Technology NIST. *CODATA value for the Compton wavelength for the electron*. 2014. URL: https://physics.nist.gov/cgi-bin/cuu/Value?ecomwl%7Csearch_for=Compton+wavelength.

[SJ03] F Stichelbaut and Y Jongen. "Verification of the proton beam position in the patient by the detection of prompt gamma-rays emission". In: *39th PTCOG meeting, San Francisco*. 2003.

[Sur15] Suleman Surti. "Update on time-of-flight PET imaging". In: *Journal of Nuclear Medicine* **56**.1 (2015), pp. 98–105.

[Tan+12] Zongqing Tan et al. "Significant systemic therapeutic effects of high-LET immunoradiation by 212Pb-trastuzumab against prostatic tumors of androgen-independent human prostate cancer in mice". In: *International journal of oncology* **40**.6 (2012), pp. 1881–1888. DOI: 10.3892/ijo.2012.1357.

[Tan+18] Masaharu Tanabashi et al. "Review of particle physics". In: *Physical Review D* **98**.3 (2018), p. 030001. DOI: 10.1103/PhysRevD.98.030001.

[TLP15] P G Thirolf, C Lang, and K Parodi. "Perspectives for Highly-Sensitive PET-Based Medical Imaging Using $\beta+$ γ Coincidences." In: *Acta Physica Polonica, A.* **127**.5 (2015). DOI: 10.12693/APhysPolA.127.1441.

[Thi+16] P G Thirolf et al. "A Compton camera prototype for prompt gamma medical imaging". In: *EPJ Web of Conferences*. Vol. **117**. Nuclear Structure. 2016, p. 05005. DOI: 10.1051/epjconf/201611705005.

[Tie+19] Eite Tiesinga et al. *Values of Fundamental Physical Constants*. 2019. URL: https://www.nist.gov/pml/fundamental-physical-constants.

[TNE74] R W Todd, J M Nightingale, and D B Everett. "A proposed γ camera". In: *Nature* **251**.5471 (1974), p. 132. DOI: 10.1038/251132a0.

[Tur+20] D Turecek et al. "Single layer Compton camera based on Timepix3 technology". In: *Journal of Instrumentation* **15**.01 (2020), p. C01014. DOI: 10.1088/1748-0221/15/01/C01014.

[VA+15] Karen Van Audenhaege et al. "Review of SPECT collimator selection, optimization, and fabrication for clinical and preclinical imaging". In: *Medical physics* **42**.8 (2015), pp. 4796–4813. DOI: 10.1118/1.4927061.

[VK15] Juan José Vaquero and Paul Kinahan. "Positron emission tomography: current challenges and opportunities for technological advances in clinical and preclinical imaging systems". In: *Annual review of biomedical engineering* **17** (2015), pp. 385–414. DOI: 10.1146/annurev-bioeng-071114-040723.

[Č37] P A Čerenkov. "Visible Radiation Produced by Electrons Moving in a Medium with Velocities Exceeding that of Light". In: *Phys. Rev.* **52** (4 1937), pp. 378–379. DOI: 10.1103/PhysRev.52.378.

[Wac+16] H V Wachter et al. "Study on coincidence time resolution with SiPM and TOFPET-ASIC utilizing LYSO GAGG and GFAG". In: *IEEE Nuclear Science Symposium and Medical Imaging Conference*. 2016.

[Wal+16] A H Walenta et al. "GamSim—A windows-based simulation tool for gamma-ray detector development". In: *2016 IEEE Nuclear Science Symposium, Medical Imaging Conference and Room-Temperature Semiconductor Detector Workshop (NSS/MIC/RTSD)*. IEEE. 2016, pp. 1–8. DOI: 10.1109/NSSMIC.2016.8069419.

[Wal+17] A H Walenta et al. "An Efficient Method for Ellipse Reconstruction Using the Hough Transform for Cherenkov Cone Detection". In: *2017 IEEE Nuclear Science Symposium and Medical Imaging Conference (NSS/MIC)*. IEEE. 2017, pp. 1–4. DOI: 10.1109/NSSMIC.2017.8533037.

[Wik17] Wiktionary. *in vivo — Wiktionary, The Free Dictionary*. [Online; accessed 11-December-2019]. 2017. URL: https://en.wiktionary.org/w/index.php?title=in_vivo&oldid=48061056.

[Wil46] Robert R Wilson. "Radiological use of fast protons". In: *Radiology* **47**.5 (1946), pp. 487–491. DOI: doi.org/10.1148/47.5.487.

[Xie+17] Yunhe Xie et al. "Prompt gamma imaging for in vivo range verification of pencil beam scanning proton therapy". In: *International Journal of Radiation Oncology* Biology* Physics* **99**.1 (2017), pp. 210–218. DOI: 10.1016/j.ijrobp.2017.04.027.

[YH+19] Kristian Smeland Ytre-Hauge et al. "A Monte Carlo feasibility study for neutron based real-time range verification in proton therapy". In: *Scientific reports* **9**.1 (2019), p. 2011. DOI: 10.1038/s41598-019-38611-w.

[YC] Zhen-Xiong Yuan and Huangshan Chen. *STiC3 User Guide*. Version 3. Heidelberg University, Kirchoff Institute for Physics.

Acknowledgements

At the beginning of this year, I was invited by the "junge Deutsche Physikalische Gesellschaft (jDPG)" to speak in front of students at the university of Siegen, who have an interest in doing a PhD in physics. I was to talk about my motivation, my project, the requirements and my experience as PhD student in general. For my presentation I chose the title *The Exciting Challenge of a PhD in Applied Particle Physics*. Looking back, I would have to say this title probably sums it up quite nicely.
One the one hand, there was the tremendous excitement of pursuing a concept and trying to realize something that has not been tried out before in that exact way by anyone else. And it is, of course, exciting to then take the obtained results and proudly present them to the scientific community, discuss with colleagues from all over the world and learn a great deal about all the work that is currently ongoing in the field.
On the other hand, the process of achieving a doctoral degree in physics is often accompanied by great challenges, occasional set-backs, unexpected complications, and always a pinch of frustration (every experimentalist would probably agree).
However, therein lies the huge potential to grow personally and professionally. A potential that I could exploit thanks to the help of several important people who supported me all along the way and who I would like to sincerely thank in the following.

At first, I would like to thank Prof. Dr. Ivor Fleck for giving me the opportunity to work on this fascinating project that allowed me to develop an own scientific mindset and follow new ideas. The great mixture of teaching, presenting, researching and publishing enabled me to extend my scientific understanding and to open up my mind about the next step in my life. And, of course, thanks a lot for providing me with all the indispensable feedback on my thesis especially throughout the last few months.

My work on this project would have been much more tedious and surely quite boring if it wasn't for the people I have worked with. First and foremost Hedia Bäcker – I have never met such a loopy yet so smart physicist, who always convinced with her incomparable humor and unswerving calmness. And of course Jona Bensberg who effortlessly implemented a whole series of complex programming and measurement tasks and proved to be my best "coffee-buddy". Nevertheless, the contribution of every single current and former member of this group made it the unique experience it was: Ayesha Ali, Sophia Denker, Waleed Khalid, Ayman Salman and Dr. Ulrich Werthenbach. Furthermore, I would like to thank every colleague at the physics department in building A at Emmy-Noether-Campus, who made my time pleasant and enjoyable.

Furthermore, I would like to thank Dr. Michael Ziolkowski, Stefan Heidbrink, Jens Winter, Waldemar Stroh and Bernd Dostal from the electronic lab on our campus. The way they

have always welcomed me with all my questions and little problems was exceptional. The very same counts for the supportive colleagues from the mechanical workshop around Uwe Krüger.
I would like to thank Sergey Druzhinin for the lively discussions on the physics of transmission and absorption and for working with me on the spectro-photometer. Thanks to Prof. Claus Grupen for his help with professional questions and for offering me his support right from the start.

A big thanks goes out to Huangshan Shen, Vera Koleva Stankova from KIT in Heidelberg and Ole Brandt from DESY in Hamburg, who helped setting up the STiC board and provided constant support. In a similar manner, I would like to thank Luis Ferramacho from PETsys Electronics in Lisbon who helped enabling single photon trigger and TOT measurements with the PETsys read-out board. I would moreover like to thank Tim Binder from LMU Munich, who also shared his experience with this device and lent us a $LaBr_3(Ce)$ crystal and spent two whole days in our lab to support the measurements. He is a prime example of an ambitious young scientist and I wish him all the best for his scientific and personal future.

I would like to thank Prof. Todd Peterson from Vanderbilt University in Nashville, USA, who visited us for 11 weeks in 2018. Not only did we have a productive and fruitful time in the office and the lab, but it was also inspiring and motivating to work with someone who is capable of criticizing in such a supportive fashion. I hope we will always keep in touch.
Thanks a lot to my former colleagues from the ECAP in Erlangen, who were always willing to discuss work or share a few rare moments of free time. Above all, I would like to thank Michael Wagenpfeil for all his thorough explanations and his endless knowledge that he was never too tired to share.

I owe deep gratitude to Lisanne Kraft, my girlfriend, companion, flat-mate and most favorite person. She has always been understanding and supportive in times where workload was massive and common moments were rare. Her kindness and laughter never failed to comfort and amuse me.

This thesis would not have been written without the support of my mother, my father and my brother Uli, who have walked all the way with me and believed in my strengths and endurance. I am very lucky that I was given the opportunity to pursue my own goals and to receive the required high-quality education.

In the end, I would not want to miss the chance of mentioning a few more very special people and friends, who always had an open ear and a cool beer in the fridge: my British friends Alex & Luke Flinders and Tom Jackson. My dear friends from Siegen Trajche Vasilevski, Melanie Wagner, Tim Homrighausen, Christian Wurmbach. The great friends i met in Erlangen: Rolf Halmen, Peter Halmen, Milena & Nicolai “James” Wiezoreck, Katharina Witzmann, Tobias Ziegler, Simon Kreuzer, Julian Wechs, Markus Poetzsch and my friends from VDSt zu Erlangen. And finally, the friends from my home town Claudia Link and Marcella Hirschmann.